



POLITECNICO DI MILANO  
DIPARTIMENTO DI ELETTRONICA, INFORMAZIONE E BIOINGEGNERIA  
DOCTORAL PROGRAMME IN INFORMATION TECHNOLOGY

---

SENSOR-ASSISTED COOPERATIVE  
LOCALIZATION AND COMMUNICATION  
IN MULTI-AGENT NETWORKS

Doctoral dissertation of:  
**Mattia Brambilla**

Supervisor:

**Prof. Monica Nicoli**

Chair of the doctoral programme:

**Prof. Barbara Pernici**

Cycle XXXIII



---

---

# Preface

This thesis presents (part of) the research activities I carried out during my PhD in Information Technology at Politecnico di Milano in the period Nov. 2017 - Sep. 2020. The PhD program has been designed to go deep in advanced localization and communication techniques for vehicular, maritime and industrial applications. Vehicular scenario is the primary interest of my research, where both localization and communication aspects are deeply analyzed. Maritime application has been introduced in my PhD journey thanks to a collaboration with NATO STO CMRE (North Atlantic Treaty Organization - Science and Technology Organization - Centre for Maritime Research and Experimentation), which hosted me as a visiting researcher for few months in 2019. At CMRE I had the opportunity to interact with expert scientists to whom I will always be grateful for having grown my research expertise and provided a scientific attitude towards problems.

The contents of this thesis mostly rely on published and unpublished works on cooperative localization and communication in multi-agent systems. A minor published research on localization in Industry 4.0 is intentionally not included as it does not accommodate the cooperative framework here addressed. To guide the reader in easy access to the published documents, the relations among research topics and publications are as follows:

- Vehicular localization  $\Rightarrow$  [1, 2],
- Vehicular communication  $\Rightarrow$  [3–7],
- Maritime localization  $\Rightarrow$  [8],
- Industrial localization  $\Rightarrow$  [9].

My gratitude goes to all co-authors who helped me in formulating, developing and validating the cited research works [1–9].

The intention of this thesis is to provide the reader insights on practical applications as well as sufficient mathematical principles behind algorithms. This way to proceed is led by my personal interests in providing practical engineering solutions to problems, still keeping a scientific background. This attitude also emerges in the use of real data for testing the developed solutions. I hope this approach allows the interested reader to go deep in technicalities, and to provide intuition and practical implications for the non-expert who might come across this thesis.





---

---

# Abstract

This thesis presents research advances on cooperative localization and communication. These two macro trends are investigated in the general context of mobile multi-agent networks for situational awareness applications, where time-varying agents of unknown absolute location are asked to fulfill positioning and information sharing tasks.

The research on localization aims to develop an integrated solution where cooperative self-localization of agents is combined with multitarget detection, localization and tracking. Targets are not only considered as unknown objects to be just localized, but their statistical properties represent valuable information to be used upside-down to refine the agents' positioning coming from self-definition of the multi-agent network. The operating framework is based on belief propagation, a message passing algorithm working on the factor graph describing all relationships among agents, measurements and external variables. The final result is the development of a generalized solution that is flexible enough to accommodate heterogeneous measurements of diverse agent types, ensuring a wide range of applications. The two primary scenarios addressed in this thesis are maritime and vehicular uses cases, but internet of things in industrial and surveillance contexts are other major applications of interest.

The research on communication is focused on vehicular applications, where the use of Vehicle-to-Everything (V2X) links to extend vehicle's sensing capability by establishing connections with nearby users represents an upgrade for a safer mobility. Such paradigm is here reverted: this thesis proposes the use of vehicles' sensors to enhance communication performances. The specific research topic consists in developing sensor-assisted beam alignment techniques, where narrow directional V2X beams are steered according to the information extracted from perception sensors. Attention is given not only to the specific technical aspects of the methodology and technologies, namely Millimeter-Wave (mmWave) and Free-Space Optics (FSO), but a system-level architecture is proposed too. Inter-vehicle cooperation and intra-vehicle sensor data fusion are combined in a unified system targeted to guarantee reliable beam-based V2X links in mobility scenarios.

Both macro-researches deal with a tight integration of heterogeneous sensors with communication in dynamic multi-agent systems. The volatility of interconnections among agents due to mobility and instability of links mandatorily calls for flexible and adaptive techniques, capable of profitably fuse diverse types of information. The outcomes of this thesis demonstrate how a statistical approach is capable of handling realistic problems and developing versatile solutions.



---

---

# Contents

Preface	I
Abstract	II
List of figures	VIII
List of tables	XIV
List of acronyms	XV
Notation	XX
<b>1 Introduction</b>	<b>1</b>
1.1 Motivations . . . . .	2
1.2 Contributions . . . . .	3
1.3 Outline . . . . .	5
<b>2 Fundamentals of statistical processing, localization and filtering</b>	<b>7</b>
2.1 Introduction to statistical processing . . . . .	8
2.1.1 Continuous and discrete distributions . . . . .	8
2.1.2 Representation of probability distribution . . . . .	12
2.2 Introduction to localization . . . . .	14
2.2.1 Problem formulation . . . . .	14
2.2.2 Localization measurements . . . . .	15
2.2.2.1 Direct measurements . . . . .	15
2.2.2.2 Indirect measurements . . . . .	17
2.3 Introduction to Bayesian filtering . . . . .	23
2.3.1 Kalman filter . . . . .	24
2.3.2 Extended Kalman filter . . . . .	25
2.3.3 Particle filter . . . . .	26
2.3.4 Factor graph and belief propagation . . . . .	27
2.3.4.1 Practical aspects of belief propagation . . . . .	32
<b>3 Cooperative localization in maritime scenarios</b>	<b>35</b>
3.1 Introduction to self-localization and multitarget tracking . . . . .	36
3.1.0.1 Scientific contributions and main limitations . . . . .	39
3.2 System model . . . . .	41

## Contents

---

3.2.1	Agent state-space model . . . . .	41
3.2.2	Target state-space model . . . . .	41
3.2.3	Measurement models . . . . .	42
3.2.3.1	Navigation measurement . . . . .	43
3.2.3.2	Direct measurement . . . . .	43
3.2.3.3	Multiobject tracking (MOT) measurement . . . . .	44
3.3	Stochastic MTT problem formulation . . . . .	45
3.3.1	Object state model . . . . .	45
3.3.2	Modeling the measurement unknown origin . . . . .	47
3.3.3	Conditional pdf of new PT states, DA vector and number of measurements . . . . .	48
3.3.4	Likelihood function of MOT measurements . . . . .	50
3.4	The proposed solution for cooperative self-localization and multi-target tracking . . . . .	51
3.4.1	Target detection and state estimation . . . . .	51
3.4.2	Joint posterior distribution and factor graph . . . . .	52
3.4.3	BP-based algorithm for joint CSL and MTT . . . . .	54
3.4.3.1	Implementation aspects . . . . .	61
3.5	Performance assessment of joint CSL and MTT in maritime scenario . . . . .	62
3.5.1	Simulation settings for maritime scenario . . . . .	62
3.5.2	Performance evaluation of joint CSL and MTT . . . . .	64
3.6	Concluding remarks . . . . .	67
<b>4</b>	<b>Cooperative localization in vehicular scenarios</b>	<b>69</b>
4.1	Introduction to localization in C-ITS . . . . .	70
4.1.0.1	Scientific contributions and main limitations . . . . .	71
4.2	Model of the vehicular scenario . . . . .	73
4.3	Deepening the data association problem . . . . .	75
4.4	Distributed ICP-DA method . . . . .	77
4.4.1	Factorization of the joint posterior pdf . . . . .	78
4.4.2	Belief propagation algorithm for data association and localization . . . . .	79
4.4.3	ICP-DA: particle filter implementation . . . . .	83
4.4.4	ICP-DA: low-complexity implementation . . . . .	85
4.4.5	Implementation aspects . . . . .	86
4.5	Performance assessment in specific road configurations . . . . .	86
4.5.1	Single-road scenario with static features . . . . .	87
4.5.2	Crossroad scenario with dynamic features . . . . .	90
4.6	Performance assessment in a realistic urban scenario in Turin road network . . . . .	93
4.6.1	Traffic modeling . . . . .	93
4.6.2	Evaluation of ICP-DA localization accuracy . . . . .	95
4.7	Concluding remarks . . . . .	100

<b>5</b>	<b>Sensor-assisted V2X communications</b>	<b>103</b>
5.1	Introduction to connected mobility . . . . .	104
5.1.1	Millimeter-Wave V2X communication . . . . .	105
5.1.2	Free-Space Optics V2X communication . . . . .	106
5.1.2.1	Scientific contributions and main limitations . . . . .	107
5.2	Envisioned V2X system architecture . . . . .	108
5.3	Vehicle dynamics modeling and beam pointing . . . . .	110
5.3.1	Vehicle dynamics modeling . . . . .	111
5.3.2	Derivation and estimation of Line-Of-Sight direction . . . . .	112
5.4	Communication system model . . . . .	113
5.4.1	Conventional time-slotted frame structure . . . . .	113
5.4.2	Proposed frame structure and beam alignment procedure . . . . .	114
5.4.3	Millimeter-Wave V2V . . . . .	115
5.4.3.1	Cylindrical array geometry . . . . .	116
5.4.3.2	Millimeter-Wave V2V performance . . . . .	118
5.4.4	Free-Space Optics V2V . . . . .	119
5.4.4.1	Laser and photodetector circular array geometry . . . . .	119
5.4.4.2	Free-Space Optics V2V performance . . . . .	119
5.5	Sensor-assisted beam alignment: performance assessment . . . . .	122
5.5.1	2D preliminary assessment of sensor-assisted V2V performance . . . . .	122
5.5.1.1	mmWave V2V: preliminary results . . . . .	122
5.5.1.2	FSO V2V: preliminary results . . . . .	124
5.5.2	3D assessment of sensor-assisted V2V performance . . . . .	127
5.5.2.1	Simulated vehicular scenario . . . . .	127
5.5.2.2	Millimeter-Wave settings . . . . .	128
5.5.2.3	Free-Space Optics settings . . . . .	130
5.5.2.4	Performance evaluation in two distinct vehicular scenarios . . . . .	131
5.5.2.5	Sensor-assisted V2V with map integration . . . . .	136
5.5.3	Concluding remarks . . . . .	140
<b>6</b>	<b>Conclusions of the PhD journey</b>	<b>143</b>
<b>A</b>	<b>Modeling a mmWave channel and developing subspace-based beam alignment techniques</b>	<b>147</b>
A.1	V2I mmWave scenario . . . . .	148
A.2	Modeling the mmWave LOS/NLOS V2I channel . . . . .	149
A.3	Beam alignment strategies . . . . .	152
A.3.1	Sensor-assisted low-rank beam alignment . . . . .	154
A.3.2	Sensor-assisted long-term geometrical beam alignment . . . . .	154
A.3.3	Sensor-assisted geometrical beam alignment . . . . .	155
A.4	Performance assessment in a LOS/NLOS V2I scenario . . . . .	155
A.5	Concluding remarks . . . . .	157
<b>Bibliography</b>		<b>158</b>



---



---

## List of Figures

1.1	Representation of maritime and vehicular scenarios with some examples of agents. . . . .	2
2.1	Three examples of distributions: Gaussian pdf, Laplace pdf and Poisson pmf. . . . .	9
2.2	Example of probability distribution $p(\mathbf{x})$ of a random vector $\mathbf{x}$ . The individual distributions of each random variable composing $\mathbf{x}$ are $p(x_1) \sim \mathcal{N}(5, 3^2)$ and $p(x_2) \sim \mathcal{N}(0, 5^2)$ . (a) uncorrelated random variables; (b) correlated random variables. Scatter plot of realization of $\mathbf{x}$ and individual probability distribution (left), 3D pdf (right). . . . .	11
2.3	Example of probability distribution $p(\mathbf{x})$ of a random vector $\mathbf{x}$ . The individual distributions of each random variable composing $\mathbf{x}$ are $p(x_1) \sim \mathcal{N}(5, 3^2)$ and $p(x_2) \sim \mathcal{P}(2)$ . Scatter plot of realization of $\mathbf{x}$ and individual probability distribution (left), 2D probability distribution (right). . . . .	11
2.4	Example of sampling a continuous Gaussian pdf. (a) uniform sampling. (b) non-uniform sampling. Two different number of samples $N_P$ are considered. . . . .	13
2.5	Example of direct measurements: distribution and error visualization.	16
2.6	Static localization scenario where four agents of known positions (access points) $\mathbf{x}_1, \mathbf{x}_2, \mathbf{x}_3, \mathbf{x}_4$ localize an unknown agent $\mathbf{x}_5$ (target).	18
2.7	Range-based localization of a target agent by four APs: top view of likelihood functions. (a-d) single-likelihood of each APs. (e) sum of all the four likelihoods. (f) product of all likelihoods. The distribution in each figure is normalized such that the integral is 1 over the whole area. . . . .	19
2.8	Angle-based localization of a target agent by four APs: top view of likelihood functions. (a-d) single-likelihood of each APs. (e) sum of all the four likelihoods. (f) product of all likelihoods. The distribution in each figure is normalized such that the integral is 1 over the whole area. . . . .	21
2.9	3D visualization of likelihood function of all APs for (a) TOA and (b) AOA measurements. . . . .	22

**List of Figures**

---

2.10	Summary of resampling and propagation of particle filter. (a) posterior pdf at time $t$ . (b) values of weights of posterior pdf at time $t$ . (c) resampled weights. (d) particles of the prior at time $t$ with equal weights. . . . .	28
2.11	Example of factor graph of $p(\mathbf{x})$ for $\mathbf{x} = \{x_1, x_2, x_3\}$ and $K = 5$ factors. Variables are indicated by circles, while squares are for factor nodes. . . . .	29
2.12	Admissible and non-admissible configurations of the graph. . . . .	30
2.13	Example of message passing over a graph. Belief propagation is used to compute the beliefs in order to have a representation of $p(\mathbf{x}) = p(x_1, x_2, x_3)$ . . . . .	31
2.14	Example of nodes and factors in a use case scenario of interest. Agents of unknown locations (to be estimated) are the nodes (circles) while the factors indicate the available measurements (such as GPS navigation measurement, or inter-agent measurements). a) Relations between nodes/variables and the localization scenario of the multi-agent network. b) Related factor graph representation. . . . .	34
3.1	Intuition of working principle: agent $\mathbf{s}_1$ pdf by considering (left) self-navigation measurements only, (middle) cooperation with other agents (CSL), (right) cooperation with other agents and exploitation of target information (CSL+MTT). . . . .	40
3.2	Visualization of possible types of measurement available at a given agent. All measurements are referred to agent $\mathbf{s}_1$ . . . . .	42
3.3	Visual representation of a navigation measurement likelihood of agent $\mathbf{s}_1$ . . . . .	43
3.4	Visual representation of likelihood in the cases of Gaussian-distributed range and bearing direct measurements between agents $\mathbf{s}_1$ and $\mathbf{s}_2$ , and used to localize agent $\mathbf{s}_1$ . . . . .	44
3.5	Visual representation of likelihood in the cases of Gaussian-distributed (bistatic) range and bearing indirect measurements between agent $\mathbf{s}_3$ (Tx) and $\mathbf{s}_1$ (Rx), and used for the localization of target $\mathbf{x}_1$ . . . . .	44
3.6	Illustrative example of measurement uncertainty for the case of two closed targets with overlapped bistatic likelihoods. . . . .	47
3.7	Bloch scheme providing the intuition of the proposed solution. Three agent pairs are represented: the first one, a generic one and the last one. Grey box refers to agents, pink for legacy PTs, new PTs are in pale green. Agent cooperative self-localization (CSL) layer is in orange, while data association (DA) is in red and pairwise MTT box in light blue. For convenience, we added the set $\mathcal{A}^*$ which contains all the agents but the transmitter and receiver of the specific agent pair $j$ . . . . .	51
3.8	Factor graph corresponding to the agent self-localization step at the beginning of each time step $t$ . In the graph, all agents are assumed to have both navigation and direct measurements. Shortcuts $\mathbf{s}_a^- \triangleq \mathbf{s}_{a,t-1}$ and $\mathbf{g}_a \triangleq \mathbf{g}(\mathbf{g}_t^{(a)}   \mathbf{s}_{a,t})$ are used. . . . .	56

**List of Figures**

---

3.9	Factor graph for MTT at time step $t$ and agent pair $j$ , with $j_1 = 1$ and $j_2 = 2$ . . . . .	57
3.10	Simulation scenario with four agents circularly counterclockwise moving and four mobile targets. . . . .	63
3.11	Localization accuracy of agents over time. Performance comparison between JLT and SLT. . . . .	65
3.12	Zoom on reconstructed trajectories of agents in outage conditions. . . . .	65
3.13	Performance comparison between JLT and SLR in MTT. a) MOSPA. b) Number of existing targets. . . . .	66
4.1	Example of C-ITS scenario with $N_v = 12$ connected vehicles and $N_f = 10$ passive features. Red links indicate V2V connections (with communication range $R_c$ ), while black ones the V2F connections (with sensing range $R_s$ ) of vehicle $i = 1$ . . . . .	74
4.2	Ego vehicle measurements: GPS (red dotted ellipse) and V2F (black dashed ellipse). . . . .	74
4.3	Details on data association, where vehicles $\mathbf{x}_{i,t}^{(V)}$ , $i \in \{1, 2\}$ jointly sense features $\mathbf{x}_{k,t}^{(F)}$ , $k \in \{1, 2\}$ , with unknown measurement-feature association. b) V2F measurements fusion after association for feature localization (filled ellipses) and enhancement of GPS accuracy (contours). . . . .	76
4.4	Factorization of $p(\boldsymbol{\theta}_t, \boldsymbol{\alpha}_t, \boldsymbol{\beta}_t   \mathbf{z}_{1:t})$ . Shortcuts $h_i = p(\mathbf{x}_{i,t}^{(V)}   \mathbf{x}_{i,t-1}^{(V)})$ , $s_i = p(\mathbf{z}_{i,t}^{(V)}   \mathbf{x}_{i,t}^{(V)})$ , $f_k = p(\mathbf{x}_{k,t}^{(F)}   \mathbf{x}_{k,t-1}^{(F)})$ , $g_{ik} = p(\mathbf{z}_{i,k,t}^{(V2F)}   \mathbf{x}_{i,t}^{(V)}, \mathbf{x}_{k,t}^{(F)})$ are used. . . . .	80
4.5	Factor graph of the BPA-DA. Shortcuts $\nu_{\ell \rightarrow k} = m_{\ell \rightarrow k}^{(p)}(\boldsymbol{\alpha}_{i,k,t})$ , $\zeta_{k \rightarrow \ell} = m_{k \rightarrow \ell}^{(p)}(\boldsymbol{\beta}_{i,\ell,t})$ , $\Psi_{k,\ell} = \Psi(\boldsymbol{\alpha}_{i,k,t}, \boldsymbol{\beta}_{i,\ell,t})$ are used. . . . .	80
4.6	Vehicle and feature location accuracy versus time. a) single-road scenario with feature spacing $d_f = 0.5$ m (b) and $d_f = 3$ m (c). The ICP-DA-PF (orange line) and ICP-DA-LC (green line) methods are compared GPS-based KF approach (blue dotted line) and ICP with known association (black line). . . . .	88
4.7	Vehicular C-ITS scenario (top). Vehicle position accuracy along the road for varying spacing $\Delta$ between features (bottom). . . . .	89
4.8	Vehicle position accuracy versus the distance to the center of the junction for the crossroad scenario in Fig. 1 with static features, for different number of features $N_f$ . The ICP-DA-LC method (green marked line) is compared to the ICP with known association (red line) and to GPS-based KF tracking (blue dotted line). . . . .	91
4.9	Percentages of association errors (blue line) and discarded measurements (orange line) versus the number of features $N_f$ . . . . .	91
4.10	Vehicle position accuracy versus the distance to the center of the junction for the crossroad scenario in Fig. 1 with $N_f = 20$ features, for different values of feature velocity $\mathbf{v}_f = \{1, 2, 5\}$ m/s. . . . .	92
4.11	Percentages of correct association (blue line) and of discarded measurements (orange line) versus the number of feature's velocity $\mathbf{v}_f$ . . . . .	92

**List of Figures**

---

4.12	Urban arterial scenario in Turin, Italy. The area has been divided in three different zones (A, B and C) associated to different GPS accuracies. Features (red triangles) have been placed along the road infrastructure. Map data copyrighted OpenStreetMap contributors and available from <a href="https://www.openstreetmap.org">https://www.openstreetmap.org</a> [10]. . . . .	93
4.13	Traffic flow over time for the two considered traffic conditions: traffic light regulated (TLR) and vehicle self regulated (VSR). Data are aggregated over 5 minutes. . . . .	96
4.14	Number of vehicles inside the scenario for the traffic light regulated (TLR) and vehicle self regulated (VSR) scenarios. Data are aggregated over 5 minutes. . . . .	96
4.15	Mean queue and stop time for the TLR (a) and VSR (b) scenarios. Data are aggregated over 5 minutes. . . . .	96
4.16	Averaged accuracy of position (a) and velocity (b) over time for the two considered scenarios: TLR (continuous line) and VSR (dashed line). The GPS-based accuracy on vehicles (blue line) is taken as reference for the ICP-DA-LC estimate on vehicle position (red line). The green line in (a) indicates the accuracy on features. . . . .	97
4.17	(a) Map of the Turin road network divided into six areas, characterized by different densities of features and GPS conditions, with highlighted locations of vehicles (blue dots) and features (red triangles). (b) CDF of vehicle position accuracy observed in the in TLR scenario over the different areas. . . . .	98
4.18	Vehicle location accuracy over time for both the along-track and cross-track directions in areas 2 (a) and 5 (b) for the TLR scenario.	99
4.19	Vehicle location accuracy over time for both the along-track and cross-track directions in area 2 for the VSR scenario. . . . .	99
5.1	Overview of the proposed sensor-assisted cooperative V2X architecture. . . . .	109
5.2	Navigation and vehicle frames showing the separate effect of the three Cardan angles. a) top view with $\varphi_v, \theta_v = 0, \psi_v \neq 0$ ; b) front view with $\varphi_v, \psi_v = 0, \theta_v \neq 0$ ; c) side view with $\theta_v, \psi_v = 0, \varphi_v \neq 0$ . . . . .	111
5.3	Geometry for a 2-vehicles network, with navigation and vehicle frames and LOS angles for Tx vehicle $v_1$ . . . . .	112
5.4	TDD frame structure. (a) a conventional protocol with BA included in the signaling; (b) the proposed architecture; (c) Sequence of frames and an example of variation of pointing angles $\alpha_v$ and $\beta_v$ in a typical vehicular scenario, normalized with respect to a beamwidth of $2\theta_{B_x^p} = 2\theta_{B_z^p} = 0.1$ deg (an achievable value for FSO systems). The frame duration is chosen $T_{BI} = 10$ ms to match 5G specifications.	114
5.5	Cylindrical array configuration of $N_r$ rings of $N_a$ elements each. . . . .	116
5.6	(a) Comparison of antenna gain in azimuth (left) and elevation (right) for directional (5.13) and omnidirectional directivity of each antenna element. (b) Directivity of the single antenna element for the adopted cosinusoidal pattern (5.13). . . . .	118

**List of Figures**

---

5.7	FSO V2V system. (a) laser/MEMS array. (b) propagation reference system for the description of the laser beam, translated along the pointing direction. . . . .	120
5.8	Properties of vehicle stroke measurements: a) time series of measured stroke; b) stroke statistical properties. . . . .	123
5.9	Straight lane scenario for preliminary analysis on the impact of vibrations over the vertical direction. . . . .	124
5.10	V2V communication throughput comparison. The inertial sensor-assisted beam tracking is compared to conventional BA protocol and to an ideal communication with perfect alignment. a) V2V throughput versus BI duration $T_{BI}$ for three different beamwidth. b) V2V throughput versus beamwidth for three different $T_{BI}$ . . .	125
5.11	V2V throughput for three different levels of compensation of vehicle dynamics and for two values of transmitted power $P_{TX}$ . . . . .	127
5.12	Array pattern for <i>mmWave LD</i> pointing towards broadside direction ( $\alpha = 0$ deg, $\beta = 0$ deg): (a) tridimensional representation of the radiation pattern and (b) the array gain in dB towards different azimuth and elevation angles. The pattern is obtained by considering directional directivity on each antenna element (5.13). . . . .	131
5.13	CDF of the SNR for the proposed sensor-assisted beam tracking method in two different scenarios. Results are plotted for both mmWave and FSO <i>LD/HD</i> configurations for three different values of delay $\tau$ (vehicle time gap $\Delta t = 1$ s). In the inset, part of the trajectory is shown. . . . .	132
5.14	CDF of the SNR in scenario S2: comparison of the proposed sensor-assisted beam tracking method with a conventional beam sweeping (CBS) approach (markers). For CBS, frame durations of 10 and 30 ms are considered. . . . .	133
5.15	Service probability of the proposed sensor-assisted method versus distance (obtained from the time gap $\Delta t$ ) on trajectory S2 for different values of delay $\tau$ . (a) FSO V2V for HD and LD configurations, (b) mmWave V2V for <i>mmWaveLD</i> ( $N_a = 32, N_r = 8$ ). . . . .	134
5.16	CDF of FDD for the proposed sensor-assisted method in scenario S2 for FSO technology and three different values of update delay $\tau$ . . . . .	135
5.17	CDF of SNR for the proposed sensor-assisted method in scenario S2 for mmWave technology under different angular accuracies. Results are plotted for <i>mmWaveHD</i> for different values of delay $\tau$ (vehicle time gap $\Delta t = 1$ s). . . . .	136
5.18	Simulated winding trajectory with variations over three axis. . . . .	137
5.19	CDF of the SNR for the different considered methods and localization accuracies $\sigma_p^L = \{10, 50, 100\}$ cm. Results are obtained for a time gap $\Delta t = 1.5$ s and laser divergence angle $2\theta_B = 1$ deg. . . . .	139
5.20	CDF of the FDD for the proposed prediction-based system (with and without map integration) for different values of localization accuracies $\sigma_p^L = \{10, 50, 100\}$ cm. . . . .	140

---

**List of Figures**

---

5.21	Outage probability $P_{out}$ versus the laser full divergence angle $2\theta_B$ , for different values of localization accuracy and for the different considered methods. . . . .	140
A.1	V2I communications at two different time instants, with beampointing depending on vehicle location. Blue refers to LOS path, red to NLOS ones. . . . .	148
A.2	Grid-based modeling of the road with $U$ road segments of length $\Delta u$ , each comprising $L$ transmission frames of spatial duration $\Delta u_f = vT_f$ . . . . .	150
A.3	An example of three temporal snapshots of the mmWave V2I channel corresponding to the vehicle positions indicated in the figure. . . .	153
A.4	mmWave V2I communication in LOS (left) and NLOS (right) conditions: scenario, BA performance, evolution of cluster angle, power and delay. . . . .	157

---

---

## List of Tables

3.1	Simulation parameters for cooperative localization in maritime environment. . . . .	64
3.2	Performance comparison of JLT and SLT in terms of percentage of Time On Target, for three different threshold distances $d$ . . . . .	67
4.1	Summary of main variables. . . . .	77
4.2	Order of magnitude of BPA-DA computational complexity at each vehicle per each time step $t$ . . . . .	86
5.1	Simulation parameters for preliminary mmWave V2V analyses. . .	124
5.2	Simulation parameters for preliminary FSO V2V analyses. . . . .	126
5.3	Simulation parameters for mmWave and FSO V2V over two trajectories. . . . .	129
5.4	Beamwidth-related parameters for mmWave and FSO in $LD$ and $HD$ configurations. . . . .	130
5.5	Simulation parameters for FSO V2V with map integration. . . . .	138
A.1	NYUSIM classification for large scale and small scale channel parameters. . . . .	149



---

---

## List of Acronyms

3GPP	3rd Generation Partnership Project
4G	Fourth Generation (of cellular networks)
5G	Fifth Generation (of cellular networks)
5GAA	5G Automotive Association
AIMSUN	Advanced Interactive Microscopic Simulator for Urban and Non-Urban Networks
AOA	Angle Of Arrival
AOD	Angle Of Departure
AP	Access Point
AUV	Autonomous Underwater Vehicle
BA	Beam Alignment
BI	Beacon Interval
BP	Belief Propagation
BPA	Belief Propagation Algorithm
BPA-DA	Belief Propagation Algorithm for Data Association
BPA-L	Belief Propagation Algorithm for Localization
C-ITS	Cooperative Intelligent Transportation Systems
C2C-CC	Car 2 Car Communication Consortium
CPHD	Cardinalized Probability Hypothesis Density
CBS	Conventional Beam Sweeping
CDF	Cumulative Distribution Function
CP	Cooperative Positioning
CSL	Cooperative Self-Localization
CSI	Channel State Information
DA	Data Association
DoF	Degrees of Freedom
EKF	Extended Kalman Filter
ETSI	European Telecommunication Standard Institute

## List of Tables

---

FDD	Fade Duration Distribution
FG	Factor Graph
FSO	Free-Space Optics
GNSS	Global Navigation Satellite System
GPS	Global Positioning System
ICP	Implicit Cooperative Positioning
ICP-DA	Implicit Cooperative Positioning with Data Association
ICP-DA-LC	Implicit Cooperative Positioning with Data Association - Low Complexity
ICP-DA-PF	Implicit Cooperative Positioning with Data Association - Particle Filter
IEEE	Institute of Electrical and Electronics Engineers
IM-DD	Intensity Modulation/Direct Detection
IMU	Inertial Measurements Unit
INS	Inertial Navigation System
IoT	Internet of Things
ITS	Intelligent Transportation Systems
JLT	Joint Localization and Tracking
JIPDA	Joint Integrated Probabilistic Data Association
JPDA	Joint Probabilistic Data Association
KF	Kalman Filter
LOA	Levels of Automation
LOS	Line-Of-Sight
LR	Low-Rank
LSP	Large Scale Parameters
LTE	Long Term Evolution
MAP	Maximum-A-Posteriori
MEMS	Micro Electro-Mechanical System
MHT	Multiple Hypothesis Tracking
MIMO	Multiple-Input Multiple-Output
mMIMO	Massive Multiple-Input Multiple-Output
MMSE	Minimum Mean Square Error
mmWave	Millimeter-Wave
MOSPA	Mean Optimal Subpattern Assignment
MOT	MultiObject Tracking
MTT	MultiTarget Tracking
NLOS	Non-Line-Of-Sight
NR	New Radio
NYUSIM	New York University Channel Simulator
PD	Photodetector

## List of Tables

---

pdf	Probability Density Function
PF	Particle Filter
PHD	Probability Hypothesis Density
PIN	Positive-Intrinsic-Negative
PLE	Path Loss Exponent
pmf	Probability Mass Function
PT	Potential Target
RF	Radio Frequency
RMSE	Root Mean Square Error
RSS	Received Signal Strength
RSU	Road Side Unit
SA	Situational Awareness
SA-G	Sensor-Assisted Geometrical
SA-LR	Sensor-Assisted Low-Rank
SA-LTG	Sensor-Assisted Long-Term Geometrical
SL	Spatial Lobes
SLAM	Simultaneous Localization And Mapping
SLT	Separate Localization and Tracking
SNR	Signal-to-Noise Ratio
SPA	Sum-Product Algorithm
SSP	Small Scale Parameters
TDD	Time Division Duplex
TDOA	Time Difference Of Arrival
TOA	Time Of Arrival
TOF	Time Of Flight
TOT	Time On Target
TRL	Traffic-Light Regulated
UE	User Equipment
URLLC	Ultra-Reliable Low-Latency Communications
V2F	Vehicle-to-Feature
V2I	Vehicle-to-Infrastructure
V2V	Vehicle-to-Vehicle
V2X	Vehicle-to-Everything
VSR	Vehicle Self-Regulated
WiFi	Wireless Fidelity



---

---

## Notation

The following univocal notation is used throughout the thesis.

Bold letters describe matrices, column vectors or sets, which can belong to natural numbers  $\mathbb{N}$ , real numbers  $\mathbb{R}$  or complex numbers  $\mathbb{C}$ .

An ordered and known indexing of elements characterizes a vector  $\boldsymbol{\theta} = [\theta_1 \cdots \theta_N]$  of  $N$  entries, while a randomly sorted disposition of entries is typical of a set  $\boldsymbol{\theta} = \{\theta_n\}_{n=1}^N$  of  $N$  elements.

The cardinality of set is identified by the symbol  $|\cdot|$ , leading to  $|\boldsymbol{\theta}| = N$  for the previous case.

Ad-hoc notation is given to widely adopted matrices:  $\mathbf{0}_{m \times n}$  is a null matrix of size  $m \times n$ , while  $\mathbf{I}_m$  denotes the identity matrix of size  $m$  (a square matrix with unitary entries on the diagonal, while the off-diagonal terms are all zeros).

Vector  $\mathbf{1}_N$  is a shortcut for describing a vector of  $N$  entries all equal to 1.

Notation  $\text{diag}(\boldsymbol{\theta})$  refers to a  $N \times N$  diagonal matrix: i.e., a matrix which is all null except for the entries on the diagonal, which are exactly  $\boldsymbol{\theta}$ .

Common vector/matrix operators are the transposition  $(\cdot)^T$ , Hermitian transpose  $(\cdot)^H$ , the Hadamard product (element-wise multiplication)  $\circ$  and the vector norm  $\|\cdot\|$ .

Symbol  $\angle(\cdot)$  is used as shortcut for angle definition: considering a vector  $\boldsymbol{\theta} = [\theta_1 \ \theta_2]^T$ , then  $\angle(\boldsymbol{\theta}) = \text{atan2}(\theta_2, \theta_1)$ .

Notation  $\text{Pr}(\cdot)$  is a shortcut for probability, while Dirac's delta is indicated with the symbol  $\delta(\cdot)$ . Pay attention that a similar symbol is also used: the Kronecker delta  $\delta_{a,b}$ , which is  $\delta_{a,b} = 1$  if  $a = b$ , otherwise  $\delta_{a,b} = 0$  for  $a \neq b$ .

Symbol  $\triangleq$  literally means “defined to be equal to”.

---

# Introduction

This chapter introduces the thesis work (Sec. 1.1), starting by illustrating the motivations and personal vision of the addressed localization and communication problems. Main contributions are highlighted in Sec. 1.2 and the thesis structure is outlined in Sec. 1.3.

## 1.1 Motivations

*Where is what? What is where?*

This thesis aims to provide (partial) answers to these two questions. The estimation of kinematic properties of objects (such as position and velocity) is a main research topic of this work. The localization problem is addressed in the cooperative framework of multi-agent networks, where multiple agents share heterogeneous information that needs to be properly processed. We use the concept of agent as a generic device with sensing and wireless communication capabilities (in principle, wired is also possible but not of interest for the considered applications). Agents can refer to static sensors as well as mobile ones. In the second case, sensing and/or communication devices are typically only a subset of the complete hardware equipment of the agent itself.

Two main application scenarios of multi-agent systems are addressed in this work: namely, vehicular and maritime environments. We will use the term “vehicular” to refer to land vehicles, being this connotation the most widespread for readers. In principle, also maritime scenarios deal with vehicles but we prefer to use the reference “maritime” as it should be of immediate understanding. In these contexts, agents can thus refer to fixed ground-based stations (e.g., Road Side Units - RSUs or coastal radar), seabed or sea surface anchored sensors (e.g., buoys), land vehicles (e.g., cars), sea surface vehicles (e.g., ships), underwater vehicles (e.g., Autonomous Underwater Vehicles - AUVs), or satellites (e.g., Global Navigation Satellite Systems - GNSSs). An illustrative example of possible agents in maritime and vehicular scenarios is sketched in Fig. 1.1.

Knowing the position of agents is a prerequisite that enables diverse services: from navigation systems to geofencing applications (position-triggered applications).

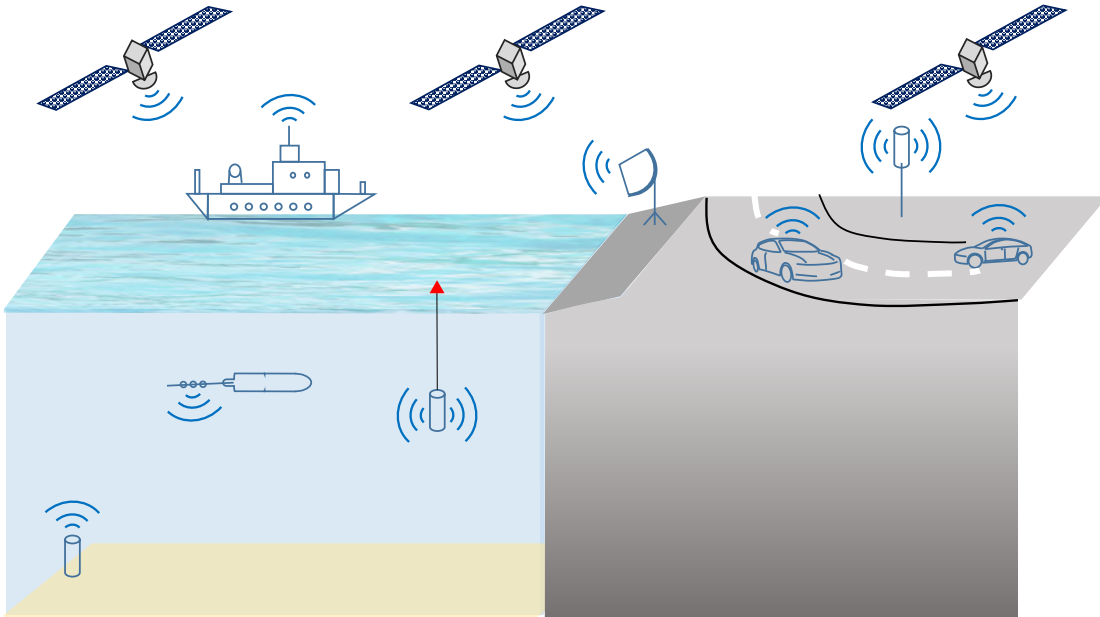


**Figure 1.1:** Representation of maritime and vehicular scenarios with some examples of agents.

Except from static ground-based agents, whose position can be uniquely determined once for all, the localization of all the others is a non trivial problem.

Thanks to worldwide coverage, GNSS offers a practical and widely adopted radio-based solution for agent positioning. However, its accuracy might not fill positioning requirements of all applications. The accuracy of GNSS measurements can vary from few meters ( $< 5$  m) in clear sky condition (full visibility) till about 36 m in the worst site [11, 12]. Moreover, in urban canyons or tunnel, GNSS signals can be lost for several seconds or minutes, preventing any update in position estimate and increasing the localization error. It follows that, for instance, GNSS data can be suited for ship localization and navigation of surface static agents. Also land vehicles can rely on GNSS only, but its performance only fits few applications (geofencing and routing) and cannot be the primary localization method for incoming enhanced (automated) mobility services where a sub-meter accuracy is required. Special care, instead, is to be given to underwater agents, as GNSS signal cannot propagate inside water [13]. In this case, acoustic signals need to be used. These preliminary considerations represent the starting point of the research projects that are presented in this thesis, whose major contribute are highlighted in next section.

## 1.2 Contributions

---

It is goal of this doctoral research to propose augmentation solutions capable of improving localization accuracy and communication efficiency in multi-agent networks, with primary scopes in vehicular and maritime applications. The underlying motivation behind the whole thesis work is the development of solutions where sensing and communication systems profitably interact, helping each other. It is studied how to improve localization of agents by exploring communication techniques as well as how to enhance communication performances by extracting information from perception sensors. Such interactions aim at integrating different aspects (e.g., self localization and target tracking, or sensing and communication), thus differentiating with respect to the historical trend of considering each task as independent. In the following, we detail the contributions on how we integrate the concepts of agent self-localization inside a network and the detection, localization and tracking of unknown objects (targets) outside the network (i.e., not connected), followed by details on how to mutually integrate (helping each other) the sensing and communication tasks within each agent for future mobility systems.

In multi-agent network, a primary task impending agents is the self-localization, such that a network topology is reconstructed through information exchange. Interconnection of agents is a typical task of a communication equipment (radiofrequency/optical/acoustic signals), from which agents can retrieve the reciprocal positioning to be used in localization. By repeated information exchanges, an iterative and cooperative refinement of the geometrical topology allows for a more precise self-localization of agent themselves. A precise agent positioning is fundamental for passive detection, localization and tracking of unknown objects (targets). A reduced uncertainty on agents' location, in fact, strongly helps in a more accurate target identification through noisy measurements. The MultiTarget

Tracking (MTT) problem is studied for both maritime and vehicular application scenarios (with respective peculiarities), with a common goal of showing benefits of a cooperative localization solution that intrinsically takes into account uncertainties on agents' positions (as well as measurement errors). Target individualization is not perceived as a stand-alone task, but the statistical properties of targets are implicitly used as valuable information to refine agents' positions as well. These unknown objects (targets) can be static (parked vehicles or road signs, rocks or wrecks) or mobile (cyclists or pedestrians, vessels or submarines), thus facilitating or hindering their estimation, but a same implicit role is played. A general formulation for Cooperative Self-Localization (CSL) and MTT in multi-agent networks is provided in Chapter 3, where we present a flexible algorithm that integrates heterogeneous data, time-variant network topology and resilient capabilities for jointly performing both CSL and MTT tasks. The algorithm is also capable of handling data association issues related to unknown target observations. Despite being specifically targeted to maritime application, the general properties of stochastic formulation allows to tailor it in any multi-agent system, where each agent might have different sensing and/or communication capabilities (different types of data). Cooperative localization is also the content of Chapter 4, where a distributed variant of a preliminary version of the algorithm in Chapter 3 is specifically proposed for the vehicular environment. A distributed implementation exploiting message passing over inter-vehicle communication links is developed to enable a cooperative consensus-based MTT to implicitly enhance vehicle positioning.

*To summarize in a tweet:* the contribution of the developed joint CSL and MTT technique resides in a flexible graph-based processing that improves localization accuracy and target detection by fusing heterogeneous sources of data and extracting valuable information “hidden” in detected targets.

Agent localization is of high importance also for a second major aspect addressed in this thesis, which is related to communication techniques. Specifically, it is analyzed (in this case for vehicular applications only) how to get benefits from precise positioning information to improve vehicular communications. Vehicle-to-Everything (V2X) communications represent a game-changer for mobility (r)evolution of incoming years, as they convey the basic support for streaming huge amount of data from vehicles to infrastructure to manufactures (or service providers), but also among vehicles themselves for advanced driving solutions. At the time of writing this thesis, examples of commercial vehicles or aftermarket devices with V2X connectivity are being offered to customers, either based on WiFi or cellular (4G LTE) technologies. The fifth generation (5G) of cellular networks has just been standardized, and it has been designed with a specific intent of improving V2X communications. Many 5G research experiments and demonstration of 5G V2X are being carried out, demonstrating that 5G is reasonably expected to become a pervasive technology for V2X market in the incoming years. The research area investigated in this thesis goes beyond 5G systems, which still consider telecommunications as independent. By this thesis, we propose to integrate automotive-specific vehicle information in the V2X communication systems, paving the way for possible new research areas and market trends. The mobility (r)evolution in this sense is expected to foresee strong integration of

multiple sectors, creating an heterogeneous ecosystem that combines together multiple sources of data of different origins. In Chapter 5 we specifically propose a system architecture for sensor-assisted beam-based V2X communications, where the information on vehicle position and orientation (acquired through on-board sensors) plays a key role in guaranteeing a reliable multi-gigabit V2X link. We consider the use of narrow beam as primary mean of communications, and go deep into the research topic of Beam Alignment (BA) techniques. The use of vehicle sensors for V2X communications can also be found in Appendix A, which is focused on channel modeling for testing BA solutions.

*To summarize in a tweet:* the contribution of the developed sensor-assisted BA technique resides in overturning the paradigm of using communication as a mean to extend sensing capabilities, by letting the pointing of narrow beams to be driven by vehicle dynamics-related inputs, improving V2X efficiency.

## 1.3 Outline

---

The thesis is structured as follows.

**Chapter 2** introduces the basic notions of statistical processing which would help the reader to familiarize with key technical contents that will be used in the following of the thesis. The reader will come across introduction on distributions, localization problem and filtering techniques.

**Chapter 3** proposes a generalized version of the conceptualized cooperative self-localization (CSL) and multitarget tracking (MTT) algorithm for multi-agent networks. The solution makes use of graph theory and message passing algorithms to perform statistical inference, allowing agents to fuse heterogeneous information and detect, localize and track targets. Performance analyses in the maritime use case show the benefits of the proposed joint solution with respect to the case of considering CSL and MTT as independent tasks.

**Chapter 4** develops a distributed implementation of cooperative self-localization and target tracking in the vehicular context. Information exchange and consensus algorithms allow vehicles to agree on a common target space and use it as implicit source of information to refine their positioning. Performance analysis on simulated realistic traffic flows highlight the potentials of the proposed technique for next generation mobility systems.

**Chapter 5** presents a sensor-assisted beam alignment architecture and methodology for beam-based vehicular communications. The use of sensors let the V2X beam to be proactively steered along the desired direction, speeding up the alignment and improving the communication efficiency. A general 3D system model, suited for both mmWave and FSO technologies is developed, and performances are evaluated in the most challenging vehicle-to-vehicle use case considering errors on both 3D position and 3D orientation.

**Chapter 6** draws conclusions of the researches carried out during my PhD journey, combining scientific achievements with personal accomplishments.



---

## Fundamentals of statistical processing, localization and filtering

This chapter is targeted to provide a background on statistical processing, which is at the basis of the whole thesis. It is thus goal of next sections to get the reader acquainted with basics notions that are relevant for a faster understanding of technical contents. Firstly, the concept of distribution is introduced, followed by a focus on the statistical approach to localization problems, presenting different types of measurement of interest. We then move to present filtering techniques enabling a real-time estimate of a time-varying agent state, the specific focus is on Bayesian approaches (Kalman Filter, Extended Kalman Filter and Particle Filter) that combine the measurement information with the state evolution model. Lastly, we introduce the concept of a different filtering technique that operates on graphs: belief propagation. The latter solution is the basis of algorithms in Chapters 3 and 4, thus we detail the basic working principles by means of a simple example to facilitate the reader approach.

The chapter is organized as follows. Sec. 2.1 introduces basic concepts of statistical processing. The localization problem is discussed in Sec. 2.2, while the concept of Bayesian filtering is in Sec. 2.3.

## 2.1 Introduction to statistical processing

---

We would like to introduce the reader the basic notions of the statistical approach used in this thesis starting from introducing the concepts of distributions, providing their mathematical definition (Sec. 2.1.1) and describing how they can be handled in practical problems (Sec. 2.1.2). It is our intention to provide the reader the intuition and an easy understanding of distributions. For this reason, key and intuitive examples with continuous and discrete random variables/vectors are provided.

### 2.1.1 Continuous and discrete distributions

For a better understanding of mathematical formulation, we would like to introduce some key concepts related to random variable/vector. To this extent, we start with a 1D random variable  $\mathbf{x}$ . If  $\mathbf{x}$  is a discrete random variable, it can assume finite values within the support it is defined in. On the other hand, if  $\mathbf{x}$  is a continuous random variable, it can assume infinite values within the support it is defined in. In the first case (discrete),  $\mathbf{x}$  is described by a Probability Mass Function (pmf), which gives the probability of the random variable to belong to a countable set  $\mathcal{X} = \{x_1, \dots, x_{|\mathcal{X}|}\}$ . An example can be a random drawn of  $\mathbf{x}$  from  $\mathcal{X}$  (consider, for instance, the set  $\mathcal{X}$  as the possible six results of a roll dice, i.e.,  $\mathcal{X} = \{1, 2, 3, 4, 5, 6\}$ ). In this case, the pmf is:

$$p(\mathbf{x}) = \sum_{m=1}^{|\mathcal{X}|} \Pr(\mathbf{x} = x_m) \delta(\mathbf{x} - x_m), \quad (2.1)$$

being  $\Pr(\mathbf{x} = x_m)$  the probability of assuming the  $m$ -th value. In case each output has the same probability, we have that  $\Pr(\mathbf{x} = x_m) = 1/|\mathcal{X}|$  (in the famous roll dice example, we have  $\Pr(\mathbf{x} = x_m) = 1/6$ , having each number the same chance of occurring). Note that, for statistical consistency, it follows that:

$$\sum_{m=1}^{|\mathcal{X}|} \Pr(\mathbf{x} = x_m) = 1. \quad (2.2)$$

In the other case (continuous), the random variable  $\mathbf{x}$  can assume any value in the support it is defined in. Examples of sets are, for instance, the set of natural numbers  $\mathbb{N}$ , real numbers  $\mathbb{R}$  or complex numbers  $\mathbb{C}$ . A continuous random variable is described by its Probability Density Function (pdf) rather than pmf. Despite pmf and pdf are intrinsically different, we indicate both of them with a same notation  $p(\mathbf{x})$ , letting the reader to distinguish the type according to the context and reference random variable. The pdf is a non-negative function such that:

$$\Pr(a \leq \mathbf{x} \leq b) = \int_a^b p(\mathbf{x}) \, d\mathbf{x}. \quad (2.3)$$

A widespread example of pdf in engineering and research area is the Gaussian pdf. The underlying motivation resided in the central limit theorem [14], which states that the pdf for the standardized sum of independent and identically distributed

random variables with finite variance converges to the normal density function in the sense of relative entropy. A random variable  $x$  is Gaussian distributed around a mean value  $m$  and with variance  $\sigma^2$  in case its pdf is:

$$p(x) = \frac{1}{\sqrt{2\pi\sigma^2}} e^{-\frac{1}{2}\left(\frac{x-m}{\sigma}\right)^2}. \quad (2.4)$$

We will refer to this distribution with the shortcut notation  $p(x) \sim \mathcal{N}(m, \sigma^2)$ . Another example of common pdf is the Laplace one. A random variable  $x$  is drawn from a Laplace pdf if:

$$p(x) = \frac{1}{2b} e^{-\frac{|x-m|}{b}}, \quad (2.5)$$

where  $m$  is the mean value and the scale parameter  $b > 0$  (also known as diversity) affects the variance:  $\text{var}(x) = 2b^2$ . We will refer to this pdf with the shortcut notation  $p(x) \sim \mathcal{L}(m, b)$ . To conclude the brief recap on basics of distributions, we also provide one example of pmf: the Poisson pmf. A random variable has a Poisson pmf with mean parameter  $m > 0$  if:

$$\Pr(x = k) = \frac{m^k e^{-m}}{k!}, \quad (2.6)$$

where the support is for  $k \in \mathbb{N}_0$  (set of natural numbers, including 0). We will refer to this pmf with the shortcut notation  $p(x) \sim \mathcal{P}(m)$ . A representation of probability distribution  $p(x)$  for the three considered cases is illustrated in Fig. 2.1 for  $\mathcal{N}(0, 1)$ ,  $\mathcal{L}(0, 1)$  and  $\mathcal{P}(2)$ , respectively.

Up to now, we considered a single random variable  $x$ . However, the extension to a random vector is (almost) straightforward. In a random vector  $\mathbf{x} = [x_1 \cdots x_N]^T$ ,

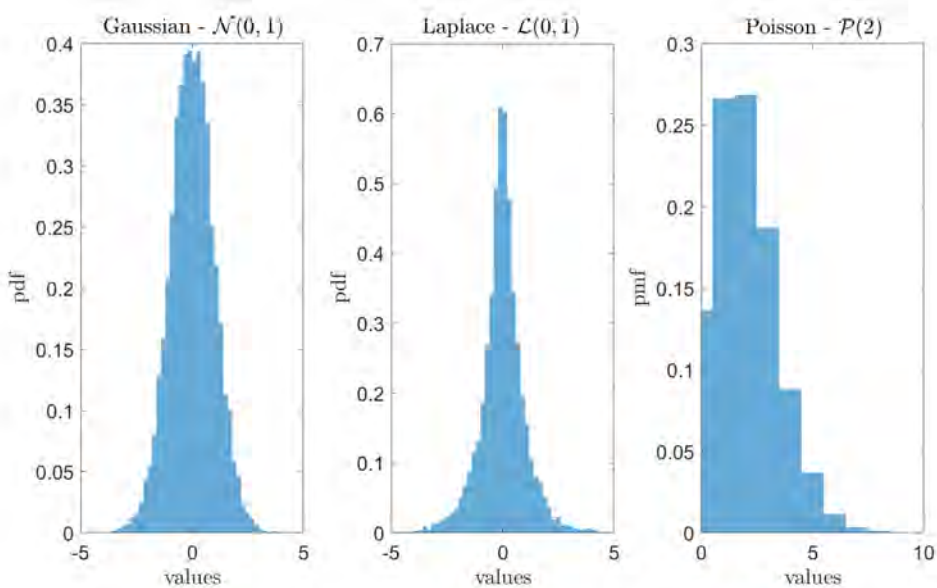


Figure 2.1: Three examples of distributions: Gaussian pdf, Laplace pdf and Poisson pmf.

each entry  $x_n, n = 1, \dots, N$  is a random variable, thus the intuition suggests to consider a random vector as a combination of random variables. A first extension is to consider the case for  $N = 2$ , i.e.,  $\mathbf{x} = [x_1 \ x_2]^T$ . The distribution of  $\mathbf{x}$  is a combination of the individual distribution of  $x_1$  and  $x_2$ , respectively. For instance, if both entries are Gaussian distributed, meaning that  $p(x_1) \sim \mathcal{N}(m_1, \sigma_1^2)$  and  $p(x_2) \sim \mathcal{N}(m_2, \sigma_2^2)$ , also  $p(\mathbf{x})$  is Gaussian as well, and it is defined as:

$$p(\mathbf{x}) = \frac{1}{(2\pi)^N |\mathbf{C}|^{1/2}} \exp\left(-\frac{1}{2}(\mathbf{x} - \mathbf{m})^T \mathbf{C}^{-1}(\mathbf{x} - \mathbf{m})\right), \quad (2.7)$$

where  $\mathbf{m} = [m_1 \ m_2]^T \in \mathbb{R}^{2 \times 1}$  is the vector containing the mean values and  $\mathbf{C} \in \mathbb{R}^{2 \times 2}$  is the  $2 \times 2$  covariance matrix of the random vector  $\mathbf{x}$ . An example for  $N = 2$  is shown in Fig. 2.2a, where the distribution of each random variable is, respectively,  $p(x_1) \sim \mathcal{N}(5, 3^2)$  and  $p(x_2) \sim \mathcal{N}(0, 5^2)$ , and the two variables are uncorrelated. Two Gaussian random variables are uncorrelated when the covariance matrix has a diagonal structure  $\mathbf{C} = \text{diag}([\sigma_1^2 \ \sigma_2^2]) = \text{diag}([3^2 \ 5^2])$  - or, equivalently, if the covariance matrix of two random variables  $x_1$  and  $x_2$  is diagonal, then  $x_1$  and  $x_2$  are uncorrelated. In case  $x_1$  and  $x_2$  are correlated, the covariance matrix presents non-zero values in correspondence of the off-diagonal terms. An example of correlated Gaussian random variables is shown in Fig. 2.2b for a correlation coefficient  $c_{12} = c_{21} = 0.5$ . In the latter case, the covariance matrix becomes:

$$\mathbf{C} = \begin{bmatrix} \sigma_1^2 & c_{12} \\ c_{21} & \sigma_2^2 \end{bmatrix} = \begin{bmatrix} 3^2 & 0.5 \\ 0.5 & 5^2 \end{bmatrix}. \quad (2.8)$$

A peculiarity of a random vector  $\mathbf{x}$  is that it is possible to have a mix of continuous and discrete random variables  $x_n$ , which creates a lattice of distribution of diverse types. An example is given in Fig. 2.3, where a combination of Gaussian pdf  $p(x_1)$  and Poisson pmf  $p(x_2)$  is shown. In this specific case, we considered  $x_1 \sim \mathcal{N}(0, 2^2)$  and  $x_2 \sim \mathcal{P}(2)$ .

From the examples, it is easy to generalize the concept of random vector to the case where  $N > 2$ . An increase in the dimension of  $\mathbf{x}$  prevents a visual representation, but the intuition should assist the reader. Increasing  $N$  also might lead to complex (potentially mathematically intractable) probability distributions. However, it exists a specific case where a closed-form expression fully characterize a pdf of a random vector  $\mathbf{x}$ : the Gaussian case. In the case where  $\mathbf{x}$  is composed of  $N$  Gaussian random variables  $x_n, n = 1, \dots, N$ , it is possible to provide the general formulation as:

$$p(\mathbf{x}) = \frac{1}{(2\pi)^{N/2} |\mathbf{C}|^{1/2}} \exp\left(-\frac{1}{2}(\mathbf{x} - \mathbf{m})^T \mathbf{C}^{-1}(\mathbf{x} - \mathbf{m})\right), \quad (2.9)$$

and the probability distribution of the complete random vector  $\mathbf{x}$  is denoted as multivariate Gaussian pdf, with  $\mathbf{m} \in \mathbb{R}^{N \times 1}$  and  $\mathbf{C} \in \mathbb{R}^{N \times N}$ .

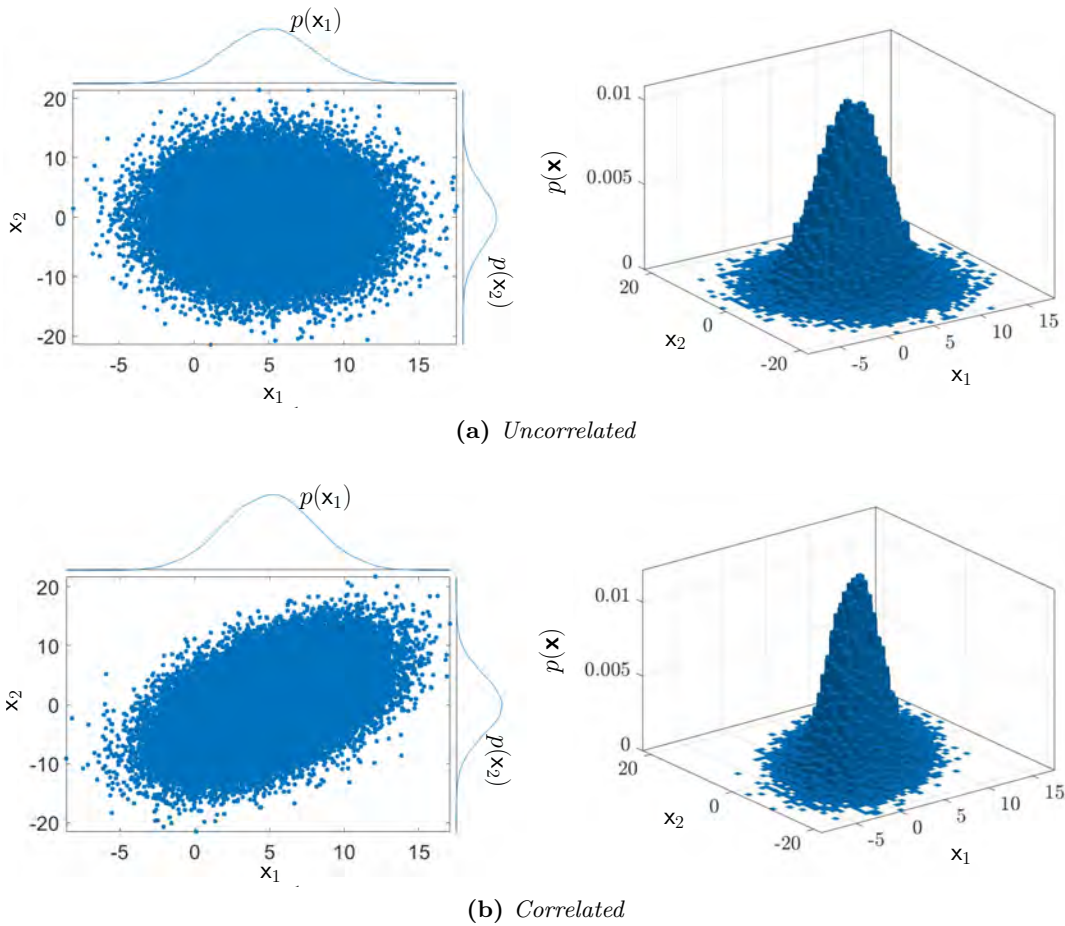


**Figure 2.2:** Example of probability distribution  $p(\mathbf{x})$  of a random vector  $\mathbf{x}$ . The individual distributions of each random variable composing  $\mathbf{x}$  are  $p(x_1) \sim \mathcal{N}(5, 3^2)$  and  $p(x_2) \sim \mathcal{N}(0, 5^2)$ . (a) uncorrelated random variables; (b) correlated random variables. Scatter plot of realization of  $\mathbf{x}$  and individual probability distribution (left), 3D pdf (right).

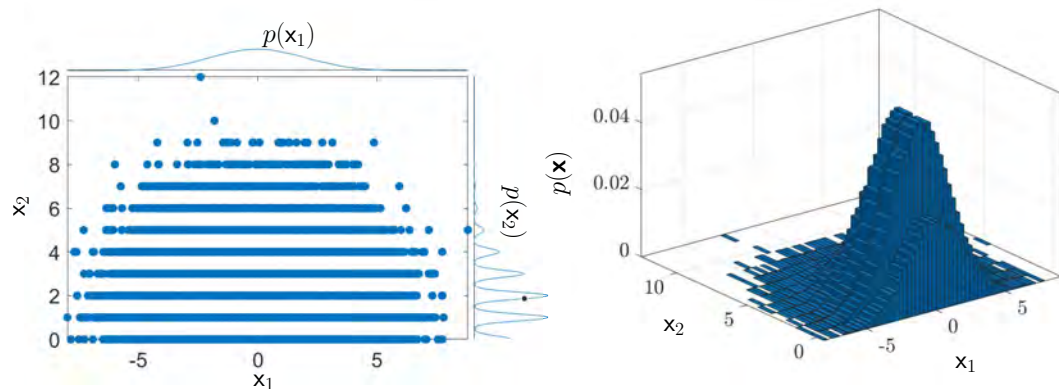


**Figure 2.3:** Example of probability distribution  $p(\mathbf{x})$  of a random vector  $\mathbf{x}$ . The individual distributions of each random variable composing  $\mathbf{x}$  are  $p(x_1) \sim \mathcal{N}(5, 3^2)$  and  $p(x_2) \sim \mathcal{P}(2)$ . Scatter plot of realization of  $\mathbf{x}$  and individual probability distribution (left), 2D probability distribution (right).

## 2.1.2 Representation of probability distribution

Despite pdfs are defined (in theory) for an infinite set, in practical applications it is common to approximate them through a set of finite samples (this is also how previous figures have been generated). We use the Gaussian case to help the disclosure on how it is possible (and convenient) to sample a pdf. The methodology, however, is also valid for any other pdf.

Fig. 2.4a reports a Gaussian pdf  $p(\mathbf{x}) \sim \mathcal{N}(0, 3^2)$ . Being a pdf, its support is infinite (here limited between -15 and +15 for visualization purposes). In practical applications, there are cases in which it is possible to (theoretically and practically) handle such pdf, but sometimes this aspect might be unfeasible. Approximation is a powerful tool for describing pdf in a convenient way, limiting the loss of information. Widely adopted techniques approximate the pdf by set of samples.

By selecting convenient sample points and assigning proper weights it is possible to have an approximation of the pdf. This concept is illustrated in Figs. 2.4b and 2.4c, where  $N_p$  samples are used to characterize the Gaussian pdf in Fig. 2.4a. The choice of sampling (uniform or non-uniform), as well as the number of points is a key factor in determining the accuracy of approximation. Intuition suggests that a higher number of points  $N_p$  leads to a more accurate approximation. Regarding the distribution of points, a similar reasoning apply: it is more convenient to place points where the pdf assumes higher values, relaxing the accuracy in areas where the pdf assumes lower values. For Gaussian pdf, this means to increase the density in correspondence of the Gaussian peak (around the mean value), and reduce the sampling at the tails. This idea is depicted in Fig. 2.4c, where the difference with respect to an equi-spaced sampling (Fig. 2.4b) immediately pops up. The concept of non-uniform sampling allows us to introduce particle representation.

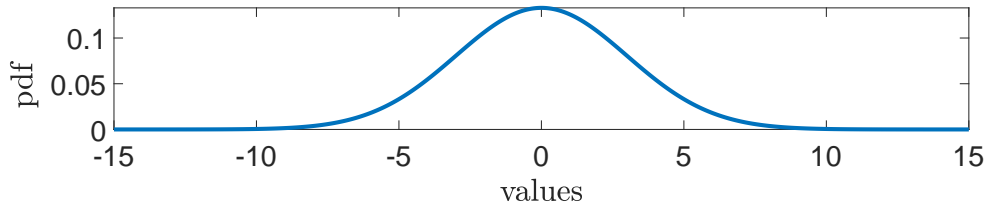
Representing a pdf  $p(\mathbf{x})$  by particles means to use a set of non-uniform weighted Dirac's deltas. Each particle comprises a state vector  $\mathbf{x}_p$ ,  $p = 1, \dots, N_p$ , and a weight  $w_p$ , such that the pdf is approximated as:

$$p(\mathbf{x}) \approx \sum_{p=1}^{N_p} w_p \delta(\mathbf{x} - \mathbf{x}_p) , \quad (2.10)$$

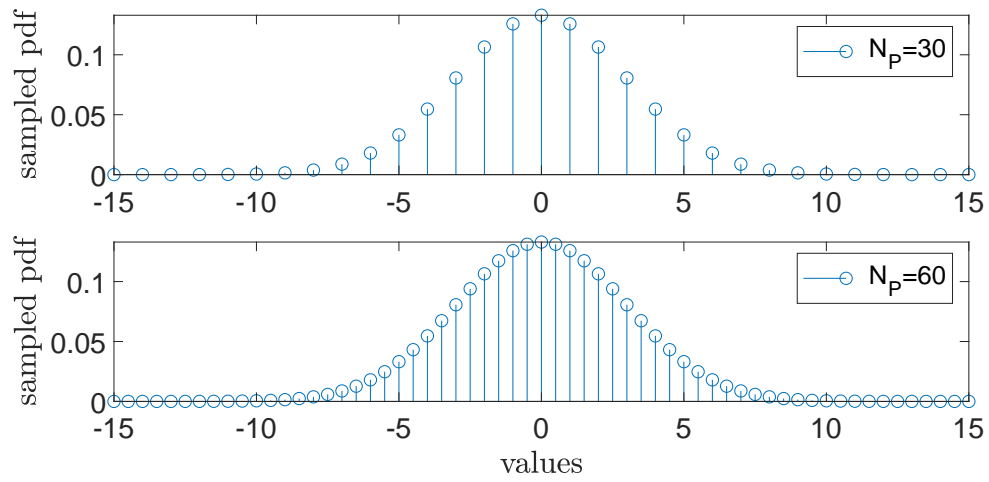
meaning that any pdf can be approximated as the sum of weighted (random) particles. The accuracy of approximation is strictly related to the chosen number of particles  $N_p$ . Being a pdf, the following condition applies:

$$\sum_{p=1}^{N_p} w_p = 1 . \quad (2.11)$$

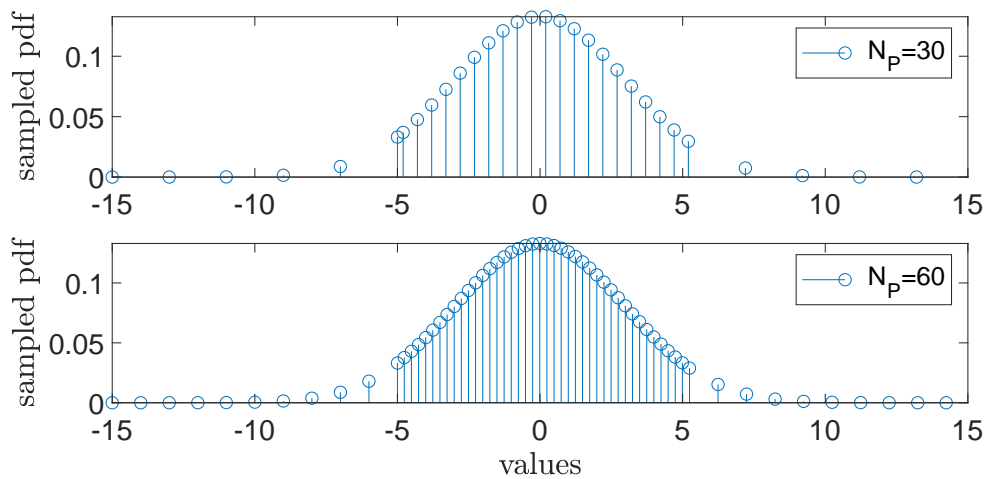
Each single particle  $\{\mathbf{x}_p, w_p\}$  is representative of (part of) the selected pdf. Throughout this thesis, particles are widely used to model non-linear localization problems as they allow to characterize pdfs of unknown type and definition.



(a) Gaussian pdf  $p(x)$ .



(b) Uniform sampling of a Gaussian pdf.



(c) Non-uniform sampling of a Gaussian pdf.

**Figure 2.4:** Example of sampling a continuous Gaussian pdf. (a) uniform sampling. (b) non-uniform sampling. Two different number of samples  $N_P$  are considered.

## 2.2 Introduction to localization

---

This section aims at introducing the localization problem at hand. The statistical formulation is alternated with illustrative examples to combine theoretical aspects with practical applications.

### 2.2.1 Problem formulation

Let us define a generic sensing agent by the state vector  $\mathbf{x}$ . For simplicity, we do not consider the time dependence at the moment, focusing on a single temporal snapshot. According to the specific problem and needs, the vector  $\mathbf{x}$  can contain position information as well as velocity or other kinematic (e.g., acceleration, orientation, etc.) or non-kinematic (e.g., binary variables, biases, etc.) parameters. To introduce the localization problem in an intuitive way, we start considering the 2D position (axis  $x$  and  $y$ ) as characterizing the agent state: namely,  $\mathbf{x} = [p_x p_y]^T$ .

The localization problem reverts in determining the values of  $\mathbf{x}$ . The only approach is to use measurements. The intuition suggests to use a direct measurement of each entry of the state vector: i.e., to evaluate individually the values of  $p_x$  and  $p_y$ . This approach, indeed, represents a straightforward solution for many human-related problems that can be summarized as determining the coordinates of a given point (agent) with respect to a known reference position. An example is the widely known Global Positioning System (GPS), which provides information on the 2D (or 3D) location of the receiving device over the Earth. Alternatively, indirect approaches retrieve localization information by processing other position-related parameters such as distance or angular information. By this approach, the state is somewhat hidden with respect to the available measurements.

Despite the type of available measurement, let us define a generic measurement of the agent state as  $z_m$ , while the vector  $\mathbf{z} = \{z_1, \dots, z_M\}_{m=1}^M$  collects all the  $M$  measurements related to agent  $\mathbf{x}$ . The entries of  $\mathbf{z}$  are, in general, arbitrarily sorted but the specific measurement model (i.e., how they have been obtained and which type of information they carry) is known.

The statistical localization problem is the evaluation of  $\mathbf{x}$  given all measurements in vector  $\mathbf{z}$ . This problem is formulated as an optimization problem where the agent position estimate  $\hat{\mathbf{x}}$  is computed by maximizing the a-posteriori distribution of agent position given the available set of measurements, i.e.,  $p(\mathbf{x}|\mathbf{z})$ , as:

$$\hat{\mathbf{x}} = \arg \max_{\mathbf{x}} p(\mathbf{x}|\mathbf{z}) . \quad (2.12)$$

In most of applications it is common to have an a-priori knowledge of the agent state  $\mathbf{x}$ . An example is represented by the confinement of a GPS receiver in a given region. Any information that is known in advance or considered as assumption falls within the so-called a-priori distribution  $p(\mathbf{x})$ . The availability of such an additional information can be of extremely high importance for the localization problem, as it can be combined with the information coming from measurements. To this extent, a powerful tool comes from the Bayesian theory [15]. According to

Bayesian theory, the a-posteriori distribution (2.12) can be written as:

$$p(\mathbf{x}|\mathbf{z}) = \frac{p(\mathbf{z}|\mathbf{x})p(\mathbf{x})}{p(\mathbf{z})} \propto p(\mathbf{z}|\mathbf{x})p(\mathbf{x}) , \quad (2.13)$$

where  $p(\mathbf{z}|\mathbf{x})$  represents the likelihood function of all measurements. It may be common to find a representation of the likelihood as  $\mathcal{L}(\mathbf{x}|\mathbf{z}) \equiv p(\mathbf{z}|\mathbf{x})$ , however we prefer to not adopt this convention as to avoid misunderstandings on the conditioned variables ( $\mathbf{x}$  in this case).

Under the assumption of measurement independence, it is possible to rewrite the likelihood  $p(\mathbf{z}|\mathbf{x})$  as:

$$p(\mathbf{z}|\mathbf{x}) = \prod_{m=1}^M p(z_m|\mathbf{x}) , \quad (2.14)$$

where  $p(z_m|\mathbf{x})$  identifies the single measurement likelihood.

By replacing (2.12) with (2.13) and inserting (2.14), it follows that the agent state can be inferred by combining a-priori information and measurement likelihood as:

$$\begin{aligned} \hat{\mathbf{x}} &= \arg \max_{\mathbf{x}} p(\mathbf{x}|\mathbf{z}) \\ &\propto \arg \max_{\mathbf{x}} p(\mathbf{z}|\mathbf{x})p(\mathbf{x}) \\ &= \arg \max_{\mathbf{x}} p(\mathbf{x}) \prod_{m=1}^M p(z_m|\mathbf{x}) . \end{aligned} \quad (2.15)$$

Equation (2.15) incorporates the localization concept of combining the information of measurements with what is already available in a general Bayesian-optimum way. In the following subsection, more details on the impact of measurements and examples are given.

## 2.2.2 Localization measurements

A measurement (direct or indirect) of the agent state allows to statistically characterize the distribution of the agent state, shaping and modifying the a-priori information. The combination of multiple measurements allows for a stronger and more reliable update of agent distribution. Further benefits arise when different types of measurements are used. In the following sections, we briefly introduce direct and indirect measurements, with specific focus on the information they carry on rather than lingering on how they are obtained.

### 2.2.2.1 Direct measurements

A direct measurement provides an immediate estimate of each entry (or part of them) of the agent state vector  $\mathbf{x}$ . In case there are no errors, the measurement and the true agent state coincide (being the measurement distribution a Dirac's delta centered at the true agent state), meaning that the estimate is exact. However, any hardware device introduces unavoidable errors that lead to an incorrect agent

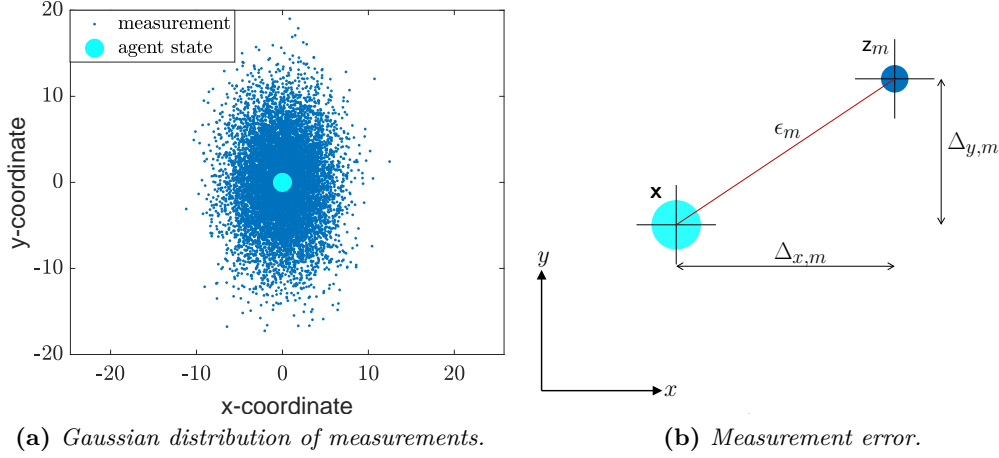


**Figure 2.5:** Example of direct measurements: distribution and error visualization.

localization. The distribution of error characterizes the likelihood function of each measurement  $p(z_m|\mathbf{x})$ . The measurement distribution (e.g., Gaussian, Rayleigh, Poisson, Laplace, etc.) depends on the specific sensor and properties, and it is evaluated in calibration setups. To introduce the intuition of direct measurement, we now provide an example in the case of Gaussian measurement pdf. We consider the agent state  $\mathbf{x} = [p_x p_y]^T = [0 0]^T$  and a set of 1000 measurements. For clarity of explanation, we identify a direct measurement as  $\mathbf{z}_m^{(D)} \triangleq \mathbf{z}_m$ .

A noisy direct measurement of a the agent state  $\mathbf{x}$  is computed as:

$$\mathbf{z}_m^{(D)} = \mathbf{x} + \mathbf{w}^{(D)}, \quad (2.16)$$

where the noise term  $\mathbf{w}^{(D)}$  is drawn from an uncorrelated Gaussian distribution with variance  $\sigma_x^{(D)2}$  on the  $x$ -axis and  $\sigma_y^{(D)2}$  on the  $y$ -axis, i.e.,  $\mathbf{w}^{(D)} \sim \mathcal{N}(\mathbf{0}, \mathbf{C}_w^{(D)})$ , being  $\mathbf{C}_w^{(D)} = \text{diag}([\sigma_x^{(D)2}, \sigma_y^{(D)2}])$ . This concept is shown in Fig. 2.5a for standard deviations  $\sigma_x^{(D)} = 3$  m and  $\sigma_y^{(D)} = 5$  m. Noise introduces an error in the agent state estimation, whose magnitude (statistically) depends on noise distribution and power.

The noisy-induced distance error  $\epsilon_m$  of a direct single-measurement  $\mathbf{z}_m$  of agent  $\mathbf{x}$  can be computed as the norm (Euclidean distance in case of 2D positioning of the considered example) of the difference between the measurement and the real agent state as (see Fig. 2.5b):

$$\epsilon_m = \|\mathbf{z}_m^{(D)} - \mathbf{x}\| = \sqrt{\Delta_{x,m}^2 + \Delta_{y,m}^2}. \quad (2.17)$$

A more statistically valid metric for quantifying the error of an estimation method is the Root Mean Square Error (RMSE), which provides a statistical evaluation of all  $M$  measurements in  $\mathbf{z}$ . The RMSE is computed as:

$$\text{RMSE} = \sqrt{\mathbb{E}[\|\hat{\mathbf{x}} - \mathbf{x}\|^2]} = \sqrt{\frac{\sum_{m=1}^M \|\mathbf{z}_m^{(D)} - \mathbf{x}\|^2}{M}}. \quad (2.18)$$

Direct measurements are extremely powerful and they require few processing of collected data. However in many practical applications (e.g., radar or sonar systems), the information for localization is extracted from radio/acoustic/optical/etc. signals (which clearly do not contain absolute position information), thus requiring further processing. Next section deals with these indirect solutions.

### 2.2.2.2 Indirect measurements

An indirect measurement typically comes from an elaboration of the radio/acoustic/optical/etc. signal. The information extracted from the signal is manipulated in order to be used for localization purposes. The following subsections refer to two types of indirect measurements that are obtained from signal processing. In particular, the discussion is focused on range and angular information.

#### Range measurement

Range measurement refers to a scalar value representing the Euclidean distance of an agent with respect to another one. For simplicity, we denote them as  $\mathbf{x}_1$  and  $\mathbf{x}_2$ , respectively. In most applications, the position of one of them is known, and the localization problem reverts to the other one. An example localization through Access Points (APs) placed at known location. On the other hand, it is possible to deal with applications where none of agents has known positions, but both of them are only statistically described through their distribution (this case will be considered later on in Chapters 3 and 4).

Range information can be retrieved, for instance, by processing radio signals and using temporal or power information. Time Of Arrival (TOA) and Time Difference Of Arrival (TDOA) are two examples of measurements that use temporal information, while Received Signal Strength (RSS) refers to power-based techniques. We focus our attention only on TOA technique, as the others are not considered in any research of interest of this thesis.

TOA-based technique uses the time difference between the transmission and reception of a given signal of interest. This concept can be alternatively identified with the so-called Time Of Flight (TOF) of the signal itself. Range measurement reverts in the conversion of the TOF in distance, by using the propagation speed  $c$ . The latter is proportional the speed of light (for radio signal) or the speed of sound (for acoustic signal), where the proportionality includes any type of medium the signal propagates in. By denoting with  $t_{\text{TX}}$  the time of transmission at agent  $\mathbf{x}_1$  and by  $t_{\text{TOA}}$  the time of reception at agent  $\mathbf{x}_2$ , it follows that  $\text{TOF} = t_{\text{TOA}} - t_{\text{TX}}$ . By defining the range as the norm between the two agents, the range measurement  $z_m^{(\text{R})}$  (as for the previous section, we introduce the superscript to distinguish the type of measurement for an immediate comprehension) is computed as:

$$z_m^{(\text{R})} = \|\mathbf{x}_1 - \mathbf{x}_2\| + \mathbf{w}^{(\text{R})} = c \text{TOF} + \mathbf{w}^{(\text{R})} = c(t_{\text{TOA}} - t_{\text{TX}}) + \mathbf{w}^{(\text{R})}. \quad (2.19)$$

The noise term  $\mathbf{w}^{(\text{R})}$  this time is a scalar value that, in case of zero-mean Gaussian distribution, has variance  $\sigma^{(\text{R})2}$ , i.e.,  $\mathbf{w}^{(\text{R})} \sim \mathcal{N}(0, \sigma^{(\text{R})2})$ .

To visualize the impact of range (indirect) measurement, we consider the example in Fig. 2.6, where five agents are involved. Four static agents ( $\mathbf{x}_1, \mathbf{x}_2, \mathbf{x}_3, \mathbf{x}_4$ ) are located at known positions, for this reason we conveniently refer them as APs.

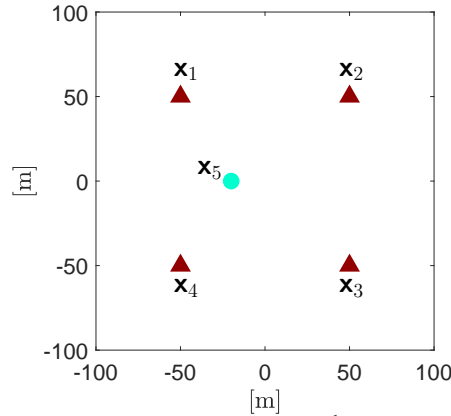


**Figure 2.6:** *Static localization scenario where four agents of known positions (access points)  $\mathbf{x}_1, \mathbf{x}_2, \mathbf{x}_3, \mathbf{x}_4$  localize an unknown agent  $\mathbf{x}_5$  (target).*

The AP positions are  $(-50, 50)$  m,  $(50, 50)$  m,  $(50, -50)$  m,  $(-50, -50)$  m, respectively. Each of them has a range measurement of a fifth agent  $\mathbf{x}_5$  located in an unknown (to the four APs) location. We equivalently refer to this fifth agent as a target, i.e., an object of unknown location that needs to be localized. We assume that its a-priori distribution is uniform in the area of interest (i.e.,  $p(\mathbf{x}_5) = \mathcal{U}(-200, 200)$ ). The likelihood functions of the range measurements of each AP are illustrated (top view) in Figs. 2.7a, 2.7b, 2.7c, 2.7d, respectively. Likelihoods are here normalized such that the integral in the considered  $200 \times 200$  m area of interest is exactly 1. The example considers a Gaussian-distributed range error with  $\sigma^{(R)} = 5$  m. It is possible to visualize how a range measurement creates a concentric distribution around the AP that generates it (green triangle in the figures). By considering all the four likelihood functions in the area of interest, we obtain the representation in Fig. 2.7e, where it is intuitive to discern the contribution of each APs as well as the most-likely position of the target. Lastly, Fig. 2.7f presents the maximum likelihood function in (2.14) (measurement independence is assumed).

The example presented in Fig. 2.7 visually shows the working principle of localization through range measurements. This example highlights how it is not possible to provide a unique estimation of the target location by using one (or two) agent(s) only. In fact, the minimum number of APs for range-based localization is three (this phenomenon is commonly known as trilateration). This aspect is a peculiarity of using range information and it also represents the basic principle of GPS-based localization.

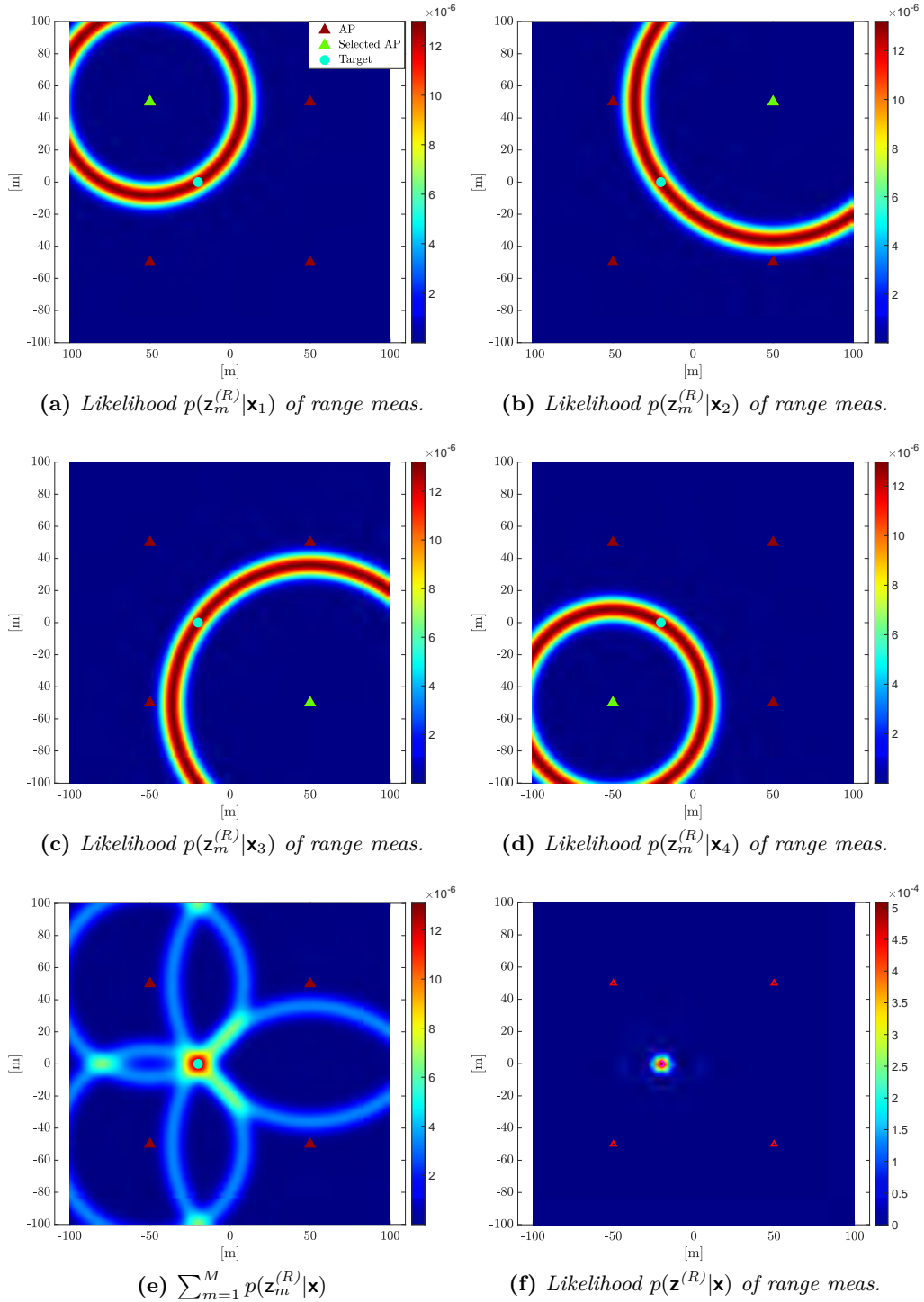


**Figure 2.7:** Range-based localization of a target agent by four APs: top view of likelihood functions. (a-d) single-likelihood of each APs. (e) sum of all the four likelihoods. (f) product of all likelihoods. The distribution in each figure is normalized such that the integral is 1 over the whole area.

### Angle measurement

Angle measurement refers to a scalar value indicating the angular displacement between two agents. As for the range measurement case, we still have many applications where the position of one agent is known, as well as the case where both agents are only statistically described (through their distributions). The same disclosure on the example of APs localizing a UE (or target) applies also in this case.

The information of the angle can be obtained, for instance, by an ad-hoc processing of a same signal collected at different receivers. This is the case of Multiple-Input Multiple-Output (MIMO) systems, where an array of many antenna elements (or microphones) receives a same radio (or acoustic) signal and exploits spatial and temporal information to estimate the Angle Of Arrival (AOA). As for the range measurement case, it is out of the scope of this thesis to analyze techniques for determining the AOA, we limit the discussion to the use of the AOA measurement for localization purposes.

Considering the case of two agents  $\mathbf{x}_1$  and  $\mathbf{x}_2$  where the agent state is characterized by the 2D position, an angular measurement  $\mathbf{z}_m^{(A)}$  (also in this case the superscript is used to distinguish the type of measurement for an immediate comprehension) is defined as:

$$\mathbf{z}_m^{(A)} = \angle(\mathbf{x}_1 - \mathbf{x}_2) + \mathbf{w}^{(A)}. \quad (2.20)$$

The noise term  $\mathbf{w}^{(A)}$  is a scalar value that, in case of Gaussian distribution, has variance  $\sigma^{(A)2}$ , i.e.,  $\mathbf{w}^{(A)} \sim \mathcal{N}(0, \sigma^{(A)2})$ .

To visualize the effect of angular measurement availability, we replicate the same plots of Fig. 2.7. Results are shown in Fig. 2.8, for a standard deviation of the noise  $\sigma^{(A)} = 5$  deg. In this case, the effect of angular measurement is to cut the area of interest with a conical distribution, with a linearly growing uncertainty from the vertex (the AP). Differently from range measurements, in this case two measurements are sufficient for a non-ambiguous estimate. Nonetheless, a higher number of measurements improves the localization accuracy.

After having presented the top view of likelihood functions, we think it is worth helping the reader by showing the 3D (normalized) likelihood functions for both TOA and AOA cases. To this purpose, the 3D equivalent of Figs. 2.7e and 2.8e are given in Figs. 2.9a and 2.9b.

Despite stand-alone measurements are enabling factors for a localization problem, it is possible to use them in combination with other types of information. Such approach is described in the following section through the concept of Bayesian filtering.

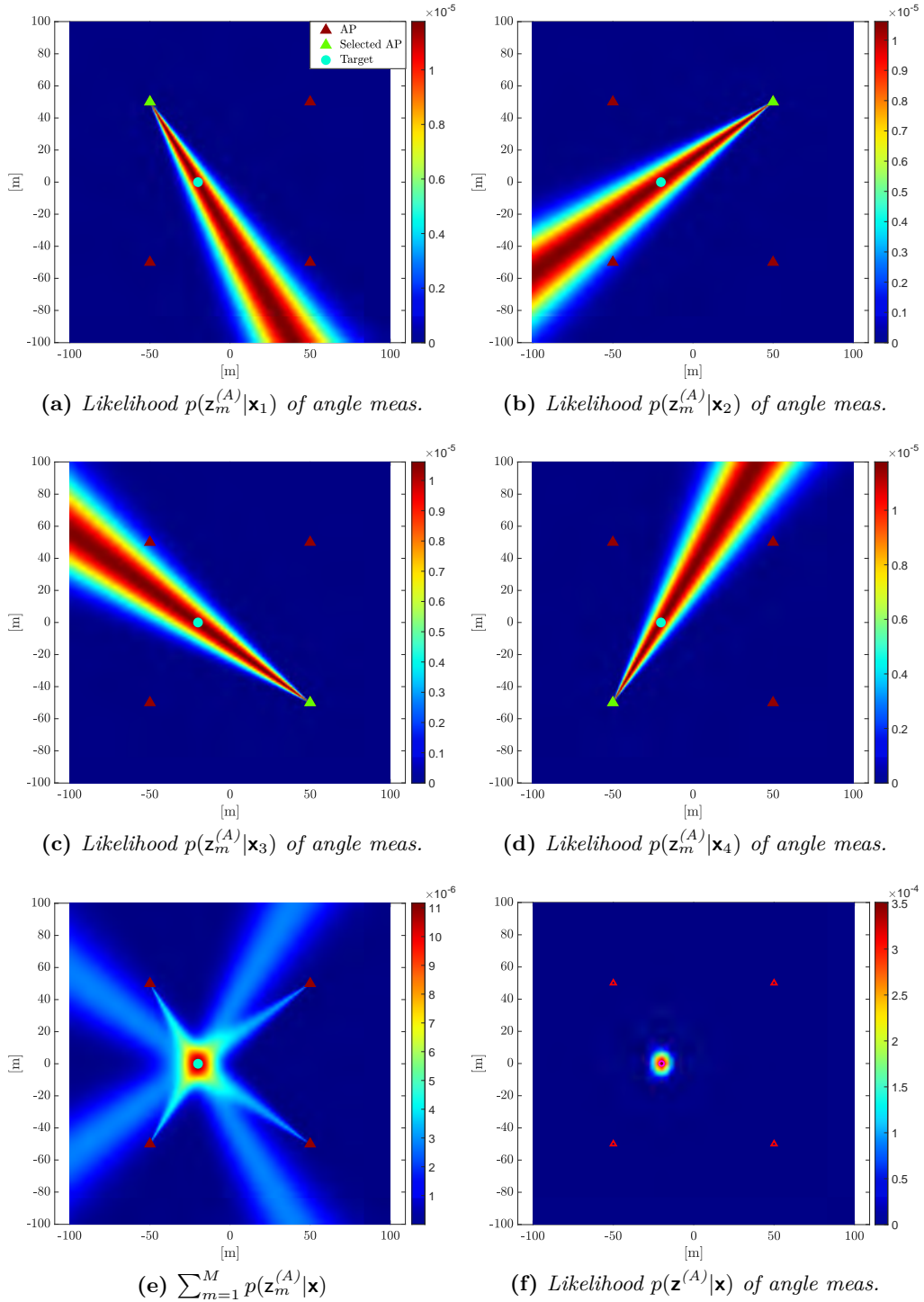


**Figure 2.8:** Angle-based localization of a target agent by four APs: top view of likelihood functions. (a-d) single-likelihood of each APs. (e) sum of all the four likelihoods. (f) product of all likelihoods. The distribution in each figure is normalized such that the integral is 1 over the whole area.

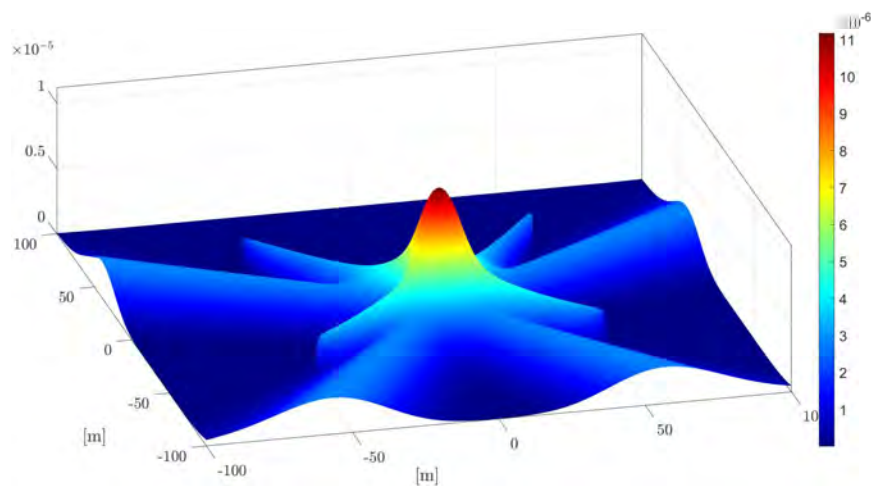
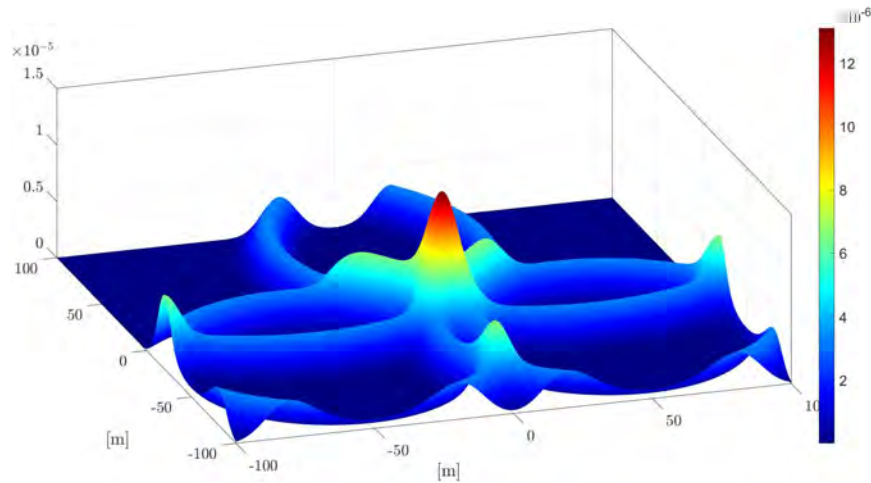


Figure 2.9: 3D visualization of likelihood function of all APs for (a) TOA and (b) AOA measurements.

## 2.3 Introduction to Bayesian filtering

---

The Bayes rule of probability theory in (2.13) has been previously introduced for the localization problem, showing how it is possible to combine an a-priori information with a likelihood function obtained from measurements. This approach can be extended such that it becomes iterative. Measurements of a same agent  $\mathbf{x}$  can be available at different time instances. Thus, we introduce the time dependability by the index  $t$ . In this way, we have the time-dependent measurement vector  $\mathbf{z}_t = \{\mathbf{z}_{1,t}, \dots, \mathbf{z}_{M,t}\}_{m=1}^M$ . If the agent of interest is static, meaning that none of the components of its state varies over time, it is possible to stack all the measurements collected at different time instants and process all together. However, most of applications include time-variant agents, where at least one component of its state varies over time. Thus, we define this type of agent with the state variable  $\mathbf{x}_t$ .

The time-variant case represents the most challenging aspect for localization purposes, as the position of the agent changes due to mobility. Bayesian theory helps the localization problem as it allows to conveniently handle the evolution of agent prior distribution at each time  $t$ . The time-varying equivalent of (2.13) for a given time  $t$  is:

$$p(\mathbf{x}_t | \mathbf{z}_{1:t}) \propto p(\mathbf{z}_t | \mathbf{x}_t) p(\mathbf{x}_t | \mathbf{z}_{1:t-1}) , \quad (2.21)$$

where  $\mathbf{z}_{1:t} = \{\mathbf{z}_1, \dots, \mathbf{z}_t\}$  collects all the measurements up to time  $t$ . Equation (2.21) states that the posterior distribution of agent  $\mathbf{x}_t$  at time  $t$  is proportional to the current likelihood  $p(\mathbf{z}_t | \mathbf{x}_t)$  and the prior pdf  $p(\mathbf{x}_t | \mathbf{z}_{1:t-1})$  (i.e., the distribution of the agent before the availability of the current measurement vector  $\mathbf{z}_t$ ). Special care needs to be assured for the first time instant  $t = 1$ , as  $\mathbf{z}_0$  is not defined. This special case is handled by assigning a default (or convenient) a-priori pdf such that  $p(\mathbf{x}_t | \mathbf{z}_{1:t-1}) = p(\mathbf{x}_0)$ , for  $t = 1$ . In all other cases ( $t > 1$ ), the agent prior pdf is computed according to the Chapman-Kolmogorov equation as:

$$p(\mathbf{x}_t | \mathbf{z}_{1:t-1}) = \int p(\mathbf{x}_t | \mathbf{x}_{t-1}) p(\mathbf{x}_{t-1} | \mathbf{z}_{1:t-1}) d\mathbf{x}_{t-1} . \quad (2.22)$$

With respect to any pdf encountered up to know, in (2.22) it appears for the first time the transition pdf  $p(\mathbf{x}_t | \mathbf{x}_{t-1})$  of the agent state from the previous time instant. The definition of such pdf requires a model of the agent state  $\mathbf{x}_t$ . In a general formulation, we indicate this model as:

$$\mathbf{x}_t = \mathbf{f}_t(\mathbf{x}_{t-1}, \mathbf{u}_t) , \quad (2.23)$$

meaning that the current agent state  $\mathbf{x}_t$  depends on the previous state  $\mathbf{x}_{t-1}$  and an additional input  $\mathbf{u}_t$ , and the relations are described by the problem-specific function  $\mathbf{f}_t(\cdot)$ . The latter is deterministic, but in principle non linear and time-variant.

In a similar way, we conveniently refer to a measurement of the agent state in a general way by defining a measurement related to the agent state  $\mathbf{x}_t$  as:

$$\mathbf{z}_t = \mathbf{g}_t(\mathbf{x}_t, \mathbf{w}_t) , \quad (2.24)$$

where the deterministic (but possibly time-varying) function  $\mathbf{g}_t(\cdot)$  depends on the specific problem (thus it can represent either a direct measurement or an indirect one), while vector  $\mathbf{w}_t$  carries information on measurement noise.

To summarize the introduction on Bayesian filtering, it has been shown that it is possible to conveniently combine two models: the agent state transition model (2.23) with the measurement model (2.24). The impact of measurement information is in the likelihood function  $p(\mathbf{z}_t|\mathbf{x}_t)$ , while the state transition rules the prediction from the previous time to the current one by linking the previous posterior pdf  $p(\mathbf{x}_{t-1}|\mathbf{z}_{1:t-1})$  to the current prior  $p(\mathbf{x}_t|\mathbf{z}_{1:t-1})$  through the transition in (2.22).

To implement Bayesian filtering techniques, many approaches are possible. Next subsections are devoted to describe popular ones, which are also useful for the purposes of this thesis.

### 2.3.1 Kalman filter

The most widespread technique for Bayesian filtering is the Kalman Filter (KF). The motivations that make KF so popular mainly resides in its simplicity and optimality: KF is easy to be implemented and it is the optimal estimator for time-varying systems in case of Gaussian processes and linear systems [16]. Here, optimality means that it provides the Minimum Mean Square Error (MMSE) between the ground truth value of the agent of interest  $\mathbf{x}_t$  and its estimate  $\hat{\mathbf{x}}_t$ . This means that in case both functions  $\mathbf{f}_t(\cdot)$  and  $\mathbf{g}_t(\cdot)$  in, respectively, (2.23) and (2.24) are linear, with Gaussian distributed terms  $\mathbf{u}_t$  and  $\mathbf{w}_t$ , there are no other filtering techniques that can provide better estimate of the time-varying agent state  $\mathbf{x}_t$ . These two peculiarities strongly motivate the use of KF in diverse engineering applications.

The assumptions of linearity and Gaussian distributions lead (2.23) and (2.24) to be:

$$\mathbf{x}_t = \mathbf{F}_t \mathbf{x}_{t-1} + \mathbf{u}_t, \quad (2.25)$$

with  $\mathbf{u}_t \sim \mathcal{N}(\mathbf{0}, \mathbf{C}_t^u)$ , and

$$\mathbf{z}_t = \mathbf{G}_t \mathbf{x}_t + \mathbf{w}_t, \quad (2.26)$$

with  $\mathbf{w}_t \sim \mathcal{N}(\mathbf{0}, \mathbf{C}_t^w)$ . The matrices  $\mathbf{F}_t$  in (2.25) and  $\mathbf{G}_t$  in (2.26) are deterministic and in some circumstances time variant, according to the considered problem.

It is not scope of this thesis to derive the steps for obtaining the final equations of KF. We limit the discussion to provide the final results which is of high importance for practical applications. The MMSE estimate  $\hat{\mathbf{x}}_t$  of agent state  $\mathbf{x}_t$  by KF is [16]:

$$\hat{\mathbf{x}}_{t|t} = \hat{\mathbf{x}}_{t|t-1} + \mathbf{K}_t (\mathbf{z}_t - \mathbf{G}_t \hat{\mathbf{x}}_{t|t-1}), \quad (2.27)$$

where  $\mathbf{K}_t$  is the Kalman gain, which is computed as:

$$\mathbf{K}_t = \mathbf{C}_{t|t-1}^x \mathbf{G}_t^\top (\mathbf{G}_t \mathbf{C}_{t|t-1}^x \mathbf{G}_t^\top + \mathbf{C}_t^w)^{-1}, \quad (2.28)$$

being  $\mathbf{C}_{t|t-1}^x$  the predicted covariance of the agent state estimate, obtained from the covariance of the estimate  $\mathbf{C}_t^x$  according to the agent state model in (2.25). These two covariance matrices are computed as:

$$\mathbf{C}_{t|t-1}^x = \mathbf{F}_t \mathbf{C}_{t-1|t-1}^x \mathbf{F}_t^\top + \mathbf{C}_t^u \quad (2.29)$$

and

$$\mathbf{C}_{t|t}^x = \mathbf{C}_{t|t-1}^x - \mathbf{K}_t \mathbf{G}_t \mathbf{C}_{t|t-1}^x. \quad (2.30)$$

The last term to be defined is  $\hat{\mathbf{x}}_{t|t-1}$ . It is the predicted agent state, which is computed from the model in (2.25) as:

$$\hat{\mathbf{x}}_{t|t-1} = \mathbf{F}_t \hat{\mathbf{x}}_{t-1|t-1}, \quad (2.31)$$

meaning that the previous estimate is propagated in a predictive way according to the considered model.

### 2.3.2 Extended Kalman filter

In the previous section it has been presented the Kalman filter as the optimal estimator for time-varying agents in case of linearity and Gaussian processes. These two constraints are quite strong and might not be satisfied in all application scenarios. In case one constraint is not met anymore, KF may not be the best option and other filters have to be considered (but optimality may not be guaranteed).

The straightforward extension of KF is the Extended Kalman Filter (EKF). It is a modified version of KF for non linear but Gaussian problems. This means that at least one function between  $\mathbf{f}_t(\cdot)$  in (2.24) and  $\mathbf{g}_t(\cdot)$  in (2.24) is not linear. This leads to rewrite (2.23) and (2.24) as:

$$\mathbf{x}_t = \mathbf{f}_t(\mathbf{x}_{t-1}) + \mathbf{u}_t, \quad (2.32)$$

$$\mathbf{z}_t = \mathbf{g}_t(\mathbf{x}_t) + \mathbf{w}_t. \quad (2.33)$$

EKF operates by linearizing  $\mathbf{f}_t(\cdot)$  and/or  $\mathbf{g}_t(\cdot)$  around the available agent estimate. Linearization is computed by considering Taylor expansion, commonly truncated to the first order, such that the following approximations are used:

$$\mathbf{f}_t(\mathbf{x}_{t-1}) \approx \underbrace{\mathbf{f}_t(\hat{\mathbf{x}}_{t-1|t-1}) + \frac{\partial \mathbf{f}_t(\mathbf{x}_{t-1})}{\partial \mathbf{x}_{t-1}} \bigg|_{\mathbf{x}_{t-1}=\hat{\mathbf{x}}_{t-1|t-1}}}_{\tilde{\mathbf{F}}_t} (\mathbf{x}_{t-1} - \hat{\mathbf{x}}_{t-1|t-1}) \quad (2.34)$$

$$\mathbf{g}_t(\mathbf{x}_{t-1}) \approx \underbrace{\mathbf{g}_t(\hat{\mathbf{x}}_{t-1|t-1}) + \frac{\partial \mathbf{g}_t(\mathbf{x}_{t-1})}{\partial \mathbf{x}_{t-1}} \bigg|_{\mathbf{x}_{t-1}=\hat{\mathbf{x}}_{t-1|t-1}}}_{\tilde{\mathbf{G}}_t} (\mathbf{x}_{t-1} - \hat{\mathbf{x}}_{t-1|t-1}) \quad (2.35)$$

Apart from the computation of the Jacobian matrices  $\tilde{\mathbf{F}}_t$  and  $\tilde{\mathbf{G}}_t$ , the steps of EKF are the same as for KF (with required adaptations). In particular, we have the prediction phase to compute the predicted agent state and covariance as:

$$\hat{\mathbf{x}}_{t|t-1} = \mathbf{f}_t(\hat{\mathbf{x}}_{t-1|t-1}), \quad (2.36)$$

$$\mathbf{C}_{t|t-1}^x = \tilde{\mathbf{F}}_t \mathbf{C}_{t-1|t-1}^x \tilde{\mathbf{F}}_t^T + \mathbf{C}_t^u, \quad (2.37)$$

and the update step that modifies the prediction according to the current available measurement as:

$$\hat{\mathbf{x}}_{t|t} = \hat{\mathbf{x}}_{t|t-1} + \mathbf{K}_t \left( \mathbf{z}_t - \mathbf{g}_t(\hat{\mathbf{x}}_{t|t-1}) \right), \quad (2.38)$$

$$\mathbf{K}_t = \mathbf{C}_{t|t-1}^x \mathbf{G}_t^\top \left( \mathbf{G}_t \mathbf{C}_{t|t-1}^x \mathbf{G}_t^\top + \mathbf{C}_t^w \right)^{-1}, \quad (2.39)$$

$$\mathbf{C}_{t|t}^x = \mathbf{C}_{t|t-1}^x - \mathbf{K}_t \mathbf{G}_t \mathbf{C}_{t|t-1}^x. \quad (2.40)$$

The relatively simplicity of EKF makes it a valid solution in many applications, however it may happen that linearization is too coarse and divergence problems arise. Moreover, the assumption of Gaussian distribution of uncertainty still remains.

### 2.3.3 Particle filter

Another possibility for Bayesian filtering is represented by Particle Filter (PF). PF is a sample-based technique where all pdfs of interests in (2.21) are approximated by a set of particles. A particle is identified by a state vector  $\mathbf{x}_{p,t}$  and an associated weight  $w_{p,t}$ , leading to the full set of particles  $\{\mathbf{x}_{p,t}, w_{p,t}\}_{p=1}^{N_p}$ . The approximation of a continuous pdf with a discrete set of samples clearly introduces a loss of information, but if the number of particles  $N_p$  is high enough, the loss can be negligible for the specific application.

With the same approach as in Sec. 2.1.2, we have that the prior pdf is approximated by equally weighted particles such that:

$$p(\mathbf{x}_t | \mathbf{z}_{1:t-1}) \propto \frac{1}{N_p} \sum_{p=1}^{N_p} \delta(\mathbf{x}_t - \mathbf{x}_{p,t}). \quad (2.41)$$

Recalling (2.24), we have that the posterior pdf is computed as:

$$p(\mathbf{x}_t | \mathbf{z}_{1:t}) \propto p(\mathbf{z}_t | \mathbf{x}_t) p(\mathbf{x}_t | \mathbf{z}_{1:t-1}) = p(\mathbf{z}_t | \mathbf{x}_t) \frac{1}{N_p} \sum_{p=1}^{N_p} \delta(\mathbf{x}_t - \mathbf{x}_{p,t}) \quad (2.42)$$

$$= \sum_{p=1}^{N_p} \underbrace{\frac{p(\mathbf{z}_t | \mathbf{x}_t = \mathbf{x}_{p,t})}{N_p}}_{\tilde{w}_{p,t}} \delta(\mathbf{x}_t - \mathbf{x}_{p,t}) \quad (2.43)$$

The weight term  $\tilde{w}_{p,t}$  represents the scaled likelihood of the  $p$ -th particle, thus it violates the importance sampling principle in (2.10). To let (2.43) representing a pdf, a normalization must be applied such that:

$$p(\mathbf{x}_t | \mathbf{z}_{1:t}) \propto \sum_{p=1}^{N_p} w_{p,t} \delta(\mathbf{x}_t - \mathbf{x}_{p,t}), \quad (2.44)$$

with

$$w_{p,t} = \frac{\tilde{w}_{p,t}}{\sum_{p=1}^{N_p} \tilde{w}_{p,t}}. \quad (2.45)$$

To summarize: (2.43) becomes the real pdf (2.44) by applying a normalization (2.45) to particles' weights.

Once obtained the posterior pdf, differently from KF and EKF, the MMSE estimate of agent state is computed as the average sum of samples:

$$\hat{\mathbf{x}}_{t|t} = \sum_{p=1}^{N_p} w_{p,t} \mathbf{x}_{p,t}. \quad (2.46)$$

The last step that still needs to be described for PF is the prediction. In PF, prediction is more critical with respect to KF and EKF. By inspecting the definitions of (2.44) and (2.41), it immediately raises that the unequal (but with unity norm) weights of the posterior needs to be somehow transformed such that all of them are equal to  $(N_p)^{-1}$ . The operations that allows to modify the weights by equalizing them is resampling, while the time transition happens through propagation of all particles.

Considering the set of particles that represent the posterior pdf at time  $t - 1$ , i.e.,  $\{\mathbf{x}_{p,t-1}, w_{p,t-1}\}_{p=1}^{N_p}$ , and the set  $\{\mathbf{x}_{p,t}, (N_p)^{-1} \mathbf{1}_{N_p}\}_{p=1}^{N_p}$  describing the prior pdf at time  $t$ , resampling allows to transform the former set into the latter one such that

$$p(\mathbf{x}_{p,t} = \mathbf{x}_{p,t-1}) = w_{p,t-1}, \quad \forall p = 1, \dots, N_p. \quad (2.47)$$

Resampling operation turns to generate new (time  $t$ ) particles in correspondence of the old (time  $t - 1$ ) particles that had the higher weights, avoiding to generate new particles in unlikely hypotheses of the agent state. This operation, however, might lead to overconfident results if there is one dominating weight  $w_{p,t-1}$ . The resampled set of particles has equal weights among all particles, but the states of many particles coincide. The new set of samples is then propagated according to the motion model in (2.23) of the specific application.

A representation of these key steps that characterize PF is provided in Fig. 2.10, where fifteen particles describe a bimodal posterior pdf at time  $t - 1$  (Fig. 2.10a). The corresponding unequal (but with unitary norm) weights are shown in Fig. 2.10b through circles (bigger the circle, bigger the associated weight). The resampling step is in Fig. 2.10c, where it is shown how the particles with higher weights give rise to multiple copies of new particles, while the particles with negligible weights are discarded. Lastly, in Fig. 2.10d, the propagation step shows how the particles describe a same state are spread and assume the same value  $(N_p)^{-1}$ .

By inspecting the definitions of pdfs for PF, an immediate concern with respect to KF or EKF is about the complexity. In fact, for instance, the computation of the likelihood (which is computed once for KF and EKF implementations) has to be performed for each  $p$ -th particle, thus linearly increasing the complexity with  $N_p$ . This is an unavoidable drawback of PF technique.

### 2.3.4 Factor graph and belief propagation

This section present a filtering technique which is different from previous approaches. This time we concentrate on a message passing algorithm that performs statistical inference (i.e., draw consistent conclusions in the presence of uncertainty) on a

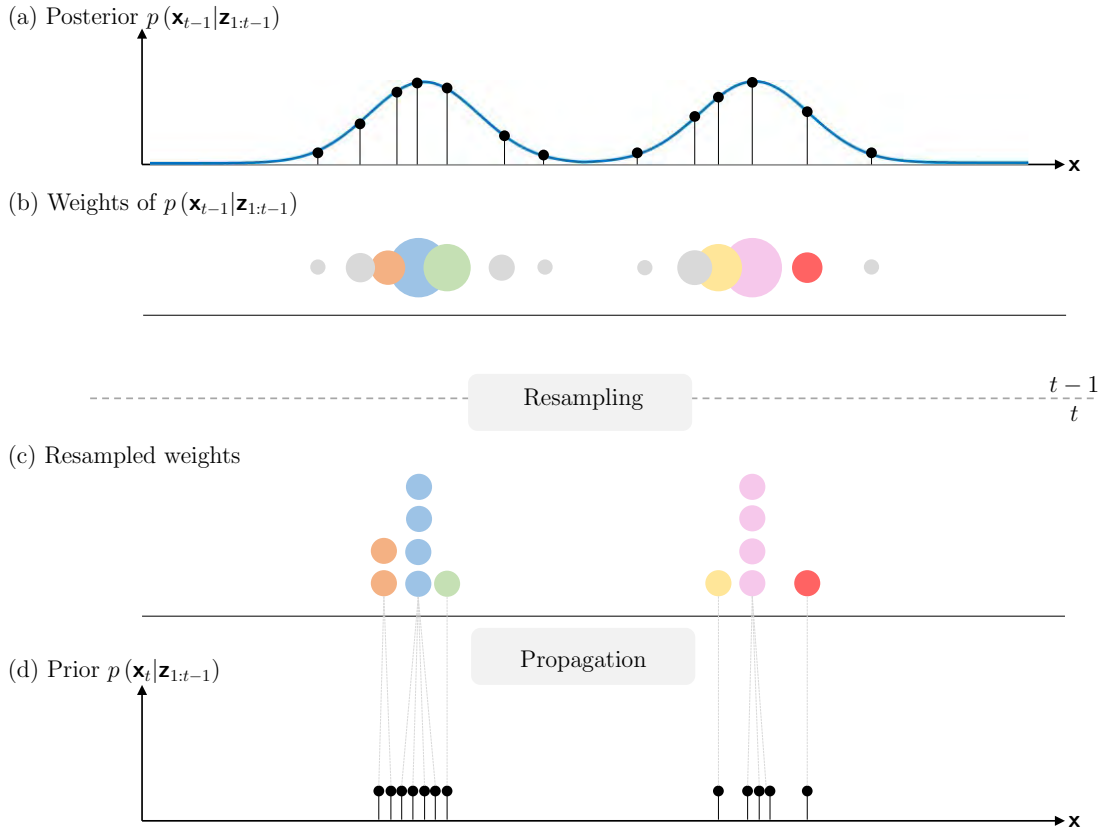


**Figure 2.10:** Summary of resampling and propagation of particle filter. (a) posterior pdf at time  $t$ . (b) values of weights of posterior pdf at time  $t$ . (c) resampled weights. (d) particles of the prior at time  $t$  with equal weights.

graphical model. We start by introducing the concept of Factor Graph (FG) which is instrumental to describe Belief Propagation (BP) technique. FG is a graphical-based intuitive way to represent the factorization of a given pdf  $p(\mathbf{x})$  by building a suitable graph with nodes, factors and (bidirectional) links among them [17]. In order to get acquainted with FG, this section is structured in such a way that a step-by-step construction of a generic (and simple) graph is proposed. The primary intent is to provide practical evidence of FG, rather than lingering on derivations of mathematical properties. We will thus highlight how to identify the starting point(s) of message passing, compute messages and evaluate the beliefs.

FG operates on the factorization of a pdf. Considering the pdf  $p(\mathbf{x}) = p(x_1, \dots, x_N)$ , a factorization allows to express  $p(\mathbf{x})$  as the product of  $K$  local functions  $f_k(\cdot)$  as:

$$p(\mathbf{x}) = \prod_{k=1}^K f_k(\tilde{\mathbf{x}}_k), \quad (2.48)$$

where  $\tilde{\mathbf{x}}_k$  is a subset of  $\mathbf{x}$  (i.e.,  $\tilde{\mathbf{x}}_k \subseteq \mathbf{x}$ ). Each variable  $x_n$  of  $\mathbf{x}$  is identified as a node (circle) in the graph, while each function  $f_k(\cdot)$  as a factor (square). For instance, in the localization problem each agent is depicted as a node, while the available measurements are the factors.

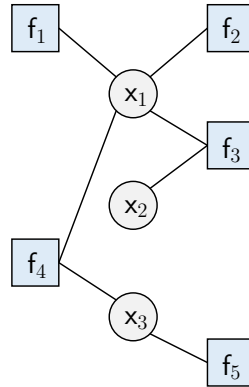


**Figure 2.11:** Example of factor graph of  $p(\mathbf{x})$  for  $\mathbf{x} = \{x_1, x_2, x_3\}$  and  $K = 5$  factors. Variables are indicated by circles, while squares are for factor nodes.

In Fig. 2.11 an example of graph is shown for  $\mathbf{x} = \{x_1, x_2, x_3\}$  and  $K = 5$  local functions. The example indicates that the following five local functions exists:  $f_1(\mathbf{x}_1)$ ,  $f_2(\mathbf{x}_1)$ ,  $f_3(\mathbf{x}_1, \mathbf{x}_2)$ ,  $f_4(\mathbf{x}_1, \mathbf{x}_3)$ ,  $f_5(\mathbf{x}_3)$ , leading to rewrite (2.48) as:

$$p(\mathbf{x}) = \prod_{k=1}^5 f_k(\tilde{\mathbf{x}}_k) = f_1(\mathbf{x}_1)f_2(\mathbf{x}_1)f_3(\mathbf{x}_1, \mathbf{x}_2)f_4(\mathbf{x}_1, \mathbf{x}_3)f_5(\mathbf{x}_3). \quad (2.49)$$

The rules to generate the graph in Fig. 2.11 are as follows: draw a circle for each variable  $x_n$ , draw a square for each local function (factor)  $f_k(\cdot)$ , connect each factor  $f_k(\cdot)$  with the related subset  $\tilde{\mathbf{x}}_k$  (only if  $\tilde{\mathbf{x}}_k$  is an argument of  $f_k(\cdot)$ ).

The factorization in (2.49) and the related FG in Fig. 2.11 suggest that graph-based technique are particularly suitable for multidimensional problems (i.e., when the dimension of  $\mathbf{x}$  is large enough), where closed-form expressions for  $p(\mathbf{x})$  may not exist. The multidimensional problem is reduced as the product of lower dimensional marginal pdfs which can be *easily* computed.

Intuition suggests that it is possible to share information over the links of the graphs, from one node to the other. This sharing is the basis of Belief Propagation (BP), where the information of a node is propagated to the neighboring nodes in terms of messages. Each message outgoing or incoming a variable node is a function of the associated variable itself (if it is not its function, there are no reasons for the existence of the link). The graph topology depends on the specific problem and, moreover, on a single graph it is possible to exchange messages in multiple ways (scheduling) leading to different solutions (if loops are present, while in case of tree structure the outcome is unique and exact). Lastly, it may occur that loops are present and a decision criteria to go out the loop must be taken.

Despite of the problem-specific issues, two simple common rules enable message passing. These rules defines the messages from a factor node to a variable node and viceversa, and can be summarized as:

- the outgoing message of a variable node is the product of incoming messages from the other connected factors;
- the outgoing message of a factor node is the sum of the product of incoming messages from the other connected variables.

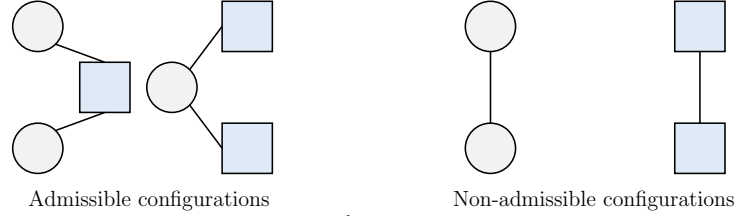


**Figure 2.12:** Admissible and non-admissible configurations of the graph.

These rules also justify the reason why BP can also be equivalently known as Sum-Product Algorithm (SPA) and highlight that it is not possible to have neither two variables nodes directly connected each other (i.e., without a factor node in between) nor two factor nodes directly connected each other (i.e., without a variable node in between). The admissible and non-admissible configurations are sketched in Fig. 2.12.

By indicating with  $m_{x_n \rightarrow f_k}(x_n)$  a generic message from variable  $x_n$  to factor  $f_k$  and with  $m_{f_k \rightarrow x_n}(x_n)$  a generic message from factor  $f_k$  to variable  $x_n$  (both of them associated to the variable  $x_n$ ), the above two statements ruling BP become:

$$m_{x_n \rightarrow f_k}(x_n) = \prod_{k' \in \mathcal{F}_{x_n} \setminus \{k\}} m_{f_{k'} \rightarrow x_n}(x_n), \quad (2.50)$$

$$m_{f_k \rightarrow x_n}(x_n) = \int f_k(\tilde{\mathbf{x}}_k) \prod_{n' \in \mathcal{V}_{f_k} \setminus \{n\}} m_{x_{n'} \rightarrow f_k}(x_{n'}) d\mathbf{x}_{-n}, \quad (2.51)$$

being  $\mathcal{F}_{x_n}$  and the set of adjacent (i.e., connected) factors to the variable node  $x_n$  and  $\mathcal{V}_{f_k}$  the set of adjacent (i.e., connected) variables to the factor node  $f_k$ . The integration in (2.51) is performed with respect to all variables  $x_{n'}$  except  $x_n$  (the integral has to be replaced by summation in case of discrete variables).

After the definition of messages, the final goal of BP (or SPA) is to calculate the beliefs (i.e., the approximation of pdf). The belief of a given variable  $x_n$  is denoted with  $\tilde{p}(x_n)$  and it is obtained by multiplying all the incoming messages to  $x_n$  (i.e., all the messages from the factors that are adjacent to the variable) and normalizing such that  $\int \tilde{p}(x_n) dx_n = 1$ . It follows that the belief is computed as:

$$\tilde{p}(x_n) = C_n \prod_{k \in \mathcal{F}_{x_n}} m_{f_k \rightarrow x_n}(x_n), \quad (2.52)$$

where  $C_n$  is introduced to guarantee the consistency of pdf (integral equal to 1).

By referring to the example in Fig. 2.11, we now take advantage of Fig. 2.13 to step-by-step illustrate how to perform BP over that graph. The starting point of BP is to identify the leaf nodes (those with single edges) and begin computing the messages for them. In our example, leaves are represented by factors  $f_1$ ,  $f_2$  and  $f_5$  and variable  $x_2$ , as highlighted in Fig. 2.13a.

As second step (Fig. 2.13b), the messages  $m_{f_1 \rightarrow x_1}(x_1)$ ,  $m_{f_2 \rightarrow x_1}(x_1)$  and  $m_{f_5 \rightarrow x_3}(x_3)$  from the factor leaves are calculated as:

$$m_{f_1 \rightarrow x_1}(x_1) = f_3(x_1), \quad (2.53)$$

$$m_{f_2 \rightarrow x_1}(x_1) = f_2(x_1), \quad (2.54)$$

$$m_{f_5 \rightarrow x_3}(x_3) = f_5(x_3). \quad (2.55)$$

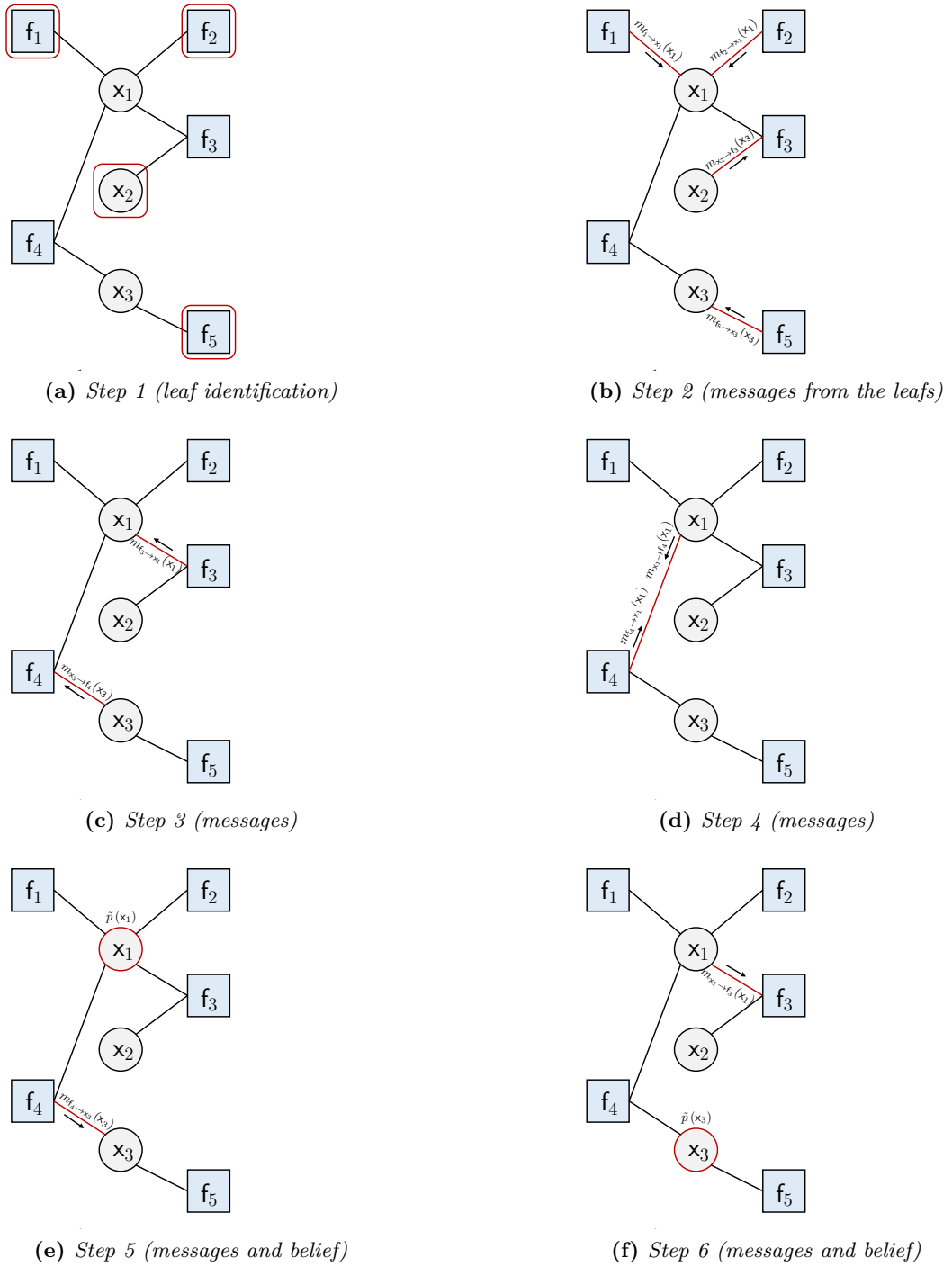


**Figure 2.13:** Example of message passing over a graph. Belief propagation is used to compute the beliefs in order to have a representation of  $p(\mathbf{x}) = p(x_1, x_2, x_3)$ .

We also have the message  $m_{x_2 \rightarrow f_3}(x_2)$  from variable  $x_2$  to factor  $f_3$ . In this case, no information is available, so a uniform uninformative information is assigned to the message.

In the third step (Fig. 2.13c), messages  $m_{f_3 \rightarrow x_1}(x_1)$  and  $m_{x_3 \rightarrow f_4}(x_3)$  are computed

as:

$$m_{f_3 \rightarrow x_1}(x_1) = \int f_3(x_1, x_2) \prod_{n' \in \mathcal{V}_{f_3} \setminus \{1\}} m_{x_{n'} \rightarrow f_3}(x_{n'}) dx_{-1} = \int f_3(x_1, x_2) m_{x_2 \rightarrow f_3}(x_2) dx_2, \quad (2.56)$$

$$m_{x_3 \rightarrow f_4}(x_3) = \prod_{k' \in \mathcal{F}_{x_3} \setminus \{4\}} m_{f_{k'} \rightarrow x_3}(x_3) = m_{f_5 \rightarrow x_3}(x_3). \quad (2.57)$$

At this point, the only link which has not been used yet is the one connecting factor  $f_4$  and variable  $x_1$ , but it is possible to compute both messages  $m_{f_4 \rightarrow x_1}(x_1)$  and  $m_{x_1 \rightarrow f_4}(x_1)$  (fourth step, Fig. 2.13d) as:

$$m_{f_4 \rightarrow x_1}(x_1) = \int f_4(x_1, x_3) m_{x_3 \rightarrow f_4}(x_3) dx_3, \quad (2.58)$$

$$m_{x_1 \rightarrow f_4}(x_1) = \prod_{k' \in \mathcal{F}_{x_1} \setminus \{4\}} m_{f_{k'} \rightarrow x_1}(x_1) = m_{f_1 \rightarrow x_1}(x_1) m_{f_2 \rightarrow x_1}(x_1) m_{f_3 \rightarrow x_1}(x_1). \quad (2.59)$$

As a fifth step (Fig. 2.13e), the belief  $\tilde{p}(x_1)$  is evaluated as:

$$\tilde{p}(x_1) = C_1 \prod_{k \in \mathcal{F}_{x_1}} m_{f_k \rightarrow x_1}(x_1) = C_1 m_{f_1 \rightarrow x_1}(x_1) m_{f_2 \rightarrow x_1}(x_1) m_{f_3 \rightarrow x_1}(x_1) m_{f_4 \rightarrow x_1}(x_1), \quad (2.60)$$

and it is also possible to compute the message  $m_{f_4 \rightarrow x_3}(x_3)$  as:

$$m_{f_4 \rightarrow x_3}(x_3) = \int f_4(x_1, x_3) m_{x_1 \rightarrow f_4}(x_1) dx_1. \quad (2.61)$$

The next step (Fig. 2.13f) is to evaluate the belief  $\tilde{p}(x_3)$  and to compute message  $m_{x_1 \rightarrow f_3}(x_1)$ , the latter being fundamental to further compute message  $m_{f_3 \rightarrow x_2}(x_2)$  and, lastly, the belief  $\tilde{p}(x_2)$ . These final passages are not detailed nor shown in Fig. 2.13 as they can be easily derived from the previous disclosure.

The presented examples allows a first understanding on the principles running BP. The problem has been taken in a generic and simple graph, without explicitly tailoring it to a specific problem. Next section tries to match mathematical graph theory with a possible practical use cases.

### 2.3.4.1 Practical aspects of belief propagation

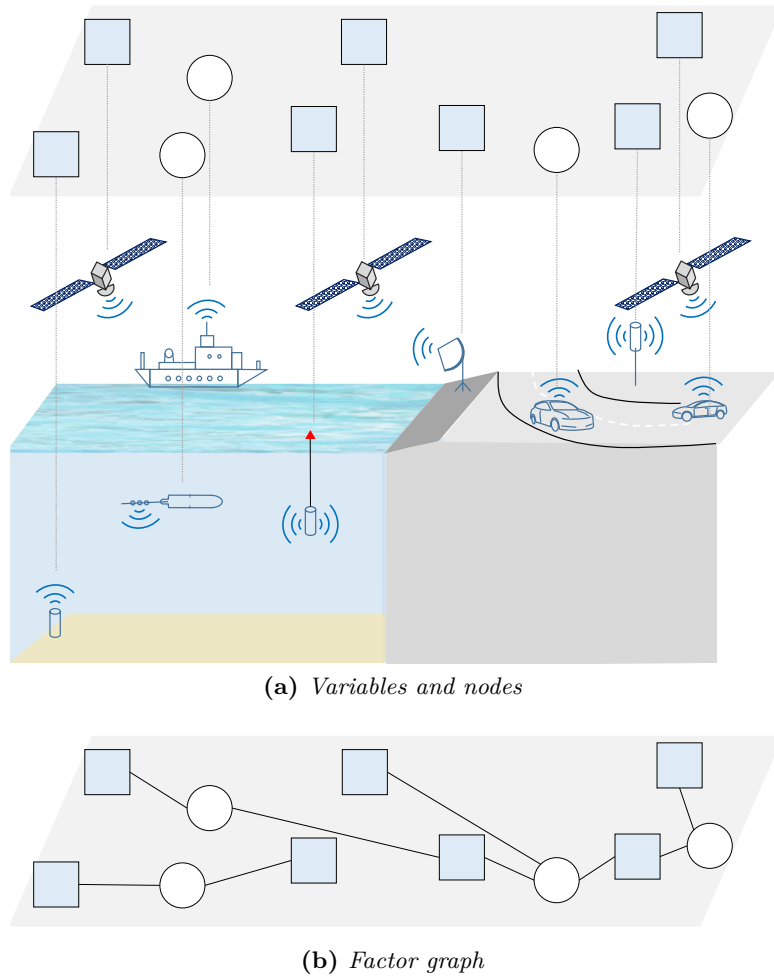
In Sec. 2.3.4, the concept of FG and BP have been introduced in an abstract way, denoting a generic vector of variables  $\mathbf{x}$  and factors  $f_k(\cdot)$ . Practical needs require BP to solve specific problems, thus assigning a physical identity to the various abstract variables and factors. For the purposes of this thesis, we would like to give a parallelism between FG and the considered scenario presented in the introduction (Fig. 1.1). The intent is to introduce the mathematical formulation approach that will be used in the remainder of the thesis to solve specific estimation problems by an illustrative example.

Fig. 2.14a presents the relation between a possible scenario of interest and the associated FG. In the considered example, variables in  $\mathbf{x}$  represent the unknown position of agents such as land and underwater vehicles or ships. Factors, instead,

are related to measurements of the agents' states, thus they are associated to sensors (GPS, seabed, sea floating, radar, RSU, etc.). The goal is to infer the estimated state  $\hat{\mathbf{x}}$  via message passing in a Bayesian-optimum fashion through the factorization of the joint posterior, i.e., by computing the marginal pdfs of each entry of  $\mathbf{x}_n$  from (the factorization of)  $p(\mathbf{x}|\mathbf{z})$ . As shown in Fig. 2.14b we can have factor-to-variable connections for GPS measurements with ships and land vehicles. A radar can be connected to both types of agents, while RSU only to land vehicles, as well as sea sensors are only connected to AUVs. This example allows to fully characterize a complex problem making it tractable for processing algorithms. It also allows to highlight that, according to the specific problem formulation, it may happen that disconnected subgraphs exist, meaning that independency properties can be explored to simplify the framework. In this example, two graphs arise, highlighting for instance that sea sensors for AUV estimation do not have any impact on land vehicles. Another aspect that appears is related to variable nodes of ship and AUV. It may be possible (this case will be considered later in Chapter 3) that relative measurements between ship and AUV are available. In this case, being a direct connection between the two variable nodes non-admissible, a new factor has to be introduced in between.

After the introduction on FG and BP of this section, the reader might perceive that the flexibility of this technique is of high interest in data fusion problems, where multiple sources of information (e.g., sensors) need to be combined together. By properly creating relations among the players (agents, sensors, etc.) in a suitable graph, message passing allows to share and use the intrinsic information carried out in each message. It follows that any link a variable node is connected to represents a partial information on (part of) the variable itself. By combining all the messages from the multiple links, all the information on that variable is conveniently fused together.

Fusion context is also of interest in cooperative environments, where multiple agents have individual measurements and relative measurements with nearby ones. Such a specific collaborative scenario with multiple agents and different sources of measurements will be considered from now on in this thesis with applications in maritime (Chapter 3) and vehicular (Chapter 4) domains. Clearly, the complexity of graph increases with respect to the simple example presented in this chapter. Loops will arise and *abstract* variables needs to be introduced. Details on how to handle these aspects will be given, but the concepts and rules described in this section will always be valid.



**Figure 2.14:** Example of nodes and factors in a use case scenario of interest. Agents of unknown locations (to be estimated) are the nodes (circles) while the factors indicate the available measurements (such as GPS navigation measurement, or inter-agent measurements).  
 a) Relations between nodes/variables and the localization scenario of the multi-agent network.  
 b) Related factor graph representation.

---

## Cooperative localization in maritime scenarios

This chapter addresses the problem of cooperative localization in multi-agent systems with known and unknown agents. The developed theoretical framework is derived to be suited to any multi-agent network, but the primary targeted application scenario is the maritime environment, where the time varying multi-agent system might be constituted by Autonomous Underwater Vehicles (AUVs), ships/vessels, sea sensors and targets. A general problem formulation is used, where agents are considered as moving nodes of a sensor network. Agents have to both localize themselves in the network and, at the same time, perform target tracking. These two problems are jointly resolved in a holistic approach where the graph theory is used to describe the relationships among agents, targets, and observations. The contents of this chapter refer to a joint probabilistic self-localization and multitarget tracking technique that allows to statistically handle unknown and arbitrary number of targets. Following a Bayesian approach, a message passing technique based on the sum-product algorithm (SPA) (or belief propagation) is used to approximate the marginal posterior distributions of both agents and targets. All the relationships among agents and targets due to mutual measurements are used to create a factor graph where messages are exchanged. The derivation is general enough to be adapted to any multi-agent network comprising transmit and receive agents and heterogeneous types of data. The contents of this chapter are yet<sup>1</sup> unpublished, but preliminary considerations are in publication [8].

The chapter is organized as follows. Sec. 3.1 introduces the self-localization and multitarget tracking problem, which is here customized according to the system model presented in Sec. 3.2. The stochastic formulation for multitarget tracking is in Sec. 3.3, while the derivation of the proposed approach is in Sec. 3.4. Numerical analysis and performance comparison are in Sec. 3.5, while Sec. 3.6 contains concluding remarks.

---

<sup>1</sup>at the time of writing this thesis (Dec. 2020)

## 3.1 Introduction to self-localization and multitarget tracking

---

Detecting unknown objects or features, understanding their intentions and take reactive countermeasures are common tasks in Situational Awareness (SA) applications, such as maritime surveillance or autonomous systems [18–23]. Different type of sensors (acoustic-based, radio frequency-based, optics-based, visual-based, etc. [24]) fulfill the tasks of sensing the environment, providing the desired information in the specific use case. Most of SA applications require a knowledge on target (we refer to target as an unknown agent) kinematics which is preferably inferred by multiple cooperative sensors [25–28] rather than single-sensor systems. Cooperative approaches dramatically increase the perception capabilities, as they rely on larger dataset of multiple type of measurements [29]. Examples can be found in many domains such as underwater networks [30,31], vehicular scenario [32–34] or Internet of Things (IoT) world [35–38]. Mobility of sensors can further improve the target tracking performance by combining a spatial sensing under different geometries, also enabling an optimized trajectory control for improved localization [39]. On the other hand, the main difference with respect to static (ground-based) sensors, is a mandatory localization of sensors themselves [40].

Cooperative Self-Localization (CSL) techniques have been widely investigated in the literature. Among these, solutions based on Belief Propagation (BP), also known as Sum-Product Algorithm (SPA) [41]) are common as their computational complexity linearly scales with the number of cooperative sensors [42–45]. The advantages of SPA methods are represented by the scalability, the possibility to handle non-linear and non-Gaussian models and the ability to cope with unknown and time-varying parameters. Alternative solutions exploring neighborhood collaboration among connected sensors are based on cooperative least square [46], Gaussian mixture [47], expectation maximization optimization [48], multi-dimensional scaling [49], convex hull constraint [50], second-order cone programming [51], semidefinite programming [52] or modified parallel projection method [53].

By combining CSL and SA, a network of cooperative agents detecting targets is established. MultiTarget Tracking (MTT) refers to the capability of a system to firstly detect and localize, and then track over time a number of hypothesized targets which behave as non-cooperative entities, i.e., they do not share direct information with the surveillance system. Usually, the presence of these targets represents a potential threat; for example targets can be illegal ships in the maritime domain, or vulnerable road users in vehicular scene, but also thieves in IoT surveillance systems. It follows that the development of robust, reliable, scalable and efficient MTT systems becomes of paramount importance as safety issues are involved.

Abundant literature on MTT is available, starting from pioneering works in [54–56] until very recent researches [57–61]. MTT is a probabilistic-based topic, as it deals with unknown targets to be localized by using set of measurements with unknown origin. Moreover, practical algorithm deal with the capability to easily remove a track in case of a death (i.e., which is no more present) target as well as

rapidly create a new track for a born target (i.e., which appears for the first time).

To manage time-variant target behaviors, different categories of MTT algorithms can be used. Following [62], MTT techniques can be distinguished as vector-based or set-based approaches. In the former, random vectors are used to describe the target states, while in the latter random sets are used as to enclose the states of hypothesized targets. In the following, more details on these two categories are provided, followed by the selected graph-based approach.

#### *Vector-type approaches.*

This category is well represented by largely adopted Joint Probabilistic Data Association (JPDA) filter and Multiple Hypothesis Tracking (MHT). The JPDA filter [63–66] is an MTT algorithm with DA that computes all possible combinations of target-measurement probabilities for a consistent combination in evaluating the target pdfs. It only works if the number of targets is fixed and a-prior known and has a complexity that exponentially grows with the number of targets. In case of unknown target cardinality, the extension to the Joint Integrated Probabilistic Data Association (JIPDA) [67, 68] must be considered as it allows to model the target existence/nonexistence. It uses a binary Markov chain to determine the existence/nonexistence of a target, initializing a new track if a measurement falls out the neighborhood of existing declared targets. This approach, however, suffers in case of closed targets and it may discard meaningful information as it approximates target pdfs to Gaussian at each time step by collapsing more hypotheses in one, thus oversimplifying the handling of multimodal pdfs. On the other hand, MHT reconstructs tracks by inspecting multiple measurements over time [69, 70], but it is unfavorable for large scale networks at the number of association hypotheses exponentially scales with the number of sensors.

#### *Set-type approaches.*

In this category, the most common techniques are the probability hypothesis density (PHD) filter [71], the cardinalized PHD (CPHD) filter [72], the Bernoulli filter [73], and the multi-Bernoulli filter [74]. By using sets, the modeling of hybrid (continuous and discrete) and time-varying problems (as MTT) is facilitated. The mentioned filters bypass the data association problem and estimate the joint posterior pdf of target state in a Bayesian way. The PHD filter approximates the target posterior pdfs by a Poisson random finite set pdf, while the cardinalized version introduces the calculation of cardinality distribution and uses an approximation based on the pdfs of independent and identically distributed clusters [75]. The multi-Bernoulli filter, instead, approximates the target state posterior pdfs by a multi-Bernoulli random finite set pdf. The mentioned set-based solutions are appropriate for single-sensor MTT. To include multi-sensors processing, the PHD and CPHD have been extended in [76–78], with a separate filter processing solution (one for each sensor) [76] or a joint single CPHD [77], as well as consensus-based Gaussian mixture CPHD [78]. The extension of Bernoulli filters to multi-sensors case can be found in [79], which shows superior performances with respect to multi-sensor CPHD filter, at a lower computational complexity too (note that the complexity of CPHD scales exponentially in the number of sensors and measurements per

sensors [38, 80]). These finite set techniques aims to approximate the joint posterior pdf of all detected targets.

*Message passing over factor graph.*

A different approach is to represent the MTT problem through a factor graph with the aim of approximating the marginal pdfs rather than the joint posterior one by message passing. A graph representation of an inference problem allows to include both continuous and discrete variables in a same framework, thus being inherently appropriate for time-varying MTT problems (where discrete variable model the existence/nonexistence of potential targets) as well as data association resolution. Additionally, time-varying graph easily accommodate for multi-sensors scenario making them particularly useful for multi-agent systems, in which many targets are detected by multiple sensors. As a matter of fact, graphical model well captures the intrinsic network-like structure of multi-agent networks, where nodes are the sensors and the links are the connections among them. Such a graph structure allows for parallel information exchange (messages) among the nodes, speeding up the flooding of individual information (at each node) to rapidly reach all nodes in few multi-hop exchanges in case of distributed implementations (as will be shown in Chapter 4). With respect to PHD, CPHD and multi-Bernoulli solutions, BP-based methods are more performing [18, 38] and, at the same time, they are suitable for large scale networks having a computational complexity that quadratically scales in the number of targets, linearly in the number of sensors, and linearly in the number of measurements per sensor. Moreover, they can handle any pdf of agents, targets and measurements [18]. The data association problem is not bypassed, but it is addressed through a direct marginalization of association variables which are iteratively refined by messages over DA iterations. In case of single-sensor single-target, BP reduces to a Bernoulli filter, while in case of contemporary presence of all targets (a known parameter) it reverts to the JPDA [38], with similar performances but with meaningfully reduced complexity, as shown in [81]. Essentially, the high flexibility and adaptability of SPA make it an ideal candidate for multi-agent systems, where multiple types of input data (observation, measurements, etc.) can be combined to provide multiple estimates of diverse variables (either continuous or discrete), as on a same backbone graph structure it is easy to customize the processing algorithm to get the desired functionalities [18].

Message passing algorithms working on graph and relying on the SPA have been proposed in the literature for both static sensor networks, with known [18, 82, 83] or unknown [84] locations, and mobile ones [2, 85–88], even if not all of them handle typical MTT problems like false alarm, missed detection and measurement origin uncertainty [89] or with possible failure in the communication. The cited works are affected by the following limitations: *(i)* sensors do not localize themselves cooperatively [87], *(ii)* neither clutter nor missed detections are considered and the number of targets is fixed and known [2], and *(iii)* the number of targets is limited and must be set a-priori [85, 86].

In this chapter, a BP technique for MTT is used as it allows an easy integration of target tracking capabilities with cooperative localization of agents. As a matter

of fact, a graph representation of in a unique framework of two different tasks (CL and MTT) facilitates their merging in a single solution.

### 3.1.0.1 Scientific contributions and main limitations

In this chapter, we resolve the above issues by relaxing all the constraints by proposing a global framework where multiple cooperative sensors can detect and track an arbitrary time-varying number of targets. We propose a holistic approach that can be applied in any SA context, even in the case of agents acting as possible sources of signal reflections. This generalization leads to include agents that are neither the Transmitter (Tx) nor the Receiver (Rx) of the signal into the Data Association (DA) problem, as they cannot be a-priori distinguished from targets. In the proposed BP-based technique, we combine CSL and MTT in a unified framework such that agents are capable of jointly localizing themselves and, at the same time, detect and track unknown targets. The proposed method performs message passing on the factor graph of the joint posterior distribution of all agent and target states given all measurements.

Compared to existing literature, the method developed in this thesis extends state-of-the-art solutions by considering *(i)* joint cooperative localization of agents, *(ii)* an unknown and arbitrary number of targets, and *(iii)* agent location uncertainty due to their intrinsic mobility. Another peculiarity of this research is related to the problem geometry, which considers both monostatic (direct) and bistatic (indirect) configurations. We would like to show that the challenging bistatic configuration can be fruitfully exploited to enhance the localization of agents. This aspect is of extremely high importance for the primary application scenario we target (i.e., the maritime domain), as the proposed joint CSL and MTT allows for a profitable use of target information, despite high errors in measurements and association uncertainties. This concept is shown in Fig. 3.1 for the case of three agents network and one target, where it is shown the improvement on agent distribution of self-navigation only due to inter-agent cooperation (CSL) and inter-agent cooperation with the exploitation of target information (CSL+MTT). Moreover, being the DA problem related to associate reflected measurements from unknown objects, we include into the DA process the agents as well (those who are not Tx or Rx) as the system cannot be able to discern if a bistatic reflection comes from a scattering target or from a reflecting agents.

The developed solution assumes each agent and target as represented by single point in a 2D space. Regarding the agents, this condition is common for multi-agent networks that operate on a confined area, where altitude coordinate is almost constant (e.g., a surveillance maritime network). Regarding the targets, instead, even if they can be located at different altitude with respect to agents (e.g., underwater targets), the specific maritime applications is characterized by unavoidable communication impairments (e.g., water channel medium) which automatically exclude the depth/altitude component. However, in case the same developed methodology has to be adapted for a 3D layout, the extension is quite straightforward as the theoretical formulation do not vary. It should be advised, however, that a particle-based representation might lead a significant increase in the number of required particles for sampling the pdfs, thus increasing the

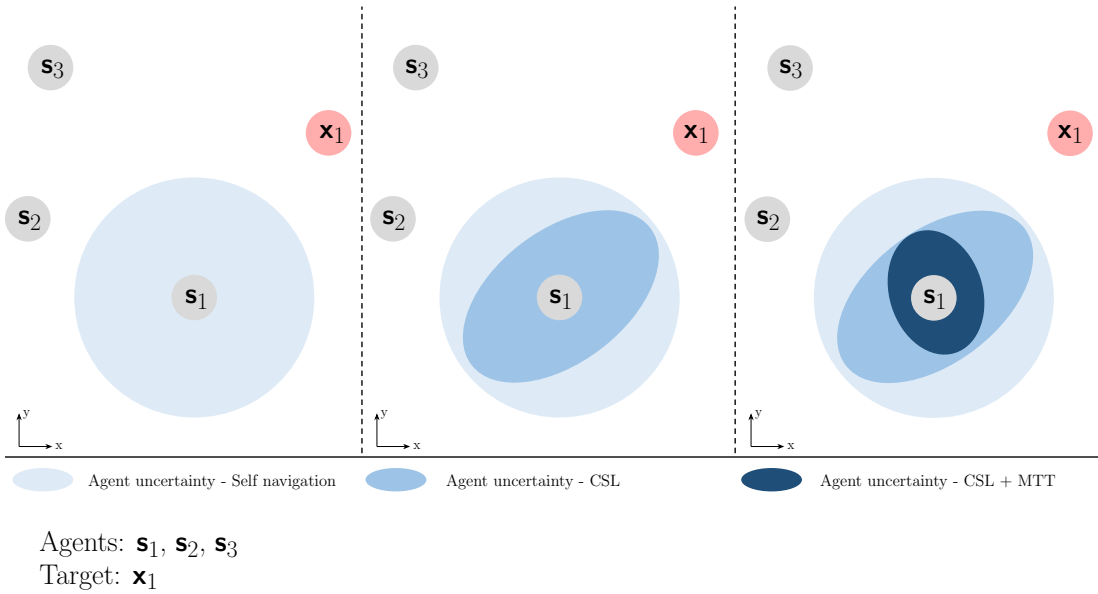


**Figure 3.1:** *Intuition of working principle: agent  $s_1$  pdf by considering (left) self-navigation measurements only, (middle) cooperation with other agents (CSL), (right) cooperation with other agents and exploitation of target information (CSL+MTT).*

computational complexity. Another strong assumption is that each measurement is considered as unique. This reduces to have no more than one measurement for navigation and inter-agent measurements (easily verified in practice) but it also prevents to have multiple copies of target-related measurements (which might not be an exact representation of practical applications). On the other hand, it is to be noticed that in maritime applications, also the one-target-one-measurement assumption is often verified. In case the algorithm has to be applied to real data which do not verify this condition, it is recommended to develop another theoretical framework that relaxes this constraints at the expenses of significantly increase both the statistical formulation and the computational complexity (examples of DA for extended objects has been recently addressed in [90] for the SPA algorithm, and in [91] for a variant of the PHD filter). In case of not modifying the algorithm, a first result should be the detection of more targets than the real ones, most of them closely located (meaning that they are copies of a same target). Relative proximity of targets also complicates the data association task, as higher uncertainty is present in assigning a measurement to a target. This implies that a same measurement turns to update more than one target pdfs, thus introducing a non-optimal processing (unavoidable in practice). Lastly, all the formulation assumes measurement availability at specific time instants. In practice, it may occur that sensors are not synchronize and have to be aligned in time to effectively match the proposed algorithm. However, this should not be a problem in maritime applications as the time scanning in the order of several seconds easily accommodates for measurement aggregation. Alternatively, each time a measurement is available, it is possible to run the presented algorithm by considering only the available information.

## 3.2 System model

In this section we detail the modeling of agent space and measurements. The model is provided in the most general configuration possible as to fit any multi-agent networks. Unlike from chapters 1 and 2 where variable  $\mathbf{x}_t$  indicated a generic agent, different notations are used to denote agents and targets to avoid ambiguities.

### 3.2.1 Agent state-space model

We denote with  $\mathcal{A}$  the set of known agents, whose cardinality  $A = |\mathcal{A}|$  is known and time-invariant. The cardinality may be modeled as being time-variant, however this does not change the following derivation. The state of agent  $a \in \mathcal{A}$  at time  $t$ , consisting of position and further kinematic parameters, is represented by the vector  $\mathbf{s}_{a,t}$ . The time evolution of the state of agent  $a$  is modeled as:

$$\mathbf{s}_{a,t} = \boldsymbol{\epsilon}(\mathbf{s}_{a,t-1}, \mathbf{u}_t^{(a)}). \quad (3.1)$$

Function  $\boldsymbol{\epsilon}(\cdot)$  and the statistics of  $\mathbf{u}_t^{(a)}$  define the agent transition pdf  $\tau(\mathbf{s}_{a,t}|\mathbf{s}_{a,t-1})$ . We define the joint agent state vector at time  $t$  as  $\mathbf{s}_t \triangleq [\mathbf{s}_t^{(1)\top} \dots \mathbf{s}_t^{(|\mathcal{A}|\top)]^\top$ , and the joint agent state vector at all times as  $\mathbf{s}_{1:t} \triangleq [\mathbf{s}_1^\top \dots \mathbf{s}_t^\top]^\top$ . Assuming that (A1) the joint agent states evolve according to a first-order Markov process and (A2) each agent state evolves independently of other agent states, the joint agent state transition pdf factorizes as:

$$f(\mathbf{s}_t|\mathbf{s}_{t-1}) = \prod_{a \in \mathcal{A}} \tau(\mathbf{s}_{a,t}|\mathbf{s}_{a,t-1}). \quad (3.2)$$

Each agent is equipped with a transmitter and/or a receiver. We indicate with  $\mathcal{T} \subseteq \mathcal{A}$  the set of agents equipped with a transmitter and with  $\mathcal{R} \subseteq \mathcal{A}$  the set of agents equipped with a receiver. Note that  $\mathcal{T} \cup \mathcal{R} = \mathcal{A}$  and that  $\mathcal{T} \cap \mathcal{R}$  represents the set of agents equipped with both a transmitter and a receiver. We formally consider the Cartesian product set  $\mathbf{r} \times \mathcal{T}$  of all the possible agents pairs receiver-transmitter and rearrange them in an arbitrary order. We denote with  $\mathcal{J}$  the index set  $\mathcal{J} = \{1 \dots J\}$  with  $J = |\mathcal{R}||\mathcal{T}|$  and we define an indexing  $\phi : \mathcal{J} \rightarrow \mathbf{r} \times \mathcal{T}$ , such that  $\phi(j)$  represents  $j$ -th receiver-transmitter pair  $(\phi(j)(1), \phi(j)(2))$ , with  $\phi(j)(1) \in \mathbf{r}$  and  $\phi(j)(2) \in \mathcal{T}$ . In order to ease the notation, we denote with  $j_1 \triangleq \phi(j)(1)$  and with  $j_2 \triangleq \phi(j)(2)$ , the receiver and transmitter of the  $j$ -th pair, respectively. Note that, agent  $j_1$  and agent  $j_2$  might also coincide. We also introduce the receiver-transmitter pair state vector  $\ddot{\mathbf{s}}_t^{(j)}$ , which is defined as  $\ddot{\mathbf{s}}_t^{(j)} \triangleq [\mathbf{s}_{j_1,t}^\top \mathbf{s}_{j_2,t}^\top]^\top$  when the receiver  $j_1$  and the transmitter  $j_2$  do not coincide, i.e., if  $j_1 \neq j_2$  and  $\ddot{\mathbf{s}}_t^{(j)} \triangleq \mathbf{s}_{j_1,t}$  when the receiver  $j_1$  and the transmitter  $j_2$  coincide, i.e., if  $j_1 = j_2$ .

### 3.2.2 Target state-space model

As in [62, 83], we account for the time-varying and unknown number of targets by introducing the concept of potential targets (PTs). In order to reduce ambiguity

between known agents and unknown agents, we prefer to indicate such passive and unknown agents as targets. The set of PTs at time  $t$  is denoted as  $\mathcal{L}_t$ . The existence/nonexistence of PT  $\ell \in \mathcal{L}_t$  is modeled by a binary variable  $r_{\ell,t} \in \{0, 1\}$ , i.e., PT  $\ell$  exists at time  $t$  if and only if  $r_{\ell,t} = 1$ . The state of PT  $\ell$  is denoted by  $\mathbf{x}_{\ell,t}$  and is formally considered also if  $r_{\ell,t} = 0$ . The time evolution of an existing PT  $\ell$  is modeled as:

$$\mathbf{x}_{\ell,t} = \varsigma(\mathbf{x}_{\ell,t-1}, \mathbf{e}_{\ell,t}). \quad (3.3)$$

The function  $\varsigma(\cdot)$  and the statistics of  $\mathbf{e}_{\ell,t}$  define the transition pdf  $f(\mathbf{x}_{\ell,t} | \mathbf{x}_{\ell,t-1})$ .

### 3.2.3 Measurement models

In this section we detail all the possible measurements that each agent  $a \in \mathcal{A}$  might produce at a given time  $t$ . Specifically, we differentiate among navigation measurements, direct (inter-agent) measurements and indirect (reflected) measurements. Fig. 3.2 provides an intuitive visualization of the different types of measurement. By referencing to agent  $\mathbf{s}_1$  (the bottom one), we show the availability of one navigation measurement (Fig. 3.2a), two direct measurements (Fig. 3.2b) and three different indirect measurements (Fig. 3.2c), both monostatic and bistatic (the latter originating from reflections either on target or another agent). The following section do not pose any constraint on the pdf of measurements, however we will use the Gaussian distribution to visualize each specific likelihood pdf for convenience. In practice, the knowledge of measurement pdf should be available for an optimal design of the algorithm, meaning that hardware calibration has to be performed. In case of inaccurate choice of measurement distribution, it may occur to come across over-confidence issues of the measurements or, on the other side, an underestimation of the same.

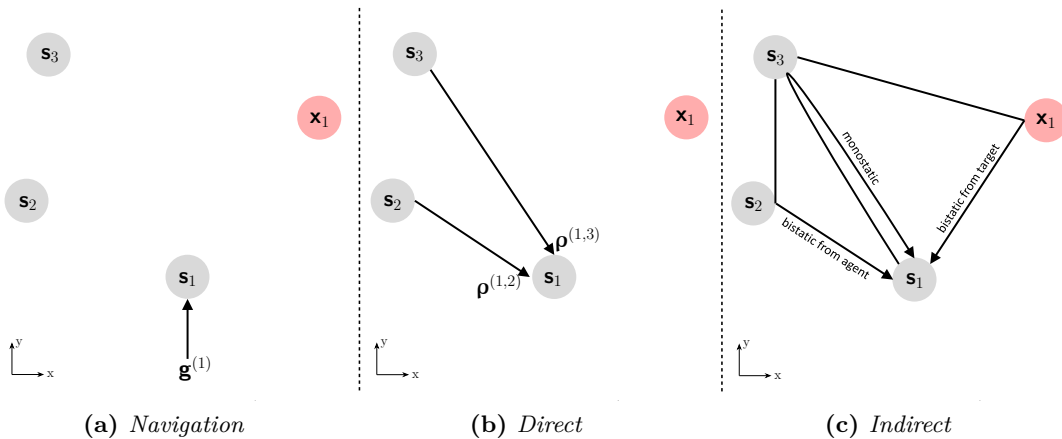


**Figure 3.2:** Visualization of possible types of measurement available at a given agent. All measurements are referred to agent  $\mathbf{s}_1$ .

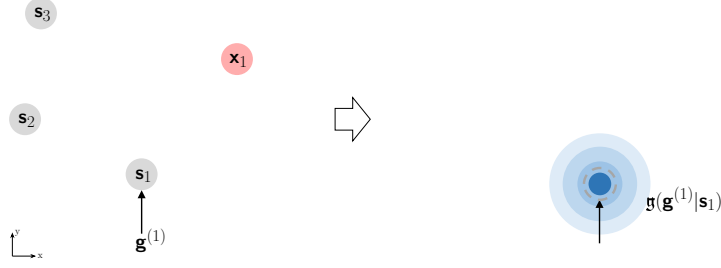


**Figure 3.3:** Visual representation of a navigation measurement likelihood of agent  $\mathbf{s}_1$ .

### 3.2.3.1 Navigation measurement

The navigation measurement collected by agent  $a \in \mathcal{A}$  at time  $t$ , represented by

$$\mathbf{g}_t^{(a)} = \boldsymbol{\theta}(\mathbf{s}_{a,t}, \mathbf{n}_t^{(a)}), \quad (3.4)$$

is an observation made by agent  $a$  of its own state, e.g., acquired with an on-board system, such as GPS or Inertial Navigation System (INS). The function  $\boldsymbol{\theta}(\cdot)$  and the statistics of  $\mathbf{n}_t^{(a)}$  define the likelihood function  $\mathfrak{g}(\mathbf{g}_t^{(a)}|\mathbf{s}_{a,t})$ . The effect of a navigation likelihood is reported in Fig. 3.3 for the case of a Gaussian measurement of agent position, for the same scene as in Fig. 3.2a. We indicate with  $\mathcal{A}_t^{\mathfrak{g}} \subseteq \mathcal{A}$  the set of agents that have a navigation measurement available at time  $t$ . Therefore, we can define the vector of all the navigation measurements from all the agents at time  $t$  as  $\mathbf{g}_t = [\mathbf{g}_t^{(a)\top}]_{a \in \mathcal{A}_t^{\mathfrak{g}}}^{\top}$ , and the vector of all the navigation measurements from all the agents at all times as  $\mathbf{g}_{1:t} \triangleq [\mathbf{g}_1^{\top} \cdots \mathbf{g}_t^{\top}]^{\top}$ . Assuming that (A3) the navigation measurements are conditional independent over  $a \in \mathcal{A}_t^{\mathfrak{g}}$  given the agent states  $\mathbf{s}_t$ , the joint likelihood  $f(\mathbf{g}_t|\mathbf{s}_t)$  factorizes as:

$$f(\mathbf{g}_t|\mathbf{s}_t) = \prod_{a \in \mathcal{A}_t^{\mathfrak{g}}} \mathfrak{g}(\mathbf{g}_t^{(a)}|\mathbf{s}_{a,t}). \quad (3.5)$$

### 3.2.3.2 Direct measurement

The direct measurement collected at time  $t$  by an agent-receiver  $a \in \mathcal{R}$  from an agent-transmitter  $a' \in \mathcal{T} - \{a\}$  is represented by:

$$\boldsymbol{\rho}_t^{(a,a')} = \boldsymbol{\vartheta}(\mathbf{s}_{a,t}, \mathbf{s}_{a',t}, \mathbf{w}_t^{(a,a')}). \quad (3.6)$$

The direct measurement  $\boldsymbol{\rho}_t^{(a,a')}$  is therefore an observation of the state of agent  $a'$  made by agent  $a$ . The function  $\boldsymbol{\vartheta}(\cdot)$  and the statistics of  $\mathbf{w}_t^{(a,a')}$  define the likelihood function  $\boldsymbol{\delta}(\boldsymbol{\rho}_t^{(a,a')}|\mathbf{s}_{a,t}, \mathbf{s}_{a',t})$ . The effect of a direct measurement likelihood is reported in Fig. 3.4 for the separate cases of Gaussian-distributed range and bearing measurements between agents  $\mathbf{s}_1$  and  $\mathbf{s}_2$ , and used to localize  $\mathbf{s}_1$ . We further indicate with  $\mathcal{T}_t^{(a)} \subseteq \mathcal{T} - \{a\}$  the set of agents that have provided a direct measurement to agent  $a$  at time  $t$ . The vector of all the direct measurements acquired by  $a$  from its neighbors at time  $t$  is  $\boldsymbol{\rho}_t^{(a)} = [\boldsymbol{\rho}_t^{(a,a')\top}]_{a' \in \mathcal{T}_t^{(a)}}^{\top}$ . We further

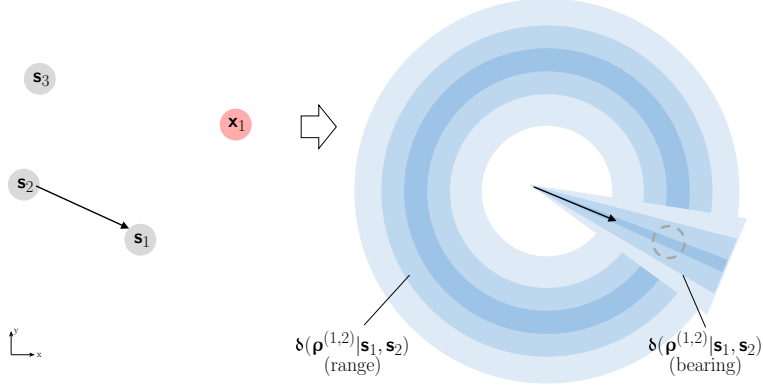


**Figure 3.4:** Visual representation of likelihood in the cases of Gaussian-distributed range and bearing direct measurements between agents  $\mathbf{s}_1$  and  $\mathbf{s}_2$ , and used to localize agent  $\mathbf{s}_1$ .

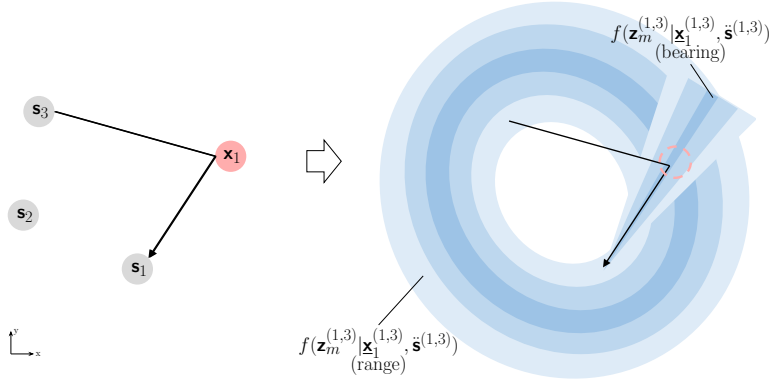


**Figure 3.5:** Visual representation of likelihood in the cases of Gaussian-distributed (bistatic) range and bearing indirect measurements between agent  $\mathbf{s}_3$  (Tx) and  $\mathbf{s}_1$  (Rx), and used for the localization of target  $\mathbf{x}_1$ .

define the vector of all the direct measurements acquired by all the agents at time  $t$  is  $\boldsymbol{\rho}_t = [\boldsymbol{\rho}_t^{(a)\top}]_{a \in \mathcal{R}}^\top$ , and the vector of all the direct measurements acquired by all the agents at all times as  $\boldsymbol{\rho}_{1:t} \triangleq [\boldsymbol{\rho}_1^\top \cdots \boldsymbol{\rho}_t^\top]^\top$ . Assuming that (A4) the direct measurements are conditional independent over  $a \in \mathcal{R}$  and  $a' \in \mathcal{T}_t^{(a)}$  given the agent states  $\mathbf{s}_t$ , the joint likelihood  $f(\boldsymbol{\rho}_t | \mathbf{s}_t)$  factorizes as:

$$f(\boldsymbol{\rho}_t | \mathbf{s}_t) = \prod_{a \in \mathcal{R}} \prod_{a' \in \mathcal{T}_t^{(a)}} \delta(\boldsymbol{\rho}_t^{(a,a')} | \mathbf{s}_{a,t}, \mathbf{s}_{a',t}). \quad (3.7)$$

For convenience, we also define with  $\mathcal{R}_t^{(a)} \subseteq \mathcal{R} - \{a\}$  the set of agents that have received a direct measurement from  $a$  at time  $t$ .

### 3.2.3.3 Multiobject tracking (MOT) measurement

We consider the  $j$ -th receiver-transmitter couple  $(j_1, j_2)$  with  $j \in \mathcal{J}$ ,  $j_1 \in \mathcal{R}$  and  $j_2 \in \mathcal{T}$ . The agent-receiver  $j_1 \in \mathcal{R}$  produces  $M_t^{(j)}$  MOT measurements from the signal broadcasted by the agent-transmitter  $j_2 \in \mathcal{T}$ . Note that we consider both

*bistatic* MOT measurements if  $j_1 \neq j_2$  and *monostatic* MOT measurements if  $j_1 = j_2$ . As for the navigation and direct measurements cases, in Fig. 3.5 we provide a visual representation of indirect measurement likelihood referred to the case of target localization, for the separate cases of Gaussian-distributed range and bearing measurements, for the same scene as in Fig. 3.2c. These MOT measurements, that result from a detection process, are due to reflections from targets, reflections from agents (except that from  $j_1$  and  $j_2$ ), or clutter. The  $m$ -th MOT measurement is represented by the vector  $\mathbf{z}_{m,t}^{(j)}$ ,  $m \in \mathcal{M}_t^{(j)} \triangleq \{1 \dots M_t^{(j)}\}$  (we use the vector and not a scalar variable as a same measurement can be composed of multiple observations, e.g., TOA+AOA). We define the vector of all the MOT measurements produced at time  $t$  by agent-receiver  $j_1 \in \mathcal{R}$  from agent-transmitter  $j_2 \in \mathcal{T}$  as  $\mathbf{z}_t^{(j)} = [\mathbf{z}_{1,t}^{(j)\top} \dots \mathbf{z}_{M_t^{(j)},t}^{(j)\top}]^\top$ , the vector of all the MOT measurements produced by all the agents at time  $t$  as  $\mathbf{z}_t = [\mathbf{z}_t^{(j)\top}]_{j \in \mathcal{J}}^\top$ , and the vector of all the MOT measurements produced by all the agents at all times as  $\mathbf{z}_{1:t} \triangleq [\mathbf{z}_1^\top \dots \mathbf{z}_t^\top]^\top$ . For convenience, we also define the vector of numbers of MOT measurements produced by all the agents at time  $t$  as  $\mathbf{m}_t = [\mathbf{M}_t^{(j)}]_{j \in \mathcal{J}}$ , and the vector of numbers of MOT measurements produced by all the agents at all times as  $\mathbf{m}_{1:t} \triangleq [\mathbf{m}_1^\top \dots \mathbf{m}_t^\top]^\top$ . Note that MOT measurements, unlike navigation and direct measurements, have *unknown* origins, i.e., it is unknown if a given MOT measurement is generated by an object — either target or agent — and by which object.

### 3.3 Stochastic MTT problem formulation

This section presents a stochastic approach to the cooperative localization problem. We first provide the modeling of new and old PTs and respective creation of a target space, then the statistical characterization of association hypothesis of MOT measurements, which leads to the derivation of the conditional pdf of new PTs with respect to old ones and of the MOT likelihood.

#### 3.3.1 Object state model

We define the augmented PT state as  $\mathbf{y}_{\ell,t} \triangleq [\mathbf{x}_{\ell,t}^\top r_{\ell,t}]^\top$ , the joint augmented state vector at time  $t$  as  $\mathbf{y}_t \triangleq [\mathbf{y}_{1,t}^\top \dots \mathbf{y}_{|\mathcal{L}_t|,t}^\top]$ , and the joint augmented state vector at all times as  $\mathbf{y}_{1:t} \triangleq [\mathbf{y}_1^\top \dots \mathbf{y}_t^\top]^\top$ . We also define the joint state vector at time  $t$  and the joint state vector at all times i.e.,  $\mathbf{x}_t \triangleq [\mathbf{x}_{1,t}^\top \dots \mathbf{x}_{|\mathcal{L}_t|,t}^\top]$  and  $\mathbf{x}_{1:t} \triangleq [\mathbf{x}_1^\top \dots \mathbf{x}_t^\top]^\top$ , respectively, as well as the joint existence vector at time  $t$  and the joint existence vector at all times, i.e.,  $\mathbf{r}_t \triangleq [r_{1,t} \dots r_{|\mathcal{L}_t|,t}]$  and  $\mathbf{r}_{1:t} \triangleq [\mathbf{r}_1^\top \dots \mathbf{r}_t^\top]^\top$ . The states  $\mathbf{x}_{\ell,t}$  of nonexisting PTs are obviously irrelevant. Therefore, all the pdfs defined for PT states  $f(\mathbf{y}_{\ell,t}) = f(\mathbf{x}_{\ell,t}, r_{\ell,t})$  are such that:

$$f(\mathbf{x}_{\ell,t}, r_{\ell,t} = 0) = f_{\ell,t} f_D(\mathbf{x}_{\ell,t}), \quad (3.8)$$

where  $\mathbf{f}_{\ell,t} \in [0, 1]$  is a constant and  $f_D(\mathbf{x}_{\ell,t})$  is an arbitrary “dummy pdf”. Each PT at time  $t$  and agent pair  $j$  is either a “legacy” PT or a “new” PT.

New PTs are used to incorporate in the state space those targets that are detected for the first time at time  $t$  and by the agent pair  $j$ . Each new PT corresponds to a measurement  $\mathbf{z}_{m,t}^{(j)}$ . The augmented state of a new PT is denoted by  $\bar{\mathbf{y}}_{m,t}^{(j)} = [\bar{\mathbf{x}}_{m,t}^{(j)\top}, \bar{\mathbf{r}}_{m,t}^{(j)\top}]^\top$ ,  $m \in \mathcal{M}_t^{(j)}$ , and  $\bar{\mathbf{r}}_{m,t}^{(j)} = 1$  meaning that measurement  $m$  was generated by a target that was never detected before. The states of newly detected targets at time  $t$  and agent pair  $j$  are a-priori independent and distributed according  $f_n(\bar{\mathbf{x}}_{m,t}^{(j)})$ . We define the joint augmented state vector of all the new PTs at time  $t$  and agent pair  $j$  as  $\bar{\mathbf{y}}_t^{(j)} \triangleq [\bar{\mathbf{y}}_{1,t}^{(j)\top} \cdots \bar{\mathbf{y}}_{\mathcal{M}_t^{(j)},t}^{(j)\top}]^\top$ , and the joint augmented state vector of all the new PTs introduced at time  $t$  as  $\bar{\mathbf{y}}_t \triangleq [\bar{\mathbf{y}}_t^{(1)\top} \cdots \bar{\mathbf{y}}_t^{(|\mathcal{J}|)\top}]^\top$ . A legacy PT is a PT that was already established in the past, either at current time  $t$  at a previous agent pair  $j - 1$ , or at previous time  $t - 1$  at the last agent pair  $J$ . Therefore, the set of legacy PTs at time  $t$  and agent pair  $j \in \mathcal{J} - \{1\}$ , denoted by  $\mathcal{L}_t^{(j)}$ , is the union of legacy PTs and new PTs established at current time  $t$  at the previous agent pair  $j - 1$ :  $\mathcal{L}_t^{(j)} = \mathcal{L}_t^{(j-1)} \cup \mathcal{M}_t^{(j-1)}$ . Note that, at the first agent pair, i.e.,  $j = 1$ ,  $\mathcal{L}_t^{(1)}$  coincides with the set of PTs at time  $t - 1$ , i.e.,  $\mathcal{L}_{t-1}$ , which is the union of legacy PTs and new PTs established at previous time  $t - 1$  at the last agent pair  $J$ , i.e.,  $\mathcal{L}_t^{(1)} = \mathcal{L}_{t-1} = \mathcal{L}_{t-1}^{(|\mathcal{J}|)} \cup \mathcal{M}_{t-1}^{(|\mathcal{J}|)}$ . (This relations are understood to include a suitable reindexing of the elements of  $\mathcal{M}_t^{(j)}$  [62, Sec. VIII-B]). The number of PTs does not actually grow by  $|\mathcal{M}_t^{(j)}|$  because the set of PTs is pruned, i.e., PTs with small existence probability are discarded. The augmented state of a legacy PT is denoted by  $\mathbf{y}_{\ell,t}^{(j)} = [\mathbf{x}_{\ell,t}^{(j)\top}, \mathbf{r}_{\ell,t}^{(j)\top}]^\top$ ,  $\ell \in \mathcal{L}_t^{(j)}$ . The joint augmented state vector of all the legacy PTs at time  $t$  and agent pair  $j \in \mathcal{J}$  is defined as  $\mathbf{y}_t^{(j)} \triangleq [\mathbf{y}_{1,t}^{(j)\top} \cdots \mathbf{y}_{|\mathcal{L}_t^{(j)},t}^{(j)\top}]^\top$ , and can also be written (for  $j \in \mathcal{J} - \{1\}$ ) as  $\mathbf{y}_t^{(j-1)} \triangleq \mathbf{y}_t^{(j)} = [\mathbf{y}_t^{(j-1)\top} \bar{\mathbf{y}}_t^{(j-1)\top}]^\top$ . Note that, at time  $t$  at the first agent pair, i.e.,  $j = 1$ , there is one legacy PT  $\mathbf{y}_{\ell,t}^{(1)} = \mathbf{y}_{\ell,t}$  for each PT  $\mathbf{y}_{\ell,t-1}$  at time  $t - 1$ , and that  $\mathbf{y}_t^{(0)} \triangleq \mathbf{y}_{t-1}$ . Then, assuming that (A5) the single augmented state of legacy PTs  $\mathbf{y}_{\ell,t}$  evolves independently, (A6) the joint augmented state vector  $\mathbf{y}_t \triangleq [\mathbf{y}_{1,t}^\top \cdots \mathbf{y}_{|\mathcal{L}_{t-1},t}^\top]^\top$  of the legacy PTs evolves according to a first-order Markov process and, recalling that  $\mathcal{L}_t^{(1)} = \mathcal{L}_{t-1}$ , the augmented state transition pdf of legacy PTs  $\mathbf{y}_t$  factorizes as:

$$f(\mathbf{y}_t | \mathbf{y}_{t-1}) = \prod_{\ell \in \mathcal{L}_{t-1}} f(\mathbf{x}_{\ell,t}, \mathbf{r}_{\ell,t} | \mathbf{x}_{\ell,t-1}, \mathbf{r}_{\ell,t-1}), \quad (3.9)$$

where [62]

$$f(\mathbf{x}_{\ell,t}, \mathbf{r}_{\ell,t} | \mathbf{x}_{\ell,t-1}, \mathbf{r}_{\ell,t-1} = 0) = \begin{cases} f_D(\mathbf{x}_{\ell,t}), & \mathbf{r}_{\ell,t} = 0, \\ 0, & \mathbf{r}_{\ell,t} = 1, \end{cases} \quad (3.10)$$

and

$$f(\mathbf{x}_{\ell,t}, \mathbf{r}_{\ell,t} | \mathbf{x}_{\ell,t-1}, \mathbf{r}_{\ell,t-1} = 1) = \begin{cases} (1 - p_s(\mathbf{x}_{\ell,t-1})) f_D(\mathbf{x}_{\ell,t}), & \mathbf{r}_{\ell,t} = 0, \\ p_s(\mathbf{x}_{\ell,t-1}) f(\mathbf{x}_{\ell,t} | \mathbf{x}_{\ell,t-1}), & \mathbf{r}_{\ell,t} = 1. \end{cases} \quad (3.11)$$

where  $p_s(\mathbf{x}_{\ell,t-1})$  is the survival probability of the target. Note that, given the definitions of  $\mathbf{y}_t$  and  $\bar{\mathbf{y}}_t$  introduced above, it follows that  $\mathbf{y}_t = [\mathbf{y}_t^\top \bar{\mathbf{y}}_t^\top]^\top$ .

### 3.3.2 Modeling the measurement unknown origin

As mentioned above, the MOT measurements  $\mathbf{z}_{m,t}^{(j)}$ ,  $m \in \mathcal{M}_t^{(j)}$ , have unknown origins, i.e., it is unknown if a given MOT measurement originated from clutter or from an object, either target or agent, and from which object. Intuitively, by referring to Fig. 3.6, the goal is to consistently combine the likelihood of each MOT measurement, a task which is far from being straightforward especially in case the proximity of objects with respect to measurement uncertainty. In the figure it is highlighted that it may occur the case of close targets with overlapped bistatic (range and bearing) likelihoods.

To handle this uncertainty, we first introduce the joint object state vector as the vector stacking the legacy PT states at time  $t$  and agent pair  $j$ , and the agent states at time  $t$ , i.e.,  $\mathbf{o}_t^{(j)} = [\mathbf{x}_t^{(j)\top} \mathbf{s}_t^\top]^\top$ . Thus, the vector  $\mathbf{o}_t^{(j)}$  includes all the  $O_t^{(j)} = |\mathcal{L}_t^{(j)}| + |\mathcal{A}|$  objects that can generate a MOT measurement at time  $t$  and agent pair  $j$ . Note that the object  $\mathbf{o}_{i,t}^{(j)}$ ,  $i \in \mathcal{O}_t^{(j)} \triangleq \{1 \dots O_t^{(j)}\}$  coincides with  $\mathbf{x}_{\ell,t}^{(j)}$  if  $i = \ell$ , and with  $\mathbf{s}_t^{(a^*)}$  if  $i = |\mathcal{L}_t^{(j)}| + a^*$ .

An existing object  $i$  is detected by the receiver-transmitter pair  $j$  — i.e., it generates a measurement  $\mathbf{z}_{m,t}^{(j)}$  at agent pair  $j$  — with a probability  $P_d(\mathbf{x}_{\ell,t}^{(j)}, \bar{\mathbf{s}}_t^{(j)})$ , if  $i = \ell$ , or, with a probability  $P_d(\mathbf{s}_{a^*,t}, \bar{\mathbf{s}}_t^{(j)})$  if  $i = |\mathcal{L}_t^{(j)}| + a^*$ . If  $\mathbf{z}_{m,t}^{(j)}$  is generated by PT  $\ell$  then its conditional distribution given PT state  $\mathbf{x}_{\ell,t}^{(j)}$  is described by the pdf  $f(\mathbf{z}_{m,t}^{(j)} | \mathbf{x}_{\ell,t}^{(j)}, \bar{\mathbf{s}}_t^{(j)})$  if  $i = \ell$ , or by the conditional pdf  $f(\mathbf{z}_{m,t}^{(j)} | \mathbf{s}_{a^*,t}, \bar{\mathbf{s}}_t^{(j)})$  if  $i = |\mathcal{L}_t^{(j)}| + a^*$ . On the other hand,  $\mathbf{z}_{m,t}^{(j)}$  may also be due to some interfering source, e.g., sea clutter in a maritime radar application. Such a measurement is referred to as a false alarm. The number of false alarm measurements at agent pair  $j$  is modeled by a Poisson pmf with mean  $\mu_c^{(j)}$ , i.e.,  $\mathcal{P}(\mu_c^{(j)})$ , and each false alarm measurement at agent pair  $j$  is distributed according to the pdf  $f_c^{(j)}(\mathbf{z}_{m,t}^{(j)})$ .

To model the measurement-origin uncertainty, we make the following data association assumption: (A7) each MOT measurement  $\mathbf{z}_{m,t}^{(j)}$  originates from an object (PT or agent) or from clutter (false alarm), and it cannot originate from more than one object simultaneously. Conversely, at time  $t$ , one object can generate at most one measurement  $\mathbf{z}_{m,t}^{(j)}$ . Additionally, the measurement  $\mathbf{z}_{m,t}^{(j)}$  can originate

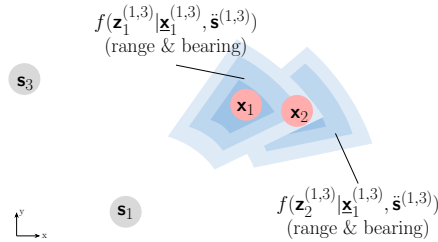


**Figure 3.6:** Illustrative example of measurement uncertainty for the case of two closed targets with overlapped bistatic likelihoods.

neither from the receiver agent  $j_1$  nor from the transmitter agent  $j_2$ , i.e., neither from object  $i = |\mathcal{L}_t^{(j)}| + j_1$  nor from object  $i = |\mathcal{L}_t^{(j)}| + j_2$ .

Following [62, 83], to model (A7) we introduce the set  $\mathcal{N}_t^{(j)}$  of new PTs that exist at time  $t$  and agent pair  $j$ , that is,  $\mathcal{N}_t^{(j)} \triangleq \{m \in \mathcal{M}_t^{(j)} : \bar{r}_{m,t}^{(j)} = 1\}$ ; the object-oriented association vector  $\boldsymbol{\alpha}_t^{(j)} \triangleq [\alpha_{1,t}^{(j)} \cdots \alpha_{\mathcal{O}_t^{(j)},t}^{(j)}]^\top$ ; and the MOT measurement-oriented association vector  $\boldsymbol{\beta}_t^{(j)} \triangleq [\beta_{1,t}^{(j)} \cdots \beta_{\mathcal{M}_t^{(j)},t}^{(j)}]^\top$ . Here,  $\alpha_{i,t}^{(j)}$ ,  $i \in \mathcal{O}_t^{(j)}$ , is defined as  $m \in \mathcal{M}_t^{(j)}$  if object  $i$  generates MOT measurement  $m$ , and 0 if object  $i$  does not generate any MOT measurement; and  $\beta_{m,t}^{(j)}$ ,  $m \in \mathcal{M}_t^{(j)}$ , is defined as  $i$  if MOT measurement  $m$  originates from object  $i$ , and 0 if MOT measurement  $m$  does not originate from an object. The point-target assumption can therefore be expressed by the indicator function  $\Phi(\boldsymbol{\alpha}_t^{(j)}, \boldsymbol{\beta}_t^{(j)})$ , defined as:

$$\Phi(\boldsymbol{\alpha}_t^{(j)}, \boldsymbol{\beta}_t^{(j)}) \triangleq \Psi(\boldsymbol{\alpha}_t^{(j)}, \boldsymbol{\beta}_t^{(j)}) \prod_{m \in \mathcal{N}_t^{(j)}} \Gamma_m(\boldsymbol{\beta}_t^{(j)}), \quad (3.12)$$

where

$$\Gamma_m(\boldsymbol{\beta}_t^{(j)}) \triangleq \begin{cases} 0, & \text{if } \beta_{m,t}^{(j)} \in \mathcal{O}_t^{(j)}, \\ 1, & \text{if } \beta_{m,t}^{(j)} = 0, \end{cases} \quad (3.13)$$

and

$$\Psi(\boldsymbol{\alpha}_t^{(j)}, \boldsymbol{\beta}_t^{(j)}) \triangleq \prod_{i \in \mathcal{O}_t^{(j)}} \prod_{m \in \mathcal{M}_t^{(j)}} \psi(\alpha_{i,t}^{(j)}, \beta_{m,t}^{(j)}), \quad (3.14)$$

with

$$\psi(\alpha_{i,t}^{(j)}, \beta_{m,t}^{(j)}) \triangleq \begin{cases} 0, & \text{if } \alpha_{i,t}^{(j)} = m \text{ and } \beta_{m,t}^{(j)} \neq i, \text{ or } \alpha_{i,t}^{(j)} \neq m \text{ and } \beta_{m,t}^{(j)} = i, \\ 1, & \text{otherwise.} \end{cases} \quad (3.15)$$

(We observe that the indicator function  $\Phi(\boldsymbol{\alpha}_t^{(j)}, \boldsymbol{\beta}_t^{(j)})$  formally depends also on the existence variables  $\bar{r}_{m,t}^{(j)}$ ,  $m \in \mathcal{M}_t^{(j)}$ .) Stated differently, function  $\Psi(\boldsymbol{\alpha}_t^{(j)}, \boldsymbol{\beta}_t^{(j)})$  is 0 if an MOT measurement is associated with two or more different objects (and, vice versa, if an object is associated with two or more MOT measurements), and 1 otherwise; and the product over  $m \in \mathcal{N}_t^{(j)}$  of  $\Gamma_m(\boldsymbol{\beta}_t^{(j)})$  is 0 if a new PTs is associated with an MOT measurement that is also associated with an object, and 1 otherwise. Note that, for convenience, we also define the vectors  $\boldsymbol{\alpha}_t \triangleq [\boldsymbol{\alpha}_t^{(1)\top} \cdots \boldsymbol{\alpha}_t^{(J)\top}]^\top$  and  $\boldsymbol{\beta}_t \triangleq [\boldsymbol{\beta}_t^{(1)\top} \cdots \boldsymbol{\beta}_t^{(J)\top}]^\top$ , as well as  $\boldsymbol{\alpha}_{1:t} \triangleq [\boldsymbol{\alpha}_1^\top \cdots \boldsymbol{\alpha}_t^\top]^\top$  and  $\boldsymbol{\beta}_{1:t} \triangleq [\boldsymbol{\beta}_1^\top \cdots \boldsymbol{\beta}_t^\top]^\top$ .

### 3.3.3 Conditional pdf of new PT states, DA vector and number of measurements

In order to obtain an expression of  $f(\bar{\mathbf{y}}_t, \boldsymbol{\alpha}_t, \boldsymbol{\beta}_t, \mathbf{m}_t | \mathbf{y}_t, \mathbf{s}_t)$ , i.e., the joint conditional pdf of  $\bar{\mathbf{y}}_t$ ,  $\boldsymbol{\alpha}_t$ ,  $\boldsymbol{\beta}_t$ ,  $\mathbf{m}_t$  given  $\mathbf{y}_t$  and  $\mathbf{s}_t$ , we additionally make the following commonly used assumptions: (A8) at time  $t$ , the MOT measurements of different pairs  $j$  are

conditionally independent given all the agents states and the legacy PTs states, and that (A9) the new PT states  $\bar{\mathbf{y}}_t^{(j')}$  related to pairs  $j' = 1, \dots, j-1$  become legacy PT states at the successive pairs  $j, \dots, |\mathcal{J}|$ . Then, using the assumptions (A8) and (A9), we get:

$$\begin{aligned}
 f(\bar{\mathbf{y}}_t, \boldsymbol{\alpha}_t, \boldsymbol{\beta}_t, \mathbf{m}_t | \mathbf{y}_t, \mathbf{s}_t) = & \\
 & C(\mathbf{m}_t) \prod_{j=1}^J \Phi(\boldsymbol{\alpha}_t^{(j)}, \boldsymbol{\beta}_t^{(j)}) \prod_{\ell \in \mathcal{L}_t^{(j)}} q_1(\mathbf{x}_{\ell,t}^{(j)}, \mathbf{r}_{\ell,t}^{(j)}, \ddot{\mathbf{s}}_t^{(j)}, \boldsymbol{\alpha}_{\ell,t}^{(j)}; \mathbf{M}_t^{(j)}) \\
 & \times \prod_{a \in \mathcal{A}} h_1(\mathbf{s}_{a,t}, \ddot{\mathbf{s}}_t^{(j)}, \boldsymbol{\alpha}_{|\mathcal{L}_t^{(j)}|+a,t}^{(j)}; \mathbf{M}_t^{(j)}) \prod_{m \in \mathcal{M}_t^{(j)}} v_1(\bar{\mathbf{x}}_{m,t}^{(j)}, \bar{\mathbf{r}}_{m,t}^{(j)}, \boldsymbol{\beta}_t^{(j)}).
 \end{aligned} \tag{3.16}$$

Here,  $C(\mathbf{m}_t)$  is a normalization factor that depends only on the vector  $\mathbf{m}_t$  and  $q_1(\mathbf{x}_{\ell,t}^{(j)}, \mathbf{r}_{\ell,t}^{(j)} = 1, \ddot{\mathbf{s}}_t^{(j)}, \boldsymbol{\alpha}_{\ell,t}^{(j)}; \mathbf{M}_t^{(j)})$  is defined as:

$$\begin{aligned}
 q_1(\mathbf{x}_{\ell,t}^{(j)}, \mathbf{r}_{\ell,t}^{(j)} = 1, \ddot{\mathbf{s}}_t^{(j)}, \boldsymbol{\alpha}_{\ell,t}^{(j)}; \mathbf{M}_t^{(j)}) &= \begin{cases} \frac{P_d(\mathbf{x}_{\ell,t}^{(j)}, \ddot{\mathbf{s}}_t^{(j)})}{\mu_c^{(j)}}, & \boldsymbol{\alpha}_{\ell,t}^{(j)} \in \mathcal{M}_t^{(j)}, \\ 1 - P_d(\mathbf{x}_{\ell,t}^{(j)}, \ddot{\mathbf{s}}_t^{(j)}), & \boldsymbol{\alpha}_{\ell,t}^{(j)} = 0, \end{cases} \\
 q_1(\mathbf{x}_{\ell,t}^{(j)}, \mathbf{r}_{\ell,t}^{(j)} = 0, \ddot{\mathbf{s}}_t^{(j)}, \boldsymbol{\alpha}_{\ell,t}^{(j)}; \mathbf{M}_t^{(j)}) &= \delta_{\boldsymbol{\alpha}_{\ell,t}^{(j)}, 0},
 \end{aligned} \tag{3.17}$$

where  $\delta_{\boldsymbol{\alpha}_{\ell,t}^{(j)}, 0}$  is 1 if  $\boldsymbol{\alpha}_{\ell,t}^{(j)}$  is equal to zero, and 0 otherwise. For  $a \neq j_1$  or  $a \neq j_2$ , the function  $h_1(\mathbf{s}_{a,t}, \ddot{\mathbf{s}}_t^{(j)}, \boldsymbol{\alpha}_{|\mathcal{L}_t^{(j)}|+a,t}^{(j)}; \mathbf{M}_t^{(j)})$  is defined as:

$$h_1(\mathbf{s}_{a,t}, \ddot{\mathbf{s}}_t^{(j)}, \boldsymbol{\alpha}_{|\mathcal{L}_t^{(j)}|+a,t}^{(j)}; \mathbf{M}_t^{(j)}) = \begin{cases} \frac{P_d(\mathbf{s}_{a,t}, \ddot{\mathbf{s}}_t^{(j)})}{\mu_c^{(j)}}, & \boldsymbol{\alpha}_{|\mathcal{L}_t^{(j)}|+a,t}^{(j)} \in \mathcal{M}_t^{(j)}, \\ 1 - P_d(\mathbf{s}_{a,t}, \ddot{\mathbf{s}}_t^{(j)}), & \boldsymbol{\alpha}_{|\mathcal{L}_t^{(j)}|+a,t}^{(j)} = 0, \end{cases} \tag{3.18}$$

while for  $a = j_1$  or  $a = j_2$ ,  $h_1(\mathbf{s}_{a,t}, \ddot{\mathbf{s}}_t^{(j)}, \boldsymbol{\alpha}_{|\mathcal{L}_t^{(j)}|+a,t}^{(j)}; \mathbf{M}_t^{(j)}) = \delta_{\boldsymbol{\alpha}_{|\mathcal{L}_t^{(j)}|+a,t}^{(j)}, 0}$ , where  $v_1(\bar{\mathbf{x}}_{m,t}^{(j)}, \bar{\mathbf{r}}_{m,t}^{(j)} = 1, \boldsymbol{\beta}_t^{(j)})$  is defined as:

$$v_1(\bar{\mathbf{x}}_{m,t}^{(j)}, \bar{\mathbf{r}}_{m,t}^{(j)} = 1, \boldsymbol{\beta}_t^{(j)}) = \begin{cases} 0, & \text{if } \boldsymbol{\beta}_{m,t}^{(j)} \in \mathcal{O}_t^{(j)}, \\ \frac{\mu_n^{(j)}}{\mu_c^{(j)}} f_n(\bar{\mathbf{x}}_{m,t}^{(j)}), & \text{if } \boldsymbol{\beta}_{m,t}^{(j)} = 0, \end{cases} \tag{3.19}$$

$$v_1^{(j)}(\bar{\mathbf{x}}_{m,t}^{(j)}, \bar{\mathbf{r}}_{m,t}^{(j)} = 0, \boldsymbol{\beta}_t^{(j)}) = f_D(\bar{\mathbf{x}}_{m,t}^{(j)}), \tag{3.20}$$

where  $\mu_n^{(j)}$  is the mean number of newly born targets.

### 3.3.4 Likelihood function of MOT measurements

To find an expression of the joint likelihood function  $f(\mathbf{z}_t | \bar{\mathbf{y}}_t, \boldsymbol{\alpha}_t, \mathbf{m}_t, \underline{\mathbf{y}}_t, \mathbf{s}_t)$ , we make the following further commonly used assumptions [62]: (A10) at time  $t$  and agent pair  $j$  the clutter-originated MOT measurements are independent of the object-originated MOT measurements; (A11) at time  $t$  and agent pair  $j$  the clutter-originated MOT measurements are independent and identically distributed with pdf  $f_c^{(j)}(\mathbf{z}_{m,t}^{(j)})$ ; (A12) at time  $t$  and agent pair  $j$ , given all the target states, the target-originated MOT measurements are conditionally independent of each other and also conditionally independent of all the clutter-originated MOT measurements. Then, using the assumptions from (A8) to (A12), the joint likelihood  $f(\mathbf{z}_t | \bar{\mathbf{y}}_t, \boldsymbol{\alpha}_t, \mathbf{m}_t, \underline{\mathbf{y}}_t, \mathbf{s}_t)$  can be expressed as [62, Eq. (63)]:

$$\begin{aligned} f(\mathbf{z}_t | \bar{\mathbf{y}}_t, \boldsymbol{\alpha}_t, \mathbf{m}_t, \underline{\mathbf{y}}_t, \mathbf{s}^{(t)}) = & \\ & C(\mathbf{z}_t) \prod_{j=1}^J \prod_{\ell \in \mathcal{L}_t^{(j)}} q_2(\mathbf{x}_{\ell,t}^{(j)}, \mathbf{r}_{\ell,t}^{(j)}, \ddot{\mathbf{s}}_t^{(j)}, \boldsymbol{\alpha}_{\ell,t}^{(j)}; \mathbf{z}_t^{(j)}) \\ & \times \prod_{a \in \mathcal{A}} h_2(\mathbf{s}_{a,t}, \ddot{\mathbf{s}}_t^{(j)}, \boldsymbol{\alpha}_{|\mathcal{L}_t^{(j)}|+a,t}^{(j)}; \mathbf{z}_t^{(j)}) \prod_{m \in \mathcal{M}_t^{(j)}} v_2(\bar{\mathbf{x}}_{m,t}^{(j)}, \bar{\mathbf{r}}_{m,t}^{(j)}, \ddot{\mathbf{s}}_t^{(j)}; \mathbf{z}_{m,t}^{(j)}), \end{aligned} \quad (3.21)$$

where,  $C(\mathbf{z}_t)$  is a normalization factor, which depends on the measurements  $\mathbf{z}_t$ , and, the function  $q_2(\mathbf{x}_{\ell,t}^{(j)}, \mathbf{r}_{\ell,t}^{(j)}, \ddot{\mathbf{s}}_t^{(j)}, \boldsymbol{\alpha}_{\ell,t}^{(j)}; \mathbf{z}_t^{(j)})$  is defined as:

$$\begin{aligned} q_2(\mathbf{x}_{\ell,t}^{(j)}, \mathbf{r}_{\ell,t}^{(j)} = 1, \ddot{\mathbf{s}}_t^{(j)}, \boldsymbol{\alpha}_{\ell,t}^{(j)}; \mathbf{z}_t^{(j)}) &= \begin{cases} \frac{f(\mathbf{z}_{m,t}^{(j)} | \mathbf{x}_{\ell,t}^{(j)}, \ddot{\mathbf{s}}_t^{(j)})}{f_c^{(j)}(\mathbf{z}_{m,t}^{(j)})}, & \boldsymbol{\alpha}_{\ell,t}^{(j)} = m \in \mathcal{M}_t^{(j)}, \\ 1, & \boldsymbol{\alpha}_{\ell,t}^{(j)} = 0, \end{cases} \\ q_2(\mathbf{x}_{\ell,t}^{(j)}, \mathbf{r}_{\ell,t}^{(j)} = 0, \ddot{\mathbf{s}}_t^{(j)}, \boldsymbol{\alpha}_{\ell,t}^{(j)}; \mathbf{z}_t^{(j)}) &= 1. \end{aligned} \quad (3.22)$$

For  $a \neq j_1$  and  $a \neq j_2$ ,  $h_2(\mathbf{s}_{a,t}, \ddot{\mathbf{s}}_t^{(j)}, \boldsymbol{\alpha}_{|\mathcal{L}_t^{(j)}|+a,t}^{(j)}; \mathbf{z}_t^{(j)})$  is defined as:

$$h_2(\mathbf{s}_{a,t}, \ddot{\mathbf{s}}_t^{(j)}, \boldsymbol{\alpha}_{|\mathcal{L}_t^{(j)}|+a,t}^{(j)}; \mathbf{z}_t^{(j)}) = \begin{cases} \frac{f(\mathbf{z}_{m,t}^{(j)} | \mathbf{s}_{a,t}, \ddot{\mathbf{s}}_t^{(j)})}{f_c^{(j)}(\mathbf{z}_{m,t}^{(j)})}, & \boldsymbol{\alpha}_{|\mathcal{L}_t^{(j)}|+a,t}^{(j)} = m \in \mathcal{M}_t^{(j)}, \\ 1, & \boldsymbol{\alpha}_{\ell,t}^{(j)} = 0. \end{cases} \quad (3.23)$$

Instead, when  $a = j_1$  or  $a = j_2$ , we have that  $h_2(\mathbf{s}_{a,t}, \ddot{\mathbf{s}}_t^{(j)}, \boldsymbol{\alpha}_{|\mathcal{L}_t^{(j)}|+a,t}^{(j)}; \mathbf{z}_t^{(j)}) = 1$ .

Finally, an expression of the function  $v_2(\bar{\mathbf{x}}_{m,t}^{(j)}, \bar{\mathbf{r}}_{m,t}^{(j)}, \ddot{\mathbf{s}}_t^{(j)}; \mathbf{z}_{m,t}^{(j)})$  is provided by:

$$v_2(\bar{\mathbf{x}}_{m,t}^{(j)}, \bar{\mathbf{r}}_{m,t}^{(j)}, \ddot{\mathbf{s}}_t^{(j)}; \mathbf{z}_{m,t}^{(j)}) = \begin{cases} \frac{f(\mathbf{z}_{m,t}^{(j)} | \bar{\mathbf{x}}_{m,t}^{(j)}, \ddot{\mathbf{s}}_t^{(j)})}{f_c^{(j)}(\mathbf{z}_{m,t}^{(j)})}, & \bar{\mathbf{r}}_{m,t}^{(j)} = 1, \\ 1, & \bar{\mathbf{r}}_{m,t}^{(j)} = 0. \end{cases} \quad (3.24)$$

## 3.4 The proposed solution for cooperative self-localization and multitarget tracking

In this section, we develop the proposed BP-based joint localization and target tracking algorithm, where CSL and MTT are combined in a unique framework. The conceptualization of the algorithm is depicted in the block scheme in Fig. 3.7, which should help the reader in an easier understanding of the contents of this section. The block scheme, in fact, is intended to provide an intuition of how the CSL and MTT problem is perceived and how the different players (agents and targets) interact in the pair-by-pair processing. The intention of the block scheme is also to highlight the different layers that coexist, namely CSL, MTT and DA. The colors are chosen such that the reader is facilitated in pairing the nodes/factors of FG with the boxes of the block scheme.

### 3.4.1 Target detection and state estimation

The ultimate task of the proposed MTT algorithm is to determine at each time instant  $t$  if a legacy PT  $\ell \in \mathcal{L}_t^{(J)}$  exists (i.e., to detect the binary target existence variables  $r_{\ell,t}^{(J)}$ ), if a new PT  $m \in \mathcal{M}_t^{(J)}$  exists (i.e., to detect the binary variables  $r_{m,t}^{(J)}$ ), to estimate the states  $\mathbf{x}_{\ell,t}^{(J)}$  and  $\mathbf{x}_{m,t}^{(J)}$  of the detected legacy and new PTs, respectively, and finally estimate the states  $\mathbf{s}_{a,t}$  of the agents. This detection/estimation is based on the past and present measurements of all the agents, i.e., on the total measurement vector  $\mathbf{z}_{1:t}$ .

In the Bayesian setting, target detection and state estimation essentially amount to calculating the marginal posterior existence probabilities  $p(r_{\ell,t}^{(J)} = 1 | \mathbf{z}_{1:t})$ ,

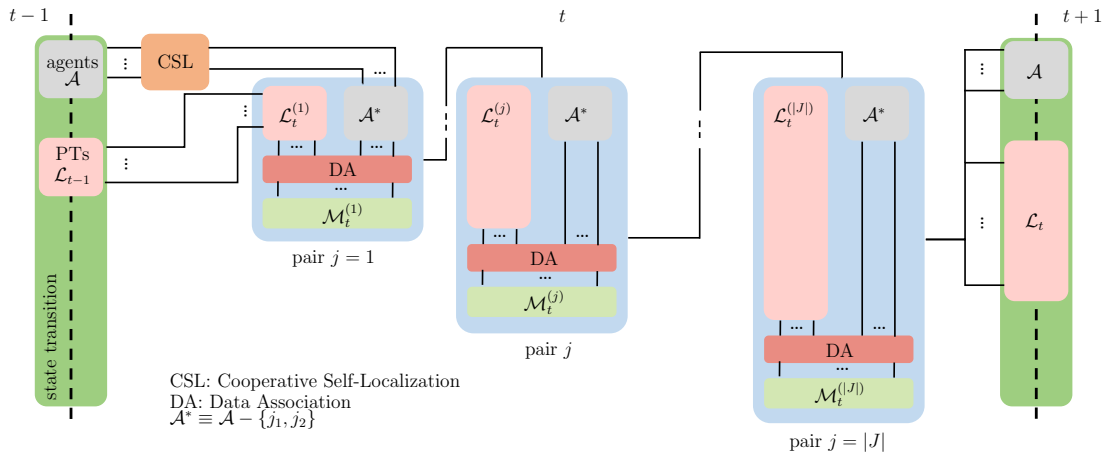


**Figure 3.7:** Block scheme providing the intuition of the proposed solution. Three agent pairs are represented: the first one, a generic one and the last one. Grey box refers to agents, pink for legacy PTs, new PTs are in pale green. Agent cooperative self-localization (CSL) layer is in orange, while data association (DA) is in red and pairwise MTT box in light blue. For convenience, we added the set  $\mathcal{A}^*$  which contains all the agents but the transmitter and receiver of the specific agent pair  $j$ .

$p(\bar{\mathbf{r}}_{m,t}^{(J)} = 1 | \mathbf{z}_{1:t})$  and the marginal posterior state pdfs  $f(\mathbf{x}_{\ell,t}^{(J)} | \mathbf{r}_{\ell,t}^{(J)} = 1, \mathbf{z}_{1:t})$  and  $f(\bar{\mathbf{x}}_{m,t}^{(J)} | \bar{\mathbf{r}}_{m,t}^{(J)} = 1, \mathbf{z}_{1:t})$ , respectively. The former and latter pdfs are obtained by direct marginalization from  $f(\mathbf{x}_{\ell,t}^{(J)}, \mathbf{r}_{\ell,t}^{(J)} = 1 | \mathbf{z}_{1:t})$  and  $f(\bar{\mathbf{x}}_{m,t}^{(J)}, \bar{\mathbf{r}}_{m,t}^{(J)} = 1 | \mathbf{z}_{1:t})$ , respectively. A legacy PT  $\ell$  or a new PT  $m$  are detected (i.e., declared to exist) if  $p(\mathbf{r}_{\ell,t}^{(J)} = 1 | \mathbf{z}_{1:t})$  or  $p(\bar{\mathbf{r}}_{m,t}^{(J)} = 1 | \mathbf{z}_{1:t})$  are larger than a suitably chosen threshold  $P_{\text{ex}}$ . For each detected legacy PT  $\ell$  and new PT  $m$ , estimates of  $\mathbf{x}_{\ell,t}^{(J)}$  and  $\bar{\mathbf{x}}_{m,t}^{(J)}$  are provided by the MMSE estimators:

$$\hat{\mathbf{x}}_{\ell,t}^{\text{MMSE}} \triangleq \int \mathbf{x}_{\ell,t}^{(J)} f(\mathbf{x}_{\ell,t}^{(J)} | \mathbf{r}_{\ell,t}^{(J)} = 1, \mathbf{z}_{1:t}) d\mathbf{x}_{\ell,t}^{(J)}, \quad (3.25)$$

and

$$\hat{\mathbf{x}}_{m,t}^{\text{MMSE}} \triangleq \int \bar{\mathbf{x}}_{m,t}^{(J)} f(\bar{\mathbf{x}}_{m,t}^{(J)} | \bar{\mathbf{r}}_{m,t}^{(J)} = 1, \mathbf{z}_{1:t}) d\bar{\mathbf{x}}_{m,t}^{(J)}. \quad (3.26)$$

The agent state estimation is instead performed by calculating the marginal posterior agent state pdfs  $f(\mathbf{s}_{a,t} | \mathbf{z}_{1:t})$ . The agent state estimate for an agent  $a$  is provided by the MMSE estimator:

$$\hat{\mathbf{s}}_{a,t}^{\text{MMSE}} \triangleq \int \mathbf{s}_{a,t} f(\mathbf{s}_{a,t} | \mathbf{z}_{1:t}) d\mathbf{s}_{a,t}. \quad (3.27)$$

Thus, the remaining problem is to calculate  $f(\mathbf{x}_{\ell,t}^{(J)}, \mathbf{r}_{\ell,t}^{(J)} | \mathbf{z}_{1:t})$ ,  $f(\bar{\mathbf{x}}_{m,t}^{(J)}, \bar{\mathbf{r}}_{m,t}^{(J)} | \mathbf{z}_{1:t})$  and  $f(\mathbf{s}_{a,t} | \mathbf{z}_{1:t})$ .

### 3.4.2 Joint posterior distribution and factor graph

The proposed SPA-based multisensor-multitarget tracking algorithm is based on a factor graph [41, 92] representing the factorization structure of the joint posterior pdf  $f(\mathbf{y}_{1:t}, \mathbf{s}_{1:t}, \boldsymbol{\alpha}_{1:t} | \mathbf{g}_{1:t}, \boldsymbol{\rho}_{1:t}, \mathbf{z}_{1:t})$  (to be derived later).

The posterior distributions  $f(\mathbf{x}_{\ell,t}^{(J)}, \mathbf{r}_{\ell,t}^{(J)} | \mathbf{z}_{1:t})$ ,  $f(\bar{\mathbf{x}}_{m,t}^{(J)}, \bar{\mathbf{r}}_{m,t}^{(J)} | \mathbf{z}_{1:t})$  and  $f(\mathbf{s}_{a,t} | \mathbf{z}_{1:t})$ , that are used for PT detection-estimation and for agent state estimation, are marginal pdfs of the joint posterior pdf  $f(\mathbf{y}_{1:t}, \mathbf{s}_{1:t}, \boldsymbol{\alpha}_{1:t} | \mathbf{g}_{1:t}, \boldsymbol{\rho}_{1:t}, \mathbf{z}_{1:t})$ .

The following assumptions are used in the derivation of the factorization:

- (A13) Given the PTs augmented states and the agents states at time  $t - 1$ , i.e.,  $\mathbf{y}_{t-1}$  and  $\mathbf{s}_{t-1}$ , respectively, the current PTs augmented states  $\mathbf{y}_t$ , the current agents states  $\mathbf{s}_t$ , the current PT-oriented association vector  $\boldsymbol{\alpha}_t$ , the current measurements  $\mathbf{g}_t$ ,  $\boldsymbol{\rho}_t$  and  $\mathbf{z}_t$ , and the current number of MOT measurements  $\mathbf{m}_t$ , are conditionally independent of the previous PTs augmented states, agents states, association vectors and measurements;
- (A14) Given  $\mathbf{y}_{t-1}$  and  $\mathbf{s}_t$ , the variables  $\mathbf{y}_t$ ,  $\boldsymbol{\alpha}_t$ ,  $\mathbf{g}_t$ ,  $\boldsymbol{\rho}_t$ ,  $\mathbf{z}_t$  and  $\mathbf{m}_t$  are conditionally independent of  $\mathbf{s}_{t-1}$ ;
- (A15) Given  $\mathbf{s}_{t-1}$ , the agents states vector at time  $t$ , i.e.,  $\mathbf{s}_t$ , is conditionally independent of  $\mathbf{y}_{t-1}$ ;
- (A16) Given  $\mathbf{y}_t$  and  $\mathbf{s}_t$ , the variables  $\bar{\mathbf{y}}_t$ ,  $\boldsymbol{\alpha}_t$ ,  $\mathbf{g}_t$ ,  $\boldsymbol{\rho}_t$ ,  $\mathbf{z}_t$  and  $\mathbf{m}_t$  are conditionally independent of  $\mathbf{y}_{t-1}$ ;

(A17) Given  $\mathbf{y}_{t-1}$ , the legacy PTs augmented states vector at time  $t$ , i.e.,  $\underline{\mathbf{y}}_t$ , is conditionally independent of  $\mathbf{s}_t$ ;

(A18) Given  $\underline{\mathbf{y}}_t$  and  $\mathbf{s}_t$ , the navigation measurements vector  $\mathbf{g}_t$  and the direct measurements vector  $\boldsymbol{\rho}_t$  are conditionally independent of  $\bar{\mathbf{y}}_t$ ,  $\boldsymbol{\alpha}_t$ ,  $\mathbf{z}_t$  and  $\mathbf{m}_t$ ;

(A19) Given  $\mathbf{s}_t$ ,  $\mathbf{g}_t$  is independent of  $\underline{\mathbf{y}}_t$ , and  $\boldsymbol{\rho}_t$  is independent of  $\underline{\mathbf{y}}_t$ .

We note that  $\mathbf{g}_{1:t}$ ,  $\boldsymbol{\rho}_{1:t}$  and  $\mathbf{z}_{1:t}$  are observed and thus fixed. The number of measurements  $M_t^{(j)}$  and the corresponding vector  $\mathbf{m}_{1:t}$  are fixed as well.

The steps to derive the joint posterior pdf (final expression in (3.37)) are as follows:

$$f(\mathbf{y}_{1:t}, \mathbf{s}_{1:t}, \boldsymbol{\alpha}_{1:t} | \mathbf{g}_{1:t}, \boldsymbol{\rho}_{1:t}, \mathbf{z}_{1:t}) \quad (3.28)$$

$$= f(\mathbf{y}_{1:t}, \mathbf{s}_{1:t}, \boldsymbol{\alpha}_{1:t} | \mathbf{g}_{1:t}, \boldsymbol{\rho}_{1:t}, \mathbf{z}_{1:t}, \mathbf{m}_{1:t}) \quad (3.29)$$

$$\propto f(\mathbf{y}_{1:t}, \mathbf{s}_{1:t}, \boldsymbol{\alpha}_{1:t}, \mathbf{g}_{1:t}, \boldsymbol{\rho}_{1:t}, \mathbf{z}_{1:t}, \mathbf{m}_{1:t}) \quad (3.30)$$

$$= f(\mathbf{y}_t, \mathbf{s}_t, \boldsymbol{\alpha}_t, \mathbf{g}_t, \boldsymbol{\rho}_t, \mathbf{z}_t, \mathbf{m}_t | \mathbf{y}_{1:t-1}, \mathbf{s}_{1:t-1}, \boldsymbol{\alpha}_{1:t-1}, \mathbf{g}_{1:t-1}, \boldsymbol{\rho}_{1:t-1}, \mathbf{z}_{1:t-1}, \mathbf{m}_{1:t-1}) \\ \times f(\mathbf{y}_{1:t-1}, \mathbf{s}_{1:t-1}, \boldsymbol{\alpha}_{1:t-1}, \mathbf{g}_{1:t-1}, \boldsymbol{\rho}_{1:t-1}, \mathbf{z}_{1:t-1}, \mathbf{m}_{1:t-1}) \quad (3.31)$$

$$= f(\mathbf{y}_t, \mathbf{s}_t, \boldsymbol{\alpha}_t, \mathbf{g}_t, \boldsymbol{\rho}_t, \mathbf{z}_t, \mathbf{m}_t | \mathbf{y}_{t-1}, \mathbf{s}_{t-1}) \\ \times f(\mathbf{y}_{1:t-1}, \mathbf{s}_{1:t-1}, \boldsymbol{\alpha}_{1:t-1}, \mathbf{g}_{1:t-1}, \boldsymbol{\rho}_{1:t-1}, \mathbf{z}_{1:t-1}, \mathbf{m}_{1:t-1}) \quad (3.32)$$

$$= \prod_{t'=1}^t f(\mathbf{y}_{t'}, \mathbf{s}_{t'}, \boldsymbol{\alpha}_{t'}, \mathbf{g}_{t'}, \boldsymbol{\rho}_{t'}, \mathbf{z}_{t'}, \mathbf{m}_{t'} | \mathbf{y}_{t'-1}, \mathbf{s}_{t'-1}) \quad (3.33)$$

$$= \prod_{t'=1}^t f(\mathbf{y}_t, \boldsymbol{\alpha}_t, \mathbf{g}_t, \boldsymbol{\rho}_t, \mathbf{z}_t, \mathbf{m}_t | \mathbf{s}_t, \mathbf{y}_{t-1}, \mathbf{s}_{t-1}) f(\mathbf{s}_t | \mathbf{y}_{t-1}, \mathbf{s}_{t-1}) \quad (3.34)$$

$$= \prod_{t'=1}^t f(\bar{\mathbf{y}}_t, \boldsymbol{\alpha}_t, \mathbf{g}_t, \boldsymbol{\rho}_t, \mathbf{z}_t, \mathbf{m}_t | \underline{\mathbf{y}}_t, \mathbf{s}_t, \mathbf{y}_{t-1}) f(\mathbf{s}_t | \mathbf{s}_{t-1}) f(\underline{\mathbf{y}}_t | \mathbf{s}_t, \mathbf{y}_{t-1}) \quad (3.35)$$

$$= \prod_{t'=1}^t f(\bar{\mathbf{y}}_t, \boldsymbol{\alpha}_t, \mathbf{z}_t, \mathbf{m}_t | \underline{\mathbf{y}}_t, \mathbf{s}_t) f(\mathbf{s}_t | \mathbf{s}_{t-1}) f(\underline{\mathbf{y}}_t | \mathbf{y}_{t-1}) f(\mathbf{g}_t | \underline{\mathbf{y}}_t, \mathbf{s}_t) f(\boldsymbol{\rho}_t | \underline{\mathbf{y}}_t, \mathbf{s}_t) \quad (3.36)$$

$$= \prod_{t'=1}^t f(\mathbf{z}_t | \bar{\mathbf{y}}_t, \boldsymbol{\alpha}_t, \mathbf{m}_t, \underline{\mathbf{y}}_t, \mathbf{s}_t) f(\bar{\mathbf{y}}_t, \boldsymbol{\alpha}_t, \mathbf{m}_t | \underline{\mathbf{y}}_t, \mathbf{s}_t) f(\mathbf{s}_t | \mathbf{s}_{t-1}) f(\underline{\mathbf{y}}_t | \mathbf{y}_{t-1}) f(\mathbf{g}_t | \mathbf{s}_t) f(\boldsymbol{\rho}_t | \mathbf{s}_t), \quad (3.37)$$

where it has been used Bayes' rule in (3.31), assumption (A13) in (3.32), Bayes' rule in (3.34), Bayes's rule and assumptions (A14) and (A15) in (3.35), Bayes's rule and assumptions (A17) (A18) in (3.36), and Bayes' rule and A19) in (3.37).

The factorization of (3.37) is:

$$\begin{aligned}
 & f(\mathbf{y}_{1:t}, \mathbf{s}_{1:t}, \boldsymbol{\alpha}_{1:t} | \mathbf{g}_{1:t}, \boldsymbol{\rho}_{1:t}, \mathbf{z}_{1:t}) \propto \\
 & \prod_{t'=1}^t \underbrace{\left( \prod_{a \in \mathcal{A}} \tau(\mathbf{s}_{t'}^{(a)} | \mathbf{s}_{t'-1}^{(a)}) \right)}_{\text{AGENT STATES PREDICTION}} \underbrace{\left( \prod_{a \in \mathcal{A}_{t'}^g} \mathfrak{g}(\mathbf{g}_{t'}^{(a)} | \mathbf{s}_{t'}^{(a)}) \right) \left( \prod_{a \in \mathcal{R}} \prod_{a' \in \mathcal{T}_{t'}^{(a)}} \delta(\boldsymbol{\rho}_{t'}^{(j)} | \mathbf{s}_{t'}^{(a)}, \mathbf{s}_{t'}^{(a')}) \right)}_{\text{COOPERATIVE SELF-LOCALIZATION}} \\
 & \times \underbrace{\left( \prod_{\ell \in \mathcal{L}_{t'-1}} f(\mathbf{x}_{\ell, t'}, \mathbf{r}_{\ell, t'} | \mathbf{x}_{\ell, t'-1}, \mathbf{r}_{\ell, t'-1}) \right)}_{\text{PT STATES PREDICTION}} \\
 & \times \prod_{j=1}^{|\mathcal{J}|} \left\{ \left[ \prod_{\ell \in \mathcal{L}_{t'}^{(j)}} \left( q(\mathbf{x}_{\ell, t'}^{(j)}, \mathbf{r}_{\ell, t'}^{(j)}, \ddot{\mathbf{s}}_{t'}^{(j)}, \boldsymbol{\alpha}_{\ell, t'}^{(j)}; \mathbf{z}_{t'}^{(j)}) \prod_{m \in \mathcal{M}_{t'}^{(j)}} \psi(\boldsymbol{\alpha}_{\ell, t'}^{(j)}, \boldsymbol{\beta}_{m, t'}^{(j)}) \right) \right] \right. \\
 & \times \left[ \prod_{a \in \mathcal{A}} \left( h(\mathbf{s}_{t'}^{(a)}, \ddot{\mathbf{s}}_{t'}^{(j)}, \boldsymbol{\alpha}_{|\mathcal{L}_{t'}^{(j)}|+a, t'}^{(j)}; \mathbf{z}_{t'}^{(j)}) \prod_{m \in \mathcal{M}_{t'}^{(j)}} \psi(\boldsymbol{\alpha}_{|\mathcal{L}_{t'}^{(j)}|+a, t'}^{(j)}, \boldsymbol{\beta}_{m, t'}^{(j)}) \right) \right] \\
 & \times \left. \left[ \prod_{m \in \mathcal{M}_{t'}^{(j)}} v(\bar{\mathbf{x}}_{m, t'}^{(j)}, \bar{\mathbf{r}}_{m, t'}^{(j)}, \ddot{\mathbf{s}}_{t'}^{(j)}, \boldsymbol{\beta}_{m, t'}^{(j)}; \mathbf{z}_{m, t'}^{(j)}) \right] \right\}, \tag{3.38}
 \end{aligned}$$

which has been obtained by using (3.2), (3.5), (3.7), (3.9), (3.16) and (3.21) into (3.37), where the function  $v(\bar{\mathbf{x}}_{m, t}^{(j)}, \bar{\mathbf{r}}_{m, t}^{(j)} = 1, \ddot{\mathbf{s}}_t^{(j)}, \boldsymbol{\beta}_{m, t}^{(j)}; \mathbf{z}_{m, t}^{(j)})$  replaces the product  $v_1(\bar{\mathbf{x}}_{m, t}^{(j)}, \bar{\mathbf{r}}_{m, t}^{(j)} = 1, \boldsymbol{\beta}_{m, t}^{(j)}) v_2(\bar{\mathbf{x}}_{m, t}^{(j)}, \bar{\mathbf{r}}_{m, t}^{(j)}, \ddot{\mathbf{s}}_t^{(j)}; \mathbf{z}_{m, t}^{(j)})$  which can be rewritten as [38]:

$$v(\bar{\mathbf{x}}_{m, t}^{(j)}, \bar{\mathbf{r}}_{m, t}^{(j)} = 1, \ddot{\mathbf{s}}_t^{(j)}, \boldsymbol{\beta}_{m, t}^{(j)}; \mathbf{z}_{m, t}^{(j)}) = \begin{cases} 0, & \boldsymbol{\beta}_{m, t}^{(j)} \in \mathcal{O}_t^{(j)}, \\ \frac{\mu_n^{(j)}}{\mu_c^{(j)}} f_n(\bar{\mathbf{x}}_{m, t}^{(j)}) \frac{f(\mathbf{z}_{m, t}^{(j)} | \bar{\mathbf{x}}_{m, t}^{(j)}, \ddot{\mathbf{s}}_t^{(j)})}{f_c^{(j)}(\mathbf{z}_{m, t}^{(j)})}, & \boldsymbol{\beta}_{m, t}^{(j)} = 0, \end{cases} \tag{3.39}$$

$$v(\bar{\mathbf{x}}_{m, t}^{(j)}, \bar{\mathbf{r}}_{m, t}^{(j)} = 0, \ddot{\mathbf{s}}_t^{(j)}, \boldsymbol{\beta}_{m, t}^{(j)}; \mathbf{z}_{m, t}^{(j)}) = f_D(\bar{\mathbf{x}}_{m, t}^{(j)}). \tag{3.40}$$

The computation of the marginal posterior pdfs  $f(\mathbf{y}_{\ell, t}^{(J)} | \mathbf{z}_{1:t}) = f(\mathbf{x}_{\ell, t}^{(J)}, \mathbf{r}_{\ell, t}^{(J)} | \mathbf{z}_{1:t})$  of legacy PTs,  $f(\bar{\mathbf{y}}_{m, t}^{(J)} | \mathbf{z}_{1:t}) = f(\bar{\mathbf{x}}_{m, t}^{(J)}, \bar{\mathbf{r}}_{m, t}^{(J)} | \mathbf{z}_{1:t})$  of new PTs and  $f(\mathbf{s}_{a, t} | \mathbf{z}_{1:t})$  of agents is obtained by running iterative SPA message passing [41, 92] on the factor graph representing the factorization in (3.38). Details on the message passing algorithm are provided in next section.

### 3.4.3 BP-based algorithm for joint CSL and MTT

We now apply the SPA algorithm to the problem of calculating the marginal posterior pdfs  $f(\mathbf{y}_{\ell, t}^{(J)} | \mathbf{z}_{1:t}) = f(\mathbf{x}_{\ell, t}^{(J)}, \mathbf{r}_{\ell, t}^{(J)} | \mathbf{z}_{1:t})$  for the legacy PTs,  $f(\bar{\mathbf{y}}_{m, t}^{(J)} | \mathbf{z}_{1:t}) = f(\bar{\mathbf{x}}_{m, t}^{(J)}, \bar{\mathbf{r}}_{m, t}^{(J)} | \mathbf{z}_{1:t})$  for the new PTs and  $f(\mathbf{s}_{a, t} | \mathbf{z}_{1:t})$  for the agents. Since the factor graph contains loops, we have to choose an order of calculating the individual

messages. In our algorithm, the order is defined by two rules: first, messages are not sent backward in time, and second, iterative message passing is only performed for data association, and at each time step sequentially from the first agent pair  $j = 1$  until the last agent pair  $J$ . Combining these rules with the generic SPA rules for calculating messages and beliefs we have the following operations to be carried out at each time step in the stated order:

1. agent states prediction,
2. agent CSL,
3. legacy PT states prediction,
4. measurement evaluation,
5. data association,
6. measurement update,
7. belief calculation.

In the following, we provide descriptions of these operations, including expressions of the various messages and beliefs.

### Agent states prediction

To predict the state of each agent, the messages  $\zeta_{\tau_a \rightarrow \mathbf{s}_a}(\mathbf{s}_{a,t})$  from the factor nodes “ $\tau_a \triangleq \tau(\mathbf{s}_{a,t} | \mathbf{s}_{a,t-1})$ ” to the variable nodes “ $\mathbf{s}_a \triangleq \mathbf{s}_{a,t}$ ” have to be calculated as:

$$\zeta_{\tau_a \rightarrow \mathbf{s}_a}(\mathbf{s}_{a,t}) = \int \tau(\mathbf{s}_{a,t} | \mathbf{s}_{a,t-1}) \tilde{f}(\mathbf{s}_{a,t-1}) d\mathbf{s}_{a,t-1}. \quad (3.41)$$

### Agents cooperative self-localization

In this phase, agents use navigation and direct measurements to perform CSL. Note that in this step, targets are not involved, nor DA issues are present as the type of measurement is exact (i.e., it is well known which are the agents affected by each measurement). The CSL-specific FG is shown in Fig. 3.8, where the incoming steps are performed for  $N_{\text{SL}}$  iterations. At each iteration  $n = 1, \dots, N_{\text{SL}}$ , the messages  $\eta_{\mathbf{s}_a \rightarrow \delta^{(a,a')}}(\mathbf{s}_{a,t})$  and  $\eta_{\mathbf{s}_a \rightarrow \delta^{(a',a)}}(\mathbf{s}_{a,t})$ , from the variable nodes “ $\mathbf{s}_a$ ” to the factor nodes “ $\delta^{(a,a')} \triangleq \delta(\rho_t^{(a,a')} | \mathbf{s}_{a,t}, \mathbf{s}_{a',t})$ ” and “ $\delta^{(a',a)} \triangleq \delta(\rho_t^{(a',a)} | \mathbf{s}_{a',t}, \mathbf{s}_{a,t})$ ”, respectively, are calculated as:

$$\eta_{\mathbf{s}_a \rightarrow \delta^{(a,a')}}^{(n)}(\mathbf{s}_{a,t}) = \zeta_{\tau_a \rightarrow \mathbf{s}_a}(\mathbf{s}_{a,t}) \zeta_{\mathbf{g}_a \rightarrow \mathbf{s}_a}(\mathbf{s}_{a,t}) \prod_{a'' \in \mathcal{T}_t^{(a)} - \{a'\}} \zeta_{\delta^{(a,a'')} \rightarrow \mathbf{s}_a}^{(n-1)}(\mathbf{s}_{a,t}) \prod_{a'' \in \mathcal{R}_t^{(a)}} \zeta_{\delta^{(a'',a)} \rightarrow \mathbf{s}_a}^{(n-1)}(\mathbf{s}_{a,t}), \quad (3.42)$$

$$\eta_{\mathbf{s}_a \rightarrow \delta^{(a',a)}}^{(n)}(\mathbf{s}_{a,t}) = \zeta_{\tau_a \rightarrow \mathbf{s}_a}(\mathbf{s}_{a,t}) \zeta_{\mathbf{g}_a \rightarrow \mathbf{s}_a}(\mathbf{s}_{a,t}) \prod_{a'' \in \mathcal{T}_t^{(a)}} \zeta_{\delta^{(a,a'')} \rightarrow \mathbf{s}_a}^{(n-1)}(\mathbf{s}_{a,t}) \prod_{a'' \in \mathcal{R}_t^{(a)} - \{a'\}} \zeta_{\delta^{(a'',a)} \rightarrow \mathbf{s}_a}^{(n-1)}(\mathbf{s}_{a,t}), \quad (3.43)$$

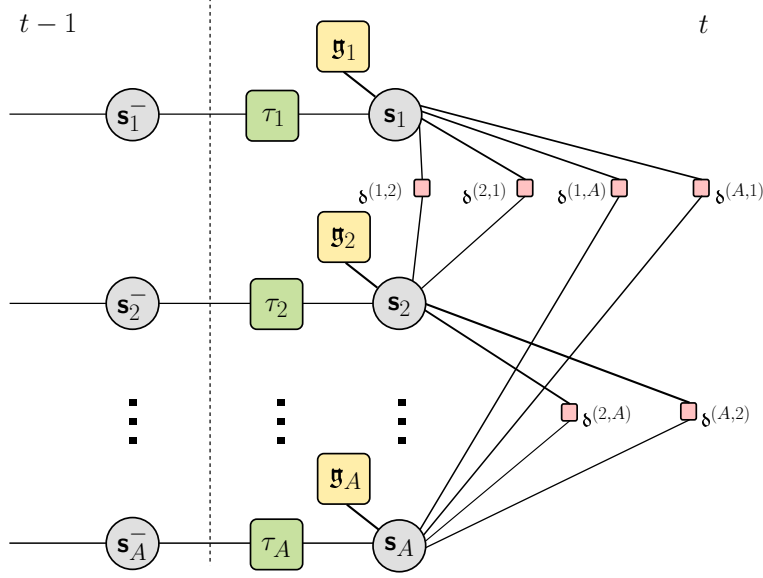


**Figure 3.8:** Factor graph corresponding to the agent self-localization step at the beginning of each time step  $t$ . In the graph, all agents are assumed to have both navigation and direct measurements. Shortcuts  $\mathbf{s}_a^- \triangleq \mathbf{s}_{a,t-1}$  and  $\mathbf{g}_a \triangleq \mathbf{g}(\mathbf{g}_t^{(a)} | \mathbf{s}_{a,t})$  are used.

where the message  $\zeta_{\mathbf{g}_a \rightarrow \mathbf{s}_a}(\mathbf{s}_{a,t})$ , that is passed from factor node “ $\mathbf{g}_a$ ” to variable node “ $\mathbf{s}_a$ ”, is computed as:

$$\zeta_{\mathbf{g}_a \rightarrow \mathbf{s}_a}(\mathbf{s}_{a,t}) = \begin{cases} \mathbf{g}(\mathbf{g}_{a,t} | \mathbf{s}_{a,t}), & \text{if } a \in \mathcal{A}_t^g, \\ 1, & \text{if } a \notin \mathcal{A}_t^g. \end{cases} \quad (3.44)$$

Then, the messages  $\zeta_{\delta^{(a,a')} \rightarrow \mathbf{s}_a}^{(n)}(\mathbf{s}_{a,t})$  and  $\zeta_{\delta^{(a',a)} \rightarrow \mathbf{s}_a}^{(n)}(\mathbf{s}_{a,t})$  from the factor nodes “ $\delta^{(a,a')}$ ” and “ $\delta^{(a',a)}$ ” to the variable nodes “ $\mathbf{s}_a$ ” are calculated as:

$$\zeta_{\delta^{(a,a')} \rightarrow \mathbf{s}_a}^{(n)}(\mathbf{s}_{a,t}) = \int \delta(\boldsymbol{\rho}_t^{(j)} | \mathbf{s}_{a,t}, \mathbf{s}_{a',t}) \eta_{\mathbf{s}_{a'} \rightarrow \boldsymbol{\rho}^{(a,a')}}^{(n)}(\mathbf{s}_{a',t}) d\mathbf{s}_{a',t}, \quad (3.45)$$

$$\zeta_{\delta^{(a',a)} \rightarrow \mathbf{s}_a}^{(n)}(\mathbf{s}_{a,t}) = \int \delta(\boldsymbol{\rho}_t^{(a',a)} | \mathbf{s}_{a,t}, \mathbf{s}_{a',t}) \eta_{\mathbf{s}_{a'} \rightarrow \boldsymbol{\rho}^{(a',a)}}^{(n)}(\mathbf{s}_{a',t}) d\mathbf{s}_{a',t}. \quad (3.46)$$

The initial belief of each agent state after self-localization is calculated as:

$$\tilde{f}_0(\mathbf{s}_{a,t}) \propto \zeta_{\tau_a \rightarrow \mathbf{s}_a}(\mathbf{s}_{a,t}) \zeta_{\mathbf{g}_a \rightarrow \mathbf{s}_a}(\mathbf{s}_{a,t}) \prod_{a' \in \mathcal{R}_t^{(a)}} \zeta_{\delta^{(a',a)} \rightarrow \mathbf{s}_a}^{(N_{\text{SL}})}(\mathbf{s}_{a,t}) \prod_{a' \in \mathcal{T}_t^{(a)}} \zeta_{\delta^{(a,a')} \rightarrow \mathbf{s}_a}^{(N_{\text{SL}})}(\mathbf{s}_{a,t}). \quad (3.47)$$

At this time, CSL lead to an estimate of the multi-agent network. The next phases introduce targets in the localization processes, which have to be detected and localized but also used upside-down to possibly refine the beliefs at the end of CSL. The following steps are then performed for each receiver-transmitter couple  $j \in \mathcal{J}$ . The relative FG for the MTT part is provided in Fig. 3.9 for a generic agent pair  $j$  at a given time  $t$ .

### Legacy PT states prediction

To predict the states of legacy PTs (i.e., the targets that were hypothesized to exist

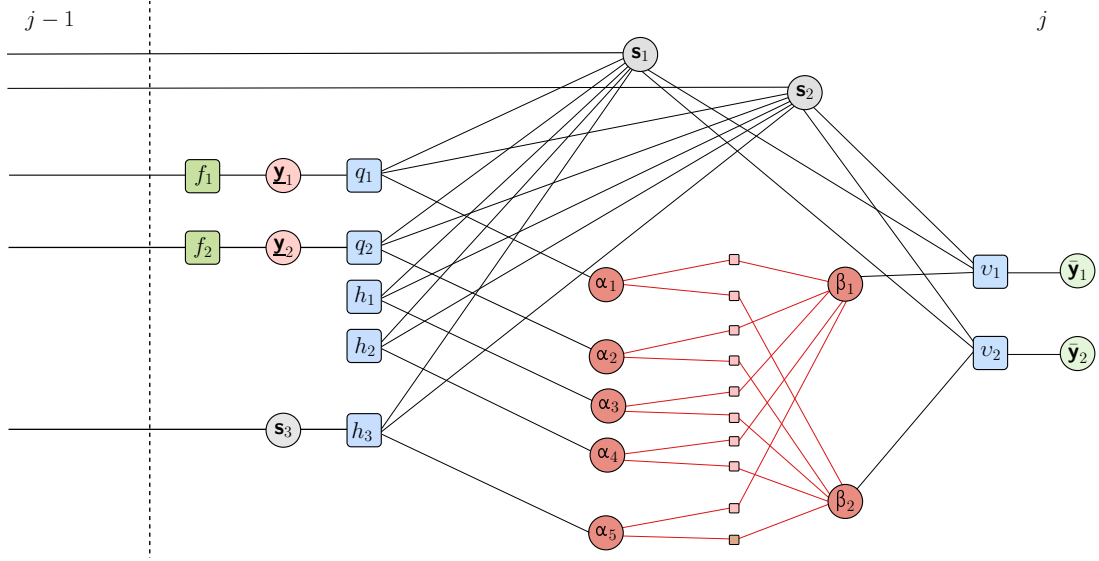


**Figure 3.9:** Factor graph for MTT at time step  $t$  and agent pair  $j$ , with  $j_1 = 1$  and  $j_2 = 2$ .

at the previous time instant) the messages  $\zeta_{f_\ell \rightarrow \mathbf{y}_\ell}(\mathbf{y}_{\ell,t}^{(j)})$  passed from the factor nodes “ $f_\ell \triangleq f(\mathbf{x}_{\ell,t}^{(j)}, \mathbf{r}_{\ell,t}^{(j)} | \mathbf{x}_{\ell,t}^{(j-1)}, \mathbf{r}_{\ell,t}^{(j-1)})$ ” to the variable nodes “ $\mathbf{y}_\ell \triangleq \mathbf{y}_{\ell,t}^{(j)}$ ” are calculated for each PT  $\ell \in \mathcal{L}_t^{(j)}$  as:

$$\zeta_{f_\ell \rightarrow \mathbf{y}_\ell}(\mathbf{y}_{\ell,t}^{(j)}) = \sum_{\mathbf{r}_{\ell,t}^{(j-1)} \in \{0,1\}} \int f(\mathbf{x}_{\ell,t}^{(j)}, \mathbf{r}_{\ell,t}^{(j)} | \mathbf{x}_{\ell,t}^{(j-1)}, \mathbf{r}_{\ell,t}^{(j-1)})^{\delta_{j,1}} \delta(\mathbf{y}_{\ell,t}^{(j-1)} - \mathbf{y}_{\ell,t}^{(j)})^{1-\delta_{j,1}} \tilde{f}(\mathbf{x}_{\ell,t}^{(j-1)}, \mathbf{r}_{\ell,t}^{(j-1)}) d\mathbf{x}_{\ell,t}^{(j-1)}, \quad (3.48)$$

where  $\delta_{j,1}$  is the Kronecker delta that is equal to 1 when  $j = 1$  and 0 when  $j \neq 1$ , and  $\delta(\mathbf{y}_{\ell,t}^{(j-1)} - \mathbf{y}_{\ell,t}^{(j)})$  is the Dirac Delta function, which is equal to 0 when  $\mathbf{y}_{\ell,t}^{(j-1)} \neq \mathbf{y}_{\ell,t}^{(j)}$  and equal to  $+\infty$  when  $\mathbf{y}_{\ell,t}^{(j-1)} = \mathbf{y}_{\ell,t}^{(j)}$ . For  $j = 1$ , we have that  $\mathbf{y}_{\ell,t}^{(j-1)} = \mathbf{y}_{\ell,t-1}$ , therefore:

$$\zeta_{f_\ell \rightarrow \mathbf{y}_\ell}(\mathbf{y}_{\ell,t}^{(j)}) = \sum_{\mathbf{r}_{\ell,t-1} \in \{0,1\}} \int f(\mathbf{x}_{\ell,t}^{(j)}, \mathbf{r}_{\ell,t}^{(j)} | \mathbf{x}_{\ell,t-1}, \mathbf{r}_{\ell,t-1}). \quad (3.49)$$

For  $j > 1$ , we have instead that

$$\begin{aligned} \zeta_{f_\ell \rightarrow \mathbf{y}_\ell}(\mathbf{y}_{\ell,t}^{(j)}) &= \sum_{\mathbf{r}_{\ell,t}^{(j-1)} \in \{0,1\}} \int \delta(\mathbf{y}_{\ell,t}^{(j-1)} - \mathbf{y}_{\ell,t}^{(j)}) \tilde{f}(\mathbf{x}_{\ell,t}^{(j-1)}, \mathbf{r}_{\ell,t}^{(j-1)}) d\mathbf{x}_{\ell,t}^{(j-1)} \\ &= \tilde{f}(\mathbf{y}_{\ell,t}^{(j)}), \end{aligned} \quad (3.50)$$

where the last step follows from the Dirac delta function  $\delta(\mathbf{x})$  general property, i.e.,  $\int \delta(\mathbf{x} - \mathbf{x}_0) f(\mathbf{x}) d\mathbf{x} = f(\mathbf{x}_0)$  for all  $\mathbf{x}_0$ .

### Measurement evaluation

Once the messages  $\zeta_{f_\ell \rightarrow \mathbf{y}_\ell}(\mathbf{y}_{\ell,t}^{(j)})$  have been evaluated, a “measurement evaluation” step is performed for the legacy PTs, the new PTs and the agents. For

the legacy PTs, the messages  $\zeta_{q_\ell \rightarrow \alpha_\ell}(\alpha_{\ell,t}^{(j)})$ , passed from the factor nodes “ $q_\ell \triangleq q(\mathbf{x}_{\ell,t}^{(j)}, \mathbf{r}_{\ell,t}^{(j)}, \alpha_{\ell,t}^{(j)}, \ddot{\mathbf{s}}_t^{(j)}; \mathbf{z}_t^{(j)})$ ” to the variable nodes  $\alpha_\ell \triangleq \alpha_{\ell,t}^{(j)}$  are calculated as:

$$\begin{aligned} \zeta_{q_\ell \rightarrow \alpha_\ell}(\alpha_{\ell,t}^{(j)}) = & \sum_{\mathbf{r}_{\ell,t}^{(j)} \in \{0,1\}} \iiint q(\mathbf{x}_{\ell,t}^{(j)}, \mathbf{r}_{\ell,t}^{(j)}, \alpha_{\ell,t}^{(j)}, \ddot{\mathbf{s}}_t^{(j)}; \mathbf{z}_t^{(j)}) \tilde{f}^{(j-1)}(\mathbf{s}_{j_1,t})^{1-\delta_{j_1,j_2}} \tilde{f}^{(j-1)}(\mathbf{s}_{j_2,t}) \\ & \times \delta(\mathbf{s}_{j_1,t} - \mathbf{s}_{j_2,t})^{\delta_{j_1,j_2}} \zeta_{f_\ell \rightarrow \mathbf{y}_\ell}(\mathbf{x}_{\ell,t}^{(j)}, \mathbf{r}_{\ell,t}^{(j)}) d\mathbf{x}_{\ell,t}^{(j)} d\mathbf{s}_{j_1,t} d\mathbf{s}_{j_2,t}. \end{aligned} \quad (3.51)$$

In the particular case of  $j_1 \neq j_2$ , we have that  $\delta_{j_1,j_2} = 0$  and  $\delta(\mathbf{s}_{j_1,t} - \mathbf{s}_{j_2,t}) = 0$ . Therefore:

$$\begin{aligned} \zeta_{q_\ell \rightarrow \alpha_\ell}(\alpha_{\ell,t}^{(j)}) = & \sum_{\mathbf{r}_{\ell,t}^{(j)} \in \{0,1\}} \iiint q(\mathbf{x}_{\ell,t}^{(j)}, \mathbf{r}_{\ell,t}^{(j)}, \alpha_{\ell,t}^{(j)}, \ddot{\mathbf{s}}_t^{(j)}; \mathbf{z}_t^{(j)}) \tilde{f}^{(j-1)}(\mathbf{s}_{j_1,t}) \tilde{f}^{(j-1)}(\mathbf{s}_{j_2,t}) \\ & \times \zeta_{f_\ell \rightarrow \mathbf{y}_\ell}(\mathbf{x}_{\ell,t}^{(j)}, \mathbf{r}_{\ell,t}^{(j)}) d\mathbf{x}_{\ell,t}^{(j)} d\mathbf{s}_{j_1,t} d\mathbf{s}_{j_2,t}. \end{aligned} \quad (3.52)$$

On the contrary, when the receiver and transmitter of the  $j$ -th couple coincide, i.e.,  $j_1 = j_2$ , we have that  $\delta_{j_1,j_2} = 1$  and  $\delta(\mathbf{s}_{j_1,t} - \mathbf{s}_{j_2,t}) = 1$ . Therefore:

$$\begin{aligned} \zeta_{q_\ell \rightarrow \alpha_\ell}(\alpha_{\ell,t}^{(j)}) & = \sum_{\mathbf{r}_{\ell,t}^{(j)} \in \{0,1\}} \iiint q(\mathbf{x}_{\ell,t}^{(j)}, \mathbf{r}_{\ell,t}^{(j)}, \alpha_{\ell,t}^{(j)}, \ddot{\mathbf{s}}_t^{(j)}; \mathbf{z}_t^{(j)}) \tilde{f}^{(j-1)}(\mathbf{s}_{j_2,t}) \\ & \times \delta(\mathbf{s}_{j_1,t} - \mathbf{s}_{j_2,t}) \zeta_{f_\ell \rightarrow \mathbf{y}_\ell}(\mathbf{x}_{\ell,t}^{(j)}, \mathbf{r}_{\ell,t}^{(j)}) d\mathbf{x}_{\ell,t}^{(j)} d\mathbf{s}_{j_1,t} d\mathbf{s}_{j_2,t} \\ & = \sum_{\mathbf{r}_{\ell,t}^{(j)} \in \{0,1\}} \iint q(\mathbf{x}_{\ell,t}^{(j)}, \mathbf{r}_{\ell,t}^{(j)}, \alpha_{\ell,t}^{(j)}, \ddot{\mathbf{s}}_t^{(j)}; \mathbf{z}_t^{(j)}) \tilde{f}^{(j-1)}(\mathbf{s}_{j_1,t}) \zeta_{f_\ell \rightarrow \mathbf{y}_\ell}(\mathbf{x}_{\ell,t}^{(j)}, \mathbf{r}_{\ell,t}^{(j)}) d\mathbf{x}_{\ell,t}^{(j)} d\mathbf{s}_{j_1,t}. \end{aligned} \quad (3.53)$$

For the new PTs, the messages  $\zeta_{v_m \rightarrow \beta_m}(\beta_{m,t}^{(j)})$  passed from the factor nodes “ $v_m \triangleq v(\bar{\mathbf{x}}_{m,t}^{(j)}, \bar{\mathbf{r}}_{m,t}^{(j)}, \beta_{m,t}^{(j)}, \ddot{\mathbf{s}}_t^{(j)}; \mathbf{z}_t^{(j)})$ ” to the variable nodes “ $\beta_m \triangleq \beta_{m,t}^{(j)}$ ” for the  $a \neq j_1$  and  $a \neq j_2$  are calculated as:

$$\begin{aligned} \zeta_{v_m \rightarrow \beta_m}(\beta_{m,t}^{(j)}) = & \sum_{\bar{\mathbf{r}}_{m,t}^{(j)} \in \{0,1\}} \iiint v(\bar{\mathbf{x}}_{m,t}^{(j)}, \bar{\mathbf{r}}_{m,t}^{(j)}, \beta_{m,t}^{(j)}, \ddot{\mathbf{s}}_t^{(j)}; \mathbf{z}_t^{(j)}) \\ & \times \tilde{f}^{(j-1)}(\mathbf{s}_{j_1,t})^{1-\delta_{j_1,j_2}} \tilde{f}^{(j-1)}(\mathbf{s}_{j_2,t}) \delta(\mathbf{s}_{j_1,t} - \mathbf{s}_{j_2,t})^{\delta_{j_1,j_2}} d\bar{\mathbf{x}}_{m,t}^{(j)} d\mathbf{s}_{j_1,t} d\mathbf{s}_{j_2,t}. \end{aligned} \quad (3.54)$$

For the agents, the messages  $\zeta_{h_a \rightarrow \alpha_{|\mathcal{L}_t^{(j)}|+a}}(\alpha_{|\mathcal{L}_t^{(j)}|+a,t}^{(j)})$  passed from the factor nodes “ $h_a \triangleq h(\mathbf{s}_a, \alpha_{|\mathcal{L}_t^{(j)}|+a,t}^{(j)}, \ddot{\mathbf{s}}_t^{(j)}; \mathbf{z}_t^{(j)})$ ” to the variable nodes “ $\alpha_{|\mathcal{L}_t^{(j)}|+a} \triangleq \alpha_{|\mathcal{L}_t^{(j)}|+a,t}^{(j)}$ ”

are calculated as:

$$\begin{aligned} \zeta_{h_a \rightarrow \alpha_{|\mathcal{L}_t^{(j)}|+a}}(\alpha_{|\mathcal{L}_t^{(j)}|+a}^{(j)}) = \\ \iiint h(\mathbf{s}_{a,t}, \alpha_{|\mathcal{L}_t^{(j)}|+a}^{(j)}, \ddot{\mathbf{s}}_t^{(j)}; \mathbf{z}_t^{(j)}) \tilde{f}^{(j-1)}(\mathbf{s}_{j_1,t}) \tilde{f}^{(j-1)}(\mathbf{s}_{j_2,t})^{1-\delta_{j_1,j_2}} \\ \times \delta(\mathbf{s}_{j_1,t} - \mathbf{s}_{j_2,t})^{\delta_{j_1,j_2}} \tilde{f}^{(j-1)}(\mathbf{s}_{a,t}) d\mathbf{s}_{a,t} d\mathbf{s}_{j_1,t} d\mathbf{s}_{j_2,t}. \end{aligned} \quad (3.55)$$

### Data association

At this time, the a statistical characterization of MOT measurements is required to calculate the association beliefs. DA is an iterative procedure where the messages  $\zeta_{q_\ell \rightarrow \alpha_\ell}(\alpha_{\ell,t}^{(j)})$ ,  $\zeta_{h_a \rightarrow \alpha_{|\mathcal{L}_t^{(j)}|+a}}(\alpha_{|\mathcal{L}_t^{(j)}|+a}^{(j)})$  and  $\zeta_{v_m \rightarrow \beta_m}(\beta_{m,t}^{(j)})$  are converted into the messages  $\eta_{\alpha_\ell \rightarrow q_\ell}(\alpha_{\ell,t}^{(j)})$ ,  $\eta_{\alpha_{|\mathcal{L}_t^{(j)}|+a} \rightarrow h_a}(\alpha_{|\mathcal{L}_t^{(j)}|+a}^{(j)})$  and  $\eta_{\beta_m \rightarrow v_m}(\beta_{m,t}^{(j)})$ , respectively. This step involves the calculation of iterated messages and is equal to the corresponding step in [62]. For this reason, we remind that work for details. Alternatively, a detailed description of DA and related messages is provided in Chapter 4, in which a Maximum-A-Posteriori (MAP) implementation is also discussed so as to reduce DA complexity by selectively associate a measurement to the originating target. In the last case, performance degradation has to be evaluated for the specific application scenario.

### Measurement update

A “measurement update” step is now performed for both the legacy PTs and the new PTs. For the legacy PTs, the messages  $\zeta_{q_\ell \rightarrow \mathbf{y}_\ell}(\mathbf{x}_{\ell,t}^{(j)}, \mathbf{r}_{\ell,t}^{(j)})$  from the factor nodes “ $q_\ell$ ” to the variable nodes “ $\mathbf{y}_\ell$ ” are calculated as:

$$\begin{aligned} \zeta_{q_\ell \rightarrow \mathbf{y}_\ell}(\mathbf{x}_{\ell,t}^{(j)}, \mathbf{r}_{\ell,t}^{(j)}) = \\ \sum_{\alpha_{\ell,t}^{(j)=0} \mathbf{M}_t^{(j)}} \eta_{\alpha_\ell \rightarrow q_\ell}(\alpha_{\ell,t}^{(j)}) \iint q(\mathbf{x}_{\ell,t}^{(j)}, \mathbf{r}_{\ell,t}^{(j)}, \alpha_{\ell,t}^{(j)}, \ddot{\mathbf{s}}_t^{(j)}; \mathbf{z}_t^{(j)}) \\ \times \tilde{f}^{(j-1)}(\mathbf{s}_{j_1,t})^{1-\delta_{j_1,j_2}} \tilde{f}^{(j-1)}(\mathbf{s}_{j_2,t}) \delta(\mathbf{s}_{j_1,t} - \mathbf{s}_{j_2,t})^{\delta_{j_1,j_2}} d\mathbf{s}_{j_1,t} d\mathbf{s}_{j_2,t}. \end{aligned} \quad (3.56)$$

For the new PTs, the messages  $\zeta_{v_m \rightarrow \bar{\mathbf{y}}_m}(\bar{\mathbf{x}}_{m,t}^{(j)}, \bar{\mathbf{r}}_{m,t}^{(j)})$  passed the factor nodes “ $v_m$ ” to the variable nodes “ $\bar{\mathbf{y}}_m$ ” are calculated as:

$$\begin{aligned} \zeta_{v_m \rightarrow \bar{\mathbf{y}}_m}(\bar{\mathbf{x}}_{m,t}^{(j)}, \bar{\mathbf{r}}_{m,t}^{(j)}) = \\ \sum_{\beta_{m,t}^{(j)=0} |\mathcal{L}_t^{(j)}|} \eta_{\beta_m \rightarrow v_m}(\beta_{m,t}^{(j)}) \iint v(\bar{\mathbf{x}}_{m,t}^{(j)}, \bar{\mathbf{r}}_{m,t}^{(j)}, \beta_{m,t}^{(j)}, \ddot{\mathbf{s}}_t^{(j)}; \mathbf{z}_{m,t}^{(j)}) \\ \times \tilde{f}^{(j-1)}(\mathbf{s}_{j_1,t})^{1-\delta_{j_1,j_2}} \tilde{f}^{(j-1)}(\mathbf{s}_{j_2,t}) \delta(\mathbf{s}_{j_1,t} - \mathbf{s}_{j_2,t})^{\delta_{j_1,j_2}} d\mathbf{s}_{j_1,t} d\mathbf{s}_{j_2,t}. \end{aligned} \quad (3.57)$$

For the agents, the messages  $\zeta_{h_a \rightarrow \mathbf{s}_a}(\mathbf{s}_{a,t})$  passed from the factor nodes “ $h_a$ ” to the

variable nodes “ $\mathbf{s}_a$ ” for  $a \neq j_1$  and  $a \neq j_2$  are calculated as:

$$\begin{aligned} \zeta_{h_a \rightarrow \mathbf{s}_a}(\mathbf{s}_{a,t}) = & \\ & \sum_{\alpha_{\ell,t}^{(j)}=0}^{M_t^{(j)}} \eta_{\alpha_{\ell,t} \rightarrow q_{\ell}}(\alpha_{\ell,t}^{(j)}) \iint h(\mathbf{s}_{a,t}, \alpha_{|\mathcal{L}_t^{(j)}|+a,t}^{(j)}, \ddot{\mathbf{s}}_t^{(j)}; \mathbf{z}_t^{(j)}) \\ & \times \tilde{f}^{(j-1)}(\mathbf{s}_{j_1,t})^{1-\delta_{j_1,j_2}} \tilde{f}^{(j-1)}(\mathbf{s}_{j_2,t}) \delta(\mathbf{s}_{j_1,t} - \mathbf{s}_{j_2,t})^{\delta_{j_1,j_2}} d\mathbf{s}_{j_1,t} d\mathbf{s}_{j_2,t}. \end{aligned} \quad (3.58)$$

The next step consists of calculating the messages from the factor nodes “ $q_{\ell}$ ”, “ $v_m$ ” and “ $h_a$ ” to the variable nodes “ $\mathbf{s}_{j_i}$ ”, for  $i \in \{1, 2\}$ . In particular, the messages  $\zeta_{q_{\ell} \rightarrow \mathbf{s}_{j_i}}(\mathbf{s}_{j_i})$  from the factor nodes “ $q_{\ell}$ ” to the variable nodes  $\mathbf{s}_{j_i}$  are calculated for  $i = 1$  and  $i' = 2$  or  $i = 2$  and  $i' = 1$  as:

$$\begin{aligned} \zeta_{q_{\ell} \rightarrow \mathbf{s}_{j_i}}(\mathbf{s}_{j_i,t}) = & \\ & \sum_{\alpha_{\ell,t}^{(j)}=0}^{M_t^{(j)}} \sum_{\mathbf{r}_{\ell,t}^{(j)} \in \{0,1\}} \eta_{\alpha_{\ell,t} \rightarrow q_{\ell}}(\alpha_{\ell,t}^{(j)}) \iint q(\mathbf{x}_{\ell,t}^{(j)}, \mathbf{r}_{\ell,t}^{(j)}, \alpha_{\ell,t}^{(j)}, \ddot{\mathbf{s}}_t^{(j)}; \mathbf{z}_t^{(j)}) \\ & \times \tilde{f}^{(j-1)}(\mathbf{s}_{j_{i'},t})^{1-\delta_{j_i,j_{i'}}} \delta(\mathbf{s}_{j_i,t} - \mathbf{s}_{j_{i'},t})^{\delta_{j_i,j_{i'}}} \zeta_{f_{\ell} \rightarrow \mathbf{y}_{\ell}}(\mathbf{x}_{\ell,t}^{(j)}, \mathbf{r}_{\ell,t}^{(j)}) d\mathbf{x}_{\ell,t}^{(j)} d\mathbf{s}_{j_{i'},t}. \end{aligned} \quad (3.59)$$

Next, the messages  $\zeta_{h_a \rightarrow \mathbf{s}_{j_i}}(\mathbf{s}_{j_i,t})$  from the factor nodes “ $h_a$ ” to the variable nodes “ $\mathbf{s}_{j_i}$ ” are calculated as:

$$\begin{aligned} \zeta_{h_a,t \rightarrow \mathbf{s}_{j_i}}(\mathbf{s}_{j_i,t}) = & \\ & \sum_{\alpha_{|\mathcal{L}_t^{(j)}|+a}^{(j)}=0}^{M_t^{(j)}} \eta_{\alpha_{|\mathcal{L}_t^{(j)}|+a} \rightarrow h_a}(\alpha_{|\mathcal{L}_t^{(j)}|+a}^{(j)}) \iint h(\mathbf{s}_{a,t}, \alpha_{|\mathcal{L}_t^{(j)}|+a,t}^{(j)}, \ddot{\mathbf{s}}_t^{(j)}; \mathbf{z}_t^{(j)}) \\ & \times \tilde{f}^{(j-1)}(\mathbf{s}_{j_{i'},t})^{1-\delta_{j_i,j_{i'}}} \delta(\mathbf{s}_{j_i,t} - \mathbf{s}_{j_{i'},t})^{\delta_{j_i,j_{i'}}} \tilde{f}^{(j-1)}(\mathbf{s}_{a,t}) d\mathbf{s}_{a,t} d\mathbf{s}_{j_{i'},t}. \end{aligned} \quad (3.60)$$

Note that when  $a = j_1$  or  $a = j_2$  we have that:

$$\zeta_{h_a,t \rightarrow \mathbf{s}_{j_i}}(\mathbf{s}_{j_i,t}) = \eta_{\alpha_{|\mathcal{L}_t^{(j)}|+a} \rightarrow h_a}(\alpha_{|\mathcal{L}_t^{(j)}|+a} = 0). \quad (3.61)$$

as the function  $h(\cdot)$  is non-zero if and only if  $\alpha_{|\mathcal{L}_t^{(j)}|+a} = 0$ .

Finally, the messages  $\zeta_{v_m \rightarrow \mathbf{s}_{j_i}}(\mathbf{s}_{j_i,t})$  from the factor nodes “ $v_m$ ” to the variable nodes “ $\mathbf{s}_{j_i}$ ” are calculated as:

$$\begin{aligned} \zeta_{v_m \rightarrow \mathbf{s}_{j_i}}(\mathbf{s}_{j_i,t}) = & \\ & \sum_{\beta_{m,t}^{(j)}=0}^{|\mathcal{L}_t^{(j)}|} \sum_{\mathbf{r}_{m,t}^{(j)} \in \{0,1\}} \eta_{\beta_{m,t} \rightarrow v_m}(\beta_{m,t}^{(j)}) \iint v(\bar{\mathbf{x}}_{m,t}^{(j)}, \mathbf{r}_{m,t}^{(j)}, \beta_{m,t}^{(j)}, \ddot{\mathbf{s}}_t^{(j)}; \mathbf{z}_{m,t}^{(j)}) \\ & \times \tilde{f}^{(j-1)}(\mathbf{s}_{j_{i'},t})^{1-\delta_{j_i,j_{i'}}} \delta(\mathbf{s}_{j_i,t} - \mathbf{s}_{j_{i'},t})^{\delta_{j_i,j_{i'}}} d\bar{\mathbf{x}}_{m,t}^{(j)} d\mathbf{s}_{j_{i'},t}. \end{aligned} \quad (3.62)$$

### Belief calculation

Finally, for the legacy PTs, beliefs  $\tilde{f}(\mathbf{y}_{\ell,t}^{(j)}) = \tilde{f}(\mathbf{x}_{\ell,t}^{(j)}, \mathbf{r}_{\ell,t}^{(j)})$  approximating the marginal

posterior pdfs  $f(\underline{\mathbf{y}}_{\ell,t}^{(j)} | \mathbf{z}_{1:t}) = f(\underline{\mathbf{x}}_{\ell,t}^{(j)}, \underline{\mathbf{r}}_{\ell,t}^{(j)} | \mathbf{z}_{1:t})$  are calculated as:

$$\tilde{f}(\underline{\mathbf{x}}_{\ell,t}^{(j)}, \underline{\mathbf{r}}_{\ell,t}^{(j)}) = \frac{1}{\underline{C}_{\ell,t}^{(j)}} \zeta_{f_{\ell} \rightarrow \underline{\mathbf{y}}_{\ell}}(\underline{\mathbf{x}}_{\ell,t}^{(j)}, \underline{\mathbf{r}}_{\ell,t}^{(j)}) \zeta_{q_{\ell} \rightarrow \underline{\mathbf{y}}_{\ell}}(\underline{\mathbf{x}}_{\ell,t}^{(j)}, \underline{\mathbf{r}}_{\ell,t}^{(j)}), \quad (3.63)$$

where the normalization constant  $\underline{C}_{\ell,t}^{(j)}$  is defined as:

$$\underline{C}_{\ell,t}^{(j)} \triangleq \sum_{\substack{\underline{\mathbf{x}}_{\ell,t}^{(j)} \\ \underline{\mathbf{r}}_{\ell,t}^{(j)} \in \{0,1\}}} \int \zeta_{f_{\ell} \rightarrow \underline{\mathbf{y}}_{\ell}}(\underline{\mathbf{x}}_{\ell,t}^{(j)}, \underline{\mathbf{r}}_{\ell,t}^{(j)}) \zeta_{q_{\ell} \rightarrow \underline{\mathbf{y}}_{\ell}}(\underline{\mathbf{x}}_{\ell,t}^{(j)}, \underline{\mathbf{r}}_{\ell,t}^{(j)}) d\underline{\mathbf{x}}_{\ell,t}^{(j)}. \quad (3.64)$$

Similarly, for the new PTs, beliefs  $\tilde{f}(\underline{\mathbf{y}}_{m,t}^{(j)}) = \tilde{f}(\bar{\underline{\mathbf{x}}}_{m,t}^{(j)}, \bar{\underline{\mathbf{r}}}_{m,t}^{(j)})$  approximating the marginal posterior pdfs  $f(\underline{\mathbf{y}}_{m,t}^{(j)} | \mathbf{z}_{1:t}) = f(\bar{\underline{\mathbf{x}}}_{m,t}^{(j)}, \bar{\underline{\mathbf{r}}}_{m,t}^{(j)} | \mathbf{z}_{1:t})$  are calculated as:

$$\tilde{f}(\bar{\underline{\mathbf{x}}}_{m,t}^{(j)}, \bar{\underline{\mathbf{r}}}_{m,t}^{(j)}) = \frac{1}{\bar{C}_{m,t}^{(j)}} \zeta_{v_m \rightarrow \bar{\underline{\mathbf{y}}}_m}(\bar{\underline{\mathbf{x}}}_{m,t}^{(j)}, \bar{\underline{\mathbf{r}}}_{m,t}^{(j)}), \quad (3.65)$$

where  $\bar{C}_{m,t}^{(j)}$  is a normalization constant equal to  $\bar{C}_{m,t}^{(j)} \triangleq \int \zeta_{v_m \rightarrow \bar{\underline{\mathbf{y}}}_m}(\bar{\underline{\mathbf{x}}}_{m,t}^{(j)}, \bar{\underline{\mathbf{r}}}_{m,t}^{(j)}) d\bar{\underline{\mathbf{x}}}_{m,t}^{(j)}$ . Finally, the last step consists of updating the agent's beliefs, which are calculated as:

$$\begin{aligned} \tilde{f}^{(j)}(\mathbf{s}_{a,t}) = \\ \frac{1}{C_{a,t}^{(j)}} \tilde{f}^{(j-1)}(\mathbf{s}_{a,t}) \left[ \prod_m \zeta_{v_m \rightarrow \mathbf{s}_{j_i,t}}(\mathbf{s}_{j_i,t}) \prod_{a \in \mathcal{A}} \zeta_{h_a \rightarrow \mathbf{s}_{j_i}}(\mathbf{s}_{j_i}) \prod_{\ell} \zeta_{q_{\ell} \rightarrow \mathbf{s}_{j_i}}(\mathbf{s}_{j_i,t}) \right]^{\delta_{j_i,a}} \zeta_{h_a \rightarrow \mathbf{s}_a}(\mathbf{s}_{a,t})^{1-\delta_{j_i,a}}, \end{aligned} \quad (3.66)$$

where  $C_{a,t}^{(j)}$  is a normalization constant to the consistency of belief.

### 3.4.3.1 Implementation aspects

The statistical problem formulation deeply detailed in this section is implemented following a particle-based approach, where each pdf is described by a set of  $N_p$  particles. This choice is particularly appropriate for non-Gaussian settings and pdf, which intrinsically appear in data association problems [43, 82, 83, 87]. The use of particles, on the other hand, impacts on the complexity of the algorithm, which cubically scales with  $N_p$ . This drawback is unavoidable due to the introduction of both agents and targets' uncertainties, differentiating this approach with respect to previous works which assumed perfect knowledge of agents' positions [62, 82, 83].

Practically speaking, considering the CSL of agents (i.e., excluding the MTT issue) the complexity linearly scales with the iterations  $N_{SL}$  and quadratically with the number of connected agents (in case of full connectivity and direct measurement availability), To be more rigorous, it scales quadratically with the number of neighboring agents with direct measurements. The MTT part, instead, impacts on the overall complexity as follows. The sequential MTT procedure linearly scales with the number of agents' pair. For each pair, a linear contribution to the complexity has to be ascribed to the number of indirect measurements per pair, while the heaviest burden comes from the number of hypothesized legacy targets which quadratically affect the complexity due to DA operations [93].

## 3.5 Performance assessment of joint CSL and MTT in maritime scenario

The performance assessment of the proposed joint CSL and MTT approach is here provided in simulated environment. We target maritime surveillance as primary use case of the proposed technique. The kinematics of agents, targets, accuracy of measurement and other parameters are chosen accordingly.

### 3.5.1 Simulation settings for maritime scenario

As simulation scenario we consider the  $10 \times 10$  km area of Fig. 3.10, with three agents ( $\mathbf{s}_1$ ,  $\mathbf{s}_2$  and  $\mathbf{s}_3$ ) moving counterclockwise at a constant radial velocity of 2.5 km/h around a circle of radius 3.5 km, while another one ( $\mathbf{s}_4$ ) is anchored in the center (e.g., it can represent a buoy with sensing and communication devices). Agents can communicate and sense over the whole area (i.e., no limitation on sensing/communication range). The state of each agent  $\mathbf{s}_{a,t} = [\mathbf{p}_{a,t}^\top, \mathbf{v}_{a,t}^\top]^\top \in \mathbb{R}^4$  comprises both position and velocity over a 2D space. We represent the pdf of each agent  $a \in \mathcal{A}$  through a set of  $N_P = 1000$  particles. Navigation measurements  $\mathbf{g}_t^{(a)} = \mathbf{p}_{a,t} + \mathbf{n}_t^{(a)}$  are available at agents  $\mathbf{s}_{2,t}$  and  $\mathbf{s}_{4,t} \forall t = nT_s, n = 1, \dots, 50$ , with sampling time  $T_s = 30$  s. The noise term has a Gaussian distribution, i.e.,  $\mathbf{n}_t^{(a)} \sim \mathcal{N}(\mathbf{p}_{a,t}, \sigma_{a,g}^2)$ , where the noise statistics are defined as:

$$\sigma_{a,g} = \begin{cases} 20 \text{ m}, & a = 2, \\ 5 \text{ m}, & a = 4, \end{cases} \quad (3.67)$$

to differentiate between the two agents. Each agent's prior pdf is set as a uniform in a circle of 150 m radius around the true position.

Agents localize themselves by combining state measurements  $\mathbf{g}_t^{(a)}$  (if available) with direct measurements  $\mathbf{p}_t^{(a,a')}$  (if available). The latter here include range and bearing between an agent-transmitter  $a' \in \mathcal{T} - \{a\}$  and an agent-receiver  $a \in \mathcal{R}$  as follows:

$$\mathbf{p}_t^{(a,a')} = \begin{cases} \|\mathbf{p}_{a,t} - \mathbf{p}_{a',t}\| + \mathbf{w}_{r,t}^{(a,a')}, & \text{(range)}, \\ \angle(\mathbf{p}_{a',t}, \mathbf{p}_{a,t}) + \mathbf{w}_{b,t}^{(a,a')}, & \text{(bearing)}, \end{cases} \quad (3.68)$$

with noise terms  $\mathbf{w}_{r,t}^{(a,a')} \sim \mathcal{N}(0, \sigma_r^2)$  and  $\mathbf{w}_{b,t}^{(a,a')} \sim \mathcal{N}(0, \sigma_b^2)$  equal for each agent pair  $(a, a')$  and time instance  $t$  and with noise standard deviation (std.)  $\sigma_r = 20$  m and  $\sigma_b = 1$  deg. The latter value is a typical accuracy for towed array of hydrophones which have been used for decades in the underwater domain as to compensate for the heavy power loss of acoustic propagation in water medium [19, 38]. To avoid over confidentiality issues, we opt for  $N_{SL} = 1$  iterations of self localization, also considering the fully connected graph which does not need multi-hop message passing.

The scenario includes a time-variant number of mobile targets  $\mathbf{x}_{\ell,t} = [\mathbf{p}_{\ell,t}^\top, \mathbf{v}_{\ell,t}^\top]^\top \in \mathbb{R}^4$  which are moving at constant speed. Target velocities are randomly chosen between  $\pm 3$  knots. Also for target, a particle-based modeling of  $N_P = 1000$

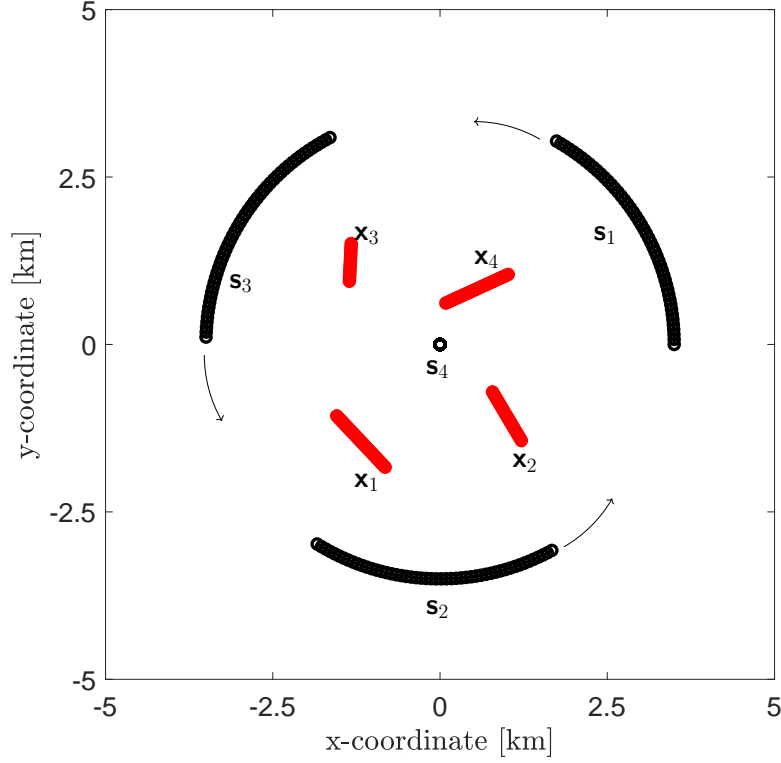


**Figure 3.10:** Simulation scenario with four agents circularly counterclockwise moving and four mobile targets.

is adopted. Target a-priori pdf is a Gaussian pdf centered around the true target position (non-practical but still widely adopted initialization) and with standard deviation of 500 m. In order to assess the tracking robustness in the detection of new targets, they appear at different time instants and persists for a limited amount of time. The  $\ell$ -th target is in the scenario for time instants  $n$  as follow:  $n \in \{5, 35\}$  for  $\ell = 1$ ,  $n \in \{10, 40\}$  for  $\ell = 2$ ,  $n \in \{20, 40\}$  for  $\ell = 3$  and  $n \in \{30, 45\}$  for  $\ell = 4$ .

The presence of agents and targets gives rise to MOT measurements  $\mathbf{z}_{m,t}^{(j)}$  (see Sec. 3.2.3.3) at each  $j$ -th pair of agents. These measurements are subject to data association issues, as well as to missed detection and clutter. Also in this case, we consider range and bearing information, with noise terms as for the direct measurement case. The detection probability is assumed as constant among each agent pair, it is also independent on the type of origin (i.e., if a MOT measurement is originated from a target or an agent) and set equal to  $P_d = P_d(\mathbf{x}_{\ell,t}^{(j)}, \mathbf{s}_t^{(j)}) = P_d(\mathbf{s}_{a^*,t}, \mathbf{s}_t^{(j)}) = 0.7$ . For each agent pair  $j$ , clutter measurements are distributed as:  $\mathcal{P}(\mu_c^{(j)}) = \mathcal{P}(3)$ , while the false alarm distribution  $f_c^{(j)}(\mathbf{z}_{m,t}^{(j)})$  is considered as uniform in the whole area. For algorithmic tractability, at each time instant  $t$  a pruning step of PTs is performed after the last agent pair: any PT  $\ell$  with existence probability  $p(r_{\ell,t}^{(j)} = 1 | \mathbf{z}_{1:t}) < \Gamma_{pr}$  and  $p(\bar{r}_{m,t}^{(j)} = 1 | \mathbf{z}_{1:t}) < \Gamma_{pr}$  is removed from the set  $\mathcal{L}_t$  of legacy PTs. Table 3.1 summarizes the main simulation parameters used for the performance evaluation.

**Table 3.1:** Simulation parameters for cooperative localization in maritime environment.

Parameter	Symbol	Value
Number of agents	$A$	4
Set of Tx agents	$\mathcal{T}$	$\{\mathbf{s}_4\}$
Set of Rx agents	$\mathcal{R}$	$\{\mathbf{s}_1, \mathbf{s}_2, \mathbf{s}_3\}$
Set of agents with state meas.	$\mathcal{A}^g$	$\{\mathbf{s}_2, \mathbf{s}_4\}$
Navigation meas. accuracy (std.) - $\mathbf{s}_2$	$\sigma_{2,g}$	20 m
Navigation meas. accuracy (std.) - $\mathbf{s}_4$	$\sigma_{4,g}$	5 m
Direct/indirect meas. range accuracy (std.)	$\sigma_r$	20 m
Direct/indirect meas. bearing accuracy (std.)	$\sigma_b$	1 deg
Detection probability	$P_d$	0.7
Mean number of clutter per pair	$\mu_c^{(j)}$	3
Mean number of new PTs per pair	$\mu_n^{(j)}$	0.1
Target survival probability	$p_s(\mathbf{x}_{\ell,t-1})$	0.99
Pruning threshold	$\Gamma_{pr}$	0.01
Target existence threshold	$P_{ex}$	0.75
Number of particles	$N_P$	1000

### 3.5.2 Performance evaluation of joint CSL and MTT

This section aims to evaluate the localization performance of the proposed CSL and MTT technique. Specifically, we test the capability of estimating agent positions as well as detecting unknown targets.

In the previously detailed settings, we compare the performance of the proposed joint CSL and MTT algorithm with a solution which first performs CSL and then MTT, without combining them. To ease the notation and facilitate the reader, we refer to these two methodologies as Joint Localization and Tracking (JLT) and Separate Localization and Tracking (SLT). In following figures, JLT is marked with a dotted line, while SLT with a dashed line. It is important to stress that in the JLT approach targets are not only unknown objects to be just localized, but they represent a valuable information used upside-down by the agents to refine their own localization through the proposed cooperative mechanism. To highlight this, in the simulation we induce an outage condition to agents  $\mathbf{s}_{1,t}$  and  $\mathbf{s}_{3,t}$  for  $t = [300, 1200]$  s, where no direct nor navigation measurements are available. Such condition, in practical use cases, can be related to hardware malfunctioning, interference or hacking issue, meaning that the agent is going to be lost if target information is not used. Results are averaged over 100 Monte Carlo iterations.

As first result, in Fig. 3.11 we report the position error over time for each agent individually, for both JLT and SLT. The most interesting result is related to the agents in outage conditions ( $\mathbf{s}_{1,t}$  and  $\mathbf{s}_{3,t}$ ): we show that it is still possible to localize them by exploring target information (JLT) even during the outage period. In case of SLT, instead, targets cannot contribute in localizing “lost” agents, and the estimate of agent positions can only rely on the motion prediction model, leading to high errors. Considering practical implementation, the use of JLT might allow, for instance, the recovery of the agent, which would be hardly achieved in case of SLR. Regarding other agents, we report that moderate improvements on agent  $\mathbf{s}_{2,t}$  localization can be achieved by combining target information with navigation

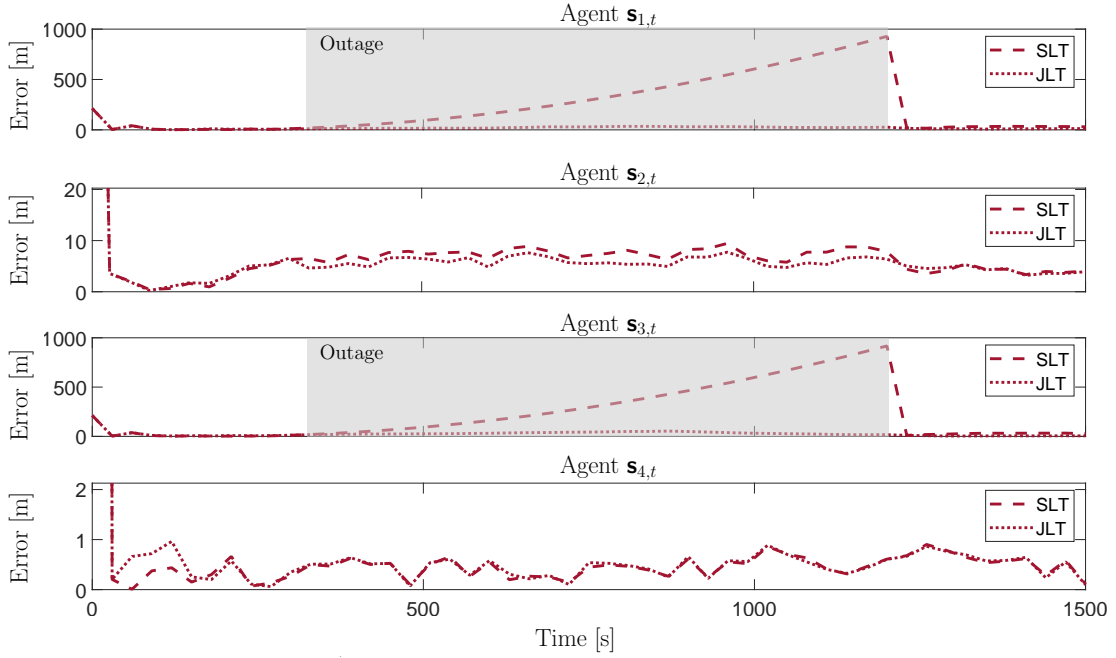


**Figure 3.11:** Localization accuracy of agents over time. Performance comparison between JLT and SLT.

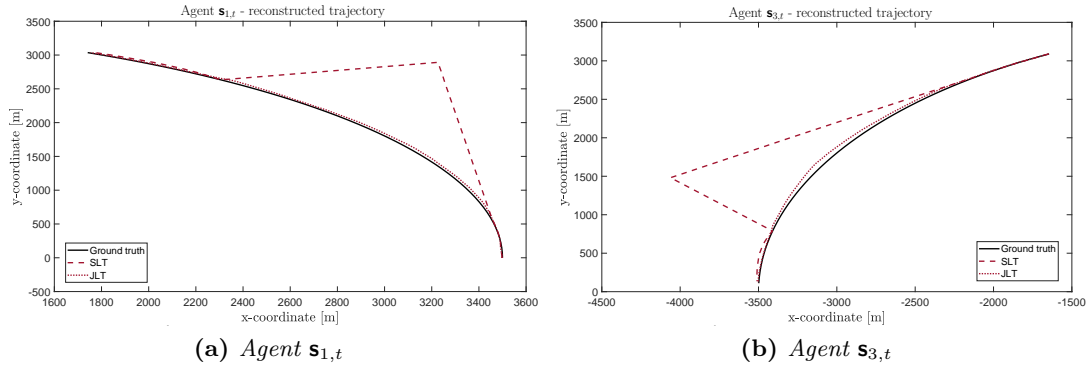
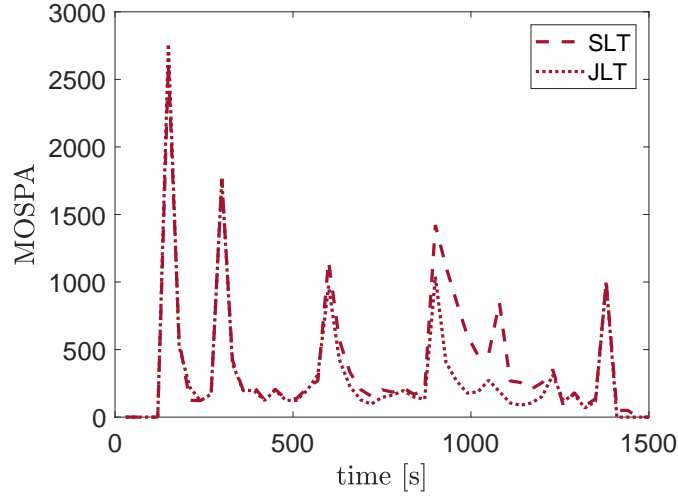


**Figure 3.12:** Zoom on reconstructed trajectories of agents in outage conditions.

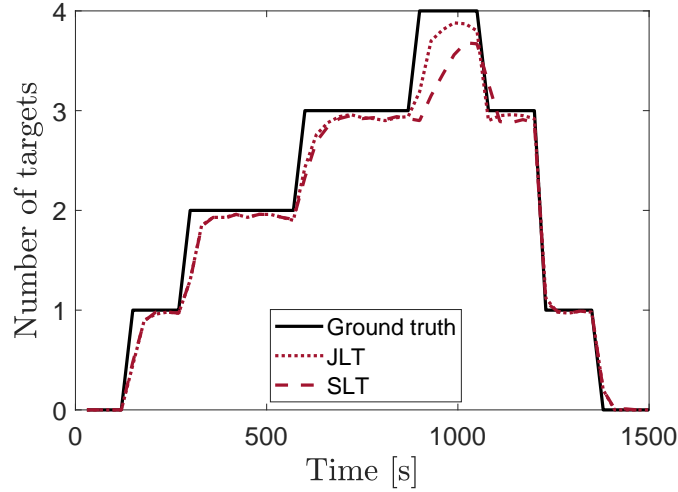
measurements, while no benefits are for agent  $\mathbf{s}_{4,t}$  as navigation measurements are extremely precise (the intended scenario is a GPS-based positioning of a buoy).

A deeper focus on the agents with outage condition is provided in Fig. 3.12, where the reconstructed trajectories of agents  $\mathbf{s}_{1,t}$  (Fig. 3.12a) and  $\mathbf{s}_{3,t}$  (Fig. 3.12b) are plotted in the 2D space. This visualization allows to highlight the huge drifts are induced by SLT on the agent localization in case of relying only on prediction model (SLS), and remarks, on the other hand, how profitable is the use of target information (JLT) in “keeping the track”.

After the analysis on agent localization, we now analyze the capability of the proposed technique in performing MTT, which is a primary task of the application. Results are given in terms of Mean Optimal Subpattern Assignment (MOSPA), Fig. 3.13a, and number of detected targets, Fig. 3.13b. The MOSPA metric [94] of order 1 is used, with a cut off parameter of 5000. Results in Fig. 3.13a indicate



(a) MOSPA



(b) Number of targets

**Figure 3.13:** Performance comparison between JLT and SLR in MTT. a) MOSPA. b) Number of existing targets.

superior tracking capabilities of JLT with respect to SLT. Major benefits are in the detection of the fourth new target ( $t = 900$  s), where the outage condition of agents  $\mathbf{s}_{1,t}$  and  $\mathbf{s}_{3,t}$  significantly affect a SLT system. In SLT the contribution of the joint sensing is missing, and MOT measurements of the not-in-outage agent  $\mathbf{s}_{2,t}$  are not confirmed over time (or poorly confirmed in the very first outage time instants). The tardiness in target detection is also highlighted in Fig. 3.13b, where a target (either legacy or new one) is declared to exist at time  $t$  if  $p(\mathbf{r}_{\ell,t}^{(J)} = 1 | \mathbf{z}_{1:t}) > P_{\text{ex}}$  or  $p(\bar{\mathbf{r}}_{m,t}^{(J)} = 1 | \mathbf{z}_{1:t}) > P_{\text{ex}}$ , with  $P_{\text{ex}} = 0.75$ .

Another metrics that might be of interest for MTT is the Time On Target (TOT), which characterizes the percentage of time in which the MTT system is capable of detecting an existing target  $\mathbf{x}_{\ell,t}$  and localizing it with an error less than a threshold  $\mathbf{d}$ . We report in Tab. 3.2 a summary for three different threshold values  $\mathbf{d} = \{50, 100, 200\}$  m, highlighting superior detection capabilities for the

proposed JLT with respect to SLT, especially related to the third target.

**Table 3.2:** Performance comparison of JLT and SLT in terms of percentage of Time On Target, for three different threshold distances  $d$ .

	d = 50 m		d = 100 m		d = 200 m	
target	SLT	JLT	SLT	JLT	SLT	JLT
$\mathbf{x}_1$	73.1%	87.2%	92.3%	95.3%	95.4%	95.4%
$\mathbf{x}_2$	50.7%	89.2%	84.3%	95.0%	94.2%	95.0%
$\mathbf{x}_3$	28.5%	86.6%	61.0%	93.8%	89.4%	93.8%
$\mathbf{x}_4$	48.0%	73.1%	71.3%	91.0%	78.6%	91.0%

Results demonstrate how target information is of high importance for practical application, e.g., in maritime surveillance. We proved the convenience of considering a joint CSL and MTT solution rather than perform the two tasks independently. A JLT approach allows for a more robust localization of both agents and targets, despite the coarse measurement accuracies of the maritime scenario.

### 3.6 Concluding remarks

In this chapter, we developed a cooperative technique for self-localization and multitarget tracking in multi-agent networks. Despite being primary intended to maritime scenarios, the algorithm is general enough to be tailored to any multi-agent system with agents equipped with diverse perception systems and communication devices. The proposed solution performs the mandatory tasks of determining the agent positions in the network (i.e., create the multi-agent network) and detecting and localizing an unknown and arbitrary number of targets, where existence probabilities are used to declare their existences as well as for opting for their removal (pruning). Surveillance systems are thus an immediate application of this technique. Besides joint Cooperative Self-Localization (CSL) and MultiTarget Tracking (MTT), the developed solution also takes advantage of target information to update and refine the agent positions obtained during CSL. This latter benefit might provide few enhancements in case of large availability of navigation and/or inter-agent direct measurements, but has been proven through simulations to be of utmost importance in case malfunctioning or outage conditions which may occur in daily operations at sea and require recovery of the agent. An important aspect of belief-propagation technique as the proposed one is the flexibility: the algorithm intrinsically handles time-variant properties of agents and network topology (such as a connection of a new agent, or the disappearing of an existing one) and it also admits the coexistence of different type of measurements (navigation, direct or indirect) of (part of) the agent state. Lastly, the extension of data association issues to include agent as well (and not only targets) allows to consider realistic conditions of signal propagation, where multiple reflections from both agents and targets are unavoidably present and affect the signal processing chain.

*Future research directions:* the performance developed algorithm presented in this chapter has been validated by simulations. However, to assess its robustness and resilient capabilities in real operations, a validation over collected real data

is mandatory to fill the gap between research and real systems. As anticipated by the disclosure on main limitations, the use of real measurements might lead to an overestimation of the number of targets due to multiple reflections of a same signal at different locations of a same target due to unavoidable physical properties and space occupancy. Thus, it would be suggested to relax the assumption that only one measurement can originate from one target, and develop a more complex stochastic formulation. If this might not be the case of a maritime environment, we deem the extension to be highly recommended for indoor scenarios, where it is more likely to have multiple reflections of a same target. Moreover, multiple data association hypothesis would be helpful in discriminating among many multipath components of a same reflected signals, enhancing the localization in non-ideal environments.

---

## Cooperative localization in vehicular scenarios

This chapter addresses the problem of cooperative localization in vehicular networks. The time varying multi-agent systems is constituted by land vehicles and targets (here generically referred as “features”). A scenario of connected vehicles exchanging information on detected targets (obtained through processing on-board perception sensors, e.g., radar, lidar, ultrasound and camera) in the environment is used to formulate a cooperative localization algorithm where both vehicles and target need to be localized. A cooperative vehicles/targets localization solution is developed based on the sum-product algorithm working on a time-varying graph created by vehicle connections, customizing the centralized implementation of previous chapter into a fully distributed implementation. Direct Vehicle-to-Vehicle (V2V) communications allow information exchange among vehicles, being thus the enabler of distributed approaches. Cooperative target localization is used as hidden information for refining GPS-based positioning, leading to the definition of the Implicit Cooperative Positioning (ICP) algorithm, with nested data association on multitarget measurements (ICP-DA). The objective is to demonstrate potentialities of cooperative localization in vehicular application, which not only leads to a more accurate estimation of targets but can also be correspondingly used to improve GPS-based vehicle positioning as well.

The chapter is organized as follows. Sec. 4.1 introduces the problem of cooperative localization in cooperative intelligent transportation systems which is here customized according to the system model presented in Sec. 4.2. Sec. 4.3 is entirely devoted to explain the details of the data association issue of multiple measurements originating from unknown targets, which is fundamental for the proposed distributed cooperative localization solution describe in Sec. 4.4. Performances are evaluated in simulated ad-hoc scenarios in Sec. 4.5 as well as in realistic urban arterials in Sec. 4.6. Lastly, Sec. 4.7 contains concluding remarks.

The contents of this chapter are adapted from publications [1,2].

## 4.1 Introduction to localization in C-ITS

---

Cooperative Intelligent Transportation Systems (C-ITS) rely on V2X communications to enable data sharing among road users, to increase situation awareness and take preventive actions to anomalous events, improving road safety. The existing V2X standards are based on a WiFi mode (i.e., IEEE 802.11p WAVE [95] and ETSI ITS-G5 [96], for US and EU respectively) or on cellular communications (i.e., the recently released 3GPP LTE C-V2X standard [97]), while new millimeter-wave technologies are emerging in the context of the fifth-generation (5G) mobile networks to cover higher levels of automation [98,99]. 5G and beyond technologies enable cooperative perception and maneuvering functionalities by direct Vehicle-to-Vehicle (V2V) exchange of massive sensor data and mobility patterns among vehicles, paving the way for a new cooperative, connected and automated mobility [100–104]. The V2V interactions allow vehicles to fuse local data (ego-sensors) with information from nearby road users, extending the field of view of individual perception sensors and thus improving road safety [105]. Vehicles can also share the intended trajectories and synchronize mobility patterns, forming high-density platoons and enhancing traffic efficiency [106].

In many safety-critical C-ITS applications [107–110], a fundamental requirement is precise vehicle positioning. GPS, even when augmented by inertial sensors, differential corrections or multi-constellation receivers, cannot guarantee the required navigation performance in terms of availability and accuracy, especially in highly built-up areas, where the satellite signal is severely attenuated or even denied [11,12]. To improve GPS performance, many approaches are available in the literature and are here grouped into non-cooperative and cooperative solutions. In non-cooperative methods, vehicles rely only on their own sensors, without any data fusion with other vehicles. An example is Simultaneous Localization And Mapping (SLAM) [111,112], where an ego vehicle builds detailed map by integrating GPS information in the mapping process, enhancing the localization accuracy [113,114]. On the other hand, Cooperative Positioning (CP) techniques [115–123] make use of V2X technologies to perform data sharing and enrich the set of locally available information. Overviews on CP technologies, protocols and algorithms can be found in [124–126]. Most of CP methods rely on explicit inter-vehicle measurements (distance, velocity or angle) extracted from the received V2X radio signals, such as time-of-flight [127], received signal strength [128], angle of arrival [129] or Doppler shift of the carrier frequency [122].

Recently, the Implicit Cooperative Positioning (ICP) technique has been proposed where vehicles use on-board sensing equipment to detect passive objects in the driving environment. Indeed, common on-board perception sensors (e.g., radar, lidar, ultrasound and camera) let a vehicle to acquire environmental awareness of the surroundings by detecting objects. In the ICP, the processed output of multi-sensor fusion (i.e., the position of estimated objects and related pdfs), is used as input for a cooperative localization mechanism. ICP is multi-agent MTT methods [62,88], where non-cooperative objects (targets) are sensed by a network of cooperative mobile agents and used for localization. With respect to other CP methods, the advantage is that ICP relies on conventional communication and

sensing devices already available on current vehicles (e.g., radar, lidar, camera), and it does not require any inter-vehicle ranging procedure. The location statistics of detected targets are the only information that is exchanged among vehicles (or RSU) and it is enough to enable inter-vehicle cooperative localization [130, 131].

The first version of ICP method was developed in [130, 131], where perfect association between measurements and sensed objects was assumed. Such strong assumptions do not fit real C-ITS scenarios, where DA is a mandatory step to be performed before any fusion of measurements from multiple vehicles. The DA issue, in fact, consists of solving (or at least handling) the uncertainty on the origin of measurements. A solution to the DA problem has been proposed in [83] for centralized tracking of passive targets in sensor networks with known sensor locations, using an efficient association algorithm [93]. A similar centralized approach has been developed in [132] for vehicular environments. These methods employ particle filtering to sample the location statistics, which are non-Gaussian due to the association uncertainty. Unfortunately, in highly dynamic C-ITS scenarios where both vehicles and features have to be tracked, precise positioning requirements strongly impact on the number of required particles to accurately describe the vehicle/feature pdfs, easily leading the computational burden unfeasible. Moreover, these DA-enabled methods rely on a central unit for data gathering and processing, whereas decentralized techniques are preferred in vehicular networks that rapidly vary according to mobility patterns.

#### 4.1.0.1 Scientific contributions and main limitations

In this chapter, we develop and propose a fully distributed DA-enabled CP solutions, extending the original ICP method. An in-depth performance analysis in realistic environments with large numbers of vehicles/features and varying traffic conditions is provided in order to highlight how the localization accuracy scales with the traffic demand and to validate the method robustness.

The first main contribution is the extension of the ICP method [131] to integrate the DA task into the distributed framework for localization of features and vehicles. The proposed ICP method with Data Association (ICP-DA) relies on two Belief Propagation Algorithms (BPA) [133]: one for data association (BPA-DA), and the other for localization of features and vehicles (BPA-L). At first, vehicles use their on-board sensing equipment to detect a number of nearby features and individually run to solve the association task through BPA-DA. Then, they use BPA-L to combine the Vehicle-To-Feature (V2F) information with the local GPS measurement, sharing the information with neighbors by V2V interactions. Regarding the practical implementation, we design a PF algorithm which relies on a particle-based representation of the non-Gaussian vehicle/feature location beliefs, combined with a consensus algorithm [134] for distributed computation of feature-related information at vehicles. We also propose a low-complexity (LC) suboptimal method, referred to as ICP-DA-LC, based on a *hard* Maximum-A-Posteriori (MAP) Bayesian detection for feature-measurement pairing, which keeps Gaussian properties of message passing. The proposed MAP-based solution uses a threshold detector to exclude ambiguous association hypothesis, mitigating the impact of association errors.

The second main contribution is the validation of the proposed technique in a realistic urban road network by simulating traffic flow along an urban arterial in Turin, Italy, including primary roads and several secondary junctions. With respect to other studies where the positioning precision is randomly and exogenously generated, as in [135], in this work the vehicle localization accuracy is considered as dependent on traffic conditions over the roads and the related traffic control systems, that rule the spatial distribution of the vehicles and their mutual interactions. A key element is the control strategy implemented at road intersections which affects the traffic flow in terms of delays, queues and capacity at the nodes, as well as the density of vehicles along the arterials. Two different traffic scenarios are analyzed: a standard one, where traffic lights regulate the vehicles dynamics at intersections, and a vehicle self-regulated scenario (representative of higher levels of automation) where vehicles individually and autonomously decide if they can safely cross an intersection avoiding conflicts. The simulation of real-life traffic conditions is instrumental for the assessment of the potential benefits of the proposed cooperative methods in typical urban conditions. An important goal is to show the strengths and drawbacks of one method with respect to the other, with main focus on the localization performance in terms of accuracy and computational complexity, which are key points to be addressed in vehicular applications. Furthermore, we aim to demonstrate that a sub-meter accuracy can be reached by the proposed cooperative localization approach which thus enables new C-ITS services, such as turn-by-turn route guidance, including lane selection, or queue length monitoring for optimal tuning of traffic light control [136].

The developed solution assumes each vehicle and target (feature) as represented by a single point in a 2D space. The vertical component is not considered as in the vehicular environment the localization operates on a limited area (due to communication technology coverage constraints) with nearly-constant altitude. Moreover, current on-board ranging sensors (e.g., radar, lidar, camera) might not be able to provide vertical information. On the other hand, the mentioned sensors often produced multiple observation of a same detected objects (especially lidar and radar, less for camera). An example regards the detection of a parked car, which occupancy leads to multiple reflections of a same lidar/radar sounding signal. This unavoidable physical effect is not taken into account as the statistical formulation assumes unique measurements (i.e., a target can generate at most one detection measurement). The link between the considered assumption and the realistic use case is represented by the sensor processing chain, in the sense that raw sensing data (where multiple observations of a same target can be present) are assumed to be processed (either by the chipset of the sensor itself or by the vehicle) such that a unique output measurement is provided. This outcome represents the unique input for the cooperative localization algorithm discussed in this chapter. Another non-negligible assumption behind the theoretical formulation of the vehicular cooperative localization problem resides in considering ideal target detection (differently from Chapter 3), i.e., there are no false measurements and all targets within the vehicle sensing range are detected. As before, also this case is not matching a real vehicular operation condition in which detection sensors gather noise data from background. However, also in this case the relation filling the gap

between practice and developed algorithm resides in the sensor or vehicle capability to produce a unique single output for each detected target. As a final comment, it is to be mentioned that latency constraints have been neglected. Latency both regards the target detection (with negligible impact) and inter-vehicle cooperation (with strong impact). Regarding the latter, a distributed solution where vehicles need to exchange local information to reach a consensus unavoidably has to deal with latency issue of the communication protocol (V2X in this case). However, by considering the 5G communication technology which should allow ultra-low latency (down 1 ms in perspective), if cooperative measurements are available at 1 Hz, it would mean that hundreds of V2V interactions (message exchange) can be performed to reach a consensus among vehicles, guaranteeing the feasibility of the proposed solution.

## 4.2 Model of the vehicular scenario

We consider a 2D C-ITS scenario with a set  $\mathcal{V} = \{1, \dots, N_v\}$  of interconnected vehicles as illustrated in Fig. 4.1. Each vehicle  $i \in \mathcal{V}$  is characterized by time-varying (time index  $t$ ) position  $\mathbf{p}_{i,t}^{(V)} = [\mathbf{p}_{x_{i,t}}^{(V)} \mathbf{p}_{y_{i,t}}^{(V)}]^\top$  and velocity  $\mathbf{v}_{i,t}^{(V)} = [\mathbf{v}_{x_{i,t}}^{(V)} \mathbf{v}_{y_{i,t}}^{(V)}]^\top$  vectors. We denote with  $\mathcal{J}_{i,t} = \{j \in \mathcal{V} : \|\mathbf{p}_{i,t}^{(V)} - \mathbf{p}_{j,t}^{(V)}\| \leq R_c\}$ , the set of neighbors that directly communicate with vehicle  $i \in \mathcal{V}$ , which has a communication range  $R_c$ . The scenario also comprises a set  $\mathcal{F} = \{1, \dots, N_f\}$  of non-cooperative features (objects to be detected) described in terms of position  $\mathbf{p}_{k,t}^{(F)} = [\mathbf{p}_{x_{k,t}}^{(F)} \mathbf{p}_{y_{k,t}}^{(F)}]^\top$  and velocity  $\mathbf{v}_{k,t}^{(F)} = [\mathbf{v}_{x_{k,t}}^{(F)} \mathbf{v}_{y_{k,t}}^{(F)}]^\top$  as well. Features that fall within the sensing range  $R_s$  of the vehicle are detected through relative position-velocity measurements. The subset of features detected by vehicle  $i$  is  $\mathcal{F}_{i,t} = \{k \in \mathcal{F} : \|\mathbf{p}_{k,t}^{(F)} - \mathbf{p}_{i,t}^{(V)}\| \leq R_s\}$ .

The vector  $\mathbf{x}_{i,t}^{(V)}$  of vehicle kinematic states is assumed to evolve over time  $t$  according to the inertial sensor model [137]:

$$\mathbf{x}_{i,t}^{(V)} = \begin{bmatrix} \mathbf{p}_{i,t}^{(V)} \\ \mathbf{v}_{i,t}^{(V)} \end{bmatrix} = \mathbf{A} \mathbf{x}_{i,t-1}^{(V)} + \mathbf{B} \mathbf{a}_{i,t-1}^{(V)} + \mathbf{w}_{i,t-1}^{(V)}, \quad (4.1)$$

with

$$\mathbf{A} = \begin{bmatrix} \mathbf{I}_2 & T_s \mathbf{I}_2 \\ \mathbf{0}_{2 \times 2} & \mathbf{I}_2 \end{bmatrix} \quad \text{and} \quad \mathbf{B} = \begin{bmatrix} 0.5 T_s^2 \mathbf{I}_2 \\ T_s \mathbf{I}_2 \end{bmatrix}. \quad (4.2)$$

The matrix  $\mathbf{A}$  describes the state transition while  $\mathbf{B}$  relates the vehicle state to the acceleration information  $\mathbf{a}_{i,t-1}^{(V)}$ , provided by an on-board inertial sensor.  $T_s$  is the sampling interval and  $\mathbf{w}_{i,t-1}^{(V)}$  is the Gaussian driving noise (modeling sensor measurement error and non-deterministic behaviors not accounted by matrices  $\mathbf{A}$  and  $\mathbf{B}$ ) with pdf  $p(\mathbf{w}_{i,t-1}^{(V)}) = \mathcal{N}(\mathbf{0}, \mathbf{Q}_{i,t-1}^{(V)})$ .

The state  $\mathbf{x}_{k,t}^{(F)}$  of each feature evolves over time  $t$  according to the first order Markov model as:

$$\mathbf{x}_{k,t}^{(F)} = \begin{bmatrix} \mathbf{p}_{k,t}^{(F)} \\ \mathbf{v}_{k,t}^{(F)} \end{bmatrix} = \mathbf{A} \mathbf{x}_{k,t-1}^{(F)} + \mathbf{w}_{k,t-1}^{(F)}, \quad (4.3)$$

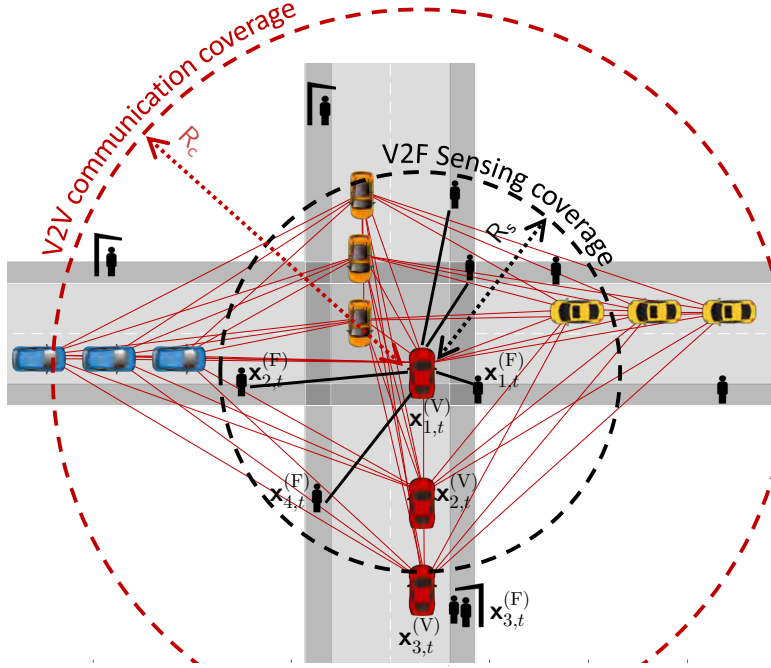


**Figure 4.1:** Example of C-ITS scenario with  $N_v = 12$  connected vehicles and  $N_f = 10$  passive features. Red links indicate V2V connections (with communication range  $R_c$ ), while black ones the V2F connections (with sensing range  $R_s$ ) of vehicle  $i = 1$ .

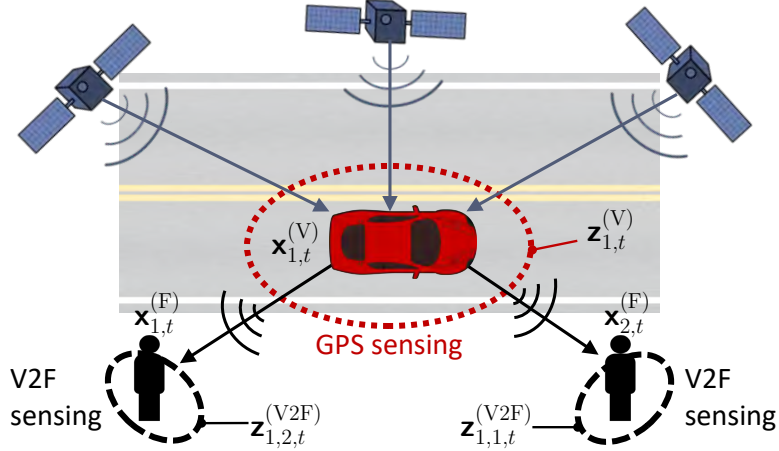


**Figure 4.2:** Ego vehicle measurements: GPS (red dotted ellipse) and V2F (black dashed ellipse).

where  $\mathbf{w}_{k,t-1}^{(F)}$  is the Gaussian driving noise with pdf  $p(\mathbf{w}_{k,t-1}^{(F)}) = \mathcal{N}(\mathbf{0}, \mathbf{Q}_{k,t-1}^{(F)})$ .

At each vehicle, two different types location measurement are available, as highlighted in Fig. 4.2. The first one is the (direct) measurement provided by a GPS receiver of the vehicle state (indicated with the red dotted line) which is modeled as:

$$\mathbf{z}_{i,t}^{(V)} = \mathbf{x}_{i,t}^{(V)} + \mathbf{n}_{i,t}^{(V)}, \quad (4.4)$$

where the GPS measurement noise  $\mathbf{n}_{i,t}^{(V)}$  has pdf  $p(\mathbf{n}_{i,t}^{(V)}) = \mathcal{N}(\mathbf{0}, \mathbf{R}_{i,t}^{(V)})$ . Moreover, each vehicle collects a set of V2F observation  $\mathcal{O}_{i,t} = \{1, \dots, O_{i,t}\}$  of the surrounding

features  $k \in \mathcal{F}_{i,t}$ . Note that these are relative location/velocity measurements referred to vehicle  $i$  and their association to the features is unknown. Assuming that at vehicle  $i$  each feature  $k \in \mathcal{F}_{i,t}$  can generate at most one V2F measurement  $\ell \in \mathcal{O}_{i,t}$ , the relative V2F observation (e.g., as a result of radar, lidar, ultrasound or camera processing) is:

$$\mathbf{z}_{i,\ell,t}^{(\text{V2F})} = \mathbf{x}_{k,t}^{(\text{F})} - \mathbf{x}_{i,t}^{(\text{V})} + \mathbf{n}_{i,\ell,t}^{(\text{V2F})}, \quad (4.5)$$

where  $k$  is the (unknown) feature associated to measurement  $\ell$  and the V2F uncertainty  $\mathbf{n}_{i,\ell,t}^{(\text{V2F})}$  has pdf  $p(\mathbf{n}_{i,\ell,t}^{(\text{V2F})}) = \mathcal{N}(\mathbf{0}, \mathbf{R}_{i,\ell,t}^{(\text{V2F})})$ .

The V2F measurements available at each vehicle are shared with neighbors in order to enable a cooperative sensing of the surrounding environment with enhanced localization performance. This process is a part of the ICP method which is described in the following sections.

### 4.3 Deepening the data association problem

---

The ICP method is a CP technique that augments the GPS positioning of the ego vehicle by combining local GPS data with high-resolution information on cooperative features localization. The GPS initial measurement  $\mathbf{z}_{i,t}^{(\text{V})}$  is refined by a cooperative iterative procedure that fuses the V2F measurements  $\mathbf{z}_{j,\ell,t}^{(\text{V2F})}$  of multiple vehicles  $j \in \mathcal{V}$  through the V2V links. Multiple observations of a same feature at different vehicles enables to cooperatively localize these objects with an enhanced accuracy. This information is then used upside-down to improve positioning of the vehicles themselves. Being features passively detected, the association with originating V2F measurements represents a main issue to be solved. Details on DA process are now provided.

The ICP-DA working principle is illustrated in Fig. 4.3, where two vehicles jointly sense two features. As shown in Fig. 4.3a, in order to consistently fuse the measurements collected by the two vehicles, each vehicle  $i \in \{1, 2\}$  needs at first to pair each observation  $\mathbf{z}_{i,\ell,t}^{(\text{V2F})}$ ,  $\ell \in \{1, 2\}$ , with the corresponding feature  $k \in \{1, 2\}$  that generated that measurement. In the specific example, the observation  $\mathbf{z}_{1,2,t}^{(\text{V2F})}$  must be fused with the observation generated by the same feature at the second vehicle, i.e.  $\mathbf{z}_{2,1,t}^{(\text{V2F})}$ . Only by associating these two measurements to the same features it is possible to properly combine them and get a more accurate information on the feature itself, as shown in Fig. 4.3b and, as a consequence, an enhanced localization of both vehicles observing the features.

We propose to solve the association problem jointly with localization using a Bayesian approach. Let  $\mathbf{x}_t^{(\text{V})} = [\mathbf{x}_{i,t}^{(\text{V})}]_{i \in \mathcal{V}} \in \mathbb{R}^{4N_v \times 1}$  and  $\mathbf{x}_t^{(\text{F})} = [\mathbf{x}_{k,t}^{(\text{F})}]_{k \in \mathcal{F}} \in \mathbb{R}^{4N_f \times 1}$  be the vehicles' and features' states at time  $t$ , and  $\boldsymbol{\theta}_t = \begin{bmatrix} \mathbf{x}_t^{(\text{V})\top} & \mathbf{x}_t^{(\text{F})\top} \end{bmatrix}^\top \in \mathbb{R}^{(4N_v + 4N_f) \times 1}$  the combined state vector for the overall set of connected vehicles and sensed features. A complete recap of variables, with their dimensions and meanings is presented in Table 4.1.

By defining the aggregate vector of GPS measurements  $\mathbf{z}_t^{(\text{V})} = [\mathbf{z}_{i,t}^{(\text{V})}]_{i \in \mathcal{V}} \in \mathbb{R}^{4N_v \times 1}$  and of V2F measurements  $\mathbf{z}_t^{(\text{V2F})} = [\mathbf{z}_{i,\ell,t}^{(\text{V2F})}]_{i \in \mathcal{V}} \in \mathbb{R}^{4O \times 1}$ , with  $O = \sum_{i=1}^{N_v} O_{i,t}$

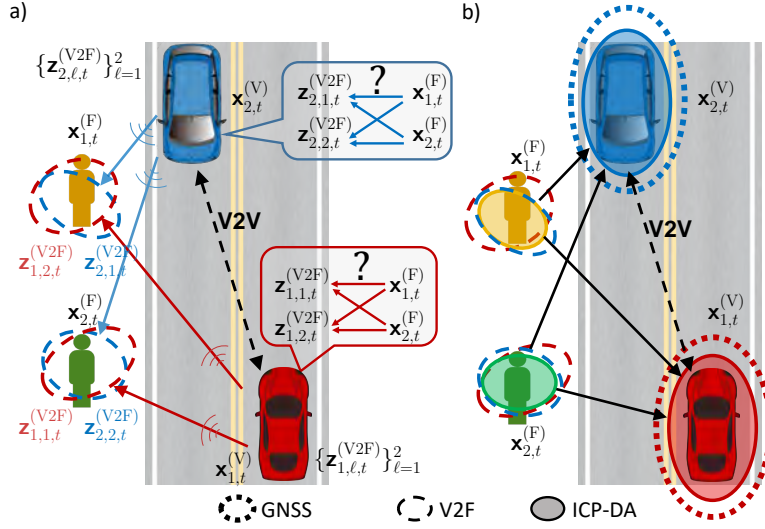


**Figure 4.3:** Details on data association, where vehicles  $\mathbf{x}_{i,t}^{(V)}$ ,  $i \in \{1, 2\}$  jointly sense features  $\mathbf{x}_{k,t}^{(F)}$ ,  $k \in \{1, 2\}$ , with unknown measurement-feature association. b) V2F measurements fusion after association for feature localization (filled ellipses) and enhancement of GPS accuracy (contours).

denoting the total number of V2F observations  $\mathbf{z}_{i,t}^{(V2F)} = [\mathbf{z}_{i,\ell,t}^{(V2F)}]_{\ell \in \mathcal{O}_{i,t}} \in \mathbb{R}^{4\mathcal{O}_{i,t} \times 1}$ , the MMSE estimate of the vehicle-feature states based on the whole aggregated measurements  $\mathbf{z}_t = [\mathbf{z}_t^{(V)\top} \mathbf{z}_t^{(V2F)\top}]^\top$  is calculated as:

$$\hat{\boldsymbol{\theta}}_{t|t} = \begin{bmatrix} \hat{\mathbf{x}}_{t|t}^{(V)} \\ \hat{\mathbf{x}}_{t|t}^{(F)} \end{bmatrix} = \int \boldsymbol{\theta}_t p(\boldsymbol{\theta}_t | \mathbf{z}_{1:t}) d\boldsymbol{\theta}_t, \quad (4.6)$$

where  $\mathbf{z}_{1:t} = [\mathbf{z}_\tau]_{\tau=1,\dots,t}$  collects all measurements up to time  $t$  and  $p(\boldsymbol{\theta}_t | \mathbf{z}_{1:t})$  is the pdf of the vehicle-feature state.

The evaluation of  $p(\boldsymbol{\theta}_t | \mathbf{z}_{1:t})$  requires a preliminary pairing of the measurements  $\mathbf{z}_t^{(V2F)}$  with the features states in  $\boldsymbol{\theta}_t$ , in order to compute the related observation likelihoods. To this aim, we model the association problem according to [93] by introducing the *feature-oriented* ( $F \rightarrow O$ ) association variable  $\alpha_{i,k,t}$ ,  $\forall i \in \mathcal{V} \wedge k \in \mathcal{F}$ , defined as:

$$\alpha_{i,k,t} = \begin{cases} \ell \in \mathcal{O}_{i,t}, & \text{if at time } t \text{ feature } k \text{ generates} \\ & \text{measurement } \ell \text{ at vehicle } i, \\ 0, & \text{if at time } t \text{ feature } k \text{ does not generate any} \\ & \text{measurement at vehicle } i \text{ (i.e., } k \notin \mathcal{F}_{i,t}\text{),} \end{cases} \quad (4.7)$$

which relates each observation  $\ell \in \mathcal{O}_{i,t}$  of vehicle  $i$  to the corresponding feature  $k \in \mathcal{F}_{i,t}$ . Defining the  $N_f \times 1$  stacked association vector of all the features sensed by vehicle  $i$  as  $\boldsymbol{\alpha}_{i,t} = [\alpha_{i,k,t}]_{k \in \mathcal{F}}$  and the overall  $N_v N_f \times 1$  association vector at time  $t$  as  $\boldsymbol{\alpha}_t = [\boldsymbol{\alpha}_{i,t}]_{i \in \mathcal{V}}$ , we model  $\boldsymbol{\alpha}_t$  as a random process and we evaluate the posterior pdf of the vehicle-feature dynamic states as:

$$p(\boldsymbol{\theta}_t | \mathbf{z}_{1:t}) = \sum_{\boldsymbol{\alpha}_t \in \mathcal{A}} p(\boldsymbol{\theta}_t, \boldsymbol{\alpha}_t | \mathbf{z}_{1:t}) = \sum_{\boldsymbol{\alpha}_t \in \mathcal{A}} p(\boldsymbol{\theta}_t | \boldsymbol{\alpha}_t, \mathbf{z}_{1:t}) p(\boldsymbol{\alpha}_t | \mathbf{z}_{1:t}), \quad (4.8)$$

Table 4.1: Summary of main variables.

Symbol	Dimension	Meaning
$\mathbf{x}_{i,t}^{(V)}$	$4 \times 1$	position-velocity of veh. $i$
$\mathbf{x}_t^{(V)}$	$4N_v \times 1$	aggregated states of all vehicles
$\mathbf{x}_{k,t}^{(F)}$	$4 \times 1$	position-velocity of fea. $k$
$\mathbf{x}_t^{(F)}$	$4N_f \times 1$	aggregated states of all features
$\boldsymbol{\theta}_t$	$4(N_v + N_f) \times 1$	global vehicle and feature states
$\mathbf{z}_{i,t}^{(V)}$	$4 \times 1$	GPS measurement at veh. $i$
$\mathbf{z}_t^{(V)}$	$4N_v \times 1$	aggregated GPS measurements
$\mathbf{z}_{i,\ell,t}^{(V2F)}$	$4 \times 1$	V2F measurement $\ell$ at veh. $i$
$\mathbf{z}_{i,t}^{(V2F)}$	$4\mathcal{O}_{i,t} \times 1$	overall V2F measurements at veh. $i$
$\mathbf{z}_t^{(V2F)}$	$4O \times 1$	aggregated V2F measurements
$\mathbf{z}_t$	$4(N_v + O) \times 1$	global GPS and V2F measurements
$\boldsymbol{\alpha}_{i,k,t}$	$1 \times 1$	F→O association for fea. $k$ at veh. $i$
$\boldsymbol{\alpha}_{i,t}$	$N_f \times 1$	overall F→O associations at veh. $i$
$\boldsymbol{\alpha}_t$	$N_v N_f \times 1$	global F→O associations
$\boldsymbol{\beta}_{i,\ell,t}$	$1 \times 1$	O→F association for meas. $\ell$ at veh. $i$
$\boldsymbol{\beta}_{i,t}$	$\mathcal{O}_{i,t} \times 1$	overall O→F associations at veh. $i$
$\boldsymbol{\beta}_t$	$O \times 1$	global O→F associations

where the summation is over the set  $\mathcal{A}$  of all the admissible association values  $\boldsymbol{\alpha}_t$ , i.e. such that each feature can generate at most one measurement at vehicle  $i$  and each measurement at vehicle  $i$  can be generated by at most one feature.

Since a centralized solution is undesirable in vehicular scenarios, in the following section, we propose a distributed method for the evaluation of the marginal pdfs in (4.8). The choice of a distributed offload of processing task is led by the application itself, which is characterized by a fast-varying evolution of connectivity and creation of clusters of locally-connected vehicles. It results that it is preferable not to collect the whole dataset of vehicle measurements in a single processing unit (e.g., RSU) but it would be an advantage to let the vehicles iteratively refine their knowledge by combining information from neighbors. In this way, an improved robustness to communication and data aggregation failures allows for a more resilient solution. The method extends the former ICP method for known association [131], by the integration of an algorithm that solves the association problem through the computation of  $p(\boldsymbol{\alpha}_t | \mathbf{z}_{1:t})$ . Note that, differently from [131], here the pdf (4.8) is not Gaussian due to the association ambiguity. For this reason, we design the ICP-DA method leveraging on a PF-based approach.

## 4.4 Distributed ICP-DA method

In this section we present the distributed implementation of the ICP-DA method that allows the estimate of marginal pdfs based on belief propagation. The computation of  $p(\boldsymbol{\theta}_t, \boldsymbol{\alpha}_t | \mathbf{z}_{1:t})$  in (4.8) is performed after factorizing  $p(\boldsymbol{\theta}_{1:t}, \boldsymbol{\alpha}_{1:t} | \mathbf{z}_{1:t})$  over vehicles and performing a sequential approximate marginalization by running BPA over the related FG [81]. In the following, we first derive the factorization

(Sec. 4.4.1) and then the distributed ICP-DA method based on BPA and consensus algorithms (Sec. 4.4.2). Finally, a PF-based implementation of the ICP-DA method is discussed (Sec. 4.4.3) together with a hard-decision low-complexity (LC) algorithm (Sec. 4.4.4).

#### 4.4.1 Factorization of the joint posterior pdf

Following [93], besides the *feature-oriented* (F $\rightarrow$ O) association variable  $\alpha_{i,k,t}$ , we introduce the *observation-oriented* (O $\rightarrow$ F) association variable  $\beta_{i,\ell,t}$  defined as:  $\beta_{i,\ell,t} = k$ , if at time  $t$  the measurement  $\ell$  at vehicle  $i$  is generated by feature  $k \in \mathcal{F}_{i,t}$ ,  $\beta_{i,\ell,t} = 0$ , if the measurement  $\ell$  is not related to any feature. Despite the fact that clutter measurements are not present in the considered scenario, the case  $\beta_{i,\ell,t} = 0$  is introduced to exclude ambiguous measurements and reduce errors during the detection process as it will be detailed in the performance analysis. Though this formulation is redundant - as  $\beta_{i,\ell,t}$  can be derived from  $\alpha_{i,k,t}$  and vice-versa - the use of  $\alpha_{i,k,t}$  alongside with  $\beta_{i,\ell,t}$  allows to efficiently enforce the constraint that at any time  $t$  each feature  $k$  can generate at most one measurement  $\ell$  at vehicle  $i$  and vice-versa (i.e., a one-to-one F-O mapping). This is enabled by introducing the exclusion-enforcing function

$$\Psi(\alpha_{i,k,t}, \beta_{i,\ell,t}) = \begin{cases} 0, & \text{if } (\alpha_{i,k,t} = \ell \wedge \beta_{i,\ell,t} \neq k) \vee (\alpha_{i,k,t} \neq \ell \wedge \beta_{i,\ell,t} = k), \\ 1, & \text{otherwise,} \end{cases} \quad (4.9)$$

which is null for any inconsistent F-O pairing.

By defining the  $O_{i,t} \times 1$  vector  $\beta_{i,t} = [\beta_{i,\ell,t}]_{\ell \in \mathcal{O}_{i,t}}$  and the  $O \times 1$  vector  $\beta_t = [\beta_{i,t}]_{i \in \mathcal{V}}$  collect all the O $\rightarrow$ F associations for, respectively, vehicle  $i$  and all vehicles, the joint posterior pdf of the association and the vehicle-feature states  $p(\theta_{1:t}, \alpha_{1:t} | \mathbf{z}_{1:t})$  is rewritten as:

$$p(\theta_{1:t}, \alpha_{1:t}, \beta_{1:t} | \mathbf{z}_{1:t}) \propto p(\mathbf{z}_{1:t} | \theta_{1:t}, \alpha_{1:t}, \beta_{1:t}) p(\theta_{1:t}, \alpha_{1:t}, \beta_{1:t}). \quad (4.10)$$

where the likelihood function is  $p(\mathbf{z}_{1:t} | \theta_{1:t}, \alpha_{1:t}, \beta_{1:t}) = p(\mathbf{z}_{1:t} | \mathbf{x}_{1:t}^{(V)}) p(\mathbf{z}_{1:t}^{(V2F)} | \theta_{1:t}, \alpha_{1:t})$  under the hypothesis of conditionally independent measurements (4.4)-(4.5). Assuming also the measurements as independent over time and vehicles, and the V2F observations as independent over features, the likelihood factorizes as:

$$p(\mathbf{z}_{1:t} | \theta_{1:t}, \alpha_{1:t}) = \prod_{t'=1}^t \prod_{i=1}^{N_v} p(\mathbf{z}_{i,t'}^{(V)} | \mathbf{x}_{i,t'}^{(V)}) \prod_{k=1}^{N_f} p(\mathbf{z}_{i,t'}^{(V2F)} | \mathbf{x}_{i,t'}^{(V)}, \mathbf{x}_{k,t'}^{(F)}, \alpha_{i,k,t'}). \quad (4.11)$$

Moreover, assuming the observation-feature association as independent over time and from vehicle/feature states, the prior pdf in (4.10) simplifies to  $p(\theta_{1:t}, \alpha_{1:t}, \beta_{1:t}) = p(\alpha_{1:t}, \beta_{1:t}) p(\theta_{1:t})$  with, according to (4.9),

$$p(\alpha_{1:t}, \beta_{1:t}) \propto \prod_{t'=1}^t \prod_{i=1}^{N_v} \prod_{k=1}^{N_f} \prod_{\ell=1}^{O_{i,t'}} \Psi(\alpha_{i,k,t'}, \beta_{i,\ell,t'}). \quad (4.12)$$

Recalling that vehicle and feature states evolve independently according to Markovian dynamic models (4.1) and (4.3), the prior pdf of the overall vehicle/feature

states factorizes as:

$$p(\boldsymbol{\theta}_{1:t}) = \left( \prod_{i=1}^{N_v} p(\mathbf{x}_{i,0}^{(V)}) \prod_{t'=1}^t p(\mathbf{x}_{i,t'}^{(V)} | \mathbf{x}_{i,t'-1}^{(V)}) \right) \times \left( \prod_{k=1}^{N_f} p(\mathbf{x}_{k,0}^{(F)}) \prod_{t''=1}^t p(\mathbf{x}_{k,t''}^{(F)} | \mathbf{x}_{k,t''-1}^{(F)}) \right), \quad (4.13)$$

where  $p(\mathbf{x}_{i,0}^{(V)})$  and  $p(\mathbf{x}_{k,0}^{(F)})$  denote the prior pdfs at time  $t = 0$ .

Considering (4.11), (4.12) and (4.13), it is possible to derive the factorization of the joint posterior pdf (4.10) as:

$$p(\boldsymbol{\theta}_{1:t}, \boldsymbol{\alpha}_{1:t}, \boldsymbol{\beta}_{1:t} | \mathbf{z}_{1:t}) \propto \left( \prod_{i=1}^{N_v} p(\mathbf{x}_{i,0}^{(V)}) \prod_{t'=1}^t p(\mathbf{x}_{i,t'}^{(V)} | \mathbf{x}_{i,t'-1}^{(V)}) p(\mathbf{z}_{i,t'}^{(V)} | \mathbf{x}_{i,t'}^{(V)}) \right) \quad (4.14)$$

$$\times \prod_{k=1}^{N_f} p(\mathbf{z}_{i,t'}^{(V2F)} | \mathbf{x}_{i,t'}^{(V)}, \mathbf{x}_{k,t'}^{(F)}, \boldsymbol{\alpha}_{i,k,t'}) \prod_{\ell=1}^{O_{i,t'}} \Psi(\boldsymbol{\alpha}_{i,k,t'}, \boldsymbol{\beta}_{i,\ell,t'}) \times \left( \prod_{k=1}^{N_f} p(\mathbf{x}_{k,0}^{(F)}) \prod_{t''=1}^t p(\mathbf{x}_{k,t''}^{(F)} | \mathbf{x}_{k,t''-1}^{(F)}) \right), \quad (4.15)$$

where the V2F likelihood  $p(\mathbf{z}_{i,t}^{(V2F)} | \mathbf{x}_{i,t}^{(V)}, \mathbf{x}_{k,t}^{(F)}, \boldsymbol{\alpha}_{i,k,t})$  is:

$$p(\mathbf{z}_{i,t}^{(V2F)} | \mathbf{x}_{i,t}^{(V)}, \mathbf{x}_{k,t}^{(F)}, \boldsymbol{\alpha}_{i,k,t}) = \begin{cases} p(\mathbf{z}_{i,\ell,t}^{(V2F)} | \mathbf{x}_{i,t}^{(V)}, \mathbf{x}_{k,t}^{(F)}), & \text{if } \boldsymbol{\alpha}_{i,k,t} = \ell \in \mathcal{O}_{i,t}, \\ 1, & \text{if } \boldsymbol{\alpha}_{i,k,t} = 0, \end{cases} \quad (4.16)$$

where  $p(\mathbf{z}_{i,\ell,t}^{(V2F)} | \mathbf{x}_{i,t}^{(V)}, \mathbf{x}_{k,t}^{(F)})$  is Gaussian with mean  $\mathbf{x}_{k,t}^{(F)} - \mathbf{x}_{i,t}^{(V)}$  and covariance  $\mathbf{R}_{i,\ell,t}^{(V2F)}$ , while  $p(\mathbf{z}_{i,t}^{(V2F)} | \mathbf{x}_{i,t}^{(V)}, \mathbf{x}_{k,t}^{(F)}, \boldsymbol{\alpha}_{i,k,t} = 0)$  is set to 1 to guarantee the coherency of factorization in the case of undefined V2F measurement  $\mathbf{z}_{i,\ell=0,t}^{(V2F)}$ . Furthermore,  $p(\mathbf{x}_{i,0}^{(V)})$  and  $p(\mathbf{x}_{k,0}^{(F)})$  denote the prior pdfs at time  $t = 0$ , while  $p(\mathbf{z}_{i,t}^{(V)} | \mathbf{x}_{i,t}^{(V)})$  stands for the GPS likelihood. This factorization enables the joint association and localization problem to be solved locally at vehicles in a distributed manner, as discussed in the following section.

#### 4.4.2 Belief propagation algorithm for data association and localization

The ICP-DA problem is solved by running a loopy BP Algorithm (BPA) [93, 133] on the factor graph (FG) in Fig. 4.4 describing the factorization of (4.15) at time  $t$ . For visualization purposes, the DA part in Fig. 4.4 is highlighted in a green box and it is expanded in Fig. 4.5. According to [138] and FG principles described in Sec. 2.3.4, vehicle/feature state variables and association variables are indicated with circles, while squares stands for the factors. Being the presence of cycles, the BPA is iterative and consists of the cascade of two BPAs. The first one is a BPA for data association (BPA-DA). It approximates through the iterations  $\mathbf{p} = 1, \dots, P$  the marginal posterior pdf of the association variable by the belief  $b_{i,k,t}^{(\mathbf{p})}(\boldsymbol{\alpha}_{i,k,t}) \approx p^{(\mathbf{p})}(\boldsymbol{\alpha}_{i,k,t} | \mathbf{z}_{i,t})$ . This iterative algorithm operates on the FG in Fig.

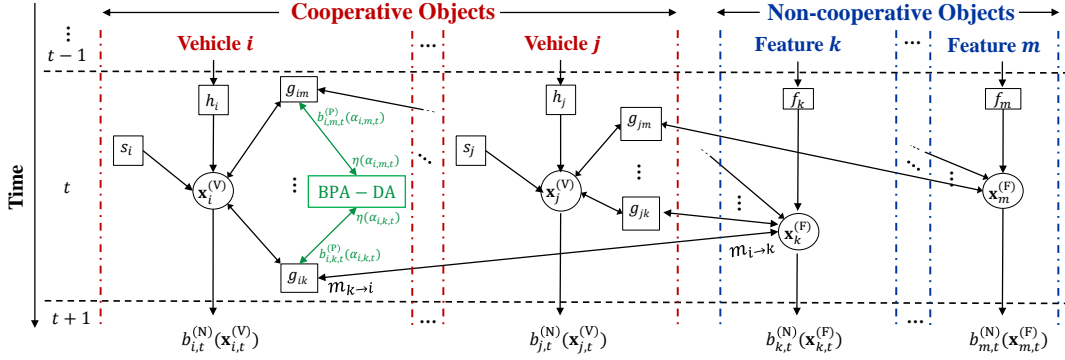


**Figure 4.4:** Factorization of  $p(\boldsymbol{\theta}_t, \boldsymbol{\alpha}_t, \boldsymbol{\beta}_t | \mathbf{z}_{1:t})$ . Shortcuts  $h_i = p(\mathbf{x}_{i,t}^{(V)} | \mathbf{x}_{i,t-1}^{(V)})$ ,  $s_i = p(\mathbf{z}_{i,t}^{(V)} | \mathbf{x}_{i,t}^{(V)})$ ,  $f_k = p(\mathbf{x}_{k,t}^{(F)} | \mathbf{x}_{k,t-1}^{(F)})$ ,  $g_{ik} = p(\mathbf{z}_{i,k,t}^{(V2F)} | \mathbf{x}_{i,t}^{(V)}, \mathbf{x}_{k,t}^{(F)})$  are used.

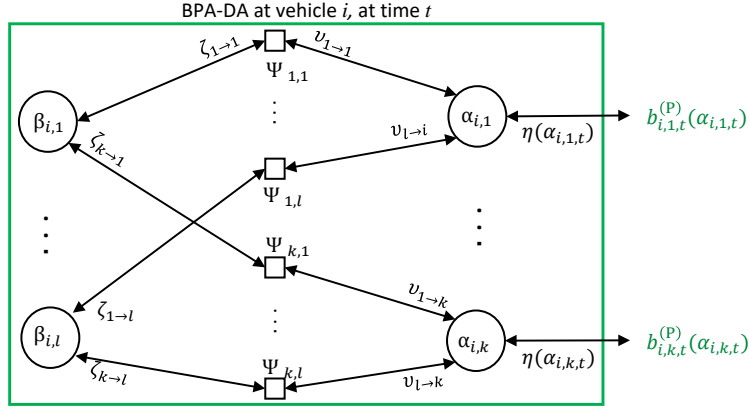


**Figure 4.5:** Factor graph of the BPA-DA. Shortcuts  $\nu_{\ell \rightarrow k} = m_{\ell \rightarrow k}^{(p)}(\alpha_{i,k,t})$ ,  $\zeta_{k \rightarrow \ell} = m_{k \rightarrow \ell}^{(p)}(\beta_{i,\ell,t})$ ,  $\Psi_{k,\ell} = \Psi(\alpha_{i,k,t}, \beta_{i,\ell,t})$  are used.

4.5 and it is implemented following the approach in [93]. The second BPA, instead, aims at estimating the vehicle/feature states. For this reason, we refer to it as BPA for localization (BPA-L). It takes the outputs of BPA-DA to perform the ICP localization and it computes over the iterations  $n = 1, \dots, N$  the beliefs of all the vehicles' and features' states:  $b_{i,t}^{(n)}(\mathbf{x}_{i,t}^{(V)}) \approx p^{(n)}(\mathbf{x}_{i,t}^{(V)} | \mathbf{z}_{1:t})$  and  $b_{k,t}^{(n)}(\mathbf{x}_{k,t}^{(F)}) \approx p^{(n)}(\mathbf{x}_{k,t}^{(F)} | \mathbf{z}_{1:t})$ , respectively. In the following, we detail the steps required to successfully perform the ICP-DA algorithm. We first provide a general formulation and then we specifically describe the PF-based version, which is extremely useful for handle non-Gaussian beliefs. We also describe the log-likelihood consensus algorithm for distributed evaluation of features' beliefs.

The ICP-DA algorithm is structured in such a way that following steps are executed:

### 1. Prediction

The beliefs of all vehicles' and features' states at iteration  $n = 0$  at time  $t$  are initialized using the final beliefs of previous time step ( $b_{i,t-1}^{(N)}(\mathbf{x}_{i,t-1}^{(V)})$  and

$b_{k,t-1}^{(N)}(\mathbf{x}_{k,t-1}^{(F)})$ , the state models in (4.1)-(4.3) and the current GPS data as:

$$b_{i,t}^{(0)}(\mathbf{x}_{i,t}^{(V)}) = p(\mathbf{z}_{i,t}^{(V)} | \mathbf{x}_{i,t}^{(V)}) \int p(\mathbf{x}_{i,t}^{(V)} | \mathbf{x}_{i,t-1}^{(V)}) b_{i,t-1}^{(n)}(\mathbf{x}_{i,t-1}^{(V)}) d\mathbf{x}_{i,t-1}^{(V)}, \quad (4.17)$$

$$b_{k,t}^{(0)}(\mathbf{x}_{k,t}^{(F)}) = \int p(\mathbf{x}_{k,t}^{(F)} | \mathbf{x}_{k,t-1}^{(F)}) b_{k,t-1}^{(n)}(\mathbf{x}_{k,t-1}^{(F)}) d\mathbf{x}_{k,t-1}^{(F)}, \quad (4.18)$$

where the motion transition pdfs are  $p(\mathbf{x}_{i,t}^{(V)} | \mathbf{x}_{i,t-1}^{(V)}) = \mathcal{N}(\mathbf{x}_{i,t}^{(V)} + \mathbf{B}\mathbf{a}_{i,t-1}^{(V)}, \mathbf{Q}_{i,t-1}^{(V)})$  and  $p(\mathbf{x}_{k,t}^{(F)} | \mathbf{x}_{k,t-1}^{(F)}) = \mathcal{N}(\mathbf{x}_{k,t}^{(F)}, \mathbf{Q}_{k,t-1}^{(F)})$ , and  $p(\mathbf{z}_{i,t}^{(V)} | \mathbf{x}_{i,t}^{(V)}) = \mathcal{N}(\mathbf{x}_{i,t}^{(V)}, \mathbf{R}_{i,t}^{(V)})$  is the likelihood of the GPS measurement from (4.4).

#### 2. V2F measurement evaluation for association.

Each vehicle  $i$  evaluates each O→F association by integrating the V2F measurement likelihood over all possible feature locations, and weighting with the prior beliefs (4.17)-(4.18):

$$\eta(\alpha_{i,k,t}) = p(\mathbf{z}_{i,t}^{(V2F)} | \alpha_{i,k,t}) = \iint p(\mathbf{z}_{i,t}^{(V2F)} | \mathbf{x}_{i,t}^{(V)}, \mathbf{x}_{k,t}^{(F)}, \alpha_{i,k,t}) b_{i,t}^{(0)}(\mathbf{x}_{i,t}^{(V)}) b_{k,t}^{(0)}(\mathbf{x}_{k,t}^{(F)}) d\mathbf{x}_{i,t}^{(V)} d\mathbf{x}_{k,t}^{(F)}. \quad (4.19)$$

where  $p(\mathbf{z}_{i,t}^{(V2F)} | \mathbf{x}_{i,t}^{(V)}, \mathbf{x}_{k,t}^{(F)}, \alpha_{i,k,t}) = \mathcal{N}(\mathbf{x}_{k,t}^{(F)} - \mathbf{x}_{i,t}^{(V)}, \mathbf{R}_{i,\alpha_{i,k,t},t}^{(V2F)})$ , see (4.16).

#### 3. BPA-DA for measurement-feature association.

Following [93], in this step each vehicle  $i$  computes the association beliefs  $b_{i,k,t}^{(p)}(\alpha_{i,k,t})$  by a repeated exchange of messages from the F→O association variable  $\alpha_{i,k,t}$  to the O→F association variable  $\beta_{i,\ell,t}$  and vice-versa, so as to exclude inconsistent pairings (e.g., the same measurement associated to two different features) and restrict the belief evaluation to one-to-one associations. The message from  $\alpha_{i,k,t}$  to  $\beta_{i,\ell,t}$  is initialized at BPA-DA iteration  $p = 0$  as:

$$m_{k \rightarrow \ell}^{(0)}(\beta_{i,\ell,t}) = \sum_{\alpha_{i,k,t}=0}^{O_{i,t}} \eta(\alpha_{i,k,t}) \Psi(\alpha_{i,k,t}, \beta_{i,\ell,t}), \quad (4.20)$$

while at subsequent iterations,  $p = 1, 2, \dots$ , the messages are updated as follows:

$$m_{\ell \rightarrow k}^{(p)}(\alpha_{i,k,t}) = \sum_{\beta_{i,\ell,t}=1}^{|\mathcal{F}_{i,t}|} \Psi(\alpha_{i,k,t}, \beta_{i,\ell,t}) \prod_{k' \in \mathcal{F} \setminus \{k\}} m_{k' \rightarrow \ell}^{(p-1)}(\beta_{i,\ell,t}), \quad (4.21)$$

$$m_{k \rightarrow \ell}^{(p)}(\beta_{i,\ell,t}) = \sum_{\alpha_{i,k,t}=0}^{O_{i,t}} \eta(\alpha_{i,k,t}) \Psi(\alpha_{i,k,t}, \beta_{i,\ell,t}) \prod_{\ell' \in \mathcal{O}_{i,t} \setminus \{\ell\}} m_{\ell' \rightarrow k}^{(p)}(\alpha_{i,k,t}). \quad (4.22)$$

At the last iteration,  $p = P$ , the belief of the association variable  $\alpha_{i,k,t}$  is obtained as:

$$b_{i,k,t}^{(P)}(\alpha_{i,k,t}) = \prod_{\ell \in \mathcal{O}_{i,t}} m_{\ell \rightarrow k}^{(P)}(\alpha_{i,k,t}). \quad (4.23)$$

#### 4. V2F measurement evaluation for localization.

The association beliefs (4.23) (output of BPA-DA) are here used by each

vehicle to compute the V2F likelihood as:

$$p(\mathbf{z}_{i,t}^{(\text{V2F})} | \mathbf{x}_{i,t}^{(\text{V})}, \mathbf{x}_{k,t}^{(\text{F})}) = \sum_{\alpha_{i,k,t}=0}^{Q_{i,t}} p(\mathbf{z}_{i,t}^{(\text{V2F})} | \mathbf{x}_{i,t}^{(\text{V})}, \mathbf{x}_{k,t}^{(\text{F})}, \alpha_{i,k,t}) b_{i,k,t}^{(\text{P})}(\alpha_{i,k,t}), \quad (4.24)$$

which are fundamental for the ICP localization in the next step.

##### 5. BPA-L for localization.

The BPA algorithm for vehicle/feature localization approximates the posterior pdf of vehicles' and features' states over the iterations  $n$  by the beliefs  $b_{i,t}^{(n)}(\mathbf{x}_{i,t}^{(\text{V})})$ ,  $\forall i$ , and  $b_{k,t}^{(n)}(\mathbf{x}_{k,t}^{(\text{F})})$ ,  $\forall k$ . The procedure starts from the vehicle/feature beliefs obtained at step  $n - 1$ . In order to evaluate a belief for the  $k$ th feature  $\mathbf{x}_{k,t}^{(\text{F})}$ , vehicle  $i$  combines the belief of its own state  $\mathbf{x}_{i,t}^{(\text{V})}$  from step  $n - 1$  with the V2F likelihood  $p(\mathbf{z}_{i,t}^{(\text{V2F})} | \mathbf{x}_{i,t}^{(\text{V})}, \mathbf{x}_{k,t}^{(\text{F})})$  in (4.24), leading to the definition of the following message from vehicle  $i$  to feature  $k$ :

$$m_{i \rightarrow k}^{(n)}(\mathbf{x}_{k,t}^{(\text{F})}) \propto \int \frac{b_{i,t}^{(n-1)}(\mathbf{x}_{i,t}^{(\text{V})})}{m_{k \rightarrow i}^{(n-1)}(\mathbf{x}_{i,t}^{(\text{V})})} p(\mathbf{z}_{i,t}^{(\text{V2F})} | \mathbf{x}_{i,t}^{(\text{V})}, \mathbf{x}_{k,t}^{(\text{F})}) d\mathbf{x}_{i,t}^{(\text{V})}. \quad (4.25)$$

All the messages received by feature  $k$  are then gathered to compute the refined belief as follows:

$$b_{k,t}^{(n)}(\mathbf{x}_{k,t}^{(\text{F})}) \propto b_{k,t}^{(0)}(\mathbf{x}_{k,t}^{(\text{F})}) \prod_{i \in \mathcal{V}_{k,t}} m_{i \rightarrow k}^{(n)}(\mathbf{x}_{k,t}^{(\text{F})}), \quad (4.26)$$

where  $\mathcal{V}_{k,t}$  is the set of vehicles that sense feature  $k$ . Note that if a feature  $\mathbf{x}_{k,t}^{(\text{F})}$  is not observed by any vehicle  $i \in \mathcal{V}$ , the related belief (4.26) is reset to a uniform distribution. Based on the updated feature's belief (4.26) and the V2F likelihood, vehicle  $i$  receives the following message from feature  $k$ :

$$m_{k \rightarrow i}^{(n)}(\mathbf{x}_{i,t}^{(\text{V})}) \propto \int \frac{b_{k,t}^{(n)}(\mathbf{x}_{k,t}^{(\text{F})})}{m_{i \rightarrow k}^{(n)}(\mathbf{x}_{k,t}^{(\text{F})})} p(\mathbf{z}_{i,t}^{(\text{V2F})} | \mathbf{x}_{i,t}^{(\text{V})}, \mathbf{x}_{k,t}^{(\text{F})}) d\mathbf{x}_{k,t}^{(\text{F})}. \quad (4.27)$$

Finally, vehicle  $i$  refines its own belief by combining the local information with all messages coming from the sensed features  $k \in \mathcal{F}_{i,t}$ :

$$b_{i,t}^{(n)}(\mathbf{x}_{i,t}^{(\text{V})}) \propto b_{i,t}^{(0)}(\mathbf{x}_{i,t}^{(\text{V})}) \prod_{k \in \mathcal{F}_{i,t}} m_{k \rightarrow i}^{(n)}(\mathbf{x}_{i,t}^{(\text{V})}). \quad (4.28)$$

The BPA-L steps (4.25)-(4.28) are repeated until convergence is reached.

In the above algorithm we treated the features as cooperative entities that are actively involved in the message passing procedure. However, being passive objects, features cannot compute their own belief in (4.26) nor communicate with vehicles. Following [131], this problem can be solved by using a consensus algorithm which enables vehicles to compute the feature belief in (4.26) in a distributed way by exchanging data through V2V links. More details are given in the following section where a PF-based implementation is discussed.

### 4.4.3 ICP-DA: particle filter implementation

The introduction of the non-Gaussian variables,  $\alpha_{i,k,t}$  and  $\beta_{i,\ell,t}$ , makes the use of Kalman filtering, as originally proposed in [131], suboptimal for the extension of ICP with data association. To deal with non-Gaussian statistics, we propose a PF-based ICP-DA algorithm (ICP-DA-PF) where each vehicle belief  $b_{i,t}^{(n)}(\mathbf{x}_{i,t}^{(V)})$  is described by the set of  $J_v$  particles and related weights,  $\{\mathbf{s}_{i,t}^{(v)}, \mathbf{w}_{i,t}^{(v)}\}_{v=1}^{J_v}$ ,  $\forall i \in \mathcal{V}$ . Similarly each feature belief  $b_{k,t}^{(n)}(\mathbf{x}_{k,t}^{(F)})$  is represented by the set of  $J_f$  particles with associated weights  $\{\mathbf{s}_{k,t}^{(f)}, \mathbf{w}_{k,t}^{(f)}\}_{f=1}^{J_f}$ ,  $\forall k \in \mathcal{F}$ . The iteration index  $n$  is dropped to simplify the notation. The computation of particles and weights is performed as described below.

Following the previously described BPA steps, vehicles' and features' beliefs (4.26)-(4.28) are initialized (*Step 1*) as:

$$b_{i,t}^{(0)}(\mathbf{x}_{i,t}^{(V)}) \approx \frac{1}{J_v} \sum_{v=1}^{J_v} p(\mathbf{z}_{i,t}^{(V)} | \mathbf{s}_{i,t}^{(v)}) \delta(\mathbf{x}_{i,t}^{(V)} - \mathbf{s}_{i,t}^{(v)}), \quad (4.29)$$

$$b_{k,t}^{(0)}(\mathbf{x}_{k,t}^{(F)}) \approx \frac{1}{J_f} \sum_{f=1}^{J_f} \delta(\mathbf{x}_{k,t}^{(F)} - \mathbf{s}_{k,t}^{(f)}), \quad (4.30)$$

with equal weights and particles distribution compliant with the prediction of the beliefs of previous time-instant according to the state models in (4.1)-(4.3). The GPS likelihood function is evaluated for each particle as  $p(\mathbf{z}_{i,t}^{(V)} | \mathbf{s}_{i,t}^{(v)}) = \mathcal{N}(\mathbf{s}_{i,t}^{(v)}, \mathbf{R}_{i,t}^{(V)})$  according to (4.4).

In *Step 2*, the likelihood function for association can be computed by inserting (4.29)-(4.30) in (4.19) as follows:

$$\eta(\alpha_{i,k,t}) \approx \frac{1}{J_v J_f} \sum_{v=1}^{J_v} \sum_{f=1}^{J_f} p(\mathbf{z}_{i,t}^{(V)} | \mathbf{s}_{i,t}^{(v)}) p(\mathbf{z}_{i,t}^{(V2F)} | \mathbf{s}_{i,t}^{(v)}, \mathbf{s}_{k,t}^{(f)}, \alpha_{i,k,t}), \quad (4.31)$$

where  $p(\mathbf{z}_{i,t}^{(V2F)} | \mathbf{s}_{i,t}^{(v)}, \mathbf{s}_{k,t}^{(f)}, \alpha_{i,k,t}) = \mathcal{N}(\mathbf{s}_{k,t}^{(f)} - \mathbf{s}_{i,t}^{(v)}, \mathbf{R}_{i,\alpha_{i,k,t},t}^{(V2F)})$ ,  $\forall \alpha_{i,k,t} \in \mathcal{O}_{i,t}$ , according to (4.5) and (4.16).

The BPA-DA procedure in *Step 3* does not involve particles and can thus be implemented by simply using (4.31) in the association equations (4.20)-(4.22).

The likelihood function for localization can now be computed (*Step 4*) using (4.24) for each pair of feature-vehicle particles.

The BPA-L procedure (*Step 5*) requires particle-based definition of messages as follows. The message  $m_{i \rightarrow k,t}(\mathbf{x}_{k,t}^{(F)})$  in (4.25) is represented by the set of particles and weights  $\{\mathbf{s}_{k,t}^{(f)}, \mathbf{w}_{h \rightarrow k,t}^{(f)}\}_{f=1}^{J_f}$ , with

$$\mathbf{w}_{h \rightarrow k,t}^{(f)} \propto \frac{1}{J_v} \sum_{v=1}^{J_v} p(\mathbf{z}_{i,t}^{(V)} | \mathbf{s}_{i,t}^{(v)}) \prod_{\substack{h \in \mathcal{F}_{i,t} \\ h \neq k}} w_{h \rightarrow i,t}^{(v)} p(\mathbf{z}_{i,t}^{(V2F)} | \mathbf{s}_{i,t}^{(v)}, \mathbf{s}_{h,t}^{(f)}). \quad (4.32)$$

The PF representation of the  $k$ th feature belief in (4.26) is:

$$b_{k,t}^{(n)}(\mathbf{x}_{k,t}^{(F)}) \propto \sum_{f=1}^{J_f} \frac{1}{J_f} \underbrace{\prod_{i \in \mathcal{V}_{k,t}} w_{h \rightarrow k,t}^{(f)}}_{\tilde{w}_{k,t}^{(f)}} \delta(\mathbf{x}_{k,t}^{(F)} - \mathbf{s}_{k,t}^{(f)}), \quad (4.33)$$

with  $\tilde{w}_{k,t}^{(f)}$  denoting the weight related to feature particle  $f$ , that has to be normalized as  $w_{k,t}^{(f)} = \frac{\tilde{w}_{k,t}^{(f)}}{\sum_{f=1}^{J_f} \tilde{w}_{k,t}^{(f)}}$ . Similarly, the message from feature  $k$  to vehicle  $i$ ,  $m_{k \rightarrow i}^{(n)}(\mathbf{x}_{i,t}^{(V)})$ , is represented by the set  $\{\mathbf{s}_{i,t}^{(v)}, \mathbf{w}_{k \rightarrow i,t}^{(v)}\}_{v=1}^{J_v}$ , with weights computed according to (4.27) as:

$$w_{k \rightarrow i,t}^{(v)} \propto \frac{1}{J_f} \sum_{f=1}^{J_f} \prod_{\substack{j \in \mathcal{V}_{k,t} \\ j \neq i}} w_{j \rightarrow k,t}^{(f)} p(\mathbf{z}_{i,t}^{(V2F)} | \mathbf{s}_{j,t}^{(v)}, \mathbf{s}_{k,t}^{(f)}). \quad (4.34)$$

The PF representation of the  $i$ th vehicle belief is then given by:

$$b_{i,t}^{(n)}(\mathbf{x}_{i,t}^{(V)}) \propto \sum_{v=1}^{J_v} \frac{1}{J_v} p(\mathbf{z}_{i,t}^{(V)} | \mathbf{s}_{i,t}^{(v)}) \underbrace{\prod_{k \in \mathcal{F}_{i,t}} w_{k \rightarrow i,t}^{(v)}}_{\tilde{w}_{i,t}^{(v)}} \delta(\mathbf{x}_{i,t}^{(V)} - \mathbf{s}_{i,t}^{(v)}), \quad (4.35)$$

where  $\tilde{w}_{i,t}^{(v)}$  is the non-normalized weight, related to vehicle particle  $\mathbf{s}_{i,t}^{(v)}$ , to be normalized as  $w_{i,t}^{(v)} = \frac{\tilde{w}_{i,t}^{(v)}}{\sum_{v=1}^{J_v} \tilde{w}_{i,t}^{(v)}}$ . All vehicle and feature particles finally undergo importance resampling so as to avoid the particle degeneracy [139]. Note that identical sets of particles are assumed to be sampled at all vehicles for feature  $k$  and at all features for vehicle  $i$  to enable message fusion as in in (4.33)-(4.35), i.e. the set  $\{\mathbf{s}_{k,t}^{(f)}\}_{f=1}^{J_f}$  is the same for all vehicles  $i \in \mathcal{V}$  and  $\{\mathbf{s}_{i,t}^{(v)}\}_{v=1}^{J_v}$  is the same for all features  $k \in \mathcal{F}$ . This requires local random number generators to be synchronized at all vehicles. At convergence, the estimates of the feature/vehicle states are obtained according to the MMSE criterion, respectively as:

$$\hat{\mathbf{x}}_{k,t}^{(F)} = \sum_{f=1}^{J_f} w_{k,t}^{(f)} \mathbf{s}_{k,t}^{(f)}, \quad \forall k, \quad (4.36)$$

$$\hat{\mathbf{x}}_{i,t}^{(V)} = \sum_{v=1}^{J_v} w_{i,t}^{(v)} \mathbf{s}_{i,t}^{(v)}, \quad \forall i. \quad (4.37)$$

The ICP-DA-PF method requires the computation of the belief (4.33) at each feature  $k$ , which is however unfeasible since features are not actively involved in the localization process. We thus propose this belief to be evaluated cooperatively by the vehicles by a consensus-based algorithm that enables the distributed computation of the features' weights  $w_{k,t}^{(f)}$ ,  $\forall f \in J_f, \forall k \in \mathcal{F}$ . By defining the product of messages over the vehicles sensing the same feature  $k$  in (4.28) as:

$$\mathbf{q}_{k,t}^{(f)} = \prod_{i \in \mathcal{V}_{k,t}} w_{h \rightarrow k,t}^{(f)}, \quad \forall f = 1, \dots, J_f, \quad (4.38)$$

and taking the logarithm  $L(\mathbf{q}_{k,t}^{(f)}) = \log(\mathbf{q}_{k,t}^{(f)})$ , we get:

$$L(\mathbf{q}_{k,t}^{(f)}) = \sum_{i \in \mathcal{V}_{k,t}} \log(\mathbf{w}_{h \rightarrow k,t}^{(f)}) = \frac{1}{|\mathcal{V}_{k,t}|} \sum_{i=1}^{|\mathcal{V}_{k,t}|} \log(\mathbf{w}_{h \rightarrow k,t}^{(f)}), \quad (4.39)$$

which is an arithmetic average that can be evaluated in a distributed manner by vehicles through average consensus [134]. We thus propose the distributed computation of the feature weights by successive refinements of local weights at vehicles based on information exchange with neighbors. Once a consensus is reached by all vehicles on the  $L(\mathbf{q}_{k,t}^{(f)})$ , the weight in (4.33) is obtained as  $\mathbf{q}_{k,t}^{(f)} = \exp(L(\mathbf{q}_{k,t}^{(f)}))$  and is used for the evaluation of the feature belief. It may occur, on the other hand, that the number of average-consensus operations to reach a unique convergence is high, thus not guaranteeing a practical feasibility. To cope with the unavoidable effect of real-life constraint, a max-consensus algorithm to be performed after the exceeding of a fixed pre-established threshold (e.g., given by latency constraints) on the number of iterations is suggested as to obtain the same feature weights at each vehicle.

#### 4.4.4 ICP-DA: low-complexity implementation

The PF-based method presented in the previous section represents an optimal approach for solving the non-Gaussian ICP-DA estimation problem. However, as the BPA-DA quadratically scales with the number of features [83], the computational complexity at single vehicle  $i$  for each BPA-DA iteration scales as  $\mathcal{O}(J_v J_f N_f^2)$ . Note that the evaluation of the complexity is done considering all-to-all V2V and V2F connectivity (i.e.,  $|\mathcal{O}_{i,t}| = N_f$ ,  $|\mathcal{J}_{i,t}| = N_v$ ) and assuming  $J_v \gg N_v$  and  $J_f \gg N_f$ .

To reduce the computational burden, in this section we propose a suboptimal low-complexity (LC) implementation of the ICP-DA method (ICP-DA-LC), in which a hard decision is made on the association variable at the end of BPA-DA, so as to approximate the features' beliefs with Gaussian pdfs and implement the BPA-L in a Gaussian fashion where only the first two moments of the vehicle/feature beliefs are needed. In the proposed method, each vehicle performs a Bayesian detection to decide if it has sensed a feature  $k \in \mathcal{F}_{i,t}$ , by comparing the belief of the association variable to any of its measurements with a threshold  $\Gamma_{\text{TH}}$ . If  $b_{i,k,t}^{(P)}(\alpha_{i,k,t} = 0) < \Gamma_{\text{TH}}$ , the feature  $k$  is detected and paired with the most probable measurement:

$$\hat{\alpha}_{i,k,t} = \arg \max_{\ell \in \mathcal{O}_{i,t}} b_{i,k,t}^{(P)}(\alpha_{i,k,t}). \quad (4.40)$$

With the above MAP decision the V2F likelihood in (4.24) is substituted by:

$$p(\mathbf{z}_{i,t}^{(\text{V2F})} | \mathbf{x}_{i,t}^{(\text{V})}, \mathbf{x}_{k,t}^{(\text{F})}) = p(\mathbf{z}_{i,t}^{(\text{V2F})} | \mathbf{x}_{i,t}^{(\text{V})}, \mathbf{x}_{k,t}^{(\text{F})}, \hat{\alpha}_{i,k,t}). \quad (4.41)$$

The ICP-DA-LC solution still has a computational complexity that quadratically scales with the number of features, but it avoids the intensive computations of the huge number of particles that is required in dynamic vehicular scenarios to sample both feature and vehicle beliefs.

**Table 4.2:** Order of magnitude of BPA-DA computational complexity at each vehicle per each time step  $t$ .

	ICP (known DA)	ICP-DA-PF	ICP-DA-L
BPA-DA	–	$\mathcal{O}(J_v J_f N_f^2)$	$\mathcal{O}(N_f^2)$
BPA-L	$\mathcal{O}(N_{\text{BPA-L}} N_{\text{cons}} N_v N_f)$	$\mathcal{O}(N_{\text{BPA-L}} N_{\text{cons}} N_v J_v J_f N_f)$	$\mathcal{O}(N_{\text{BPA-L}} N_{\text{cons}} N_v N_f)$

#### 4.4.5 Implementation aspects

The ICP-DA algorithm presented in this section has a computational complexity per each vehicle that scales as follows. A distinction between the two BPAs is provided as to discriminate the individual complexities. The computational burden of BPA-L linearly scales with the number of features  $N_f$  and (neighboring) vehicles  $N_v$ , as well as it linearly depends on the number of iterations the localization ( $N_{\text{BPA-L}}$ ) and consensus ( $N_{\text{cons}}$ ) tasks have to be performed, leading to a complexity order of  $\mathcal{O}(N_{\text{BPA-L}} N_{\text{cons}} N_v N_f)$ . The latter value further increases in case of particle representation of vehicle/feature pdfs, as the number of particles strongly increases the number of required operations as  $\mathcal{O}(N_{\text{BPA-L}} N_{\text{cons}} N_v J_v J_f N_f)$ . On the other hand, the BPA-DA complexity quadratically scales with the number of features, i.e.,  $\mathcal{O}(N_f^2)$ , a value that is linearly increased by the number of vehicle and feature particles.

A comparison of computational complexity of the ICP-DA methods (for both particle-based implementation and the low-complexity one) and the ICP without DA is summarized in Table 4.2. As it can be easily inferred from the table, the dominant term of ICP-DA-PF complexity is represented by the number of particles used to sample the vehicle/feature beliefs. Note also that, while in the ICP-DA-PF implementation both the average consensus and the max-consensus algorithms are computed for each particle of the feature belief, by considering the ICP-DA-LC solution only the average consensus on the first two moments of  $b_{k,t}^{(n)}(\mathbf{x}_{k,t}^{(F)})$  is required [131]. Based on this, the ICP-DA-LC can provide high benefits in term of computational complexity and communication overhead, which would make it recommended for practical implementations.

### 4.5 Performance assessment in specific road configurations

---

In this section, we analyze the performance of the proposed cooperative positioning method in simulated road scenarios, to highlight the benefits provided by the ICP-DA approach with respect to GPS-based tracking. The first scenario (Sec. 4.5.1) is a single straight road (Sec. 4.5.1), in which we compare the two different implementations of the ICP-DA method, i.e. PF and LC, in a controlled environment with two features, to highlight the impact of feature spacing on the association process. The straight road use case is also used to analyze the effect of association error with respect to feature density. The second scenario (Sec. 4.5.2), instead, is a crossroad junction, a more complex environment with

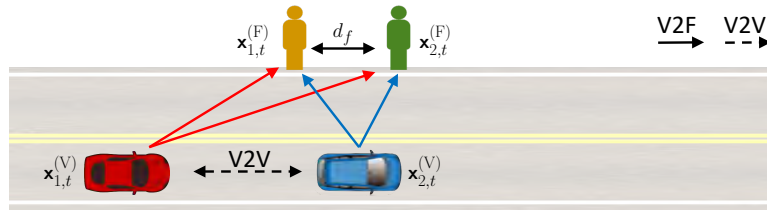
more vehicle interactions, in which we extend the analysis for varying number of features and degree of feature mobility. The GPS benchmark is implemented as a non-cooperative tracking filter (i.e., a KF) that uses model (4.1) for integrating the position-velocity estimate provided by the GPS receiver with the inertial sensor measurement at the single vehicle. The performance assessment is also targeted to evaluate the impact of DA uncertainty and the feature mobility on the vehicle localization accuracy.

### 4.5.1 Single-road scenario with static features

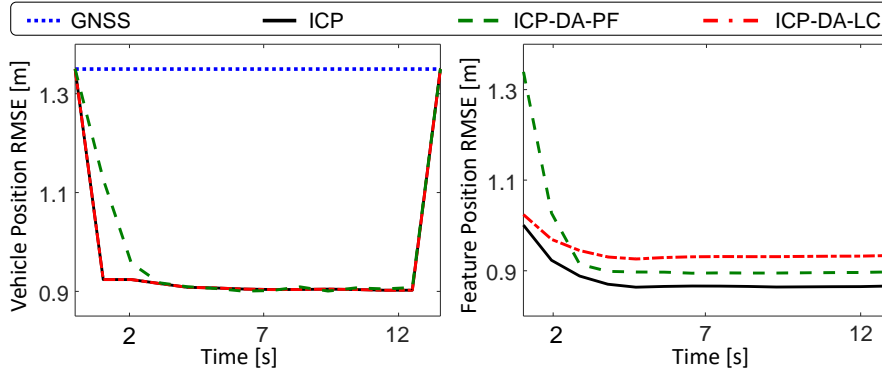
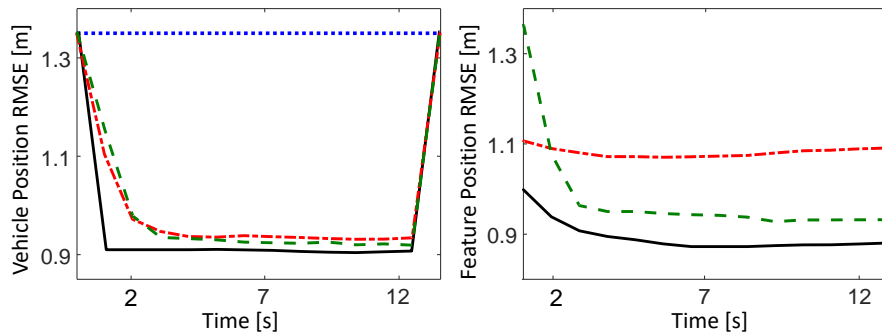
We consider two interconnected vehicles traveling in the same direction at an average speed of 25 km/h, with space headway of 5 m, on the straight road scenario in Fig. 4.6a. The vehicle motion is simulated according to the inertial sensor model in (4.1) with zero mean acceleration  $\mathbf{a}_{i,t-1}^{(V)}$  and sampling time  $T_s = 1$  s. The covariance of the Gaussian driving noise in (4.1) is  $\mathbf{Q}_{i,t-1}^{(V)} = \mathbf{B} \text{diag}(\sigma_{a_i,x}^{(V)^2}, \sigma_{a_i,y}^{(V)^2}) \mathbf{B}^T$ , where  $\sigma_{a_i,x}^{(V)}$  and  $\sigma_{a_i,y}^{(V)}$  represent the acceleration fluctuations along the vehicle longitudinal and transversal directions. They are set to  $\sigma_{a_i,x}^{(V)} = 0.2 \text{ m/s}^2$   $\sigma_{a_i,y}^{(V)} = 0.001 \text{ m/s}^2$ , respectively. The GPS accuracy on the whole area is set to  $\mathbf{R}_{i,t}^{(V)} = \text{blockdiag}(\sigma_p^{(V)^2} \mathbf{I}_2, \sigma_v^{(V)^2} \mathbf{I}_2)$  with standard deviations of  $\sigma_p^{(V)} = 8$  m and  $\sigma_v^{(V)} = 0.1$  m/s, respectively. Vehicles simultaneously sense  $N_f = 2$  static features placed along the sidewalk at a relative distance  $d_f$  with V2F measurement accuracies of  $\sigma_p^{(V2F)} = 0.2$  m for the position and  $\sigma_v^{(V2F)} = 0.1$  m/s for the velocity. The choice of these values matches the specifications of typical automotive sensors [140].

In this first result, the performance of the ICP-DA method is assessed using both the PF and LC implementations. A conventional (non-cooperative) Kalman filter over GPS measurements and ICP with known data association are simulated as well as benchmarks. For the ICP implementation, the stopping criterion of the iterative BPA-L procedure is obtained by comparing the MMSE location/velocity estimates (for both features and vehicles) with those obtained in the previous iteration. When the difference between the two consecutive estimates is below 10 cm for the position and below 0.1 m/s for the velocity, the iterations are stopped. For the ICP-DA-PF method, the vehicle/feature beliefs are approximated by using  $J_v = J_f = 5 \cdot 10^3$  particles. For ICP-DA-LC, the threshold on the association belief is set to  $\Gamma_{TH} = 1$ , meaning that all the V2F measurements are paired to the originating features. The performance is evaluated in terms of position/velocity accuracy computed according the Root Mean Square Error (RMSE) of the position/velocity estimate, by averaging over Monte Carlo simulations.

The performance of the localization methods are shown in Fig. 4.6 for feature spacing  $d_f = 0.5$  m (a) and  $d_f = 3$  m (b). For the ICP-DA-LC method, we measured a probability of correct measurement-feature association of, respectively, 54% and of 92% in the two cases. The results in Fig. 4.6a show that for  $d_f = 0.5$  m the ICP-DA-PF and ICP-DA-LC accuracies on vehicles reach the lower bound for known data association, as the errors due to wrong associations are compensated by the proximity of features. The worse performance of the ICP-DA-PF method in the first two seconds of V2F sensing is due to the limited number of particles which



(a) Simulated single road scenario


 (b)  $d_f = 0.5$  m

 (c)  $d_f = 3$  m

**Figure 4.6:** Vehicle and feature location accuracy versus time. a) single-road scenario with feature spacing  $d_f = 0.5$  m (b) and  $d_f = 3$  m (c). The ICP-DA-PF (orange line) and ICP-DA-LC (green line) methods are compared GPS-based KF approach (blue dotted line) and ICP with known association (black line).

affects the tracking capability in the transitory. For higher feature inter-distance as in Fig. 4.6b for  $d_f = 3$  m, the association errors decrease the positioning accuracy for both the ICP-DA-PF and ICP-DA-LC methods, with slightly better results for the PF implementation. The performance loss due to the wrong association is more evident on features than on vehicles, as inaccuracies on feature localization have minor impact when they are propagated back to vehicles. We also tested the performance for feature spacing up to  $d_f = 6$  m and we found that above this threshold the association is not critical anymore, as the ICP-DA methods reach the same performance of the ideal ICP with known association, with similar results as in Fig. 4.6a.

From the above results, we can conclude that DA is a crucial issue for cooperative positioning but, if features are close enough (i.e., with spacing comparable with

the vehicle localization accuracy) the effect on positioning is negligible. The same is observed for well separated features (i.e.,  $d_f = 6$  m in the considered setting) as data association can be easily solved in this case. For intermediate feature spacing (for  $d_f$  from 3 m to 6 m), a moderate performance loss is observed due to DA errors and PF slightly outperforms LC. Considering the computational complexity, that for ICP-DA-PF scales quadratically with the number of particles, the preferred solution is ICP-DA-LC which guarantees both high accuracy and efficiency.

Being the LC implementation more favorable, a more in depth analysis is provided in the following. In a similar straight road scenario, the ICP-DA-LC method is validated to assess the impact of DA error in a more complex scene. To this purpose, we consider the scenario in Fig. 4.7(top), where a convoy of  $N_v = 6$  vehicles, interconnected with V2V range  $R_c = 250$  m and traveling in open sky with average velocity 60 km/h and average inter vehicle distance of 20 m, enters a road section of length 200 m where the GPS accuracy suddenly degrades (e.g., a tunnel/canyon use case). GPS measurement are simulated with accuracies  $\sigma_p^{(V)} = 5$  m and  $\sigma_v^{(V)} = 0.1$  m/s outside the canyon, and  $\sigma_p^{(V)} = 17$  m and  $\sigma_v^{(V)} = 2.5$  m/s inside. A set of  $N_f = 200/\Delta$  static features is uniformly distributed over the canyon area, with spacing  $\Delta \in \{1, 1.5, 2, 4\}$  m. Vehicles sense these features with V2F range  $R_s = 50$  m and V2F accuracies  $\sigma_p^{(V2F)} = 0.1$  m and  $\sigma_v^{(V2F)} = 0.1$  m/s. In Fig. 4.7(bottom) the RMSE of the location estimate (averaged over vehicles) is plotted along the road for ICP-DA-LC, ICP with known DA [131] and GPS-based Kalman filtering. As the feature density increases, it can be seen that the probability of correct association,  $P_{CA}$ , decreases and the ICP-DA-LC performance degrades with respect to ICP, still maintaining a significant gain over GPS in the canyon. On the other hand, when the feature spacing is large enough compared to the location accuracy ( $\Delta > 1.5$  m), the association becomes highly reliable and the ICP-DA-LC closely approaches the ICP method with perfect association. After having analyzed the behavior of ICP-DA-LC method in straight road scenarios,

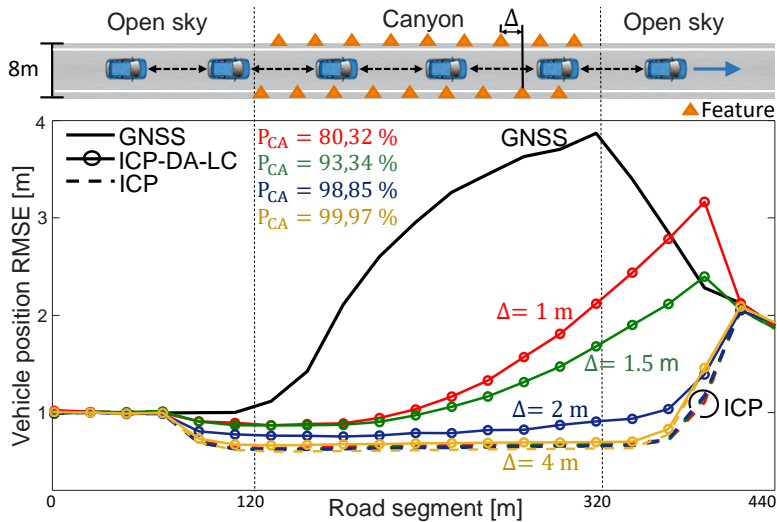


**Figure 4.7:** Vehicular C-ITS scenario (top). Vehicle position accuracy along the road for varying spacing  $\Delta$  between features (bottom).

we now move to consider a more complex intersection.

### 4.5.2 Crossroad scenario with dynamic features

We consider the crossroad scenario of Fig. 4.1, in which  $N_v = 12$  interconnected vehicles ( $R_c = 250$  m), grouped in four clusters of three vehicles each, are driving straight ahead along their respective lanes approaching a cross-junction. Spatial coordinates are referred to the center of the junction located in  $(0, 0)$ . The edges of the considered area are placed at 250 m in any direction from the center, thus each lane is 500 m long. The vehicle motion is simulated as in (4.1), with sampling time  $T_s = 1$  s and average velocity of 50 km/h along the motion direction. The driving process standard deviations for the longitudinal and lateral directions are set to  $\sigma_{a_i, \parallel}^{(V)} = 0.35$  m/s<sup>2</sup> and  $\sigma_{a_i, \perp}^{(V)} = 0.001$  m/s<sup>2</sup>, respectively. Then, the uncertainties along the axes  $x$  and  $y$  ( $\sigma_{a_i, x}^{(V)}$  and  $\sigma_{a_i, y}^{(V)}$ ) are defined according to the vehicle motion direction. The GPS provides measurements with the same accuracy over the whole area of, respectively,  $\sigma_p^{(V)} = 9$  m and  $\sigma_v^{(V)} = 0.25$  m/s, as to simulate a mid-urban environment.

The scenario also includes a set of  $N_f$  features, randomly deployed on the sidewalks, and sensed by vehicles in proximity ( $R_s = 75$  m). The feature's prior pdf is uniformly distributed within a circle of radius 150 m centered in  $(0, 0)$ . Feature motion is simulated as in (4.3), with initial velocity  $v_f$  and driving process covariance  $\mathbf{G}_{k,t}^{(F)} = \mathbf{G} \text{diag}(\sigma_{v_x}^{(F)^2}, \sigma_{v_y}^{(F)^2}) \mathbf{G}^T$ , with  $\mathbf{G} = [T_s \mathbf{I}_2 \ \mathbf{I}_2]^T$ . As for vehicles, a higher mobility is assumed along the road direction, i.e., the velocity standard deviation in the direction of sidewalk is  $\sigma_{v, \parallel}^{(F)} = \frac{v_f}{100}$  m/s, while in the orthogonal direction it is  $\sigma_{v, \perp}^{(F)} = 0.5 \sigma_{v, \parallel}^{(F)}$  m/s. Thus, depending on the driving direction of the feature, the velocity uncertainties along the axes  $x$  and  $y$ ,  $\sigma_{v, x}^{(F)}$  and  $\sigma_{v, y}^{(F)}$  respectively, are defined accordingly. The V2F covariance matrix is structured as  $\mathbf{R}_{i, \ell, t}^{(V2F)} = \text{blockdiag}(\sigma_p^{(V2F)^2} \mathbf{I}_2, \sigma_v^{(V2F)^2} \mathbf{I}_2)$ , with  $\sigma_p^{(V2F)} = 0.1$  m and  $\sigma_v^{(V2F)} = 0.1$  m/s for each vehicle.

We evaluate the RMSE positioning performance by averaging over 5000 Monte Carlo simulations. Fig. 4.8 shows the vehicle location accuracy in the proximity of the junction for  $N_f = \{3, 10, 20, 60\}$  static features. The GPS-based KF (blue dotted line) is plotted as a reference, while the ICP method with perfect association (continuous line) is the lower bound. The proposed ICP-DA-LC method is implemented in two different versions, using for feature detection in (4.40) the threshold  $\Gamma_{\text{TH}} = 0.5$  (i.e., discarding ambiguous V2F measurements) and  $\Gamma_{\text{TH}} = 1$  (i.e., using all V2F measurements). The results in Fig. 4.8 show a negligible performance loss of the proposed ICP-DA-LC method with respect to the ICP with perfect association. It can be noticed that a selection criteria is required when the number of features increase and they get closer, while for moderate feature densities ( $N_f \leq 20$ ) the ICP-DA-LC method without measurement selection does not have significant drawbacks. In fact, for  $N_f = 60$ , the vehicle location accuracy of the ICP-DA-LC with  $\Gamma_{\text{TH}} = 1$  is even worse than the reference GPS one, unless in close proximity of the junction, where all vehicles are connected each other and can sense a higher number of features thanks to the geometry of the selected cross

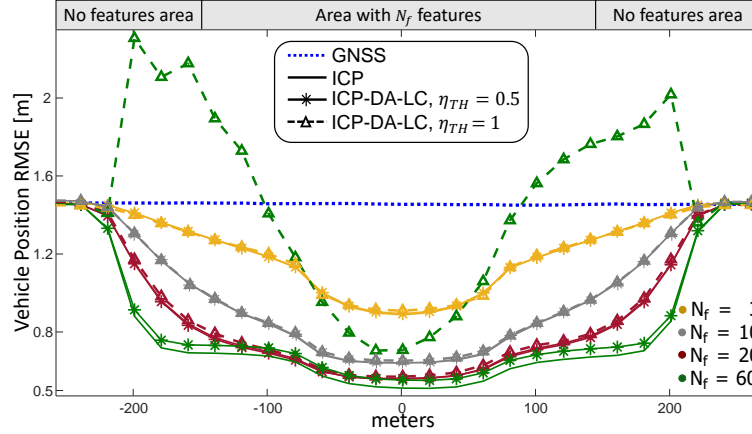


**Figure 4.8:** Vehicle position accuracy versus the distance to the center of the junction for the crossroad scenario in Fig. 1 with static features, for different number of features  $N_f$ . The ICP-DA-LC method (green marked line) is compared to the ICP with known association (red line) and to GPS-based KF tracking (blue dotted line).

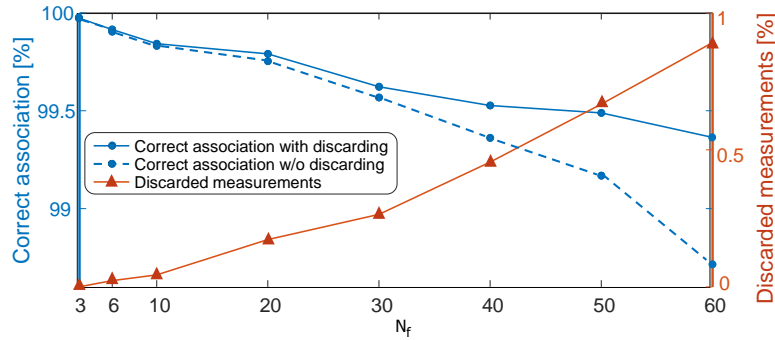


**Figure 4.9:** Percentages of association errors (blue line) and discarded measurements (orange line) versus the number of features  $N_f$ .

junction. For  $N_f = 60$ , the reduced spacing between features generates ambiguity problems in the association, as proved by the performance loss of ICP-DA-LC with  $\Gamma_{TH} = 1$  compared to ICP with perfect association. Increasing the number of features from  $N_f = 20$  to  $N_f = 60$  does not provide any benefit, as the performance is limited by the association errors.

The probability of correct association for the different values of  $N_f$ , together with the percentage of discarded measurements, is presented in Fig. 4.9. The figure shows a reduction on the probability of correct association as the number of features increases. This reduction is far more evident for the implementation which uses all measurements ( $\Gamma_{TH} = 1$ ) rather than for the ICP-DA-LC with association selection ( $\Gamma_{TH} = 0.5$ ). In this latter case the number of discarded measurements increases with  $N_f$  and contributes to a significant improvement of the probability of correct association as unreliable measurements (which are likely to be wrongly associated) are discarded.

The results in Fig. 4.8 and 4.9 indicate that a moderate number of features, i.e.  $N_f = 20$  corresponding approximately to an average of four features simultaneously sensed by each vehicle (this value is obtained considering the selected sensing

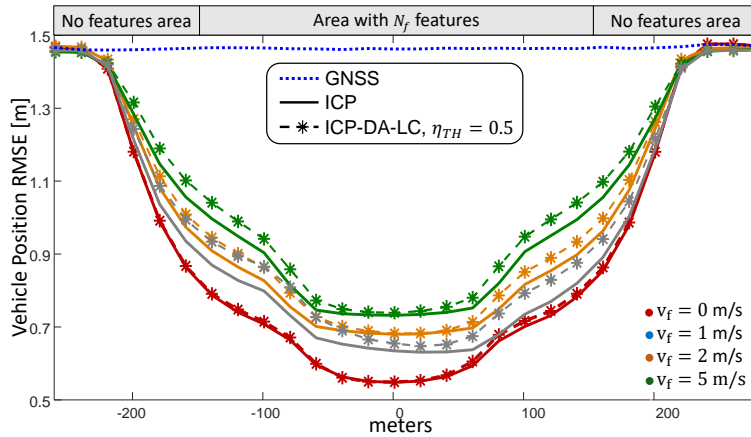


**Figure 4.10:** Vehicle position accuracy versus the distance to the center of the junction for the crossroad scenario in Fig. 1 with  $N_f = 20$  features, for different values of feature velocity  $v_f = \{1, 2, 5\}$  m/s.

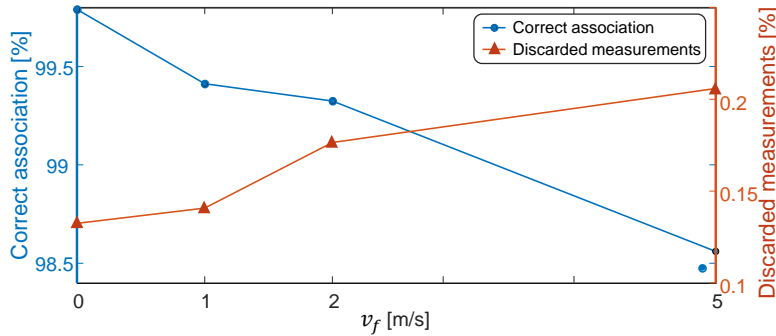


**Figure 4.11:** Percentages of correct association (blue line) and of discarded measurements (orange line) versus the number of feature's velocity  $v_f$ .

radius), is enough for the ICP-DA-LC method to significantly outperform the GPS-based localization. A higher number of features, on the other hand, does not provide any meaningful benefit, as it increases both the probability of erroneous association and the computational complexity. Moreover, the comparable performance obtained by ICP-DA-LC with measurement selection and ICP with known data association demonstrates that a low-complexity solution avoiding the computational overhead of PF is an efficient approach for vehicular environments.

Fig. 4.10 illustrates the impact of feature mobility on the ICP-DA performance in a scenario with  $N_f = 20$  features moving at an average velocity  $v_f = \{1, 2, 5\}$  m/s. The analysis shows that in case of highly dynamic scenarios (i.e., with feature mobility above the typical pedestrian velocity of 1.5 m/s) the positioning performance degrades but the ICP-DA-LC method with measurement selection is still able to significantly improve the conventional GPS solution. This conclusion is also confirmed by the analysis of the probability of correct association and measurement discarding in Fig. 4.11.

## 4.6 Performance assessment in a realistic urban scenario in Turin road network

In this section, we assess by simulation the performance of the ICP-DA method in realistic traffic conditions along an urban arterial in Turin, Italy. We focus on the ICP-DA-LC implementation with association selection (i.e., with  $\Gamma_{TH} = 0.5$ ), as this solution was shown to provide the best trade-off between performance and computational complexity in Sec. 4.5. This analysis aims at evaluating the impact on the proposed ICP-DA method of traffic control systems, which affect the vehicle distributions over the selected area. The degree of V2V connectivity (and the impact of cooperative sensing) is highly dependent on control strategies which determines the traffic flows and queues at nodes. For this reason, two different traffic conditions are analyzed, as will be detailed later on. Moreover, this analysis in a real urban environment is intended to show that ICP-DA can provide a sub-meter accuracy on vehicle positioning and, thus, it can enable advanced C-ITS services for high levels of automated driving.

### 4.6.1 Traffic modeling

We consider the Turin road network in Fig. 4.12, which includes an urban arterial crossed by three primary roads and several secondary junctions along approximately 2 km. We divide the area into three zones with different GPS performance, ranging from open sky to built-up scenarios, namely: two external regions (zone A) characterized by high GPS accuracy  $\sigma_p^{(V)} = 3$  m and  $\sigma_v^{(V)} = 0.1$  m/s, an intermediate zone B with  $\sigma_p^{(V)} = 8$  m and  $\sigma_v^{(V)} = 0.17$  m/s and an extreme urban area (zone C) with very poor GPS accuracy  $\sigma_p^{(V)} = 15$  m and  $\sigma_v^{(V)} = 0.45$  m/s. This variability aims at emulating random behavior of a GPS receiver, artificially creating a variability that (on top of Gaussian noise) increases the randomness

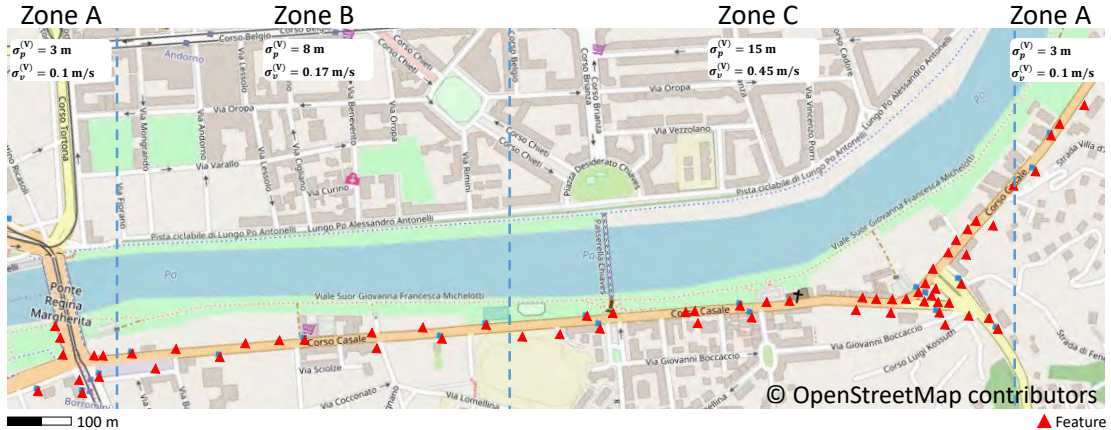


**Figure 4.12:** Urban arterial scenario in Turin, Italy. The area has been divided in three different zones (A, B and C) associated to different GPS accuracies. Features (red triangles) have been placed along the road infrastructure. Map data copyrighted OpenStreetMap contributors and available from <https://www.openstreetmap.org> [10].

of location fixes. Clearly, it cannot match real conditions where GPS accuracy rapidly varies according to the multipath propagation due to the environment and road topology, however it is a good tool to simulate such a non-static characteristic. Vehicles randomly enter the road network according to observed traffic demands, and are localized by simulating a GPS receiver in fast start condition, with prior location belief centered around the true vehicle state, with standard deviations  $\sigma_p^{(V)} = 2$  m and  $\sigma_v^{(V)} = 0.1$  m/s. Since the analysis on feature mobility in Sec. V proved that static features are more beneficial for localization enhancement,  $N_f = 64$  static features are considered in correspondence of bus stops, traffic lights, road signs and car parks. V2F measurement accuracies are set to  $\sigma_p^{(V2F)} = 0.1$  m and  $\sigma_v^{(V2F)} = 0.1$  m/s, and features are sensed if they fall within the vehicle sensing range  $R_s = 50$  m.

Traffic flow is simulated by using the micro-simulator AIMSUM (Advanced Interactive Microscopic Simulator for Urban and Non-Urban Networks) [141], which updates the vehicles' dynamics every time step of duration  $T_s = 0.75$  s. The simulations replicate realistic conditions, including the observed road geometry and traffic control systems at junctions, traffic flows and public transport lines affected by vehicles behaviors and their interactions. The model has been calibrated using real data and describes a common urban scenario with traffic lights affecting the vehicular patterns. The traffic demand in the time slot 20:30-21:30 is chosen, with calibrations on real observations of the number of trips performed by the considered vehicle types from origins to destinations. Five traffic control systems regulate the main nodes along the arterial, which is divided in road sections. Each section is composed by one or more lanes according to the vehicle maneuvers detected during the observation phase, as described in [142]. Vehicular traffic along the road sections is simulated by modeling the following components:

- lane changing for the lateral behavior along the sections,
- car following for the longitudinal behavior along the sections,
- traffic control and gap acceptance model for the crossing behavior at nodes.

Traffic control is expected to have a significant impact on the cooperative positioning accuracy. Control strategies tend to form platoons of vehicles closed together and improve the road capacity, thereby they contribute to increase the V2V connectivity and ease the cooperation between vehicles. To investigate the impact of traffic control on the ICP localization techniques, we consider two different scenarios of traffic regulation as follows:

1. Traffic-Light Regulated (TLR) scenario: intersections are regulated by traffic lights. This scenario represents current mobility systems (no automation, no self-driving vehicles);
2. Vehicle Self-Regulated (VSR) scenario: vehicles apply gap acceptance models to decide whether they can safely cross the intersection, avoiding conflicts [143]. This scenario emulates at first approximation an automated driving use-case,

where vehicles autonomously detect other vehicles in the conflict area and act during the crossing maneuvers on the basis of gap availability decisions.<sup>1</sup>

The VSR scenario can be considered as representative of a vehicle automated driving system of level 4 (according to the definition in [144]), which can also evolve to a cooperative scenario where safety issues can be improved by V2X applications [145]. In both settings, the flow level is decreasing from the peak-hour to off-peak. Therefore, it is possible to observe over the same simulation a variable saturation rate of the arterials and its impact on the positioning accuracy.

The simulated traffic conditions are shown in Fig. 4.13, where we show the total flow exiting from the network in the VSR and TLR scenarios. According to the traffic demands of the selected slot, the flow ranges from about 2800[veh/h] at the beginning of the considered period to 1800[veh/h] at the end. This similarity on the output flow trend between TLR and VSR scenarios is not maintained inside the road network, as expected. As shown in Fig. 4.14, the number of vehicles inside the network for the TLR scenario is higher with respect to the VSR one. The explanations resides in the fact that in the second settings vehicles are more distributed over the arterial and more fluently (less stops) travel across the arterials. This is confirmed by the results in Figs. 4.15a and 4.15b which show the mean queue and stop time for, respectively, the TLR and VSR scenarios. In Fig. 4.15a, the mean queue decreases from almost 40 to 20 vehicles during simulation and the stopped time decreases from 40 s to 35 s per km, while in Fig. 4.15b the values are considerably lower. A mean queue less than 1 vehicle and a stop time of approximately 1 s prove the reduction on the number of vehicles inside the arterial.

These two different traffic conditions create two completely independent vehicular network scenarios with different V2V and V2F connections. This diversity is compared in the next section to assess the performance of the proposed cooperative positioning method.

## 4.6.2 Evaluation of ICP-DA localization accuracy

In this section, we compare the performance of ICP-DA-LC method with the conventional GPS-based tracking in both the TLR and VSR traffic scenarios. In Fig. 4.16, the aggregate RMSE (with aggregation interval of 5 minutes) of the vehicle/feature state estimates, is plotted versus time for the two different traffic conditions, i.e. the TLR scenario (continuous line) and the VSR one (dashed line). The RMSE has been obtained by averaging over vehicles and features. Top figure (Fig. 4.16a) is referred to vehicle position, while the bottom one (Fig. 4.16b) is dedicated to the vehicle velocity. Blue and red lines denote the accuracy of vehicle tracking for, respectively, the GPS and ICP-DA-LC methods, while the green line indicates the ICP-DA-LC accuracy on features.

The results in Fig. 4.16a prove that the ICP-DA-LC method outperforms the conventional GPS over the whole simulation time, thanks to the dense V2V connectivity that eases the cooperation in the urban area. The improvement is far more relevant in the TLR scenario (continuous line) than in the VSR one (dashed

<sup>1</sup>Although automated vehicles have lower reaction times with respect to human drivers, in our experiments we used the same reaction time to compare the two scenarios in the same conditions and focus on the effects of traffic light control.

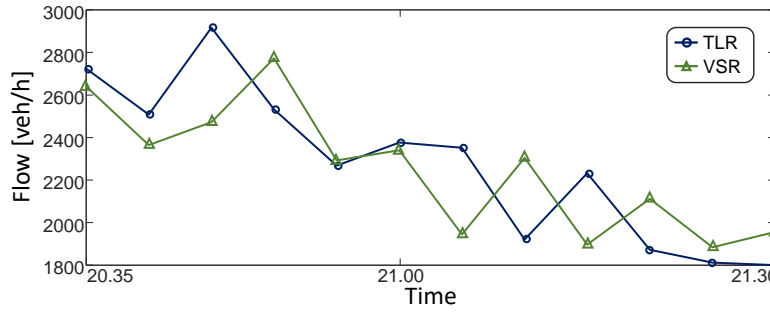


Figure 4.13: Traffic flow over time for the two considered traffic conditions: traffic light regulated (TLR) and vehicle self regulated (VSR). Data are aggregated over 5 minutes.

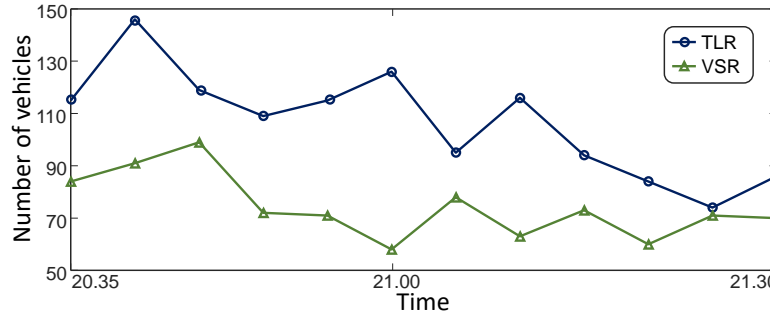
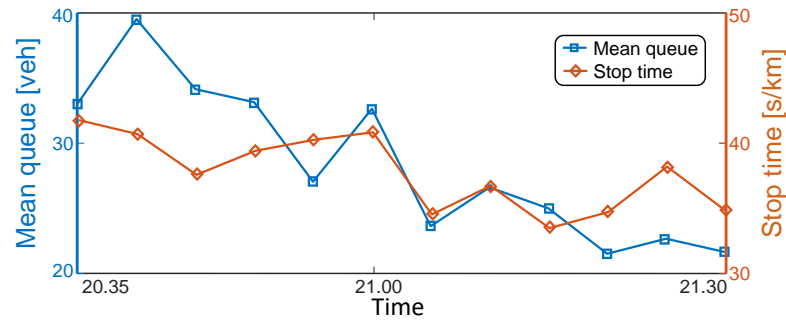
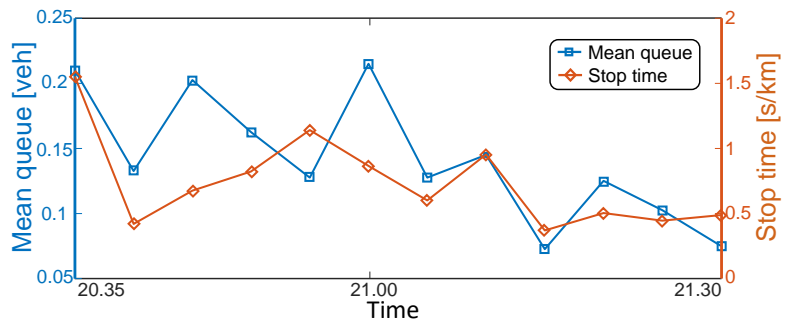


Figure 4.14: Number of vehicles inside the scenario for the traffic light regulated (TLR) and vehicle self regulated (VSR) scenarios. Data are aggregated over 5 minutes.



(a) Traffic-Light Regulated (TLR) scenario



(b) Vehicle Self Regulated (VSR) scenario

Figure 4.15: Mean queue and stop time for the TLR (a) and VSR (b) scenarios. Data are aggregated over 5 minutes.

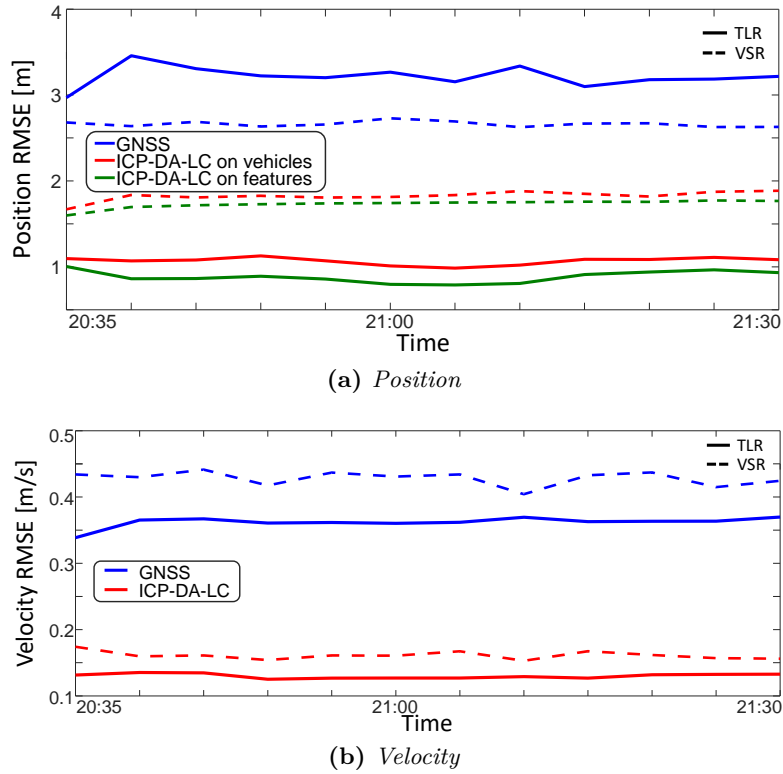
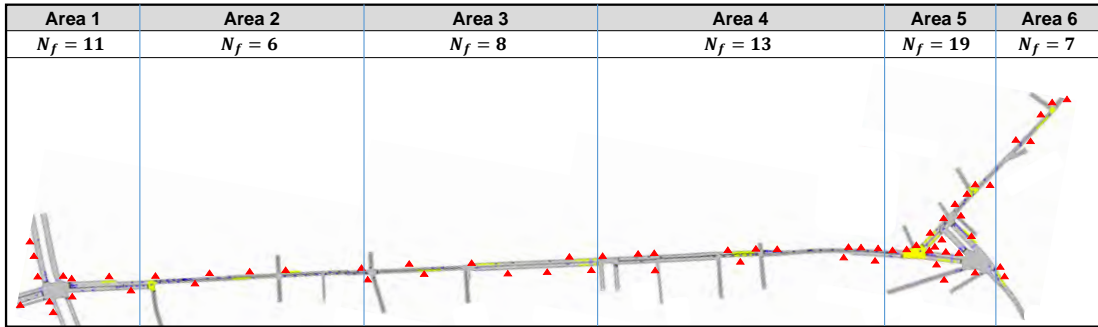


**Figure 4.16:** Averaged accuracy of position (a) and velocity (b) over time for the two considered scenarios: TLR (continuous line) and VSR (dashed line). The GPS-based accuracy on vehicles (blue line) is taken as reference for the ICP-DA-LC estimate on vehicle position (red line). The green line in (a) indicates the accuracy on features.

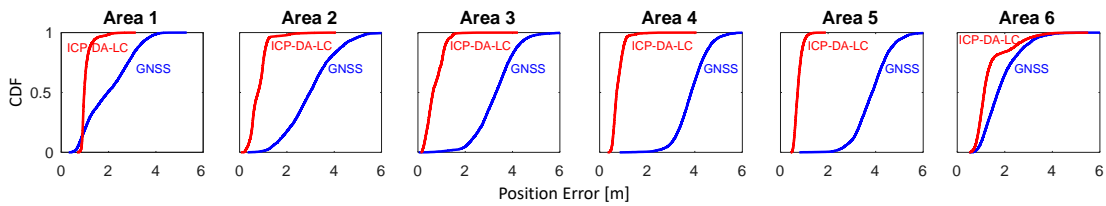
line), due to the higher number of vehicles and the continuous refinement of the feature estimates performed by vehicles during the stop periods. On the other hand, the average GPS tracking accuracy is better in VSR than TLR, as vehicles do not stop at the numerous intersections of the built-up zone C and thus spend less time in this area with highly degraded GPS signals. For the cooperative approach, Fig. 4.16a shows similar accuracy results for vehicles and features, confirming that the precise localization of features obtained by the V2V cooperation directly reflects on the vehicle location accuracy. In the ideal case of perfectly localized features, the ICP method behaves as an augmented positioning system with many fixed anchors (i.e., the features) along the road infrastructure.

The analysis on the location estimate accuracy is extended to the velocity in Fig. 4.16b. Again, the performance of the ICP-DA-LC method is better in TLR scenario than in VSR one. This now holds also for the GPS method, as the length of time the vehicle remains stationary at junctions allows the averaging effect of the observations.

A deeper analysis of the location accuracy over the space domain is carried out in Fig. 4.17a for the TLR traffic scenario. The road network is divided into six areas characterized by different GPS accuracies and feature densities, as indicated in Fig. 4.17a. The Cumulative Distribution Function (CDF) of the vehicle position accuracy averaged over the whole simulation time is computed for each area in



(a) Area of analysis of the Turin traffic scenario

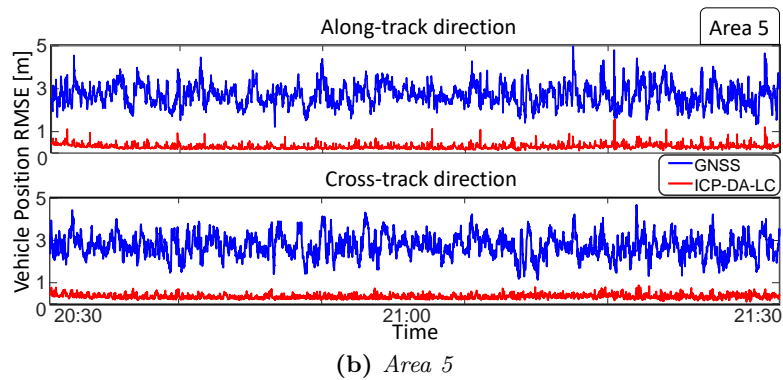
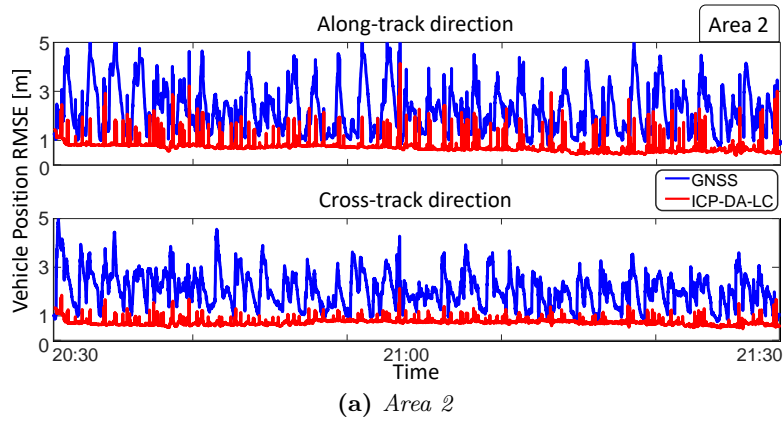


(b) CDF of the vehicle position accuracy

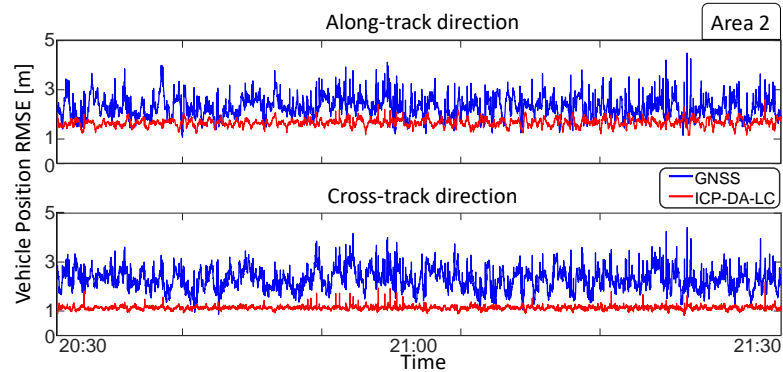
**Figure 4.17:** (a) Map of the Turin road network divided into six areas, characterized by different densities of features and GPS conditions, with highlighted locations of vehicles (blue dots) and features (red triangles). (b) CDF of vehicle position accuracy observed in the in TLR scenario over the different areas.

Fig. 4.17b. The performance augmentation provided by the ICP-DA-LC method is significantly different from one area to the other. In particular, a meaningful gain is obtained in the critical built-up areas 4 and 5, while minor improvements are observed in areas 1 and 6 where the GPS tracking is already highly reliable. Specifically, the highest improvement in localization is in Area 5, where the CDF at 95% of confidence for the GPS solution indicates a vehicle position error of 5 m, while the ICP-DA is able to improve this value to 1 m.

The analysis of vehicle location accuracy over time is given in Fig. 4.18, for the along-track and the cross-track directions in areas 2 (Fig. 4.18a) and 5 (Fig. 4.18b). Numerical results show that the ICP-DA-LC method is able to provide a sub-meter level accuracy in both directions, compensating the degradation introduced by higher GPS measurement errors. The large number of sensed features along with a road configuration that facilitates, with its numerous intersections, the formation of platoons of cooperative vehicles continuously refining their estimates on the surrounding features, has an extremely positive impact on the localization performance. The figure also highlights a marked periodicity of the GPS accuracy pattern over time in Area 2, due to the cyclic regulation of the traffic flows by the sequence of traffic lights along the arterial. During stop phases vehicles can refine their positioning accuracy by averaging over time. The ICP-DA-LC method, on the other hand, provides a more stable performance over time, as the accuracy benefits from space averaging thanks to the cooperation among spatially distributed vehicles. This equalization effect is more evident in the cross-track direction, as expected. This important remark, along with the high precision provided by ICP-DA-LC (below 1 m), makes the proposed method a reliable solution for lane



**Figure 4.18:** Vehicle location accuracy over time for both the along-track and cross-track directions in areas 2 (a) and 5 (b) for the TLR scenario.



**Figure 4.19:** Vehicle location accuracy over time for both the along-track and cross-track directions in area 2 for the VSR scenario.

detection in urban contexts.

Finally, Fig. 4.19 presents a similar analysis for the VSR scenario in area 2. In this case, the GPS estimate is no more affected by traffic lights and the localization accuracy pattern is non periodic. The overall average accuracy is worse than in the TLR scenario for both GPS and ICP-DA-LC, but the performance gain of the proposed cooperative method is still remarkable, especially in the cross-track direction.

## 4.7 Concluding remarks

---

In this chapter, it has been developed a distributed Bayesian framework for cooperative localization of vehicles and targets. The analysis has been carried out considering smart vehicles capable of extracting information from the surrounding environment through sensing and communicating with Vehicle-to-Everything (V2X) devices, as envisioned in the Cooperative Intelligent Transportation Systems (C-ITS) context. Two solutions for solving the data association issue have been provided, leading to two versions of the Implicit Cooperative Positioning with Data Association (ICP-DA) technique: a PF-based solution that handles the non-Gaussian statistics and a low-complexity solution that hardly select the association hypothesis and keeps a Gaussian formulation and implementation. The latter, was shown to provide the best trade-off between complexity and accuracy, closely attaining the performance of the ICP method with known association.

The validation in realistic traffic scenarios confirmed the improvements of ICP-DA over GPS filtering, reaching a sub-metric accuracy. The investigation on the DA performance highlighted the importance of a feature selection mechanisms, to avoid association errors that could degrade the cooperative positioning performance. Quasi-stationary features have to be preferred as they can be localized with higher accuracy acting as virtual anchors for the positioning process.

Traffic flow micro-simulation over a real urban network showed how traffic control systems affect the distribution of vehicles over the roads and impact on the graph connectivity for inter-vehicle cooperation. In particular, a high density of vehicles and features, as well as the formation of vehicle platoons as induced by traffic-light systems (or, in perspective, by cooperative maneuvering strategies) guarantees a high degree of Vehicle-to-Vehicle (V2V) connectivity and increases the accuracy of the cooperative sensing method. The analysis also showed that in urban scenarios the vehicle dynamics and the severe degradation of satellite signals induce high fluctuations of the GPS tracking over space and time, while the ICP-DA method is capable to mitigate this non-stationary behavior, reducing the impact of external factors on the localization performance.

The performance assessment demonstrated that the diffusion of smart vehicles with on-board ranging sensors and V2X communication technologies enables cooperative strategies for perception and localization which can significantly improve vehicle positioning in urban areas. This enhancement is expected to enable new innovative C-ITS services especially in emerging automated driving scenarios, where the formation of tight convoys or platoons of vehicles facilitate the cooperation process. Examples of services include high-precision traffic monitoring, lane-change assistance, infractions detection, inter-vehicle communication efficiency and so forth.

*Future research directions:* as for the previous chapter, the performance has been validated by simulations. Also in this case it would be useful to integrate real measurements from positioning (GPS) sensing (radar/lidar/camera) automotive hardware as to deeply assess the benefit of joint cooperative localization. With respect to the centralized algorithm of the previous chapter where an assessment over real data fills the gap between the research and practical implementation,

in the case of the distributed approach of this chapter the evaluation with real data is only instrumental to better understand the potentials. Indeed, a real-time operability is still far from research, due to technological (5G V2V communication links) and software limitations. Regarding the properties of technology, on the other hand, it might be clever to introduce active direct measurements among vehicles, e.g., by extracting the range from time of arrivals of V2V direct link for instance, thus letting the distributed approach of this chapter to match the conceptualized general solution of the previous one.



---

## Sensor-assisted V2X communications

This chapter addresses the problem of vehicular communications, where road users act as agents. Among them, we can have static (e.g, infrastructure/road side unit), fast moving (vehicles) or slowly-moving (e.g., pedestrians) agents. Multi-agent connectivity is ensured by Vehicle-to-Everything (V2X) communications. Among V2X possibilities, the focus of this chapter is on the Vehicle-to-Vehicle (V2V) use case where vehicles need to exchange information each other. Specifically, the analyses of this chapter refer to beam-based V2V communications. Communicating at narrow beam is currently considered as the frontier for next generation mobility systems, as it is deemed as the only technology able to meet high-data rate requirements for advanced autonomous automotive systems. The two key technologies for beam-based communication, namely millimeter Wave (mmWave) and Free-Space Optics (FSO), are here considered and compared. In this chapter it is proposed a solution where beam-based V2V communications take advantage of available on-board sensors that are capable of accurately estimating the vehicle state. The exchange of vehicle navigation information is used as enabler to fasten the alignment of narrow V2V beams such that the benefits of high frequency links are fully exploited. The entire work is focused on the V2V link degradation due to beam misalignment as a consequence of vehicle mobility and a sensor-assisted solution for this specific problem is designed for V2V systems operating in line-of-sight.

The chapter is organized as follows. Sec. 5.1 introduces the concepts of connected mobility and details the use of mmWave and FSO technologies in V2X. Sec. 5.2 describes the considered vision of the V2X ecosystem and details how the proposed sensor-assisted solutions fits therein. The model of vehicle dynamics is in Sec. 5.3 while Sec. 5.4 contains communication channel models for both mmWave and FSO. Performance analysis are presented in Sec. 5.5 for multiple conditions, technologies and scenarios. Lastly, Sec. 5.5.3 contains concluding remarks.

The contents of this chapter are adapted from publications [3–7].

## 5.1 Introduction to connected mobility

---

The technological development of connected, cooperative and automated systems is expected to represent a game-changer for mobility, with benefits for individual road users and effects on the societal impact in terms of sustainability and quality of life, changing the perspective of cities' design [146–148]. C-ITS are expected to improve the mobility experience in terms of efficiency, safety and comfort. New technology are emerging in the context of 5G networks, which go beyond a simple upgrade of current mobile radio networks [149, 150]. In the incoming years V2X communications are required to guarantee fast sharing of massive mobility data, with unprecedented requirements on latency, data rate and reliability [151]. Examples include the exchange of raw sensor data among vehicles to provide “extended sensors” functionalities for active safety applications such as “see-through” and “bird’s eye view”, enabling high Levels of Automation (LoAs). High-LoA services are based on the exchange of heavy data streams, coming from a huge number of different sensors that equip modern vehicles and in the order of tens/hundreds of Mbps each [152]. The demand of such services cannot be fulfilled by the currently available V2X technologies, namely the WiFi-based IEEE 802.11p [153] and the C-V2X [97]. These two standards are operating in the 5.9 GHz spectrum, as decided by the European Commission [154], providing interoperable and non-interfering C-ITS services targeted to improve safety in mobility [155], but they are not ready for the game-changing breakthrough of automated and connected automotive services. In this perspective, two partnerships, namely the Car 2 Car Communication Consortium (C2C-CC) [156] and the 5G Automotive Association (5GAA) [157], are being working towards the development of new standards specifically intended for the automotive vertical sector. The IEEE 802.11bd and 5G New Radio (NR) V2X standards are planned to fulfill the demand of high-LoA services [158, 159], introducing operating capabilities at Millimeter-Wave (mmWave) bands (as well as at sub-6 GHz).

The mmWave radio is a viable candidate to match the challenging V2X requirements thanks to wide transmission bandwidth availability. The latter aspect is also experienced by considering Free-Space Optics (FSO) technology. Although presenting several peculiarities, both technologies can be categorized as beam-based communications relying on near pencil propagating beams. This implies that both mmWave and FSO need extremely precise Beam Alignment (BA), a condition which is not trivial to be met in high mobility. In this rapidly-varying scenario, two main aspects limit high-speed V2X communications: Line-Of-Sight (LOS) blockage and beam pointing misalignment. The analyses carried out in this chapter are entirely devoted to the latter problem, meaning that full focus is for BA-related issues, neglecting any analysis on blockage. The modeling of LOS/NLOS channel propagation is a different research area, still extremely useful to validate BA strategies. The interested reader can refer to Appendix A for a mmWave channel modeling in a V2I LOS and NLOS mobility scenario.

A dedicated introduction to mmWave and FSO V2X technologies is provided in the following sections 5.1.1 and 5.1.2, where we discuss about their major benefits and challenges, highlighting how we conceive them as suitable solutions

for next-generation mobility.

### 5.1.1 Millimeter-Wave V2X communication

Today, mmWave is considered the only viable Radio Frequency (RF) technology capable of satisfying the extreme requirements (latency and data rate) of enhanced V2X (eV2X) services thanks to the huge bandwidth available in this spectrum portion. Nevertheless, the use of mmWave for eV2X scenarios presents several challenges. Firstly, high frequencies are subject to severe path loss, leading to significant communication performance degradations. Mobility, Doppler effect, blockage and lack of context information are also critical issues that need to be properly addressed in the system design. In this regard, a promising solution is to deploy antenna arrays with a large number of elements at both Transmitter (Tx) and Receiver (Rx) sides, i.e., massive Multiple-Input Multiple-Output (mMIMO) systems. The mMIMO technology allows to shape multiple highly directive radiation beams in a confined spatial region, counteracting the severe path loss and minimizing the mutual interference. Furthermore, the reduced wavelength of mmWave (10 mm at 30 GHz) allows packing hundreds of antennas in a small array, making mMIMO suitable for short-range ( $< 1$  km) smart-mobility applications.

Practical implementation of mmWave mMIMO technology poses two main issues: (i) traditional MIMO systems require dedicated RF and baseband hardware at each antenna element to control signals' amplitude/phase, and this is not viable for such a massive number of antennas, thus forcing mmWave mMIMO systems to heavily rely on analog or RF processing; (ii) mmWave mMIMO systems require precise BA and tracking procedures to keep the pencil beams aligned along the LOS directions. Regarding the former (still open) issue, the implementation of full digital baseband beamforming is currently prohibitive for complexity and cost reasons of using a dedicated RF chain for each antenna element, and hybrid solutions are discussed in [160–162]. They consist in a trade-off between analog and digital beamforming, where the precoding circuit is jointly designed in both analog and digital domains as to reduce the number of RF chains but still having satisfactory beamforming capabilities. Indeed, performance results in [163, 164] show that hybrid solutions closely approach ideal full-digital beamforming by adaptive optical analog processing [163] or exploiting the sparse-scattering structure of mmWave channels [164]. The latter issue, instead, is the main focus of the research presented in this chapter, which is entirely targeted to analyze communication performance degradation due to beam mis-pointing. Conventional BA solutions that perform an exhaustive search of the optimal Tx/Rx beam pair are too time demanding for vehicular scenarios due to the latency constraints. Different solutions have been proposed in the literature to speed up the BA procedure [165–170]. The authors of [171] propose to explore the channel and queue state information to optimize both transmission and reception beamwidths. Other approaches exploit side information such as location data provided by a radar signal operating in a different mmWave band [172], motion prediction [173, 174] or GPS [175]. As detailed in the following, we follow a different approach, whereby BA and tracking are carried out based on the information retrieved from on-board sensors that are mutually exchanged among vehicles.

## 5.1.2 Free-Space Optics V2X communication

FSO is a mature form of optical wireless communication where the information is exchanged through a modulated laser link, mostly operating in the visible or infrared spectrum portions [176, 177]. Although currently not standardized, FSO is envisioned for a wide range of applications: from high-capacity back-haul links for next generation cellular networks [178] to multi-agent networks of unmanned aerial vehicles, aircrafts, satellites, trains and cars [179–183].

For the considered V2X context, FSO is interesting for many different aspects: *(i)* huge optical bandwidth (currently unlicensed); *(ii)* immunity from RF interference; *(iii)* immunity from Doppler effect when Intensity Modulation/Direct Detection (IM/DD) is employed; *(iv)* availability of low-cost, small-size, high-speed integrated components and, more importantly, *(v)* high spatial collimation of beams, which allows to achieve wide operational ranges (from few meters to kilometers, depending on the visibility conditions) with low power expenditure and no interference between different FSO links in dense multi-agent networks. Most of the benefits of FSO in terms of signal coverage come from the use of extremely directive beams. However, beside being highly sensitive to atmospheric conditions such as turbidity (fog, haze, rain, etc.) and turbulence [184, 185], FSO systems are subject to frequent loss of the optimal LOS direction due to random obstacles and, mostly, Tx-Rx misalignments. A straightforward solution to cope with this issue is to widen the optical beam: this approach, although useful for very short range systems [186], would lead to an unacceptable power density reduction at typical V2X distances, nullifying the advantages of a naively directive modulated laser beam. The most fruitful solution to exploit the high collimation of laser beams is, instead, to employ sophisticated acquisition, tracking and pointing mechanisms to keep a seamless connection [187]. The FSO system must be able to firstly acquire the position of the receiver (scanning phase), and successively perform a continuous steering of the beam based on Rx tracking.

Diverse techniques have been proposed in the literature in order to address the laser pointing issue [187]. Works [183] and [188] are particularly interesting for our purposes as they provide an experimental proof-of-concept land-mobile FSO V2I system, which capable of transmitting information from a moving vehicle (max speed of 30 km/h) to a fixed receiver (road infrastructure) at a distance of approximately 1 km. The mobile transmitter knows the position of the fixed platform and combines it with its own location (using GPS) to coarsely steer the laser towards the receiver, while the tracking is performed with the aid of two cameras and a beaconing system. Although interesting, [183, 188] do not consider the more challenging V2V scenario with higher mobility of all vehicles (i.e.,  $\gg 30$  km/h), in which the locations of Tx and Rx terminals cannot be known in advance. This is precisely the V2V context considered in this paper, which proposes to share information of the instantaneous dynamics of the vehicles by a data fusion of on-board sensor data. The exchange of pose data over a parallel low-rate control link provides each vehicle a precise and timely information to be used for an accurate laser pointing.

### 5.1.2.1 Scientific contributions and main limitations

In the remainder of this chapter we introduce the envisioned dual-layer C-ITS architecture enabling highly directive beam-based V2X communications assisted by on-board sensors. We describe the different tasks a vehicle has to perform to guarantee a reliable mmWave or FSO V2X link, by differentiating between intra-vehicle data fusion and inter-vehicle cooperation. In the first case, the pose of the V2X terminal of the ego-vehicle is estimated by fusing data from different on-board sensors accounting for their temporal variability. In the second case, instead, such pose information is broadcasted through a parallel low-rate, low-latency signaling channel such that any connected road user is aware of the V2X geometry and can proactively determine the optimal beam for the mmWave/FSO link. Then, we evaluate the feasibility of the proposed high data-rate mmWave- and FSO-based V2X solutions by simulations. Preliminary 2D analysis are firstly shown, then the performance is assessed on a more complete 3D system model. The performance assessment is entirely focused on the impact of vehicle dynamics on the beam pointing, with the evaluation of the impact of misalignment on the V2V Signal-to-Noise ratio (SNR), outage probability and duration of fade events, by considering different beam dimensions and vehicle sensors' accuracies.

A primary limitation of the developed solution resides in the applicability, which is restricted to V2X communication in visibility (i.e., in Line-Of-Sight - LOS), where there is no blockage between Tx and Rx. As a matter of fact, determining the optimal beam pointing direction using the positions of both vehicles, i.e., Tx and Rx, does not take into account the real propagation condition of mmWave/FSO signal. If FSO communications cannot work in case of blockage, meaning that only LOS conditions are applicable, mmWave communications can work even in Non-Line-Of-Sight (NLOS) conditions thanks to multipath propagation, at the expenses of reducing the communication efficiency due to a lower Rx power. The scope of the addressed beam alignment issue is primary related to V2V links, where vehicles need to exchange massive data only to close neighbors (which are mostly in visibility). It is more likely to experience NLOS propagation for V2I communications, while it is more opportunistic to consider multi-hop V2V mesh networks of connected vehicles with short-range LOS links. Another unavoidable consequence of relying on vehicle estimate for beam alignment is trusting on such information, if it is not accurate it leads to a completely mis-pointing of the beams, unavoidably impeding the communication itself. A same consequence comes if the broadcasting of vehicle state information is denied or unreliable, as it prevents an exact knowledge of near real-time vehicular network topology. For this reasons, accurate sensing and reliable communication links become fundamental for both automated driving functionalities and sensor-assisted V2X communication capabilities. The envisioned tight integration between sensing and communication fails in case one of the two core building blocks stops working properly. Lastly, the research presented in this chapter deals with ideal communication channels: there is no mmWave/FSO communication channel modeling. If, on one side, this decision is motivated by the intended goal to assess misalignment performance degradation only, without introducing other propagation impairments (such as multipath and NLOS condition, blockage, depolarization, atmospheric effects or

inaccurate channel estimation), on the other side it does not perfectly match realistic channel conditions. Decoupling multiple effects allows for the analysis on ad-hoc countermeasure to each specific impairment, but at the same time it exclude possible correlations among diverse effects. A more complete work would integrate a realistic channel modeling as to assess a joint effect of as many detriments as possible. Nevertheless, it would enable a comparison with geometry-based beamforming and subspace-based techniques that do not rely on the LOS angles for beamforming but exploit the channel structure to discriminate the dominant eigenvectors to be used as precoder/combiner.

## 5.2 Envisioned V2X system architecture

---

Even though mmWave and FSO present different peculiarities, both leverage a V2X communication over narrow beams (beam-based communications). A common challenge is keeping the alignment between transmitter and receiver units, and this is the addressed topic of interest herein. Conventional beam tracking is based on various scanning strategies that are activated once the alignment is lost and the connection interrupted, or in setting up the first connection. This approach is undoubtedly effective and provides precise results, but it implies a severe reduction of the communication efficiency due to the additional signaling overhead and wast of time resources. Scanning is highly time-consuming, preventing to fulfill the V2X latency requirements [189]. In contrast, the proposed solution is a seamless BA strategy based on V2V sharing of sensor data. A non standalone V2X architecture, combined with a sensor-assisted control system for tracking highly directive beams, is the envisioned V2X ecosystem. The coexistence of two parallel communication technologies allows for the exchange of vehicle pose data on a low-rate control channel, such that the multi-gigabit link (either FSO- or mmWave-based) is fully exploited to meet the stringent requirements of advanced C-ITS services and high-LoAs. The low data-rate link (e.g., sub-6 GHz C-V2X or 5G NR Frequency Range (FR) 1) is only used for signaling vehicle dynamics information for BA control. This is in line with the 5G vision for V2X communications which foresees a multi-connectivity approach (non-standalone architecture [190]) to guarantee the reliability constraints of V2X Ultra-Reliable Low-Latency Communications (URLLC) through the combination of different communication modes (e.g., V2X and Vehicle-to-Network-to-Everything - V2N2X) or different radio access technologies. In the proposed approach, the low-rate V2X link is a parallel control link used to improve the reliability of the high data-rate V2X link.

Sensor data are typically collected in vehicles by on-board Inertial Measurement Units (IMU, including 3D accelerometers, 3D gyroscopes and magnetometers), along with camera systems, radar, GNSS and other technologies. Nowadays, vehicles on the market use these heterogeneous sensors for driver assistance and partial automation applications. In our solution, we suggest to process these sensor data not only to infer the ego vehicle dynamics, but primarily to extract information on the relative V2V dynamics by distributed processing of such data over the vehicular cloud. Seamless BA and tracking is designed based on the exchange of dynamic pose information (position and orientation) among the networked

vehicles. A key aspect is the integration of sensing with communication: in the proposed architecture, sensing and communication are tightly coupled. It is widely acknowledged that V2X can extend the on-board sensing capability, here the novelty is the other way round: i.e., the use of (shared) on-board to augment the V2X performance, by implementing a system for signaling information of vehicles' dynamics for predictive beam control.

The envisioned V2X architecture is represented in Fig. 5.1. It comprises a number of inter-connected vehicles, which are assumed to be fully equipped with many different sensors such as IMU, cameras, GNSS, radar, lidar and others. The RSUs, whenever existing, enhance the V2V network performance, e.g., by providing internet connection, forwarding control messages in case of Non-Line-Of-Sight (NLOS) conditions or providing updated road maps. The role of the RSU can be covered by the radio access network such as 5G macro/micro cells. The main feature of the proposed architecture is the two-layer V2X system, which operates in parallel to provide (i) a high data-rate link (either mmWave or FSO) for high-LoA scenarios (green beams in Fig. 5.1) and (ii) a low data-rate link (either V2V or V2I) for exchanging locally processed information about vehicles' states (yellow arcs in Fig. 5.1).

As stressed in the introduction, both mmWave and FSO require advanced beam tracking mechanisms to comply with the reliability and latency requirements of V2X communications, and this is where the need of a low-rate, low-latency,

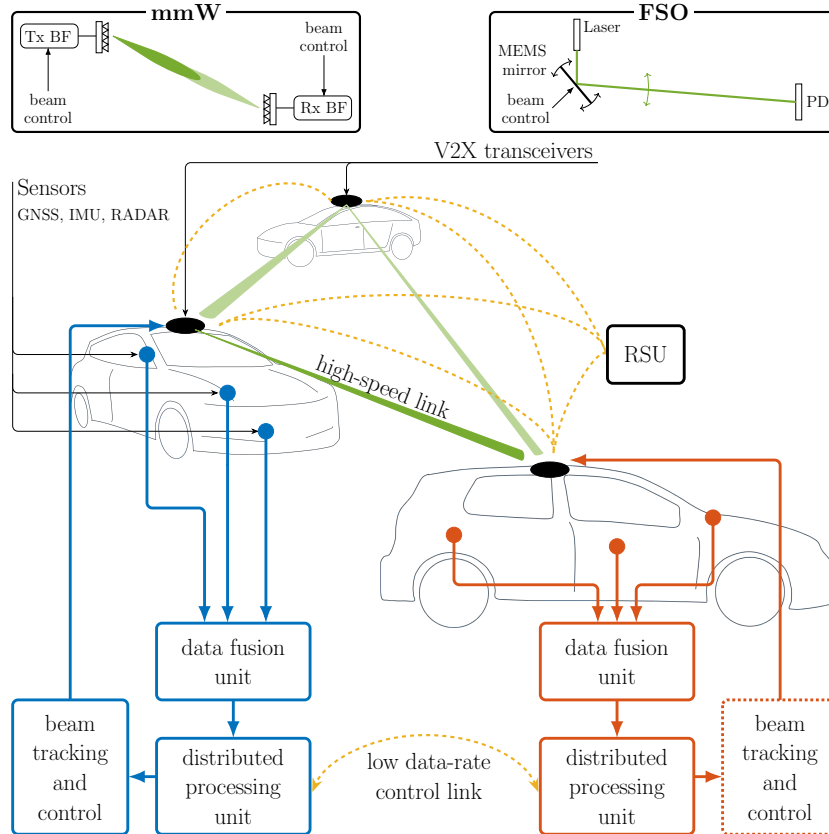


Figure 5.1: Overview of the proposed sensor-assisted cooperative V2X architecture.

dedicated control link comes from. As shown in Fig. 5.1, at first each vehicle fuses the data from the many various on-board sensors in order to estimate/predict the temporal evolution of its own pose (data fusion unit). Then pose data are shared among all vehicles in the network through the low-rate control link. The distributed processing unit of each vehicle has then an accurate knowledge of the updated V2X network geometry, consisting in the position and orientation in space and time of all the V2X agents (vehicles and possibly RSUs). In this way, all agents have the information needed to compute the pointing directions without scanning.

The proposed architecture comprises different types of V2X links, but we will specifically focus the attention to the V2V case, which is the most challenging one due to the high mobility of both Tx and Rx terminals. The sensor-assisted methodology, however, also applies to any V2X communication system with straightforward adaptations. For example, it can be easily extended to V2I communications, in which one Tx/Rx terminal is fixed and, thus, it is not required to continuously estimate its pose.

### 5.3 Vehicle dynamics modeling and beam pointing

---

In this section we provide a 3D geometrical model for V2V communications generalized to an arbitrary number of vehicles and capable of describing the alignment for both mmWave and FSO V2V communication scenarios. A correct alignment of the beams relies on the knowledge of the relative pose of Tx and Rx vehicles. Each vehicle is described by 6 Degrees of Freedom (DoFs), collecting its position and orientation with respect to a local navigation frame, that is Earth-fixed and common to all connected vehicles.

In this direction, the problem at hand is twofold: at each time instant we first need to determine the pose of each vehicle with respect to the common local navigation reference system, and then to derive the pointing directions in each individual vehicle reference system. These directions are the input to the beam pointing, that is composed by Tx and Rx beamformers for mmWave, and by a Micro Electro-Mechanical System (MEMS) mirror at the Tx side for FSO. As shown in Figs. 5.2-5.3, the reference systems are defined as follows: the local navigation reference system is fixed with respect to the Earth, centered in a suitable point to describe the local vehicular network, and with the  $x$  axis pointing towards East,  $y$  axis towards North and  $z$  axis upwards. Each vehicle reference system, identified by the superscript  $v$ , is fixed with respect to the corresponding vehicle, centered at the mmWave/FSO transceiver (that we place on top of the vehicle, unless otherwise specified as for preliminary 2D performance assessment), and with  $y^v$  axis pointing towards the front bumper,  $x^v$  to the right,  $z^v$  towards the sky.

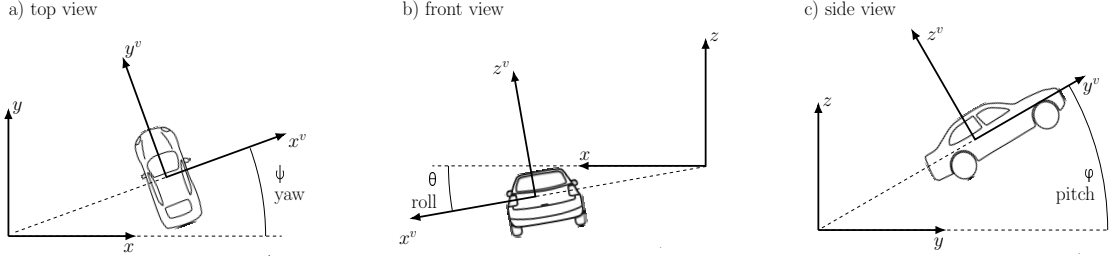


**Figure 5.2:** Navigation and vehicle frames showing the separate effect of the three Cardan angles. a) top view with  $\varphi_v, \theta_v = 0, \psi_v \neq 0$ ; b) front view with  $\varphi_v, \psi_v = 0, \theta_v \neq 0$ ; c) side view with  $\theta_v, \psi_v = 0, \varphi_v \neq 0$ .

### 5.3.1 Vehicle dynamics modeling

The time-varying vehicle pose is typically affected by vibrations and tilting, and it can be modeled as the superimposition of a low-pass random process, modeling the "smooth" motion of the vehicle (e.g., a sharp turn, or a high-speed curve that induces a roll rotation), and a fast-varying random process induced by road roughness, bumps, etc. Their combination induce a time variability of the vehicle pose that requires a fast tracking of beam pointing directions to steer the V2X beams. In this scenario, also the sensors' sampling frequency and their accuracy, as well as the latency on the low-data rate link play a major role to guarantee the robustness and reliability of the whole systems.

The dynamics of each vehicle (which is modeled as a rigid body in this paper), is uniquely described by its position vector with respect to the navigation reference system:

$$\mathbf{p}_v(t) = [\mathbf{p}_{v,x}(t) \ \mathbf{p}_{v,y}(t) \ \mathbf{p}_{v,z}(t)]^T, \quad (5.1)$$

and its orientation  $\boldsymbol{\gamma}_v(t)$ . The latter can be represented in many different ways such as quaternion notation or composing three elemental rotations. Here we use the Cardan angles convention, leading to the orientation vector:

$$\boldsymbol{\gamma}_v(t) = [\varphi_v(t) \ \theta_v(t) \ \psi_v(t)]^T, \quad (5.2)$$

that collects the pitch, roll and yaw, respectively. The separate effect of the three Cardan angles on the vehicle orientation with respect to the navigation frame is in Fig. 5.2. The reference system of vehicle  $v$  is therefore obtained from a roto-translation of the navigation reference: a translation by  $\mathbf{p}_v(t)$  composed with a rotation described by the matrix  $\mathbf{R}^v(\boldsymbol{\gamma}_v(t))$ . This matrix is the result of three successive rotations around  $x$  (by  $\varphi_v(t)$ ),  $y$  (by  $\theta_v(t)$ ) and  $z$  (by  $\psi_v(t)$ ), and its final expression (for a given time  $t$  and vehicle  $v$ , thus omitted to fit page limits) is [191]:

$$\mathbf{R}^v(\boldsymbol{\gamma}_v) = \begin{bmatrix} \cos \theta \cos \psi & -\cos \theta \sin \psi & -\sin \theta \\ \cos \varphi \sin \psi - \sin \varphi \cos \psi \sin \theta & \cos \varphi \cos \psi - \sin \varphi \sin \theta \cos \psi & -\sin \varphi \cos \theta \\ \sin \varphi \sin \psi + \cos \varphi \cos \psi \sin \theta & \sin \varphi \cos \psi + \cos \varphi \sin \theta \cos \psi & \cos \varphi \cos \theta \end{bmatrix}. \quad (5.3)$$

The dynamics of vehicle  $v$  as a rigid body is then described by 6 DoFs, summarized by the position  $\mathbf{p}_v(t)$  and the Cardan angles  $\boldsymbol{\gamma}_v(t)$  with respect to an absolute

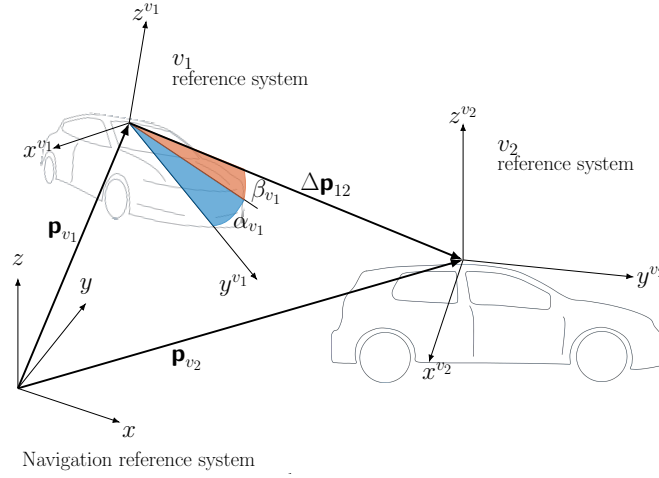


**Figure 5.3:** Geometry for a 2-vehicles network, with navigation and vehicle frames and LOS angles for Tx vehicle  $v_1$ .

reference system. These position and orientation vector are now used to derive the optimal LOS direction of V2V communication link.

### 5.3.2 Derivation and estimation of Line-Of-Sight direction

Let us consider a V2V communication between two vehicles as in Fig. 5.3, in which  $v_1$  is the transmitter and  $v_2$  is the receiver: the pose vector of two vehicles in the navigation reference system are  $\mathbf{p}_{v_1}(t)$  and  $\mathbf{p}_{v_2}(t)$ , and the two rotation matrices  $\mathbf{R}^{v_1}(t) = \mathbf{R}^v(\boldsymbol{\gamma}_{v_1}(t))$  and  $\mathbf{R}^{v_2}(t) = \mathbf{R}^v(\boldsymbol{\gamma}_{v_2}(t))$ .

At the transmitter side ( $v_1$ ), the V2V distance vector is computed as:

$$\Delta \mathbf{p}_{21}^{v_1}(t) = \mathbf{R}^{v_1}(t) \left( \mathbf{p}_{v_2}(t) - \mathbf{p}_{v_1}(t) \right) = \left[ \Delta p_{21,x}^{v_1}(t) \quad \Delta p_{21,y}^{v_1}(t) \quad \Delta p_{21,z}^{v_1}(t) \right]^T, \quad (5.4)$$

and the LOS direction for vehicle  $v_1$  is identified by the couple of azimuth  $\alpha_{v_1}(t)$  and elevation  $\beta_{v_1}(t)$  angles, respectively defined as:

$$\alpha_{v_1}(t) = \text{atan} \frac{\Delta p_{21,x}^{v_1}(t)}{\Delta p_{21,y}^{v_1}(t)}, \quad \beta_{v_1}(t) = \text{asin} \frac{\Delta p_{21,z}^{v_1}(t)}{\|\Delta \mathbf{p}_{21}^{v_1}(t)\|}. \quad (5.5)$$

Similarly, at the receiver side, the vector connecting the two vehicles is  $\Delta \mathbf{p}_{12}^{v_2}(t) = \mathbf{R}^{v_2}(t) \left( \mathbf{p}_{v_1}(t) - \mathbf{p}_{v_2}(t) \right)$ , and the computation of the pointing angles  $\alpha_{v_2}(t)$  and  $\beta_{v_2}(t)$  directly follows from (5.5) with straightforward modifications.

Ideally, the best communication performance are obtained when the Tx and Rx are perfectly aligned along the LOS direction. This means that, for mmWave, the radiating beams of both Tx and Rx vehicles point towards the LOS angles in (5.5) for every time  $t$ , while for FSO that the Tx laser is always perfectly illuminating the Rx photodiode (or array of photodiodes). In practice, the knowledge of the optimal time-varying pointing angles (corresponding to the LOS directions) is a crucial issue, and the update rate of the pointing directions is a key design parameter for the system.

Pose estimation consists in evaluating the dynamics over time of each vehicle frame (orientation and position) with respect to the navigation frame, which represents a highly challenging task. As a matter of fact, GPS typically provides a position estimate that is not accurate enough for eV2X applications. Concerning the orientation estimation, gyroscope, accelerometer and magnetometer data from the IMU can be integrated, provided that techniques are used to handle integration drift [192]. Measurement and dynamic models can be included in an extended Kalman filtering approach, possibly combining also camera and radar data [191].

Position and orientation estimates for each vehicle are thus affected by various noise sources yielding to noisy pose estimates as:

$$\hat{\mathbf{p}}_v(t) = \mathbf{p}_v(t) + \mathbf{w}_{p,v}(t), \quad (5.6)$$

$$\hat{\boldsymbol{\gamma}}_v(t) = \boldsymbol{\gamma}_v(t) + \mathbf{w}_{\gamma,v}(t), \quad (5.7)$$

where  $\mathbf{w}_{p,v} \sim \mathcal{N}(0, \mathbf{C}_p)$  and  $\mathbf{w}_{\gamma,v} \sim \mathcal{N}(0, \mathbf{C}_\gamma)$  can be modeled as stationary Gaussian processes [191]. It is to be noticed that the errors on Cardan angles are in general mutually correlated. The same holds for the errors on position and orientation, as these are jointly obtained by a pose estimator, and the estimation of LOS angles, i.e., the outcome of the BA, is from the pose of at least two different vehicles. A thorough characterization of these stochastic terms is beyond the scope of this research.

## 5.4 Communication system model

---

In the following, we first describe how the proposed V2X architecture fits into standardized communication protocols (Sec. 5.4.1 and 5.4.2), and then detail the peculiarities of the mmWave and FSO communication channels in Sec. 5.4.3 and 5.4.4, respectively.

### 5.4.1 Conventional time-slotted frame structure

The following description is intended to provide a generalized overview of a Time Division Duplex (TDD) frame, without referring to any specific existing protocol. The frame structures of the IEEE 802.11ad standards and the draft of IEEE 802.11ay amendment [193, 194] are used as references, since they are both tailored for mmWave communications operating at 60 GHz, even if originally intended for stationary/quasi-stationary applications. Since no communication protocol has been standardized yet for FSO communications [195], we assume here that the reference frame structure adopted for mmWave is suitable for FSO as well.

As a general rule, the TDD communication frame comprises two main access periods: the first is allocated to the exchange of signaling information related to protocol and network management, the latter to data transmission. In this way, the whole Beacon Interval (BI) of duration  $T_{BI}$  consists of a signaling interval ( $T_S$ ), which is further subdivided into general control signaling ( $T_C$ ) and BA-specific signaling ( $T_{BA}$ ), and a data transmission interval ( $T_D$ ), as illustrated in Fig. 5.4a. When dealing with highly directional communications, most of signaling is intended

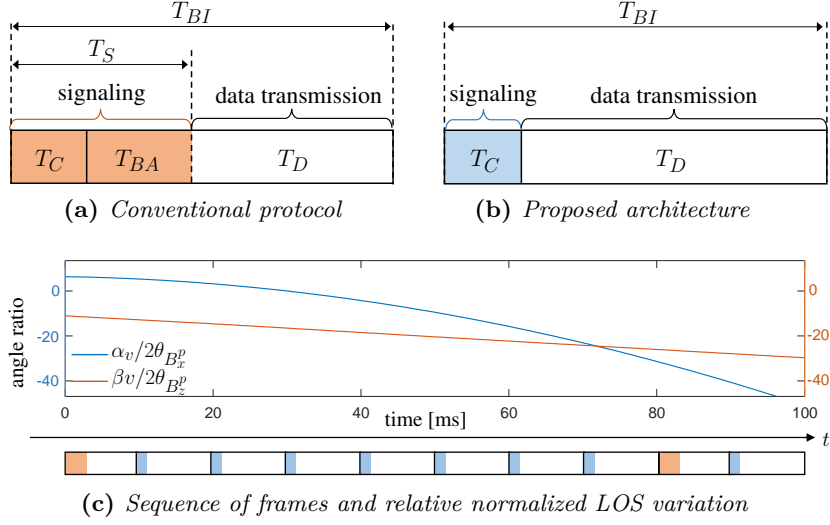


**Figure 5.4:** TDD frame structure. (a) a conventional protocol with BA included in the signaling; (b) the proposed architecture; (c) Sequence of frames and an example of variation of pointing angles  $\alpha_v$  and  $\beta_v$  in a typical vehicular scenario, normalized with respect to a beamwidth of  $2\theta_{B_x^p} = 2\theta_{B_z^p} = 0.1$  deg (an achievable value for FSO systems). The frame duration is chosen  $T_{BI} = 10$  ms to match 5G specifications.

for the implementation of beam alignment/tracking procedures which are time-consuming, especially in vehicular scenarios [175]. In conventional BA techniques, Tx and Rx discover the best direction of transmission using a closed-loop beam training strategy, based on testing some predefined beam patterns that could have different resolutions. The overall transmission efficiency  $\eta$  is given by the ratio of the time interval dedicated to data transfer over the whole BI as:

$$\eta_{\text{conv}} = 1 - \frac{T_C + T_{BA}}{T_{BI}}. \quad (5.8)$$

From (5.8) it is straightforward to conclude that a reduction of  $T_{BA}$  would significantly increase the communication efficiency, that is even worse for multiple vehicles. To this aim, the next section is fully dedicated to describe how the proposed V2X architecture addresses this issue and suggests an alternative frame structure.

### 5.4.2 Proposed frame structure and beam alignment procedure

In the proposed architecture, the beam alignment is assisted by the vehicle pose estimated from sensors data. Indeed, the angles  $\alpha_v(t)$  and  $\beta_v(t)$  in (5.5) describing the LOS direction evolve over time according to the dynamics of the vehicles ( $\mathbf{p}_v(t)$  and  $\mathbf{r}_v(t)$ ). Exchanging the pose estimates through the low-rate control link allows to update the beam pointing direction virtually without any beam

alignment signaling, and the resulting transmission efficiency would be

$$\eta = \frac{1 - \frac{T_C}{T_{BI}}}{1 + \frac{R_L}{R_H}} \approx 1 - \frac{T_C}{T_{BI}}, \quad (5.9)$$

where  $R_H \gg R_L$  are the data rates on the high-speed (mmWave or FSO) V2X link and on the low-rate parallel control link, respectively. This reduction is highlighted in the frame representation in Fig. 5.4b.

On the other hand, the proposed sensor-based beam tracking opens the following two issues: the update rate of the beam pointing with respect to the frame duration and the reliability of the geometry-based beam pointing alone. As far as the first issue is concerned, the latency of the parallel control link plays a main role in determining the accuracy of pose information. A high latency would be detrimental as the exchanged information easily becomes obsolete. Regarding the second issue, instead, the technical characteristics of sensors are pivotal to provide accurate and timely measurements of vehicle position  $\hat{\mathbf{p}}_v(t)$  and orientation  $\hat{\boldsymbol{\gamma}}_v(t)$ . In fact, the pose information is updated with a frequency given by the sampling rate of the sensors data. If 1 kHz update is deemed adequate for the V2X application at hand, and assuming 16-bit quantization of the 6 pose DoFs, each vehicle generates a 96 kbps stream on the control link. If a more frequent update is necessary, the data rate on the control link increases still satisfying the condition  $R_L \ll R_H$ .

Basing the beam pointing solely on the estimated dynamics of vehicles makes the whole high-speed V2X link prone to errors in position and orientation estimation. To improve systems robustness in this respect, it may be convenient to design a system that includes the presence, every once in a while, of a frame with a conventional sweeping procedure. Such sequence of transmission frames is sketched in Fig. 5.4c, together with the variation of the pointing angles in a typical vehicular scenario (details in Sec. 5.5). In particular, Fig. 5.4c shows the variation in pointing directions normalized to a typical beamwidth of a FSO system ( $2\theta_{B_x^p}$  and  $2\theta_{B_z^p}$ , better defined in (5.23) in Sec. 5.4.4.2), which highlights the need for a frequent update of the beam pointing. As the overhead introduced by conventional protocol is inefficient for a low-latency and multi-gigabit V2X communication, in the proposed V2X architecture, the period between two consecutive conventional BA frames (in which a sweeping search of the optimal pointing angles is carried out) is extended by introducing a series of BA-free frames with meaningful reduction of overhead. Clearly, the overall transmission efficiency depends on both types of frame, but an evaluation of the optimal combination is left to future research activities. We limit the discussion in introducing this possible realistic implementation, but all results will be provided considering a sensor-assisted only BA, meaning that no sweeping is carried out at all.

### 5.4.3 Millimeter-Wave V2V

The V2V scenario considered in this subsection includes two vehicles equipped with mMIMO arrays that communicate through a mmWave LOS link. In this subsection we define a mathematical model for the mmWave channel, as well as the array geometry, which is functional to evaluate the impact on the V2V

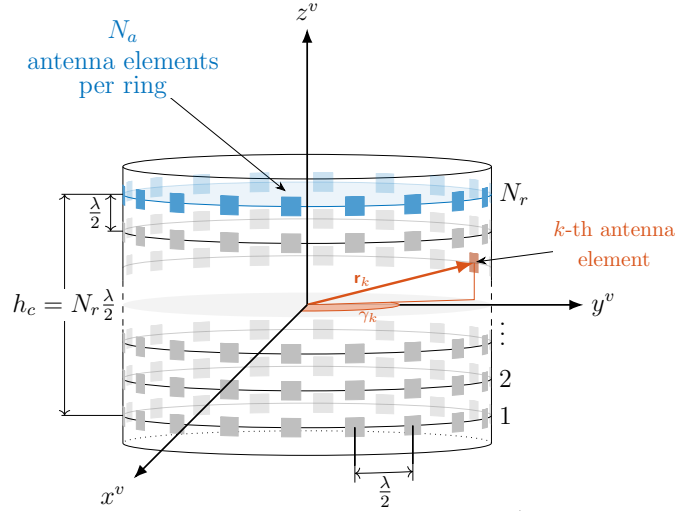


**Figure 5.5:** Cylindrical array configuration of  $N_r$  rings of  $N_a$  elements each.

performance of the mismatch between the real LOS and the estimated beam-pointing directions (i.e.,  $[\alpha_v, \beta_v]^T$  and  $[\hat{\alpha}_v, \hat{\beta}_v]^T$ ). Being the scope of the research presented in this chapter the evaluation of degradation induced by misalignment, any channel related perturbations are neglected, meaning that there is no mmWave channel modeling. This choice allows a separation of degradation effects such that ad-hoc countermeasure for a specific impairment can be taken and evaluated numerically. The mmWave channel is thus considered as ideal, without any stochastic modeling of multipath propagation, neither considering inaccurate channel estimation nor depolarization effects. Regarding the latter detriment, we recall that for LOS communications the depolarization between vertical and horizontal polarization components is minimized due to reduced reflections and scattering [196], and switchable beam polarization patterns can be used in wide-band mmWave systems to dynamically adapt to the environments and maximize the spectral efficiency [197].

#### 5.4.3.1 Cylindrical array geometry

We consider 3D mmWave communication scenario in which each vehicle is assumed to be equipped with a conformal array (such as a 3D cylindrical array) to guarantee an isotropic radiation (this general 3D geometry is replaced by a uniform linear array configuration in the preliminary results where only the vertical component of the vehicle dynamics is considered). The cylindrical array is depicted in Fig. 5.5, and it is composed of  $N_r$  rings with  $N_a$  antennas each, i.e.,  $N = N_r N_a$  antenna elements overall. This choice of array is led by the application, where the Tx and Rx can be randomly displaced all over the horizontal plane. Thus, a circular symmetric array design allows to have an array gain that is independent from the pointing direction. In order to compute the steering vector for the considered cylindrical array, it is first necessary to define the position vector  $\mathbf{r}_k^v$  of the  $k$ -th antenna element in the vehicle reference system, which is given by the array radius  $r$ , the array height  $h_c$  and the angular position  $\gamma_k$  of the  $k$ -th antenna element.

Assuming the peripheral distance between two adjacent antenna elements belonging to the same ring equal to  $\frac{\lambda}{2}$  (with  $\lambda$  denoting the carrier wavelength), the radius of the cylindrical array yields  $r = \frac{1}{2\pi} \frac{\lambda}{2} N_a$ , where  $\frac{\lambda}{2} N_a$  is the ring perimeter. Similarly, considering half-wavelength-spaced rings, the array height yields  $h_c = \frac{\lambda}{2} N_r$ , and the angular position of the  $k$ -th antenna element of each ring is  $\gamma_k = \frac{k}{N_a} 2\pi - \pi$ . It follows that, locating the origin of the reference system in the center of the array, the position vector  $\mathbf{r}_k^v$  for the  $k$ -th antenna element is computed as:

$$\mathbf{r}_k^v = \left[ r \cos \gamma_k \quad r \sin \gamma_k \quad -\frac{h_c}{2} + \left\lfloor \frac{k}{N_a} \right\rfloor \frac{\lambda}{2} \right]^\top. \quad (5.10)$$

Given the pair of pointing angles  $(\alpha_v, \beta_v)$  of vehicle  $v$ , the steering vector  $\bar{\mathbf{a}}(\alpha_v, \beta_v) \in \mathbb{C}^{1 \times N}$  for the cylindrical array with omnidirectional antenna elements is defined as:

$$\bar{\mathbf{a}}(\alpha_v, \beta_v) = \left[ e^{-\frac{j2\pi}{\lambda} \mathbf{r}_1^{v\top} \mathbf{u}^v} \quad \dots \quad e^{-\frac{j2\pi}{\lambda} \mathbf{r}_N^{v\top} \mathbf{u}^v} \right]^\top, \quad (5.11)$$

where

$$\mathbf{u}^v = [\cos \beta_v \sin \alpha_v \quad \cos \beta_v \cos \alpha_v \quad \sin \beta_v]^\top \quad (5.12)$$

identifies the instantaneous wave propagation direction in the vehicle reference system.

The steering vector in (5.11) denotes a conventional beamforming technique which is used by Tx/Rx vehicle to irradiate/capture the electromagnetic energy in/from a confined spatial region for omnidirectional pattern of the antenna elements [16]. Clearly, this model does not perfectly match a commercial hardware and its adoption could lead to inaccurate results. For this reason, along with the steering vector, we introduce a directivity vector  $\mathbf{D}(\alpha_v, \beta_v)$ , where the  $k$ -th entry is computed (under far field assumption) as [198]:

$$D_k(\alpha_v, \beta_v) = \mathbf{b} \cos^\epsilon \left( \min \left( |\alpha_v - \gamma_k|, \frac{\pi}{2} \right) \right) \cos^\epsilon(\beta_v), \quad (5.13)$$

providing a cosinusoidal pattern (on both azimuth and elevation) and baffling the back of each element<sup>1</sup>. The resulting cylindrical array response is thus

$$\mathbf{a}(\alpha_v, \beta_v) = \mathbf{D}(\alpha_v, \beta_v) \circ \bar{\mathbf{a}}(\alpha_v, \beta_v). \quad (5.14)$$

In this way, along the LOS direction, the overall gain  $G_v$  of the cylindrical array is a function of the beam-pointing direction  $(\hat{\alpha}_v, \hat{\beta}_v)$  and it is computed as:

$$G_v = G(\hat{\alpha}_v, \hat{\beta}_v | \alpha_v, \beta_v) = \frac{1}{N} \left| \mathbf{a}^H(\hat{\alpha}_v, \hat{\beta}_v) \mathbf{a}(\alpha_v, \beta_v) \right|^2. \quad (5.15)$$

To highlight the effect on antenna gain  $G_v$  of introducing a directional pattern on each antenna, we provide in Fig. 5.6a a comparison with the case of omnidirectional

<sup>1</sup>Note that the analysis of different tapering or processing techniques of the array vector is out of the scope of this work, despite significant variations on the overall antenna array gain can be experienced.

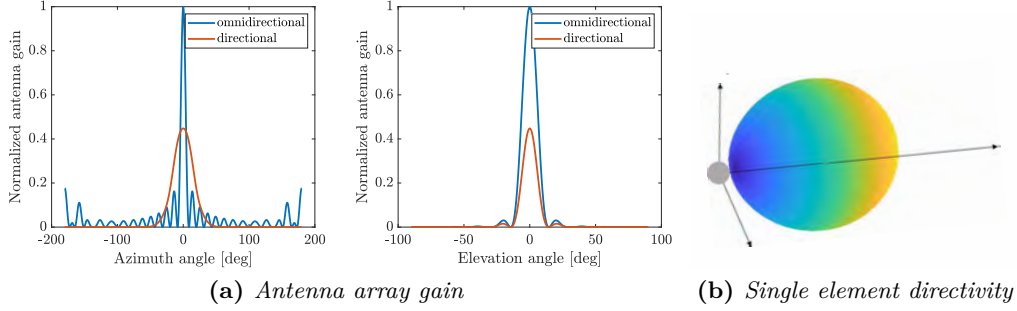


**Figure 5.6:** (a) Comparison of antenna gain in azimuth (left) and elevation (right) for directional (5.13) and omnidirectional directivity of each antenna element. (b) Directivity of the single antenna element for the adopted cosinusoidal pattern (5.13).

directivity for a cylindrical array of  $N_a = 32$  and  $N_r = 8$  at 60 GHz. It is shown how the introduction of directional emitters leads to a wider main lobe with lower directivity overall (due to limited contribution of rear antennas), but with higher suppression capability on grating lobes.

The gain in (5.15) is maximum when the pointing and LOS directions coincide. Unavoidable errors in the knowledge of the instantaneous pose (mainly due to mobility) lead to a beam-pointing mismatch that reduces the antenna gains  $G_v$  and can completely hinder the communication. This problem needs to be handled in the proposed architecture where vehicles share information on a low-rate link, as the latency makes the information slightly obsolete. We will consider this effect later on in Sec. 5.5, showing how the relatively slow evolution of vehicle dynamics with respect to communication delay impact on the V2V performance. In addition, among all parameters impacting a V2V link budget,  $G_v$  is the most affected by errors on the knowledge of the reciprocal pose, thus demonstrating that the occurrence of moderate antenna gain losses is a key aspect for the assessment of the V2V mmWave capacity, which is derived in the next section.

#### 5.4.3.2 Millimeter-Wave V2V performance

The used metric for performance evaluation is the Signal-to-Noise Ratio (SNR), defined as the ratio between the signal and the noise powers at the receiver:

$$\text{SNR}^{\text{mmWave}} = \frac{P_{\text{rx}}^{\text{mmWave}}}{P_{\text{noise}}}. \quad (5.16)$$

The received power  $P_{\text{rx}}$  is influenced by the transmit power  $P_{\text{tx}}$ , the antenna gains at both Tx and Rx sides,  $G_1$  and  $G_2$ , respectively, and the signal path loss  $PL^{\text{dB}}$ . The latter is computed as:

$$PL^{\text{dB}} = 20 \log_{10} \left( \frac{4\pi}{\lambda} \right) + 10 \kappa \log_{10} \|\Delta \mathbf{p}_{21}^{v_1}\| + \chi_{sh}, \quad (5.17)$$

where  $\kappa$  is the path loss exponent and  $\chi_{sh} \sim \mathcal{N}(0, \sigma_{\text{dB}}^2)$  is the log-normal distributed shadowing [199]. Thus, the received power (in dBm) can be expressed as:

$$P_{\text{rx}}^{\text{dBm}} = P_{\text{tx}}^{\text{dBm}} + G_{v_1}^{\text{dB}} + G_{v_2}^{\text{dB}} - PL^{\text{dB}}. \quad (5.18)$$

On the other hand, the noise power  $P_{\text{noise}}$  at the receiver is evaluated as:

$$P_{\text{noise}}^{\text{dBm}} = N_{fl} + 10 \log_{10} B + NF, \quad (5.19)$$

where  $N_{fl}$  is the noise floor,  $B$  is the signal bandwidth and  $NF$  is the noise figure. The system capacity is evaluated as:

$$C^{\text{mmWave}} = B \log \left( 1 + \text{SNR}^{\text{mmWave}} \right), \quad (5.20)$$

and the maximum effective data-rate of the V2V link is:

$$R^{\text{mmWave}} = \eta C^{\text{mmWave}}. \quad (5.21)$$

## 5.4.4 Free-Space Optics V2V

Similarly to the mmWave case, this section describes the laser and photodetectors (PDs) arrangements for the proposed FSO-based V2X communication.

### 5.4.4.1 Laser and photodetector circular array geometry

While the mmWave beam steering procedure is well known, changing the pointing direction of a laser beam involves a completely different technology. Among the available ones, we consider to employ a four-quadrant MEMS Fast Steering Mirror (FSM), which provides the best trade-off among angular range (typically,  $\pm 10$  degrees in both horizontal and vertical directions), resolution (sub- $\mu\text{rad}$ ), integrability, reduced size and power consumption [187]. Since, in general, horizontal variations of the pointing are much larger than the vertical ones due to the relative drifting of the two vehicles during their motion, we assume the presence of multiple laser beams placed in a circular-like array (as in Fig. 5.7a) to guarantee a complete coverage, similarly to the cylindrical antenna array outlined in the previous subsection. The sizing of the angular spacing must enable the continuous sampling of the azimuth direction, and must account for the MEMS' steering capability. Here we use 18 laser-mirror couples that are independently controlled to transmit up to 18 V2X data-streams. These can be reduced to 8 laser-mirror pairs if a wide-angle lens is employed ( $\pm 22.5$  degrees scanning capability [200]). Dually, the receivers are configured to be isotropic by a cylindrical PD array, where each PD is equipped with a proper telescope (or, in general, a set of focusing lenses to increase the received signal). In this way there is always one or more PDs of the receiving unit oriented towards the transmitting laser to guarantee the Tx-Rx alignment.

### 5.4.4.2 Free-Space Optics V2V performance

We consider a FSO transmission between one laser and one or more PDs belonging to the receiving unit, operating in clear sky conditions (neither turbidity nor turbulence), without obstacles. As common to standard single-mode laser diodes, the emitted signal can be well approximated by a Gaussian beam (first Transverse Electromagnetic mode,  $\text{TEM}_{00}$ ), whose propagation along a given direction is described by diffraction theory [201]. Differently from the mmWave case, the analytic description of the laser beam propagation is greatly simplified by the

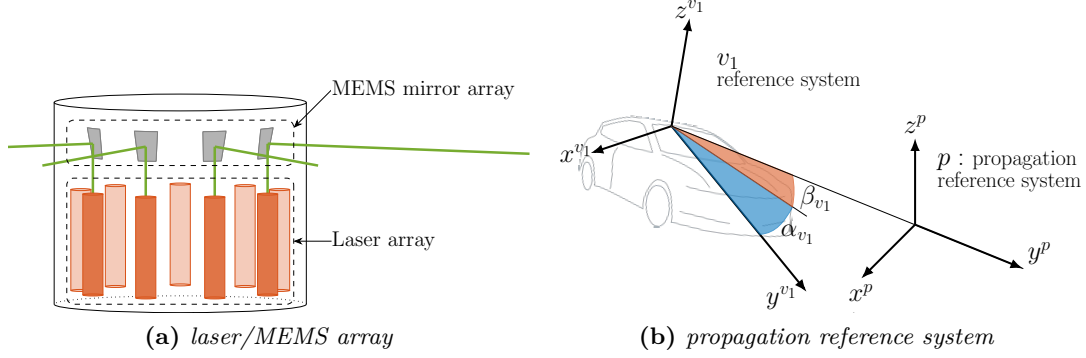


**Figure 5.7:** FSO V2V system. (a) laser/MEMS array. (b) propagation reference system for the description of the laser beam, translated along the pointing direction.

use of a Tx-based reference system in which one of the axis is pointed along the direction of propagation, as shown in Fig. 5.7b. By virtue of the geometrical model described in Sec. 5.3, this can be obtained by rotating the  $v_1$  reference system according to the estimated pointing angles  $[\hat{\alpha}_{v_1}, \hat{\beta}_{v_1}]^T$ , i.e. by applying the following rotation matrix:

$$\mathbf{R}^{pv_1} = \mathbf{R}_x(\hat{\beta}_{v_1})\mathbf{R}_z(\hat{\alpha}_{v_1}), \quad (5.22)$$

where the superscript  $p$  indicates an additional propagation reference system used to describe the laser beam. The new axes are referred to as  $(x^p, y^p, z^p)$ , where  $y^p$  identifies the location of maximum intensity of the beam, which has a Gaussian decay in the transversal directions  $(x^p, z^p)$ . In this framework, the divergence half angles along the transversal  $x^p$  and  $z^p$  coordinates are equal to:

$$\theta_{B_x^p} = \frac{\lambda}{\pi W_{0_{x^p}}} \quad , \quad \theta_{B_z^p} = \frac{\lambda}{\pi W_{0_{z^p}}}, \quad (5.23)$$

where  $\lambda$  is the wavelength of the transmitted lightwave,  $W_{0_{x^p}}$  and  $W_{0_{z^p}}$  are the beam waist sizes (minimum widths) of the beam along  $x^p$  and  $z^p$ , respectively, defining an ellipse on the plane normal to the laser direction enclosing 86.5% of the transmitted power  $P_{tx}$ . Without loss of generality, we can assume that the beam waist of the laser beam is located at the transmitting side, resulting in the Gaussian approximation for the beam intensity at distance  $d$ :

$$I(d, x^p, y^p) = \frac{2P_{tx}}{\pi W_{x^p}(d)W_{z^p}(d)} \exp\left(-\frac{2(x^p)^2}{W_{x^p}(d)}\right) \exp\left(-\frac{2(z^p)^2}{W_{z^p}(d)}\right), \quad (5.24)$$

where the transversal power decay is controlled by the spot size parameters

$$\begin{aligned} W_{x^p}(d) &= W_{0_{x^p}} \sqrt{1 + \left(\frac{\lambda d}{\pi W_{0_{x^p}}^2}\right)^2} \approx \theta_{B_{x^p}} d, \\ W_{z^p}(d) &= W_{0_{z^p}} \sqrt{1 + \left(\frac{\lambda d}{\pi W_{0_{z^p}}^2}\right)^2} \approx \theta_{B_{z^p}} d, \end{aligned} \quad (5.25)$$

that are linearly dependent on  $d$  if  $d > \pi W_{0,x^p/z^p}^2/\lambda$  (far-field condition). The optical signal is then captured by all the PDs that are in visibility with the laser. The received power at each PD is function of both the effective area  $A_{\text{rx}}$ , and of the position of the receiver with respect to the laser spot. This is defined by the distance ( $\Delta x, \Delta z$  along the coordinates  $x^p, z^p$ ) between the PD and the center of the laser beam, as a result of a pointing misalignment ( $\alpha_{v_1} - \hat{\alpha}_{v_1}, \beta_{v_1} - \hat{\beta}_{v_1}$ ). Furthermore, the non-orthogonal incidence of the laser beam onto the PD is represented by two angles ( $\beta_{v_2}$  and  $\zeta_{v_2}$ ). The overall effect is to project  $A_{\text{rx}}$  in the Rx-Tx direction.

The link budget between the Tx and the single PD is obtained by integrating the received power density as expressed in (5.24) over the collecting aperture:

$$P_{\text{rx}}^{\text{FSO}} \approx I(d, \Delta x, \Delta z) A_{\text{rx}} \cdot \cos \beta_{v_2} \cdot \cos \zeta_{v_2}, \quad (5.26)$$

where the approximation holds for the receiver collection area much smaller than the laser spot, i.e.  $A_{\text{rx}} \ll W_{x^p}(d) W_{z^p}(d)$ . The displacements can be computed as (paraxial approximation):

$$\Delta x \simeq d \tan(\alpha_{v_1} - \hat{\alpha}_{v_1}), \quad \Delta z \simeq d \tan(\beta_{v_1} - \hat{\beta}_{v_1}). \quad (5.27)$$

Finally, the electrical SNR for a IM/DD transmission and Positive-Intrinsic-Negative (PIN)-based PDs is obtained by summing up all the power received by each single element. The final expression is [186, 201]:

$$\text{SNR}^{\text{FSO}} = \frac{\sum_{k=1}^{N_{PD}} (\rho P_{\text{rx},k}^{\text{FSO}})^2}{2 e B \left( \underbrace{E_b \Delta \lambda}_{I_b} N_{PD} A_{\text{rx}} \rho + \sum_{k=1}^{N_{PD}} \rho P_{\text{rx},k}^{\text{FSO}} \right) + \text{NEP}^2 \rho^2 B}, \quad (5.28)$$

where:

- $N_{PD}$  denotes the number of PDs on which the signal impinges;
- the numerator is the sum of the squared electrical currents produced by the signal incident on each PD, having a responsivity of  $\rho$ ;
- the first term at the denominator is the shot noise associated to the background light-induced current (i.e., the solar radiation), and to the useful signal. Symbol  $e$  denotes the electron's charge. The solar irradiance  $I_b$  [ $\text{W}/\text{m}^2$ ] is assumed to be isotropic and it is obtained by multiplying the spectrum  $E_b$  [ $\text{W}/\text{m}^2/\text{nm}$ ] and the receiver's optical bandwidth  $\Delta \lambda$  (limited by the responsivity or by a proper optical filter);
- the second term at the denominator is the current noise power comprising both the dark current of the photodetector and the overall electronic noise generated by the receiving circuitry (mostly from the first amplifying stage). It is summarized by the input-referred Noise Equivalent Power NEP [ $\text{W}/\sqrt{\text{Hz}}$ ].

As the employed IM/DD transmission techniques is based on real-valued only constellation symbols, the data-rate is now computed as:

$$R^{\text{FSO}} = \eta \frac{B}{2} \log \left( 1 + \text{SNR}^{\text{FSO}} \right). \quad (5.29)$$

## 5.5 Sensor-assisted beam alignment: performance assessment

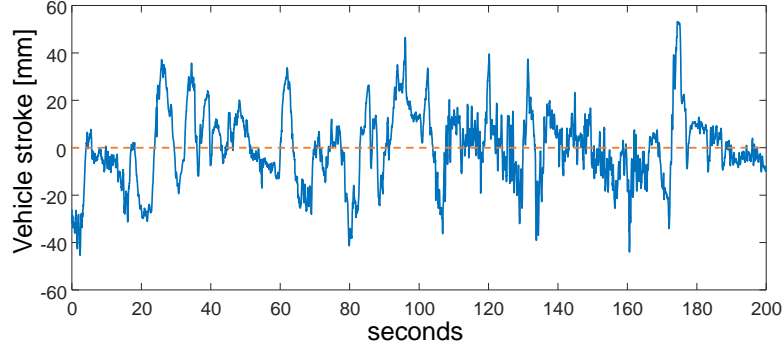
This section presents numerical results of sensor-assisted beam alignment and tracking technique. We first provide a preliminary analysis on the benefits of the proposed technique by considering the impact of vehicle vibrations along the vertical axis (pitch angle) only (Sec. 5.5.1), then we consider a complete 3D evolution of vehicle dynamics (Sec. 5.5.2). Performances are evaluated in terms of SNR, throughput, outage/service probability and Fade Duration Distribution (FDD).

### 5.5.1 2D preliminary assessment of sensor-assisted V2V performance

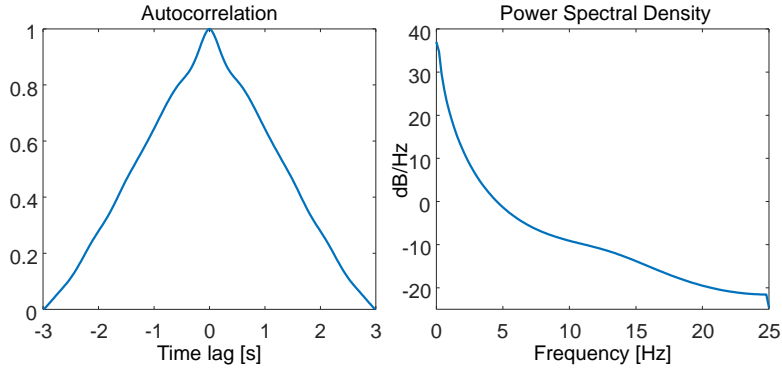
This section presents preliminary results on sensor-assisted mmWave and FSO V2V communications, where the analysis is intentionally focused only on vibration on the vertical axis. The goal is to analyze the impact on beam alignment of the chassis pitch induced by road imperfections. To this extent, a measurement campaign has been carried out to acquire accelerometer data to be used in the evaluation of the vehicle stroke  $\delta z_v(t)$ . The data have been collected on a high-end passenger car (sedan), for an acquisition interval of 200 s at a sampling frequency of 50 Hz. These data are plotted in Fig. 5.8a, while their statistical properties, namely the normalized autocorrelation and the power spectral density, are presented in Fig. 5.8b. The availability of such data allows us to model a calibrated autoregressive (AR) process with same statistical properties to be used in trajectory generation. To match the strokes resolution to the BI duration  $T_{BI}$  (Sec. 5.4.1), interpolation has been applied.

#### 5.5.1.1 mmWave V2V: preliminary results

This section provides results for mmWave V2V technology, in a straight lane scenario case (see Fig. 5.9) where two vehicles travel at a constant V2V distance (constant speed  $\mathbf{v}$ ) of  $\Delta \mathbf{p}_{21}^{v_1}(t) = \Delta \mathbf{p}_{12}^{v_2}(t) = 5$  m, which is a typical value in platooning applications. The resulting position vectors are  $\mathbf{p}_{v_1}(t) = [\mathbf{v}t \ 0 \ \delta z_{v_1}(t)]^\top$  and  $\mathbf{p}_{v_2}(t) = [\mathbf{v}(t - \Delta T) \ 0 \ \delta z_{v_2}(t)]^\top$ . The estimate of V2V distance is updated by the vehicles every 200 ms and it is computed with an accuracy of  $\sigma_r$ . These preliminary simulations considers linear vertical mMIMO antennas mounted on the rear bumper for the front vehicle and on the front bumper for the following vehicle (this configuration is going to be replaced by the cylindrical array placed on top of vehicles in later analyses). The non idealities of antenna elements are considered by introducing the RF mismatch, which accounts for the mismatches of the transceivers RF circuits at the antenna elements and array calibration errors due to hardware themselves and properties of surrounding environments (e.g., temperature and moisture). The RF mismatch is modeled as random multiplication complex coefficient for each antenna element  $n$ , defined as  $h_n = \rho_n e^{j\psi_n}$ , with log-normally distributed amplitude  $10\log(\rho_n) \sim \mathcal{N}(0, \sigma_{RF}^2)$  and uniformly



(a) Vehicle strokes reconstructed from accelerometer data.



(b) Vehicle stroke properties: autocorrelation and power spectral density.

**Figure 5.8:** Properties of vehicle stroke measurements: a) time series of measured stroke; b) stroke statistical properties.

distributed phase  $\psi_n \sim \mathcal{U}(-\phi, +\phi)$  [202, 203]. All simulation parameters are summarized in Tab. 5.1.

The goal of the analysis is to demonstrate the benefits of using sensor data to track the pitch inside the BI and dynamically steers the beam accordingly. To this purpose, at the beginning of each BI, a predictor of order 11 (the last 11 samples) is used to predict the stroke evolution for the entire frame duration, until new information is available at next frame.

We compare the performance of the proposed inertial sensor-assisted beam tracking approach with respect to conventional BA techniques, taking the IEEE 802.11ad standard as a reference protocol. We also consider as upper bound the performance of an ideal V2V communication system with perfect BA based on exact knowledge of the geometrical parameters at each time  $t$ . The maximum achievable V2V data rate (in Gbps) is used as a performance indicator and it is presented versus the array resolution (in elevation)  $\Delta\theta_{3\text{dB}}$  in Fig. 5.10-(a) and versus the BI duration  $T_{BI}$  in Fig. 5.10-(b). The results are presented for three different values of radar accuracy  $\sigma_r$ , which impacts the performance only in the sensor-assisted technique. In the throughput evaluation, we consider a frame to be erroneously received if  $\exists t \in \text{BI}$  s.t.  $\text{SNR}(t) < \text{SNR}_{\text{ideal}}(t) - 6$  dB.

Results in Fig. 5.10 indicate that sharp beams (or equivalently small  $\Delta\beta_{3\text{dB}}$ ) increase the throughput as the power is concentrated in a narrower angular space,

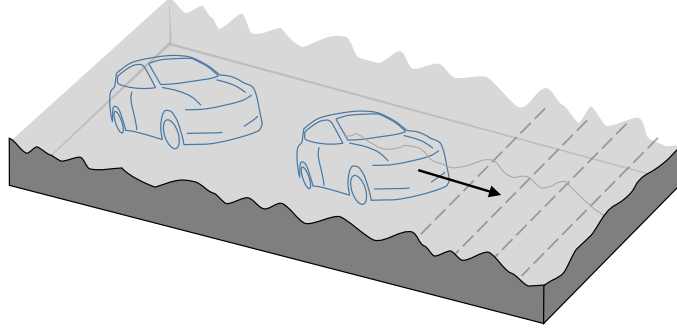


**Figure 5.9:** *Straight lane scenario for preliminary analysis on the impact of vibrations over the vertical direction.*

**Table 5.1:** *Simulation parameters for preliminary mmWave V2V analyses.*

Parameter	Symbol	Value
$v_1$ length	$\ell_1$	4.5 m
$v_2$ length	$\ell_2$	5 m
$v_1$ antenna height	$h_1$	0.5 m
$v_2$ antenna height	$h_2$	1 m
BA overhead	$T_{BA}$	1.9 ms
Control signaling overhead	$T_C$	0.1 ms
Carrier frequency	$f$	60 GHz
System bandwidth	$B$	2.16 GHz
Tx Power	$P_{tx}$	1 dBm
Path loss exponent	$\kappa$	2
Shadowing	$\sigma_{dB}$	5.8 dB
Noise factor	$NF$	6 dB
RF amplitude mismatch	$\sigma_{RF}$	1 dB
RF phase mismatch	$\phi$	3 deg

however they are more sensitive to the variation of vehicle dynamics and to the inter-distance accuracy in the V2V distance estimate. A sensor-assisted beam tracking method can closely approach the performance of an ideal communication system with perfect alignment if the V2V distance is perfectly estimated (i.e., for  $\sigma_r = 0$  cm). On the other hand, degrading effects due to poor ranging systems (e.g., for  $\sigma_r = 30$  cm) occur at small  $\Delta\beta_{3dB}$ . Considering that a typical accuracy in V2V application is  $\sigma_r = 10$  cm, we can conclude that a sensor-assisted beam tracking system can provide a higher V2V throughput for  $\beta_{3dB} > 0.2^\circ$  for any  $T_{BI}$  with respect to conventional BA protocols. Note that for long BI ( $T_{BI} = 50$  ms), the use of sharp beams reduces the throughput even for conventional BA systems, as vehicles are likely to be in misalignment conditions.

### 5.5.1.2 FSO V2V: preliminary results

Similarly to the mmWave case, we still consider the straight lane trajectory with stroke perturbations. We focus on the communication between two vehicles traveling straight ahead in a platoon formation, where  $v_2$  is the leader and  $v_1$  is the follower. The FSO Tx and Rx units are assumed to be installed on top of vehicles.

Differently from the mmWave case where it was shown how to take advantage of vehicle prediction inside a BI, the FSO analysis addresses the misalignment problem from a different perspective: we consider three case studies for beam compensation by vehicles, as detailed in the following.

1. *Case 1: V2V FSO with no pointing compensation.*

This case represents a condition where vehicle  $v_1$  is unable to orientate the laser to the desired direction: the laser is solid with the vehicle chassis and it always points at a frontal direction. Clearly, this is the worst possible case, especially in high mobility applications.

2. *Case 2: V2V FSO with static compensation.*

This case refers to a scenario where a compensation of the nominal values of the height of the FSO units. This case depicts a common condition in mobility where the transmitter knows the location of the receiver but the presence of undesired and unpredictable perturbations (on the vertical axis in this case) impairs the performance.

3. *Case 3: V2V FSO with dynamic compensation.*

This case study is the one representing the proposed dual-layer architecture, with two parallel channel (a low rate one and the FSO link) where on-board sensors measure the vehicle dynamics. By using sensors' information,  $v_1$  is able to compensate its own vibrations and tilting and, at the same time, it

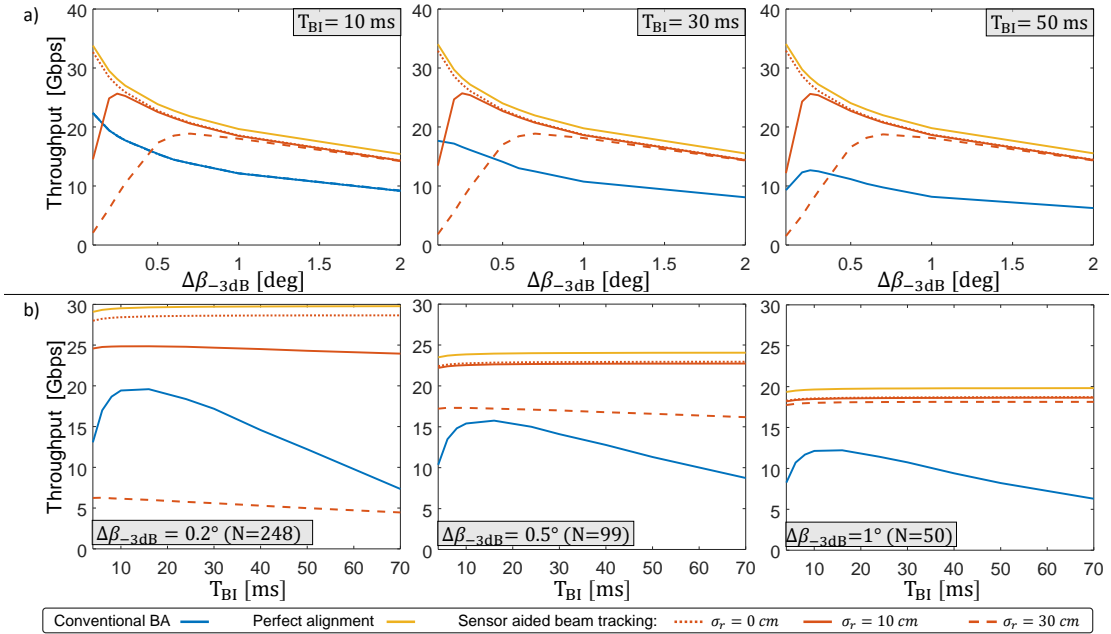


**Figure 5.10:** V2V communication throughput comparison. The inertial sensor-assisted beam tracking is compared to conventional BA protocol and to an ideal communication with perfect alignment. a) V2V throughput versus BI duration  $T_{BI}$  for three different beamwidth. b) V2V throughput versus beamwidth for three different  $T_{BI}$ .

**Table 5.2:** *Simulation parameters for preliminary FSO V2V analyses.*

Parameter	Symbol	Value
$v_1$ height	$h_1$	1.4 m
$v_2$ height	$h_2$	1.7 m
Emitted optical power	$P_{Tx}$	1, 10 mW
Tx laser wavelength	$\lambda$	1550 nm
Beam widths at the Tx	$W_{0,x}, W_{0,y}$	1 mm, 1 mm
Signal bandwidth	$B$	1 GHz
Rx area	$A_{rx}$	1 mm <sup>2</sup>
PD responsivity	$\rho$	0.8 A/W
Optical filter bandwidth	$\Delta\lambda$	50 nm
Solar irradiance	$I_b$	5.58 W/m <sup>2</sup>
Noise Equivalent Power	NEP	20 pW/ $\sqrt{\text{Hz}}$ [205]

receives an updated information from  $v_2$  on the receiver position (through the parallel link). Ideally, if no processing and/or communication delay exists, vehicle  $v_1$  always knows the exact location of  $v_2$  at each time  $t$ . In practice, the information on the dynamics of vehicle  $v_2$  which is available at  $v_1$  is slightly obsolete due to latency. In this preliminary analysis, we consider the information on  $v_2$  dynamics to be available at  $v_1$  with 20 ms delay.

We evaluate the performance of the proposed V2V FSO communication link in clear sky conditions, without any adverse weather effect, focusing the attention on the impact of misalignments. We assume to employ a laser transmitter at 1550 nm, for which there is a large availability of high-speed integrated Distributed Feed-Back (DFB) sources with emitting power ranging from 1 up to 10 mW (Class 1 lasers [204]). As common, the laser spot diameter at its waist is in the order of few mm (2 mm in our case), which is compatible for integrated MEMS-based steering mirrors. The receiver comprises a GHz-bandwidth InGaAs PIN PD with an active area of 0.1 mm<sup>2</sup> covered by a focusing lens (or set of lenses) whose size is determined by the specific application. For V2V FSO, one of the design drivers is to reduce as much as possible the extra-size and weight of the system: in this regard, we make the hypothesis to use a receiving telescope of 1 mm<sup>2</sup> area, comparable with the one of a typical gradient-index lens. A summary on simulation parameter is in Table 5.2.

Fig. 5.11 provides the V2V FSO performance, for two reference values of transmitted power  $P_{tx}$  (1 and 10 mW) at different inter-vehicle distance, ranging from 5 to 100 m. Results in Fig. 5.11 highlight that a compensation mechanism is strictly required to fully exploit the V2V FSO channel, enabling the desired high-capacity (multi-Gbps) communications when  $P_{tx} = 10$  mW.

The convincing results of the proposed sensor-assisted technique for both mmWave and FSO technologies motivated us to pursue that research area. Thus, the first natural enhancement consider th extension of the analyses to the complete 3D model, where variations on vehicle dynamics occur on each of the three axis and the alignment has to be carried out in both azimuth and elevation jointly. From now on, all the results consider this complete system model.

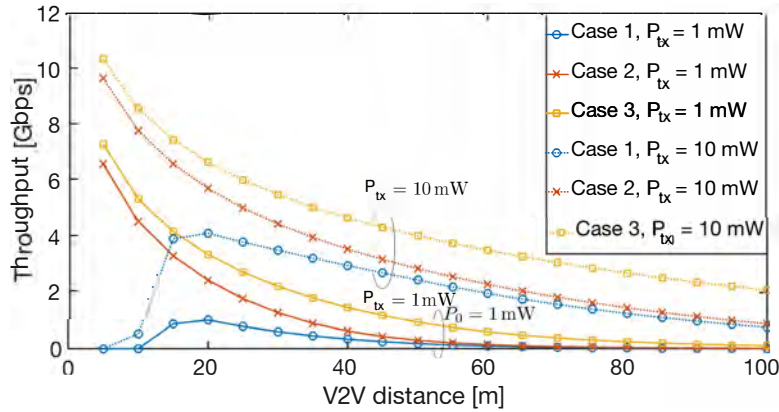


**Figure 5.11:** V2V throughput for three different levels of compensation of vehicle dynamics and for two values of transmitted power  $P_{TX}$ .

## 5.5.2 3D assessment of sensor-assisted V2V performance

After having provided an initial assessment of sensor-assisted BA technique for V2V communications, we now extend the analysis to a complete system model, where the position and orientation of the vehicles evolve over time along each of the three axis. The effect of vertical component is only one of the issues for 3D BA, whose effect is mainly experienced over the elevation pointing angle. On the other hand, a strong variation on azimuth pointing arises due to the vehicle motion (variation of the heading/yaw). In this section we provide a performance comparison of mmWave and FSO technologies, considering two different degrees of beam directivity, i.e., *High Directivity (HD)* and *Low Directivity (LD)*, respectively. However, investigating two different technologies that have specific and sensibly different physical properties, it happens that a low directivity for FSO is considered as high for mmWave, since it is relatively easy to manipulate the optical beam. Nonetheless, we adopted at the best of our possibilities comparable simulation parameters for mmWave and FSO communication links, in order to guarantee a fair performance comparison. The common simulation parameters are in Table 5.3, together with main settings of mmWave and FSO technologies.

### 5.5.2.1 Simulated vehicular scenario

Vehicles  $v_1$  and  $v_2$  are assumed to travel close each other as in a platoon formation. To evaluate the robustness of each technology and the impact of vehicles' spatial dynamics, two completely different vehicular scenarios (namely, S1 and S2) have been considered, differentiating the modeling of  $\mathbf{p}(t)$ . In particular, S1 represents a platooning scenario with vehicles that move along a straight road with constant inter-distance and mutual dynamics only on the vertical axis  $z$  (due to vibrations and tilting), while S2 describes a more complex trajectory with curves and height changes, so that the motion varies on all axes (as can be seen in the bottom right part of Fig. 5.13b). For each scenario, we define a position vector (expressed in

the navigation frame) as:

$$\mathbf{p}(t) = \begin{cases} \begin{bmatrix} vt \\ 0 \\ 0 \end{bmatrix}, & \text{for S1,} \\ \begin{bmatrix} r_0(1 + A_h \cos(\omega_h t)) \cos(\omega_0 t) \\ r_0(1 + A_h \cos(\omega_h t)) \sin(\omega_0 t) \\ A_v \cos(\omega_v t) \end{bmatrix}, & \text{for S2,} \end{cases} \quad (5.30)$$

where the trajectories' parameters are in Table 5.3. The 3D vehicle position for  $v_1$  is modeled as:

$$\mathbf{p}_{v_1}(t) = \mathbf{p}(t) + [0 \quad 0 \quad h_{v_1} + \delta z_{v_1}(t)]^\top, \quad (5.31)$$

where the term  $h_{v_1}$  defines the vehicle height with respect to the road pavement and  $\delta z_{v_1}(t)$  accounts for the vehicle stroke (calibrated on measured data). Similarly, the position of  $v_2$  is:

$$\mathbf{p}_{v_2}(t) = \mathbf{p}(t - \Delta t) + [0 \quad 0 \quad h_{v_2} + \delta z_{v_2}(t)]^\top, \quad (5.32)$$

where  $\Delta t$  stands for the vehicle time gap between  $v_1$  and  $v_2$ .

The quality and timeliness of the pointing information exchanged between the two vehicles across the parallel low-rate control link depend on two critical parameters: the sensors sampling rate  $f_{\text{data}}$  and the delay  $\tau$  (mainly due to the end-to-end latency over the low-rate control link). This last parameter, in fact, introduces a delay in the update of pointing angles  $(\alpha_v, \beta_v)$  leading to an incorrect BA. Here we assume that the sampling rate is fixed to  $f_{\text{data}} = 1$  kHz that implies the use of high-performance IMUs, and  $\tau \in [1, 15]$  ms. The choice of this value of delay is lead by considering the targeted performance of 5G (and beyond) systems which are planned to provide ultra-low latency ( $<1$  ms) communications, while a more realistic short-term hardware foresees a delay in the order of 10 ms. The signal bandwidth  $B$  and the Tx power are set to  $B = 2.16$  GHz [193] and  $P_{\text{tx}} = 1$  mW (0 dBm) for both mmWave and FSO.

Moreover, to better evaluate the mmWave and FSO robustness with respect to pose estimation errors, the covariances of measurement noise in (5.6) and (5.7) are set to

$$\mathbf{C}_p = \sigma_p^2 \mathbf{I}_3, \quad \mathbf{C}_\gamma = \sigma_\gamma^2 \mathbf{I}_3, \quad (5.33)$$

with  $\sigma_p = 10$  cm and  $\sigma_\gamma = 0.1$  deg, unless otherwise specified. Position accuracy  $\sigma_p$  is chosen as to meet the 5G service requirements for eV2X scenarios [189]. Angular accuracy can be achieved by very accurate state of the art automotive IMU.

### 5.5.2.2 Millimeter-Wave settings

In this work we assume a mmWave V2X link operating at 60 GHz carrier frequency. In order to fairly compare mmWave and FSO and analyze the impact of vehicle dynamics and vibrations (we recall that a characterization of blockage is out of

Table 5.3: Simulation parameters for mmWave and FSO V2V over two trajectories.

Parameter	Symbol	Value
Tx power	$P_{tx}$	1 mW
Signal bandwidth	$B$	2.16 GHz
Update delay	$\tau$	1 - 15 ms
Sensor sampling frequency	$f_{data}$	1 kHz
Vehicle height	$h_1, h_2$	1.5, 1.7 m
Vehicle length	$\ell_1, \ell_2$	4.7 m
Position error	$\sigma_p$	10 cm
Angular error	$\sigma_\gamma$	0.1, 1, 2 deg
<b>mmWave-specific</b>		
Carrier frequency	$f$	60 GHz
Path loss exponent	$\kappa$	2
Shadowing std.	$\sigma_{dB}$	0 dB
Noise floor	$N_{fl}$	-174 dBm/Hz
Rx Noise Figure	$NF$	6 dB
Pattern parameters	$b, c$	1.8, 1.6
<b>FSO-specific</b>		
Tx Laser wavelength	$\lambda$	1550 nm
Rx aperture (single PD)	$A_{rx}$	1 cm <sup>2</sup>
Rx array diameter	$D$	10 cm
Rx array height	$H$	5 cm
PD responsivity	$\rho$	0.9 A/W
Optical filter bandwidth	$\Delta\lambda$	50 nm
Solar irradiance	$I_b$	5.58 W/m <sup>2</sup>
Noise Equivalent Power	NEP	20 pW/ $\sqrt{\text{Hz}}$ [205]
<b>Trajectories - according to (5.30)</b>		
Vehicle speed	$v$	50 km/h
Angular velocity	$\omega_0$	0.04 $\pi$ rad/s,
Horizontal angular velocity	$\omega_h$	0.8 $\pi$ rad/s
Vertical angular vel.	$\omega_v$	0.08 $\pi$ rad/s,
Horizontal amplitude	$A_h$	0.1 m
Vertical amplitude	$A_v$	10 m
Radius	$r_0$	$v/\omega_0$ m
Vehicle time gap	$\Delta t$	0.5 - 5 s

the scope of this work), we shall consider a scenario where no obstacles are present within the LOS path, for which a FSO system would be in outage. For this reason, we assume to have a free space propagation (i.e.,  $\kappa = 2$  and  $\chi_{sh} = 0$ ), and the interaction of the propagating wave with the vehicle roof is neglected. The choice of LOS V2V link is led by the need to isolate and evaluate the impact of vehicle motion and vibrations, ignoring additional sources of perturbation that are typical of a communication link (such as shadowing, fading, blockage or interference). The cylindrical array configuration (defined by the number of rings  $N_r$  and antenna elements of each ring  $N_a$ ) described in Sec. 5.4.3.1 changes across simulations in order to provide performance results under different degrees of beam directivity. We consider two mmWave configurations described in Tab. 5.4. The first configuration, *mmWave LD* (with  $N = 256$  antenna elements) represents a mmWave solution that

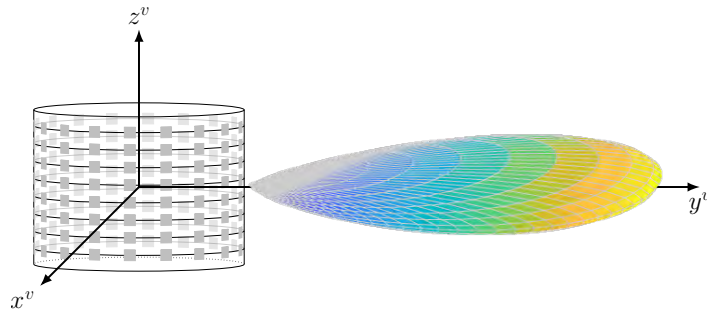
**Table 5.4:** Beamwidth-related parameters for mmWave and FSO in LD and HD configurations.

	mmWave				FSO	
	$N_a$	$N_r$	$\Delta\alpha_{-3dB}$	$\Delta\beta_{-3dB}$	$2\theta_{B_x^p}$	$2\theta_{B_z^p}$
<i>LD</i>	32	8	$\sim 34.5$ deg	$\sim 12.5$ deg	1 deg	1 deg
<i>HD</i>	180	90	$\sim 9$ deg	$\sim 1.12$ deg	0.1 deg	0.1 deg

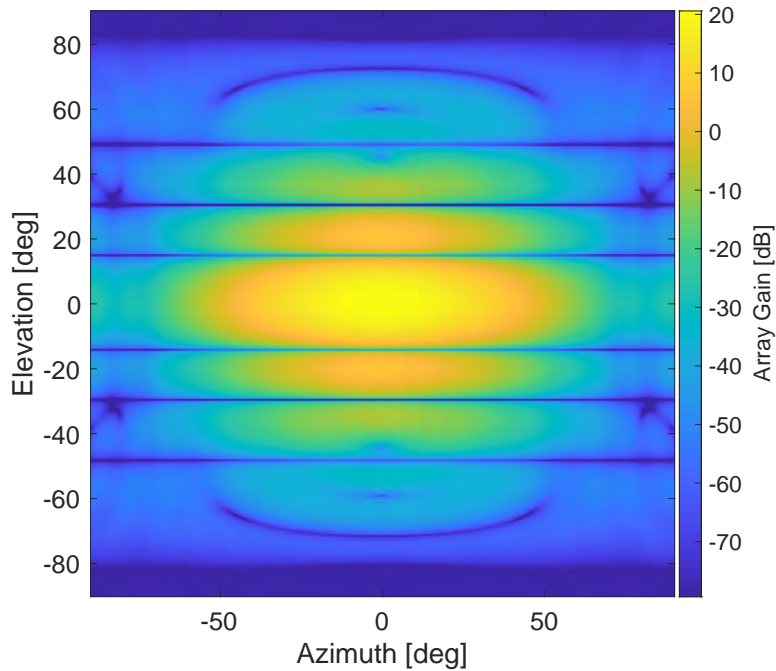
is not extremely directive and which implementation is feasible considering today's hardware limitations. The second one (*mmWave HD*), instead, considers an overly directive beam obtained with  $N = 16200$ . This second sample scenario allows us, firstly, to evaluate the potential that mmWave could achieve with prospective hardware technology and, secondly, to have a beam dimension closer to the narrow-laser FSO solution, and so to have meaningful comparisons. An example of array directivity for *mmWave LD* is illustrated in Fig. 5.12, for pointing directions coinciding with LOS at broadside ( $\alpha_v = 0$  deg,  $\beta_v = 0$  deg) and per-antenna directivity as in (5.13).

### 5.5.2.3 Free-Space Optics settings

The performance of the FSO V2V link is evaluated here in clear sky conditions, in order to focus only on the impact of beam misalignments and to avoid the loss by adverse weather conditions (this is beyond the scope of the paper and is left as future research activity). We consider a Tx laser at  $\lambda = 1550$  nm, for which there is a large availability of high-speed integrated distributed feed-back sources with emitting power ranging from fractions to few mW (eye-safe lasers [204]). As done for mmWave, we simulate two configurations of the FSO system, reported in Tab. 5.4. Our aim is to investigate the performance and the requirements of the system in case of extremely narrow beam widths, that are hardly obtainable with RF antenna arrays. Since it is relatively easy to obtain large directivity for FSO systems (by employing mm-size lenses), we explore divergences down to a full angle of 0.1 deg. The resulting laser spot diameters at their waist is bounded to be less than 2 mm, a value compatible with integrated MEMS-based steering mirrors [200]. Once more, as for mmWave, we neglect the interaction of the laser beam with the car roof. In order to collect the largest possible fraction of power while limiting as much as possible the extra-size and weight of the system, we assume the cylindrical array of receivers to be of 10 cm diameter and 5 cm height. Each single receiver comprises a GHz-bandwidth InGaAs PIN PD covered by a focusing telescope. The outer diameter (sensible area) of each single receiving unit ( $A_{rx}$ ) is set to 1 cm<sup>2</sup>. We evaluate the background light for a vertical surface in the worst possible case, i.e., when both the direct sunlight and the skylight are maximum. Therefore, we consider the solar spectrum obtained for the geographical area of Milan, on July 20th, 2018, at 12 a.m., assuming a very clear day. Finally, the receiver is also equipped with an optical filter with a bandwidth of 50 nm [206], centered around 1550 nm, in charge of reducing the background light.



(a) Radiation pattern.



(b) Array gain.

**Figure 5.12:** Array pattern for mmWave LD pointing towards broadside direction ( $\alpha = 0$  deg,  $\beta = 0$  deg): (a) tridimensional representation of the radiation pattern and (b) the array gain in dB towards different azimuth and elevation angles. The pattern is obtained by considering directional directivity on each antenna element (5.13).

#### 5.5.2.4 Performance evaluation in two distinct vehicular scenarios

This section presents the performance evaluation of the proposed sensor-assisted V2X beam tracking obtained in the two different driving scenarios. The transmission scheme for the proposed method considers a frame structure as in Fig. 5.4b for the whole simulation, meaning that the system fully relies on sensor's information and never performs an exhaustive search of the optimal beam. Results are presented in terms of Cumulative Distribution Function (CDF) of the SNR, service probability and FDD. We choose the CDF rather than the average SNR as it allows to understand the range of achieved values, providing an assessment of the V2V outage. In safety critical V2X applications, the peak (or the average) value of SNR and, in turn, of the data rate represents only one quality indicator.

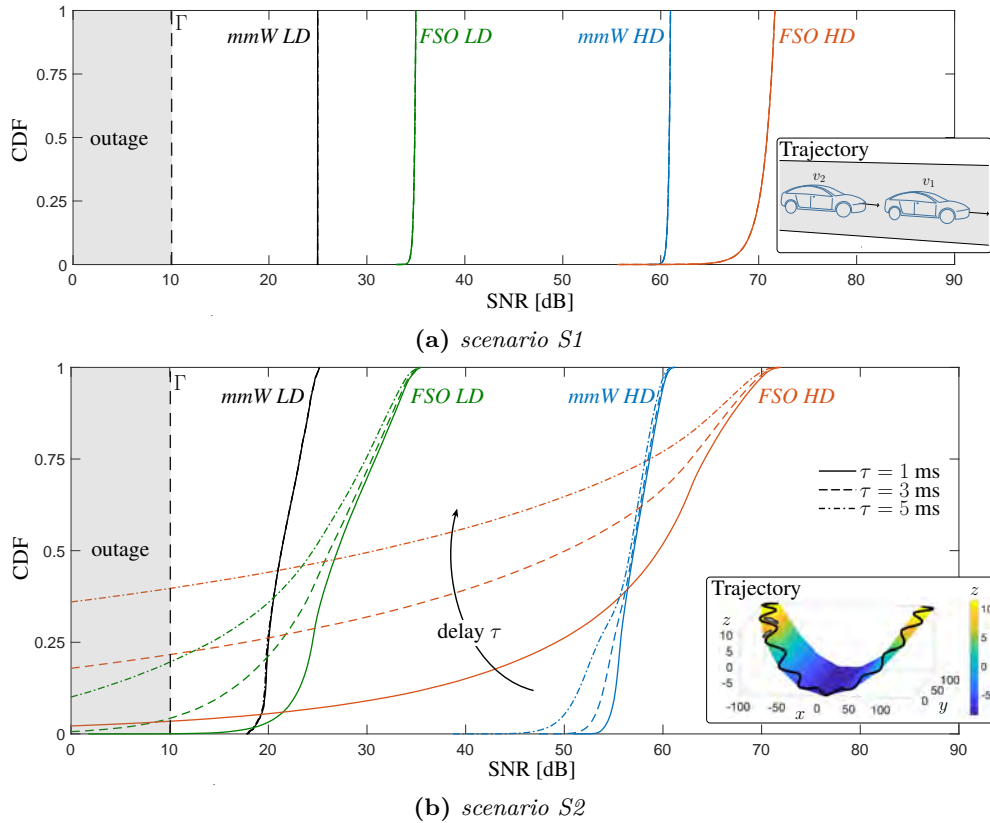


**Figure 5.13:** CDF of the SNR for the proposed sensor-assisted beam tracking method in two different scenarios. Results are plotted for both mmWave and FSO LD/HD configurations for three different values of delay  $\tau$  (vehicle time gap  $\Delta t = 1$  s). In the inset, part of the trajectory is shown.

The timeliness in providing information is another key performance indicator that must be considered in the assessment as any delay in communication or data rate drop could have a severe impact on road user safety. For this reason, it is also important to analyze the FDD as it characterizes the duration of outage periods, where the SNR persists below a given threshold  $\Gamma$  and, thus, the communication is prevented.

The CDFs of mmWave and FSO V2V systems, in both configurations and scenarios, are illustrated in Fig. 5.13, for a vehicle time gap  $\Delta t = 1$  s. By this result, besides providing insights on the maximum achievable data rate and the average one, we want to analyze the impact of delay on the V2V link as well as the type of trajectory and geometry. Referring to Fig. 5.13a, we demonstrate that in a scenario where the mutual vehicle dynamics occurs only along the  $z$  axis, meaning that vehicles oscillate around the height  $h_v$  at rest condition, it is possible to have a reliable V2V communication both at mmWave and FSO: the SNR is almost constant for any *HD* and *LD* configuration, only for *FSO HD* a slight degradation is present, due to the extreme directivity of the laser. Moreover, in these settings, no performance degradation has been experienced as a consequence of a delay in updating the pointing parameters caused by latency. On the other hand, results in Fig. 5.13b indicate that the type of trajectory and, in turn, the relative geometry,

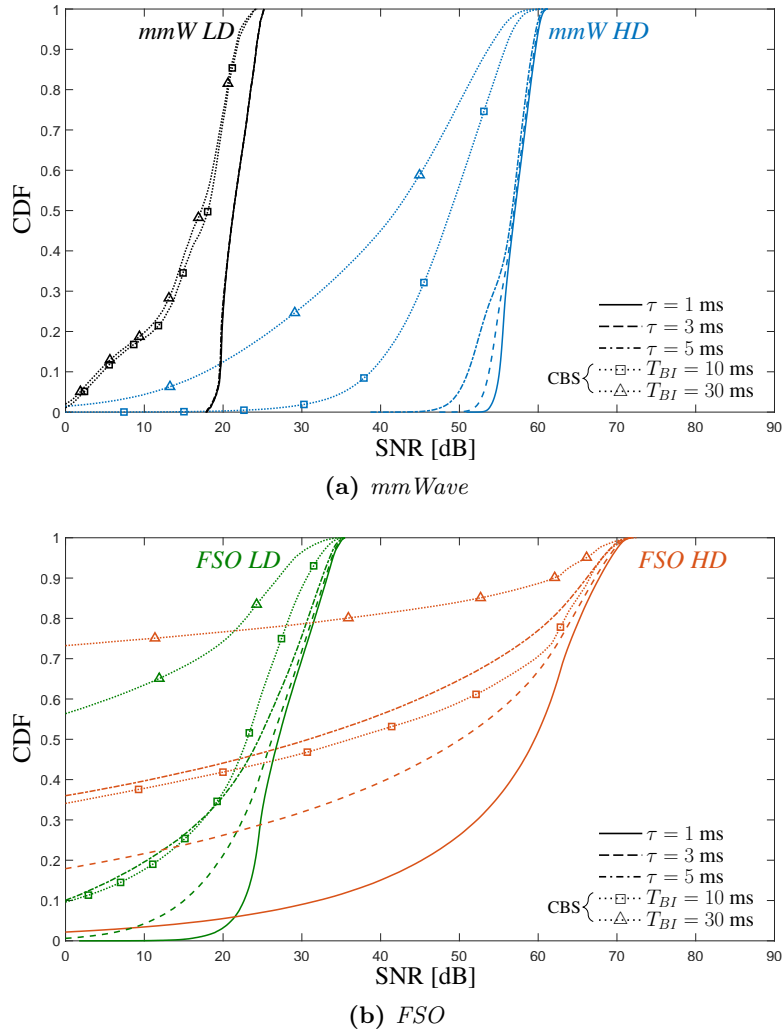


**Figure 5.14:** CDF of the SNR in scenario S2: comparison of the proposed sensor-assisted beam tracking method with a conventional beam sweeping (CBS) approach (markers). For CBS, frame durations of 10 and 30 ms are considered.

can play a major role in determining the quality of the V2V link. In fact, although the peak values of SNR are the same as in S1, in S2 the CDFs present broader tails, especially for FSO, confirming that the vehicle motion can easily lead to misalignment conditions that induce a SNR degradation on the V2V link. This reduction in SNR is directly related to the beam dimension and the timeliness of the shared information. Indeed, a significant worsening of the SNR is experienced by increasing the delay and narrowing the beam dimension, as expected.

In the challenging scenario S2, it is also interesting to compare the performance of the proposed sensor-assisted beam tracking method with a Conventional Beam Sweeping (CBS) procedure. CBS periodically performs an exhaustive search over pre-determined equispaced spatial sectors scanning all the horizontal and vertical dimensions. The periodicity coincides with the frame duration  $T_{BI}$  (see Fig. 5.4a), while the spatial spacing is given by the system resolution on both azimuth ( $\Delta\alpha_{-3dB}$  or  $2\theta_{B_z^p}$ ) and elevation ( $\Delta\beta_{-3dB}$  or  $2\theta_{B_z^p}$ ). To this extent, two different  $T_{BI}$  are

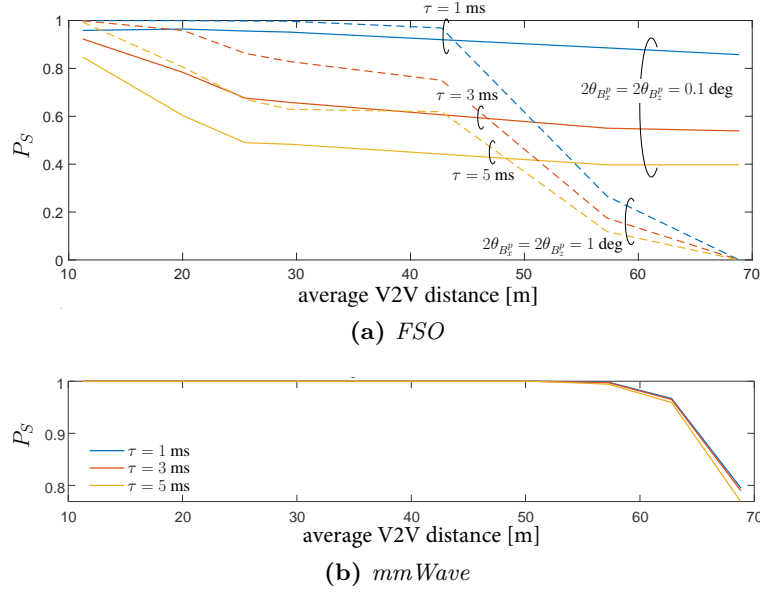


**Figure 5.15:** Service probability of the proposed sensor-assisted method versus distance (obtained from the time gap  $\Delta t$ ) on trajectory S2 for different values of delay  $\tau$ . (a) FSO V2V for HD and LD configurations, (b) mmWave V2V for mmWaveLD ( $N_a = 32$ ,  $N_r = 8$ ).

considered: 10 ms (as in 5G specifications) and 30 ms [175]. Results are shown in Fig. 5.14 for both mmWave (Fig. 5.14a) and FSO (Fig. 5.14b) technologies. The comparison highlights how the proposed sensor-assisted tracking allows for remarkable improvements in terms of SNR, especially for mmWave. It is important to mention that the considered CBS simulation assumes that the exhaustive search is instantaneously completed. This aspect, in practice, is a major impairment for the feasibility of CBS. Taking the mmWave case as example, equispaced steering vectors consider a uniform sampling of the azimuth and elevation, leading to a number of spatial sectors proportional to the square of antenna elements (i.e.,  $\mathcal{O}(N_a N_r)^2$ ). The latest 5G New Radio standard foresees a search over up to 64 sectors per frame. On one side, this limitation poses significant limitations to CBS with mMIMO systems (or, in general, narrow beam systems), on the other calls for new BA strategies. This loss of efficiency is a main motivation behind the proposed integration of sensors' information in the BA and tracking process which, besides providing improvements on the absolute value of SNR, also improves the channel capacity by significantly increasing the efficiency of the mmWave/FSO link (see Sec. 5.4.1).

Referring to the results in Figs. 5.13 and 5.14, the latency is a significant V2X degradation impairment for the proposed sensor-assisted technique, with a meaningful detrimental impact for FSO, as the transmitted power is confined in a very restricted area. This impact is deeply analyzed in Fig. 5.15, where the service probability  $P_S$  for FSO is evaluated versus the average V2V distance for S2. This probability is computed as  $P_S = \Pr(\text{SNR} > \Gamma)$ , with  $\Gamma = 10$  dB for both technologies in order to guarantee a fair comparison<sup>2</sup>. According to Fig. 5.15a,

<sup>2</sup>This value for FSO corresponds to the threshold value that guarantees a Bit Error Rate (BER)  $\leq 1.3 \times 10^{-2}$  for a Return to Zero On-Off Keying (RZ-OOK) modulation, which is the standard value for employing a 20%-overhead

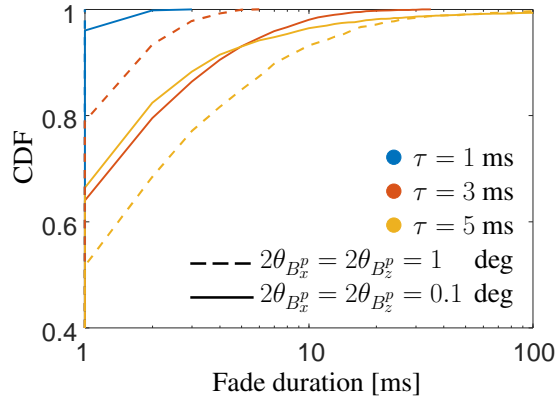


**Figure 5.16:** CDF of FDD for the proposed sensor-assisted method in scenario S2 for FSO technology and three different values of update delay  $\tau$ .

we can conclude that in a complex scenario as S2, where the vehicle dynamic is over-complicated by the presence of multiple road turnings across a contour, a relatively reliable FSO V2V communication is enabled only by a very low latency control signaling (1 ms, as foreseen by 5G systems) and for distances up to 30 m (for which  $1 - P_S \leq 10^{-2}$ ). By contrast, mmWave appears to be much more robust to delay, as can be expected from the use of less directive beams and observed from Fig. 5.15b. It is to be noticed that for distances greater than 55 m, the reduction of  $P_S$  for *mmWave LD* is to be attributed to the high path loss.

Besides the analysis of the service probability, in eV2X applications it is important to characterize the outage events. In this regard, we report the distribution of the outage event, evaluating not only its occurrence but also its duration in terms of FDD. The fade duration is defined the time interval by which the SNR persists to be below 10 dB ( $\text{SNR} < \Gamma$ ). It can be proved that the fade duration is negative exponentially distributed, with the CDF shown in Fig. 5.16 for both FSO configurations in S2. Once again, we further highlight the importance of sharing timely information to achieve a virtually continuous beam tracking. It is to be noticed that the stand-alone analysis of FDD might lead to misleading conclusions on the use of wide/narrow beams. Considering the curves for a delay of 5 ms, one may conclude that a HD system is more performing than a LD one, as it has shorter fade events. Clearly, this is not valid as it is extremely more challenging to use narrow beams rather than large ones for the considered applications, as largely motivated and proved in this article. This unexpected behavior is to be attributed to the susceptibility of narrow beams, which produces a jumping-like radiating spot at the receiver side. We found that in this specific case the number of fade events for the *FSO HD* system (yellow solid line) is 54% higher than for *FSO LD* (yellow dashed line), leading us to conclude that a narrow beam system has a higher number of fade events of shorter duration each.

To summarize, V2X over mmWave, and especially *mmWave HD* (180×90 antenna elements), guarantees a seamless service (no outage has been observed for the considered scenario), and it is a valid candidate for high-speed V2X. However,

---

Hard Detection-Forward Error Correction Code (HD-FEC) for optical communications [207, 208].

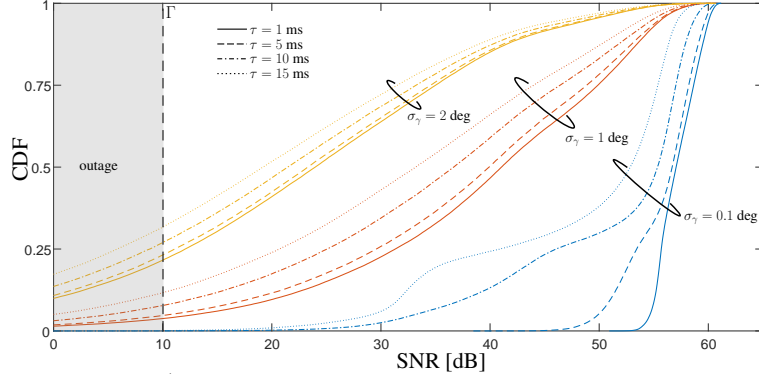


**Figure 5.17:** CDF of SNR for the proposed sensor-assisted method in scenario S2 for mmWave technology under different angular accuracies. Results are plotted for mmWaveHD for different values of delay  $\tau$  (vehicle time gap  $\Delta t = 1$  s).

it is to be noticed that the angular accuracy strongly impacts on the overall performance. In case of inaccurate sensors or orientation estimates, such that  $\sigma_\gamma$  is in the order of 1 – 2 deg, the best performing mmWave HD V2V system experiences a meaningful performance degradation, as shown in Fig. 5.17 for a reference vehicle gap  $\Delta t = 1$  s and different delay values. This result highlights the need for a very precise pose estimation that can be achieved either by single precise sensor or by proper data fusion algorithms of on-board IMU and external sensors.

### 5.5.2.5 Sensor-assisted V2V with map integration

This section present an augmentation approach for the considered sensor-assisted BA technique, where the accuracy on vehicle localization is augmented by integrating map data of the road environment. The a-priori information of road digital map can be made accessible to vehicles through V2X communications and each vehicle can combine its own pose information (obtained by GPS and IMU, for instance) with map matching, increasing positioning accuracy. A more accurate estimation of the ego vehicle location allows for a more accurate sensor-assisted beam pointing. This approach is here applied to FSO V2V, even though same considerations are still valid for mmWave as well.

The FSO performance is evaluated for V2V communications between two vehicles traveling over the winding trajectory in Fig. 5.18 (as defined in (5.31), (5.32)), with parameters  $r_0 = v/\omega_0$  m,  $v = 50$  km/h,  $\omega_0 = 0.04\pi$  rad/s,  $\omega_h = 0.6\pi$  rad/s,  $\omega_v = 0.08\pi$  rad/s,  $A_h = 0.1$  m,  $A_v = 3$  m,  $\Delta t = 1.5$  s. By indicating with  $\sigma_p^L$  the error (affecting the covariance  $\mathbf{C}_p$  in (5.6)) on vehicle position provided by the localization systems (e.g., GPS) and by  $\sigma_p^M$  the one due to map matching, it is goal of the analysis to evaluate how different combinations of such accuracy impact on BA performance. Since map only contribute in position estimation, the vehicle orientation is estimated only by vehicle on-board sensors (e.g., IMU). The error on orientation (roll, pitch and roll) measurements (affecting the covariance  $\mathbf{C}_\gamma$  in (5.7)) is assumed to be  $\sigma_\gamma = 0.1$  deg, a value which reflects state of the art

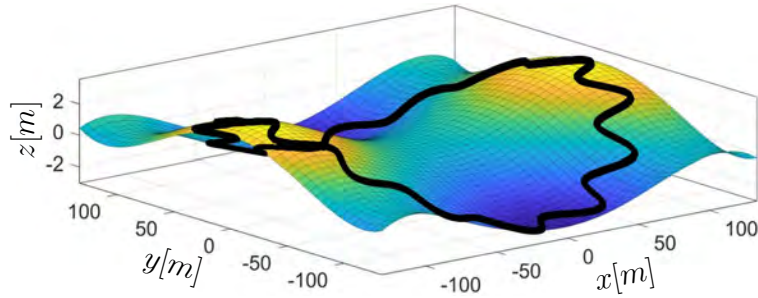


**Figure 5.18:** *Simulated winding trajectory with variations over three axis.*

automotive IMU [209].

The performance of the FSO V2V system rely on both timeliness and quality of the pose information exchanged between the two vehicles via the parallel signaling control link. The first depends on two critical parameters: the end-to-end latency  $\tau$  and the sensors' sampling rate  $f_{\text{data}}$ . The former is hereafter assumed to be equal to 3 ms, as foreseen in 5G eV2X applications [189], whereas the sampling rate  $f_{\text{data}}$  varies from 100 Hz (a standard value for commercial IMU) to 1 kHz (high-performance IMU).

We explore four different configurations of the FSO V2V communication system, ranging from an extremely directive one ( $2\theta_B = 0.1$  deg) to a relatively low directive one ( $2\theta_B = 2$  deg). Note that we conveniently refer to  $2\theta_B = 2\theta_{B_x^p} = 2\theta_{B_z^p}$  as we consider a symmetric laser spot and the reference frame is known to the reader at this point. Higher angles are not considered here as this would jeopardize the native FSO directivity. The background light is evaluated by means of the method detailed in [210], for the worst case possible in which both the direct sunlight and the skylight are maximum. The receiving unit consists of a cylindrical PD array of height  $H$  and diameter  $D$ .

We assess the performance of the proposed sensor-assisted FSO V2V beam tracking, with and without kinematic prediction and prior information on map data for map matching. Performances are evaluated for different FSO configurations and sensors' settings. Simulation parameters are summarized in Table 5.5.

The CDFs of SNR for a vehicle time gap  $\Delta t = 1.5$  s (average distance of 25.65 m), are presented in Fig. 5.19, where four different methods are compared. A clairvoyant system with oracle knowledge of all 6 DOF at any time instant is shown as upper bound (solid red line). Then, we consider the possibility for vehicles to exchange pose information without adopting any prediction algorithm (triangles in Fig. 5.19a). Lastly, the two proposed prediction-based approaches are shown, where vehicles are able to predict the respective pose with (circles) or without (crosses) map data integration. The considered localization accuracies  $\sigma_p^L$  are differentiated by the line type. In line with off-the-shelves IMU, all the results are obtained with sensor sampling  $f_{\text{data}} = 100$  Hz. Results in Fig. 5.19a highlights the importance of a precise vehicle information in order to enable a reliable FSO V2V communication. In fact, even if the localization accuracy is poor, a motion prediction significantly improves the performance. This improvement is further enhanced when map data are integrated in the whole prediction process. Fig.

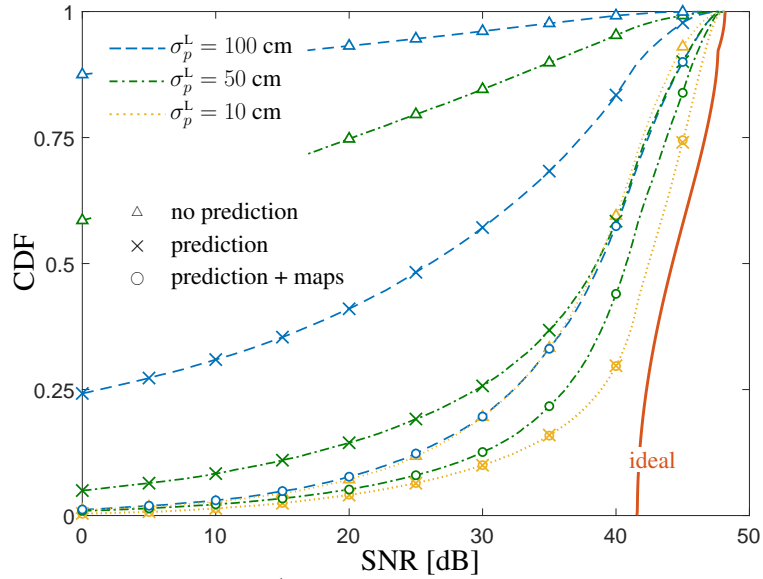
Table 5.5: Simulation parameters for FSO V2V with map integration.

Parameter	Symbol	Value
Tx power	$P_{tx}$	10 mW
Signal bandwidth	$B$	2.16 GHz
Tx laser wavelength	$\lambda$	1550 nm
Tx divergence angle	$2\theta_B$	0.1, 0.5, 1, 2 deg
Rx aperture (single PD)	$A_{rx}$	1 cm <sup>2</sup>
Rx array diameter	$D$	10 cm
Rx array height	$H$	5 cm
PD responsivity	$\rho$	0.9 A/W
Solar irradiance	$I_b$	5.58 W/m <sup>2</sup>
Noise Equivalent Power	NEP	20 pW/ $\sqrt{\text{Hz}}$
Signaling channel latency	$\tau$	3 ms
Sensor sampling	$f_{data}$	100 Hz, 1 kHz
Vehicle height	$h_1, h_2$	1.65 m
Vehicle length	$\ell_1, \ell_2$	4.7 m

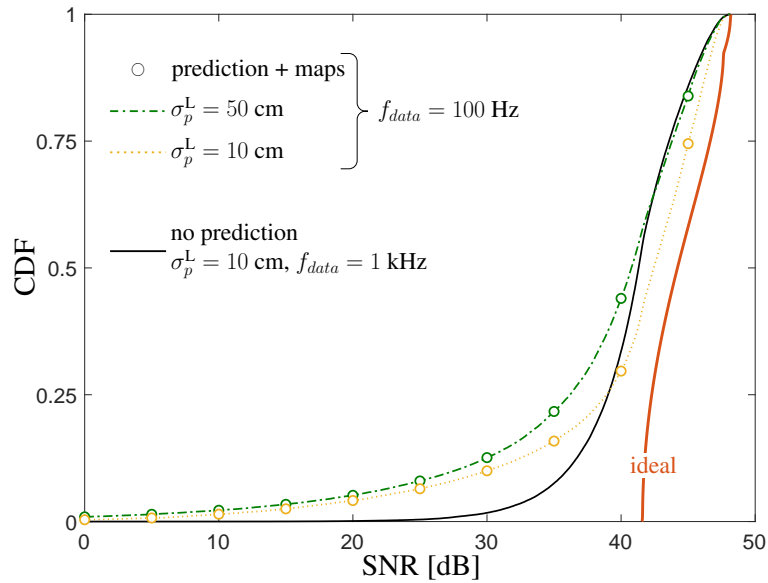
5.19b shows that the proposed enhanced pointing system is capable of improving the FSO V2V performance to the point of being comparable with that of a system with a tenfold data sampling frequency without prediction. In other words, a combination of map data with a location prediction obtained with  $f_{data} = 100$  Hz provides comparable results with respect to a system without prediction but with a faster sampling ( $f_{data} = 1$  kHz).

Another result regards the CDF of FDD, which is illustrated in Fig. 5.20 for the proposed prediction based system (with and without map integration). It is shown that integrating map information significantly reduces the fade events, which in most of the cases are below 10 ms even if the accuracy of the localization system is moderately poor (50/100 cm).

The last analysis is an assessment of the robustness with respect to the laser divergence angle  $2\theta_B$ . In particular, the selected metrics in this case is the outage probability  $P_{out}$ . The impact of  $\theta_B$  on  $P_{out}$  is shown in Fig. 5.21. With lower laser divergence the system attains a high outage probability ( $P_{out} > 10\%$ ), although the gain provided by the combination of prediction and maps is apparent. Moreover, the outage probability lowers as  $\theta_B$  increases, even though we expect that this trend would change for longer distances (time gaps), whose analysis goes beyond the scope of this paper and it is left as a future work.



(a) Fair comparison of different methods for FSO alignment in V2V systems, with  $f_{data} = 100$  Hz.



(b) Comparison of the proposed prediction-based architecture with map integration at sensors' sampling frequency  $f_{data} = 100$  Hz and a system without prediction but with  $f_{data} = 1$  kHz.

**Figure 5.19:** CDF of the SNR for the different considered methods and localization accuracies  $\sigma_p^L = \{10, 50, 100\}$  cm. Results are obtained for a time gap  $\Delta t = 1.5$  s and laser divergence angle  $2\theta_B = 1$  deg.

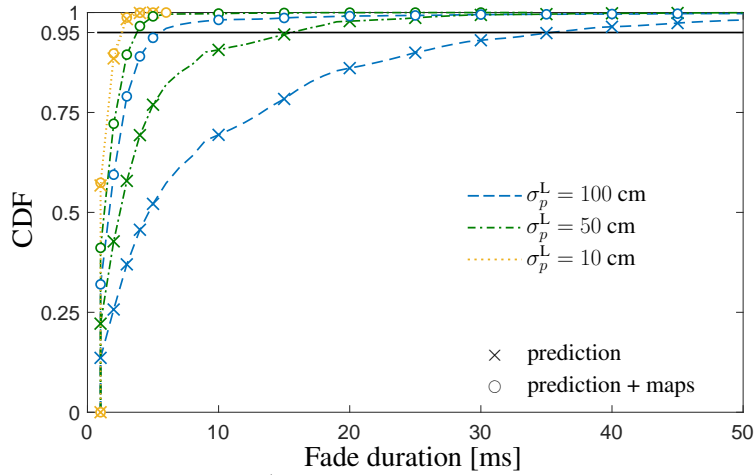


**Figure 5.20:** CDF of the FDD for the proposed prediction-based system (with and without map integration) for different values of localization accuracies  $\sigma_p^L = \{10, 50, 100\}$  cm.

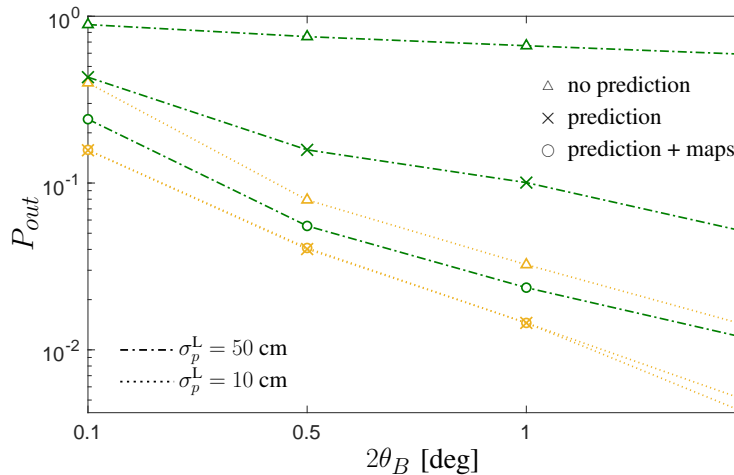


**Figure 5.21:** Outage probability  $P_{out}$  versus the laser full divergence angle  $2\theta_B$ , for different values of localization accuracy and for the different considered methods.

### 5.5.3 Concluding remarks

In this chapter, we introduced a Cooperative Intelligent Transportation Systems (C-ITS) architecture for Vehicle-to-Everything (V2X) communications based on either millimeter-Wave (mmWave) or Free-Space Optics (FSO) technologies. In order to keep the extremely narrow beams of both FSO and mmWave aligned, and thus to guarantee a seamless connectivity, we propose to integrate data from on-board sensors, which nowadays largely installed on vehicles, integrating typical mechanical information with telecommunication apparatus. Each vehicle first estimates its own pose from these sensor data, and then exchanges this information with all the others so that all vehicles in the network acquire a full knowledge of the system geometry and do not need to scan the whole beam space before transmitting. In the proposed architecture, this sensor data exchange among

vehicles is over a parallel low-rate control channel, so that vehicles can take full advantage of the multi-gigabit V2X link, i.e., either FSO- or mmWave-based, to meet the stringent low-latency and high data-rate requirements of enhanced C-ITS services.

Convincing initial numerical simulations on the effect of vertical vibrations motivated us to pursue the research to a complete and general 3D geometrical model. Performance analyses on realistic vehicles motions over a winding road confirm the feasibility of the proposed sensor-assisted mmWave- or FSO-based C-ITS architecture for Vehicle-to-Vehicle (V2V) communications, demonstrating remarkable improvements with respect to conventional beam sweeping scheme and providing an alternative to the onerous exhaustive beam search. The mmWave and FSO solutions have been compared in high and low directivity configurations in order to assess the robustness of the proposed technique with respect to the beam dimension and pose estimation errors, the latter being also considered to be reduced by integrating road map information. We verified the intuition that misalignment errors have a more detrimental impact on narrow beams by assessing the performance degradation in terms of Cumulative Distribution Function (CDF) of the Signal-to-Noise Ratio (SNR). This analysis has been used to statistically characterize the outage events in terms of occurrence probability and distribution of fade events. In particular, the main takeaways are: *(i)* mmWave and FSO technologies are attractive candidates for V2X communications, but the latter solution is viable only if precise pose information is available; *(ii)* under the same power and bandwidth settings, FSO is potentially able to provide superior performance due to its highly directive laser beams, but it is extremely sensitive to pointing errors; *(iii)* in the presence of complex motion scenarios, it is convenient to employ technologies that rely on wider beams, such as those achieved by mmWave technology; *(iv)* mmWave is in principle capable to attain the capacity of FSO, but only by deploying thousands of antenna elements, e.g.,  $180 \times 90$ , which is not feasible considering today's commercial hardware.

As a final remark, we have proposed the integration of two engineering domain that might have been considered ad standalone up to now. In our view, the evolution of connected mobility and related service requirements calls for a new paradigm of V2X communications. We deem it is highly recommended to support the telecommunication apparatus with vehicle kinematics data, using sensors' information for both advanced driving functionalities and telecommunication purposes. This is the leading idea behind the proposed approach, whose feasibility has been studied herein.

*Future research directions:* the conceptualized dual-layer sensor-assisted V2X methodology for seamless and accurate beam alignment has been intentionally assessed over artificial vehicle trajectory as to stress the misalignment induced by vehicle dynamics only. This represents a part of a more complex vehicular communication system, where multiple propagation effects (such as blockage or multipath) interact. It would be recommended to investigate the overall effect of communication and dynamics impairments to propose a robust alternative to the inefficient sweeping procedure of standardized V2X protocols. At the same time, the analysis of which on-board sensors (and motion models) should be used

for a more accurate ego-vehicle positioning as well as the possible integration of sensing sensors (such as radar, lidar, camera) to accurately estimate inter-vehicle relative distance should be considered. As a final remark, the evaluation of accurate signaling overhead has been neglected in simulations so far. This means that the exchanged information about vehicle state did not considered any quantization. On the other hand, in real systems this aspect is of high relevance, as it affects the design of the communication packet structure and the allocation of sufficient number of bits. It is then to be evaluated how quantization effect would degrade the proposed sensor-assisted solution, and at the same time understand how often should this information be exchanged not to induce significant degradation.

---

## Conclusions of the PhD journey

It is time to draw conclusions. I would like to first thank the reader who have dedicated his/her time in a careful reading of this thesis. My gratitude goes both to scientists who deeply dwell on technicalities of (part of) the contents and to any reader who got a glimpse on some ideas/concepts/applications here presented, or anyone who might have accidentally run into this work. At this point, it should be acquired to the reader that Chapters 3, 4 and 5, as well as Appendix A, deal with specific researches I carried out during my PhD and can be treated as self-consistent. Concluding remarks for each of them are present in the corresponding sections, thus I would like to devote this chapter to general conclusions about my PhD journey, where technical achievements are combined with personal aspects.

As it can be easily inferred from the contents of previous chapters, my last three years of life have been entirely devoted to scientific research in localization and communication. This PhD journey embodies the natural continuation of my previous studies in Telecommunication Engineering at Politecnico di Milano. My primary inclination to localization topics has been complemented by studies on enhancing communication techniques by feeding information from sensors. The integration of heterogeneous sensors and communications is a leitmotif of my PhD: it has been studied how to improve localization by exploring communication techniques (Chapters 3 and 4) as well as how to enhance communication performances by extracting information from perception sensors (Chapter 5 and Appendix A).

Multi-agent networks are the targeted use cases of the developed localization and communication techniques, with main (but not exclusive) applications to maritime (Chapter 3) and vehicular (Chapters 4, 5 and Appendix A) contexts. We referred to agents as static or mobile devices capable of sensing and communicating heterogeneous information. Their dynamic properties generate a time-variant network topology, where links among agents can appear and disappear according to geometrical and/or communication conditions. In the cooperative localization area (Chapters 3 and 4), graph theory has been used to describe the relations

among agents, where the existence/absence of links allows/precludes the exchange of information, enabling a robust/weak data fusion for localization. On the other hand, in the research on sensor-assisted communications (Chapter 5 and Appendix A) it has always been considered a single inter-agent (vehicle-to-vehicle) link, which is always available (LOS condition) for beam-based communication (Chapter 5) or it can be obstructed (NLOS condition) statistically (Appendix A).

Cooperative localization has been investigated in both centralized (Chapter 3) and distributed (Chapter 4) implementations, where the distinction reflects the specific targeted applications (maritime and vehicular, respectively). It is more likely to develop fully distributed solutions for vehicular networks, where the complexity and fast (order of seconds or less) variation in network topology are peculiar, and latency constraints call for decentralized processing at vehicles. Indeed, intuition suggests that in next-generation mobility vehicles directly communicate each other, without requiring support from the infrastructure, and perform a local data processing by fusing information from neighbors. On the other hand, in maritime surveillance, a different time scale (order of minutes) facilitates a centralized solution, where data from multiple agents/sensors are collected in a single fusion center. Moreover, processing offload is preferred due to intrinsic autonomy limitation of battery-powered vehicles, which are preferable to be long-lasting sensors rather than fast-processing units.

In my PhD journey I learned (or at least tried to learn) how to use a scientific attitude to statistically characterize real (existing or foreseen in the next future) problems and how to provide consistent stochastic solutions. A major contribute on this has to be ascribed to strong interactions with NATO CMRE scientists, who played a main role in building my scientific expertise, despite the few months we collaborated. The results of this collaboration are all included in Chapter 3, which represents the latest scientific enhancement of this thesis (and of my PhD journey). I am proud to succeed in finalizing the collaboration with the development of a cooperative localization technique for multi-agent systems, where a fully statistical characterization of agents allows the time-variant multi-agent network to self-localize itself and, at the same time, perform multitarget detection and tracking. A main result of the developed solution is the flexibility of adaptation in diverse contexts: from maritime to vehicular, from IoT in surveillance to industrial applications. The mere ingredients are: connected agents capable of sensing. Then, a manipulation of measurements plays it all. An initial similar technique characterizing my background on the topic is the one shown in Chapter 4 (cooperative localization in vehicular environments), where non-negligible assumptions on target existence and characterization were present, resulting in solution slightly far from being implemented in real time, but still providing evidence of the potentials. The latter being strongly supported by the simulation in realistic traffic conditions.

I also learned how beneficial (maybe mandatory) is the integration of different engineering areas. By studying sensor-assisted technique for beam-based V2X communications, I understood the need of combining telecommunications with automotive engineering in order to fasten the spread of telco in a new market. Jumping in new markets requires a fast growing of expertise, as competition is tight. Take the more advantages as possible is crucial for leading a market of new

applications, and the integration of existing facilities embodies the intention to grow, enhance and upgrade something that already exists, without imposing constraints. In this years of research, I raised the awareness of upgrading without revolutionizing, of carefully improving state of the art solutions with original contributions that may come from past experience, intuition or dame fortune (why not?). The participation in multidisciplinary projects helped me in acquiring awareness on the need of integration such that telecommunications can fulfill the demand of specific services and, at the same time, be driven by side information. This process has been considered as mandatory in the evolution of telecommunication technologies (5G and beyond) where the flexibility and adaptability to specific use cases (with different requirements) are a “must have” for success.

To conclude this thesis, I would like to recall the starting point: *Where is what? What is where?*. I hope I have managed to (partially) give answers to these questions throughout the dissertation. I wish it is clear to the reader how cooperative localization and communication have been addressed, which services can be delivered and how important is the flexibility of algorithms such that diverse types of data can be fused together. The theoretical formulation and performance assessment through simulations represent only first mandatory steps for developing and testing a given technique. Validating techniques with real data, on the other hand, is the ultimate research stage for checking robustness to unpredictable events that may occur in daily-life working conditions, refining and finalizing the algorithmic modules. This aspect has been intentionally not included here, being the works with real data in the last stage of development or currently under scientific review process. Thus, I would encourage the reader to keep updated on these aspects if he/she wishes and if I managed to grab his/her attention.





---

## Modeling a mmWave channel and developing subspace-based beam alignment techniques

The contents of this appendix refers to a minor research on the mmWave channel modeling and BA techniques, which can also be found in publication [6]. The research is strictly related to the major investigation on sensor-aided BA presented in Chapter 5, but instead of focusing on technical aspects of sensor-assisted BA, it is related to the mmWave propagation modeling in a vehicular environment. Channel modeling is not for its own sake but it is instrumental for testing different BA techniques. Specifically, we consider CBS and position sensor-aided BA, but we also develop a subspace-based technique that exploits the Low-Rank (LR) algebraic structure of the sparse mmWave channel. Another difference with respect to the V2V use case considered in Chapter 5 is that the focus of this appendix is V2I communication. We thus have a fixed agent (e.g., RSU) and a moving one (vehicle).

Besides the main challenges of mmWave communications highlighted in Chapter 5, a channel modeling specific main issue is the few availability of experimental measurements (due to the very recent hardware availability), especially in high-mobility scenarios. To overcome this limitation, mmWave channel models [211–215] are being developing. However, a complete modeling of mmWave V2X channels that also handle the evolution over space in vehicular scenarios is not yet available, being the V2X application a work in progress. Furthermore, a reliable and time efficient BA technique for high mobility has not been standardized yet, nor tested on realistic mmWave channel models.

In this research, we start from the available New York University Channel Simulator (NYUSIM) [215] mmWave channel model and we propose an extension in order to incorporate the dynamics over space of the multipath parameters. The extended NYUSIM model is then used as a tool for testing a number of BA

## Appendix A. Modeling a mmWave channel and developing subspace-based beam alignment techniques

---

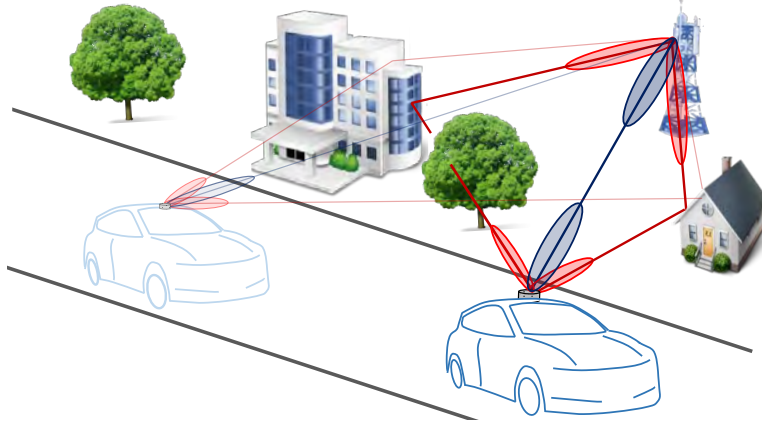


**Figure A.1:** V2I communications at two different time instants, with beampointing depending on vehicle location. Blue refers to LOS path, red to NLOS ones.

techniques. To this extend, besides CBS and sensor-assisted technique, we develop a novel BA approach that exploits the Low-Rank (LR) structure [216, 217] of the mmWave MIMO channel to select the best pair of eigen-beamformers at the two link sides based on long-term channel statistics (i.e., Angles of Arrival/Departure, AOA/AOD, and average power of dominant paths). Compared to conventional geometric BA approaches, this method does not require the computation of AOA/AOD, as it relies on a “virtual” representation of the channel. We here focus on a V2I use case and we harness the repetitiveness of the geometrical multipath pattern when vehicles travel through a same road segment several times. With this assumption, we propose to pre-compute BA codebooks constituted from the dominant eigen-beamformers of the V2I MIMO channel for each given road segment, by averaging over multiple vehicle passages. For real-time BA, location information is predicted based on GPS tracking, while eigen-beamformers are selected from pre-computed codebooks. In this way, the sequential and periodical research of the optimal beamformer is substituted by a subspace-based precoding (and combining) vector that takes into account the historical data.

### A.1 V2I mmWave scenario

---

The chosen V2I scenario is sketched in Fig. A.1, where a vehicle is moving along a straight lane at a constant velocity  $v$  and it communicates with a RSU. We consider a 2D geometry for both channel modeling and BA techniques, neglecting the vertical dimension. However, the methodology is general enough to be extended to the 3D domain. A mmWave time-slotted uplink communication is considered where the V2I transmission runs over time according to the scheduled transmission frames of duration  $T_f$ . The communication devices at Tx and Rx consist in antenna arrays of  $N_{Tx}$  and  $N_{Rx}$  elements, respectively. The multipath MIMO channel between the vehicle and the RSU at discrete time  $t$  (sampling interval is  $\Delta t$ ) is described as the superposition of  $C(t)$  clusters of  $MP_c(t)$  paths each. The

$N_{\text{Rx}} \times N_{\text{Tx}}$  complex-valued baseband channel matrix is:

$$\mathbf{H}(w, t) = \sum_{c=1}^{C(t)} \sum_{p=1}^{\text{MP}_c(t)} \alpha_{c,p}(t) \mathbf{A}(\boldsymbol{\theta}_{c,p}(t)) \mathbf{g}(wT - \text{P}_{c,p,c,p}(t)), \quad (\text{A.1})$$

where  $w = 0, \dots, W - 1$  denotes the channel tap (at symbol rate  $T^{-1}$ ) and  $W$  is the maximum temporal support of the channel response. Each path  $p$  in cluster  $c$  has complex fast-fading amplitude  $\alpha_{c,p}(t)$  (including Doppler), AOA and AOD  $\boldsymbol{\theta}_{c,p}(t) = [\boldsymbol{\theta}_{c,p}^{\text{Rx}}, \boldsymbol{\theta}_{c,p}^{\text{Tx}}]$ , and delay  $\tau_{c,p}(t)$ . The path mean power  $\text{P}_{c,p}(t) = \text{E}[|\alpha_{c,p}(t)|^2]$  (averaged over fast fading) accounts for path-loss and shadowing effects, while the cluster mean power is  $\text{P}_c(t) = \sum_p \text{P}_{c,p}(t)$ . The matrix  $\mathbf{A}(\boldsymbol{\theta}_{p,c}) = \mathbf{a}^{\text{Rx}}(\boldsymbol{\theta}_p^{\text{Rx}}) \mathbf{a}^{\text{Tx}}(\boldsymbol{\theta}_p^{\text{Tx}})^{\text{H}} \in \mathbb{C}^{N_{\text{Rx}} \times N_{\text{Tx}}}$  embeds the antenna array responses at Tx and Rx, respectively  $\mathbf{a}^{\text{Rx}}(\boldsymbol{\theta}_p^{\text{Rx}})$  and  $\mathbf{a}^{\text{Tx}}(\boldsymbol{\theta}_p^{\text{Tx}})$ , while  $\mathbf{g}(\tau)$  is the impulse response of the cascade between the Tx and Rx filters. We observe that the number of clusters, paths, angles and delays are slowly varying compared to the fast fading amplitudes. Details on how these channel parameters are modeled are given in Sec. A.2, while in Sec. A.3 we comment on how the properties of such parameters can be handled to design BA strategies.

## A.2 Modeling the mmWave LOS/NLOS V2I channel

---

In this section, we briefly recall the NYUSIM model [215] used as selected tool for mmWave channel modeling, then we detail how we extend it to include the mobility of the specific V2I scenario.

The NYUSIM model provides a stochastic description of the multipath parameters of the mmWave channel in (A.1). It is a data-driven models based on experimental data at mmWave frequencies. It groups multipath components that are close in time in temporal clusters and those that are close in space in Spatial Lobes (SL). The model comprises a number of parameters that are, in general, dependent on the specific propagation scenario (e.g., LOS or NLOS) and frequency, and evolve over time according to the wide-sense stationary uncorrelated scattering assumption. The Large Scale Parameters (LSP) model the cluster-related features while Small Scale Parameters (SSP) model the variations due to multipath propagation. Tab. A.1 summarizes the main LSP and SSP, while we remind to [215] for a complete characterization.

The NYUSIM channel model is here extended to include spatially consistent

**Table A.1:** NYUSIM classification for large scale and small scale channel parameters.

Class	Parameters
LSP	N. of clusters $C(t)$ , of paths per cluster $\text{MP}_c(t)$ and of spatial lobes; cluster shadowing and multipath shadowing; cluster delay and angle spread.
SSP	Cluster mean delay and angle; multipath amplitude $\alpha_{c,p}(t)$ , delay $\tau_{c,p}(t)$ and angles $\boldsymbol{\theta}_{c,p}(t)$ .

**Appendix A. Modeling a mmWave channel and developing subspace-based beam alignment techniques**

---

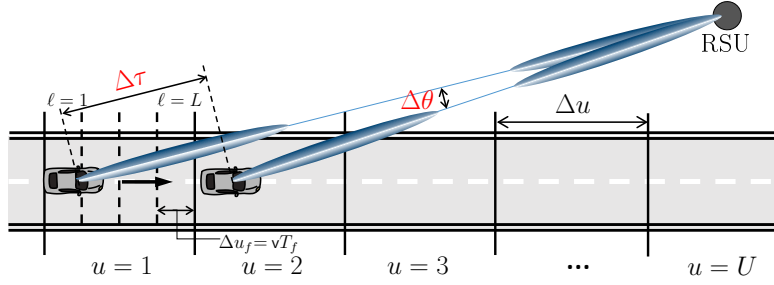


**Figure A.2:** Grid-based modeling of the road with  $U$  road segments of length  $\Delta u$ , each comprising  $L$  transmission frames of spatial duration  $\Delta u_f = vT_f$ .

dynamics of parameters, which evolve as the vehicle travels along the road. The aim is to capture fast and smooth transitions of the channel characteristics, which comprise slow variations of angles, delays and cluster mean powers when the surrounding scattering scenario is stationary, as well as sudden variations that occur when scattering objects appear/disappear generating cluster birth and death (B&D). The primary challenge is to extend a static channel model to a dynamic one, which takes into account for the fast mobility [218]. We update the channel coefficients in an iterative way along the vehicle trajectory, differentiating LSP and SSP as follows.

A grid-based approach is used to model the evolution of the LSP. The trajectory plane is divided into  $U$  road segments (see Fig. A.2) and LSP are simulated as spatially correlated over the road segments by applying an exponential spatial filter with correlation distance  $d_{\text{corr}}$  that depends on the specific scenario. 3GPP Release 14 [211] indicates a LSP correlation distance for LOS and NLOS UMi scenarios of 12 m and 15 m, respectively, even though measurements at 73 GHz in a LOS street canyon scenario suggest a smaller value of 2-5 m [219]. Here we set  $d_{\text{corr}} = 5$  m.

The road segment dimension  $\Delta u$  (see Fig. A.2) is chosen so that angles and delays, that are typically slowly-varying [217], can be assumed as constant within  $\Delta u$  (this property will be exploited for BA design in Sec. A.3). For delays, assuming the worst case of motion along the LOS path, the delay variation  $\Delta\tau$  is constrained to be lower than the system temporal resolution

$$\Delta\tau = \frac{\Delta u}{c} < \frac{1}{B}, \quad (\text{A.2})$$

where  $c$  is the propagation speed and  $B$  the signal bandwidth. For angles, in case of motion orthogonal to the LOS path, at distance  $d$  from the RSU, the angle variation  $\Delta\theta$  is set to be lower than the antenna array resolution

$$\Delta\theta \approx \frac{\Delta u}{d} < \frac{2}{N}, \quad (\text{A.3})$$

(here we assumed an ULA of  $N$  antennas with half-wavelength spacing). By combining (A.2)-(A.3), it follows that

$$\Delta u < \min\left(2\frac{d}{N}, \frac{c}{B}\right). \quad (\text{A.4})$$

As an example, for  $d = 10$  m,  $B = 400$  MHz,  $N = 20$ , we get  $\Delta u < 0.75$  m. Assuming a time frame  $T_f = 10$  ms (or 1 ms for most dynamic applications) and a vehicle velocity  $v = 50$  km/h, this road segment of length  $\Delta u$  corresponds to  $L = 5$  (or 50) transmission blocks of spatial length  $\Delta u_f = v T_f$ . Notice that fading amplitudes are fast varying and are assumed to change block by block. The update of main channel parameters over the road segments is described in the following.

**Path loss.**

Following the path loss model in [220], the evolution of path loss varies with the Tx-Rx distance  $d$  as:

$$PL(d)[\text{dB}] = 20 \log_{10} \frac{4\pi}{\lambda} + 10\kappa \log_{10}(d) + \chi, \quad (\text{A.5})$$

where  $\kappa$  is the Path Loss Exponent (PLE) and  $\chi$  is the log-normal shadow-fading with mean 0 dB and variance  $\sigma^2$ .

**Time clusters and spatial lobes.**

These LSP do not rapidly change in time and they are pre-computed for each road segment. Their evolution from a road segment to the other is spatially correlated with correlation distance  $\mathbf{d}_{\text{corr}}$  and thus it depends on the scenario and frequency. A B&D Poisson process models the variation of the mean number of clusters  $C(t)$  over the road segments. We assume that B&D always happens to the weakest or oldest cluster with a probability of occurrence

$$P_r(t) = 1 - \exp(-\lambda_c(t - t_0)), \quad (\text{A.6})$$

where  $\lambda_c$  is the B&D mean rate here set to  $\lambda_c = v/\mathbf{d}_{\text{corr}}$  [221]. Assuming only one occurrence of B&D per time instant, the following three cases can occur:

- *birth*: a new cluster appears alone;
- *death*: a cluster disappears without a new appearance;
- *regeneration*: a cluster disappears and a new one appears with different mean angle, delay and power.

**Cluster mean delay and power**

When the terminal moves, the excess delay of each cluster  $c$  evolves according to the 3GPP specifications in [211], where the update is based on the velocity, direction, and the time-variant AOA and AOD. This procedure is valid for each cluster  $c$ , except for the LOS one (if present) that has null delay. Vehicle mobility introduces variations also on the cluster power according to [211]. Thus, the shadowing factor of each cluster is generated as correlated over the road segments by applying a spatial exponential filter with correlation distance  $\mathbf{d}_{\text{corr}}$ .

**Cluster mean angles**

According to [219], the cluster mean angles for AOA ( $\theta_{c,\text{AOA}}$ ) and AOD ( $\theta_{c,\text{AOD}}$ )

evolve as:

$$\theta_{c,\text{AOD}}(t) = \theta_{c,\text{AOD}}(t_0) + S_{c,\text{AOD}} \cdot (t - t_0), \quad (\text{A.7})$$

$$\theta_{c,\text{AOA}}(t) = \theta_{c,\text{AOA}}(t_0) + S_{c,\text{AOA}} \cdot (t - t_0), \quad (\text{A.8})$$

where  $S_{c,\text{AOA}}$  and  $S_{c,\text{AOD}}$  are the slopes of the changing rates:

$$S_{c,\text{AOD}} = \frac{v \sin(\varphi_v(t_0) - \varphi_{c,\text{AOD}}(t_0) + \psi_{c,\text{AOD}})}{d}, \quad (\text{A.9})$$

$$S_{c,\text{AOA}} = \frac{v \sin(\varphi_v(t_0) - \varphi_{c,\text{AOA}}(t_0) + \psi_{c,\text{AOA}})}{d}, \quad (\text{A.10})$$

with  $\psi_{c,\text{AOA}}$  and  $\psi_{c,\text{AOD}}$  cluster specific reflection surface angles which, for NLOS clusters, are modeled as uniform random variables  $\psi_{c,\text{AOD}} \sim \mathcal{U}(0, \pi)$ ,  $\psi_{c,\text{AOA}} \sim \mathcal{U}(-\pi, 0)$ , while they are set to 0 for the LOS cluster.  $\varphi_v(t_0)$  is the vehicle motion direction on the horizontal plane.

To summarize, the evolution of SSP and LSP is simulated using different space scales, as illustrated in Fig. A.2. LSP are constant within each road segment  $u$  and spatially correlated from segment to segment, while SSP evolve also within the road segment according to the above models. The length of the road segment  $\Delta u$  is selected such that angles, delays and mean powers are almost invariant within the road segment itself, while fading amplitudes change rapidly within the segment and also from one transmission block to the other. These different varying rates are used in next section to propose channel-based BA techniques. A visual representation of the evolution over space of some LSP/SSP is in Sec. A.4.

### A.3 Beam alignment strategies

---

This section is dedicated to the description of BA strategies. We describe the proposed Sensor-Assisted (SA) subspace-based BA technique that exploit the sparsity characteristics of mmWave channel, highlighting the differences with respect to a geometric approach and CBS technique. We recall that in CBS, Tx and Rx perform an exhaustive scanning procedure over a pre-defined set of precoding and combining vectors to find the optimal pair that maximizes the received power. As intuition might suggest, such a divide and conquer approach is extremely time consuming. We would like to avoid such a waste of resources by taking advantage of vehicle on-board location sensors and LR channel structure [216, 217], such that precoding/combining vectors can be selective proactively. The idea is to explore long-term Channel State Information (CSI) to estimate the dominant channel eigen-components and accordingly tune the BA. Since the geometrical structure of the multipath channel is strongly correlated to the location (i.e., the road segment) and is slowly varying over time, these eigen-beamformers can be pre-computed from geo-referenced long-term CSI data within each road segment. As a reference, we also consider geometrical location-aided BA approaches that use as codebooks the canonical steering vectors associated with equispaced AOA/AOD [161].

According to Sec. A.3, the MIMO channel (A.1) within the road segment  $u$

## Appendix A. Modeling a mmWave channel and developing subspace-based beam alignment techniques

---

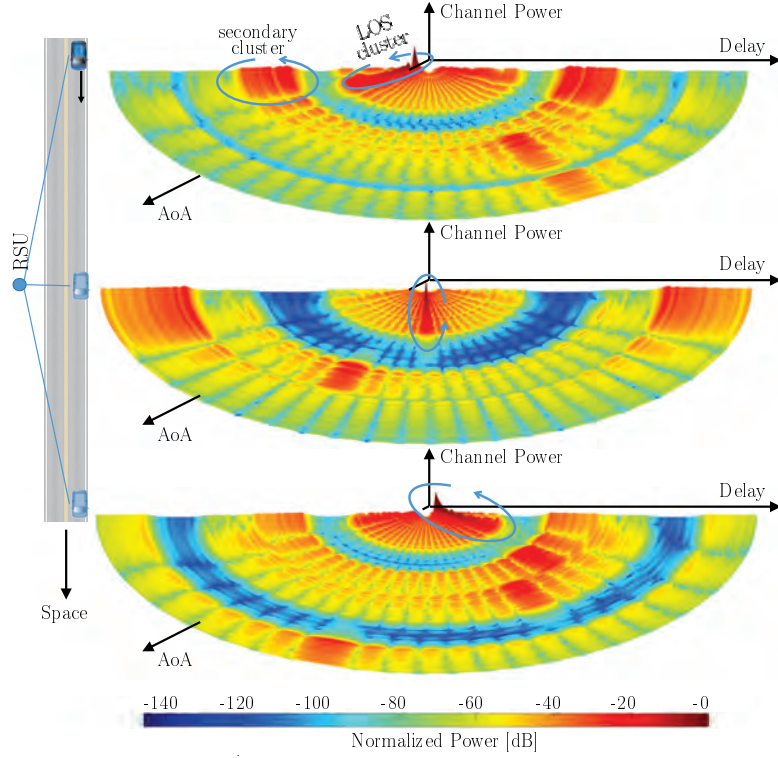


**Figure A.3:** An example of three temporal snapshots of the mmWave V2I channel corresponding to the vehicle positions indicated in the figure.

and the transmission block  $\ell$  is reparametrized as:

$$\mathbf{H}_\ell(w, u) = \sum_{c=1}^{C(u)} \sum_{p=1}^{MP_c(u)} \alpha_{c,p,\ell}(u) \mathbf{A}(\boldsymbol{\theta}_{c,p}(u)) \mathbf{g}(wT - \tau_{c,p}(u)), \quad (\text{A.11})$$

where the slow index  $u = 1, \dots, U$  runs over the road segments, while the fast index  $\ell = 1, \dots, L$  over the transmission blocks within the road segment (see Fig. 2). Angles  $\boldsymbol{\theta}_{c,p}(u)$ , delays  $\tau_{c,p}(u)$  and average powers  $P_{p,c}(u)$  are approximated as constant within the road segment for BA design, while fading amplitudes  $\alpha_{c,p,\ell}(u)$  change block by block. We also assume that the sparse mmWave channel matrix has a LR structure, with spatial and temporal subspaces (depending on slowly-varying angles and delays, respectively) that are constant within the road segment [216, 217].

To motivate the use of the LR model, in Fig. A.3 we give an example of three snapshots of the NYUSIM mmWave V2I LOS channel with dynamics modeled as in Sec. A.2 (referring to the scenario in Fig. A.1-A.2, further details in Sec. A.4) at three different time instants corresponding to the starting, middle and ending point of the considered road. The figure is intended to show how the channel is characterized by a dominant cluster (the LOS one) and few secondary clusters with much lower power (red areas). This motivates the use of a BA LR codebook with one or few eigen-beamformers.

### A.3.1 Sensor-assisted low-rank beam alignment

The SA-LR method herein proposed uses the eigen-beamformers associated to the dominant Tx/Rx channel components as precoding/combining vectors according to the model (A.11) and the LR assumption. The repetitiveness of channel conditions occurring when vehicles pass over a same road segment (similar LSP values) allows to precompute the eigen-beamformers. Under this assumption, we claim the availability of a dataset (denoted with  $\mathbf{U}^{\text{Tx}}(u)$  and  $\mathbf{U}^{\text{Rx}}(u)$ ) containing geolocalized pre-computed eigen-beamformers to be used at both Tx and Rx sides. This dataset is obtained by computing channel sample correlations over repeated vehicle passages  $m = 1, \dots, M$  on a same road segment. Though channel realization of the  $m$ -th passage  $\mathbf{H}_\ell^{(m)}(w, u)$  differs from another due to fast fading, they share similar trajectories and LSP conditions, as dominant cluster components are likely not to change significantly over time. The underlying idea is the availability of a common data center, such that any vehicle traveling along a specific road segment can query the database and use the given eigen-beamformer. The optimal precoding and combining vectors at road segment  $u$  are thus obtained as:

$$\hat{\mathbf{w}}^{\text{Rx}}(u) = \arg \max_{\mathbf{w}^{\text{Rx}} \in \mathbf{U}^{\text{Rx}}(u)} \mathbf{w}^{\text{RxH}}(u) \mathbf{R}_S^{\text{Rx}}(u) \mathbf{w}^{\text{Rx}}(u) = \mathbf{u}_1^{\text{Rx}}, \quad (\text{A.12})$$

$$\hat{\mathbf{w}}^{\text{Tx}}(u) = \arg \max_{\mathbf{w}^{\text{Tx}} \in \mathbf{U}^{\text{Tx}}(u)} \mathbf{w}^{\text{TxH}}(u) \mathbf{R}_S^{\text{Tx}}(u) \mathbf{w}^{\text{Tx}}(u) = \mathbf{u}_1^{\text{Tx}}, \quad (\text{A.13})$$

where  $\mathbf{U}^{\text{Rx}}(u)$  and  $\mathbf{U}^{\text{Tx}}(u)$  denote the eigenvectors of the sample spatial correlation matrices  $\mathbf{R}_S^{\text{Rx}}(u)$  and  $\mathbf{R}_S^{\text{Tx}}(u)$ , while  $\mathbf{u}_1^{\text{Rx}}$  and  $\mathbf{u}_1^{\text{Tx}}$  are the dominant ones.

The sample spatial correlation matrices are computed as:

$$\mathbf{R}_S^{\text{Rx}}(u) = \frac{1}{MLW} \sum_{m=1}^M \sum_{\ell=1}^L \sum_{w=0}^{W-1} \mathbf{H}_\ell^{(m)}(w, u) \mathbf{H}_\ell^{(m)H}(w, u), \quad (\text{A.14})$$

$$\mathbf{R}_S^{\text{Tx}}(u) = \frac{1}{MLW} \sum_{m=1}^M \sum_{\ell=1}^L \sum_{w=0}^{W-1} \mathbf{H}_\ell^{(m)H}(w, u) \mathbf{H}_\ell^{(m)}(w, u). \quad (\text{A.15})$$

The operational assumption is that the geometrical configuration of the main clusters of scattering/shadowing objects in the surroundings of road segment  $u$  remains quasi-stationary over vehicle passages. The approach can be extended so as to exploit multiple eigen-beamformers rather than a single one, to account for possible slight changes in the environment (e.g., the LOS cluster is blocked and the second one becomes dominant). This increases the complexity but better exploits the channel properties as will be shown Sec. A.4 when we assess the performance.

### A.3.2 Sensor-assisted long-term geometrical beam alignment

The Sensor-Assisted Long-Term Geometrical BA method (SA-LTG) is the geometrical equivalent of the SA-LR one. As SA-LR, it uses the location information to select the optimal precoding/combiner vector among pre-defined codebooks  $\mathbf{W}^{\text{Tx}}$  and  $\mathbf{W}^{\text{Rx}}$ . This time the codebooks do not contain the long-term eigen-beamformers but equi-spaced steering vectors than span all over the angular space

---

**Appendix A. Modeling a mmWave channel and developing subspace-based beam alignment techniques**

---

(e.g., 180 deg for an ULA) [161]. Similarly to CBS, BA is based on the geometrical steering vectors but, in this case, it is road-segment dependent as:

$$\hat{\mathbf{w}}^{\text{Rx}}(u) = \arg \max_{\mathbf{w}^{\text{Rx}} \in \mathcal{W}^{\text{Rx}}} \mathbf{w}^{\text{RxH}}(u) \mathbf{R}_S^{\text{Rx}}(u) \mathbf{w}^{\text{Rx}}(u), \quad (\text{A.16})$$

$$\hat{\mathbf{w}}^{\text{Tx}}(u) = \arg \max_{\mathbf{w}^{\text{Tx}} \in \mathcal{W}^{\text{Tx}}} \mathbf{w}^{\text{TxH}}(u) \mathbf{R}_S^{\text{Tx}}(u) \mathbf{w}^{\text{Tx}}(u). \quad (\text{A.17})$$

As for SA-LR, the codebooks are pre-computed using the long-term sample correlation matrices (A.15)-(A.15) that average over  $L$  blocks and  $M$  vehicle passages.

### A.3.3 Sensor-assisted geometrical beam alignment

The Sensor-Assisted Geometrical (SA-G) BA technique is based on the exchange of location information between vehicle and RSU. In this way, Tx and Rx are able to compute estimates of the LOS directions here modeled as:

$$\hat{\theta}_\ell^{\text{Rx}}(u) = \theta_\ell^{\text{Rx}}(u) + \varepsilon_\ell^{\text{Rx}}(u), \quad (\text{A.18})$$

$$\hat{\theta}_\ell^{\text{Tx}}(u) = \theta_\ell^{\text{Tx}}(u) + \varepsilon_\ell^{\text{Tx}}(u), \quad (\text{A.19})$$

where  $\varepsilon_\ell^{\text{Rx}}(u)$  and  $\varepsilon_\ell^{\text{Tx}}(u)$  define angle estimate errors as a consequence of inaccurate vehicle positioning (e.g., GPS errors). Precoding and combining vectors are selected as:

$$\hat{\mathbf{w}}_\ell^{\text{Rx}}(u) = \mathbf{a}^{\text{Rx}}(\hat{\theta}_\ell^{\text{Rx}}(u)), \quad (\text{A.20})$$

$$\hat{\mathbf{w}}_\ell^{\text{Tx}}(u) = \mathbf{a}^{\text{Tx}}(\hat{\theta}_\ell^{\text{Tx}}(u)), \quad (\text{A.21})$$

thus coinciding with conventional steering vectors for that estimated AOA and AOD (with a spatial granularity of approximately  $\frac{180}{N}$  deg). Clearly, this method relies only on the geometry of the LOS link connecting Tx and Rx, without considering multipath and possible NLOS conditions. In NLOS channels, it is clearly impracticable, as will be shown in Sec. A.4.

## A.4 Performance assessment in a LOS/NLOS V2I scenario

---

In this section we provide BA performance comparison among the diverse sensor-assisted BA strategies discussed in Sec. A.3 and CBS. The mmWave V2I channel is simulated between a vehicle and a RSU in a 2D NYUSIM UMi environment as in Figs. 1-3. The vehicle drives along 150 m on a straight road at constant  $v = 50$  km/h. The RSU is located in the middle of the simulated lane, 10 m apart the road. The whole scenario is divided into road segments of  $\Delta u = 0.7$  m to guarantee both spatial and temporal consistency, while the channel is updated every  $\Delta t = T_f = 10$  ms (frame duration of 5G systems). The V2I link operates at the carrier frequency of  $f_c = 73$  GHz with a bandwidth of  $B = 400$  MHz, and a Tx power of 40 dBm. Both Tx vehicle and Rx infrastructure are equipped with half-wavelength spaced ULAs of  $N_{\text{Tx}} = N_{\text{Rx}} = 20$  elements each. The mmWave

---

**Appendix A. Modeling a mmWave channel and developing subspace-based beam alignment techniques**

---

dynamic MIMO channel is simulated according to the NYUSIM model extended as in Sec. A.2 for both LOS and NLOS scenarios, with simulation parameters as in [215]. The pulse waveform  $\mathbf{g}(\boldsymbol{\tau})$  is a raised cosine pulse with roll-off 0.3. The performances of BA algorithms are evaluated in terms of power loss with respect to an ideal clairvoyant system. BA performances are evaluated in terms of SNR, which requires the computation of the received power as:

$$P_{\text{Rx}}(u) = \text{E} \left[ \left| \hat{\mathbf{w}}^{\text{RxH}}(u) \mathbf{H}_\ell(u) \hat{\mathbf{w}}^{\text{Tx}}(u) \right|^2 \right], \quad (\text{A.22})$$

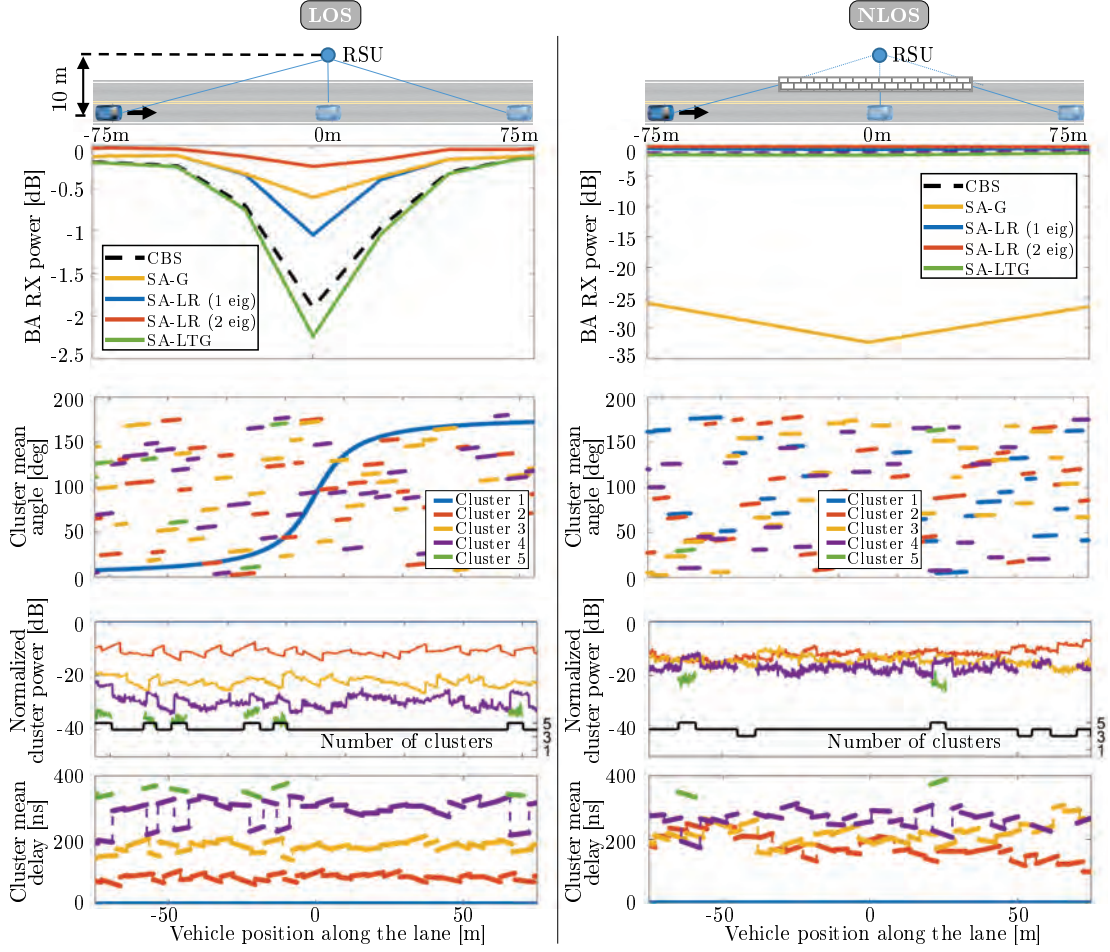
where the precoding/combining vectors are chosen for each BA method as described in Sec. A.3. The impact of position accuracy for all methods is considered by simulating a Gaussian localization error with standard deviation of 10 cm (for all methods but CBS, which is position-independent). This value is chosen to match eV2X requirements [189].

Fig. A.4 shows the channel dynamics and the BA performances versus the vehicle location over the road in LOS (left) and a NLOS (right) propagation conditions, respectively. The reported channel parameters are the number of clusters, the cluster mean power (normalized with respect to the LOS one), the cluster mean delay (with respect to the LOS one) and the cluster mean angle. The performance analysis is provided for SA-G, SA-LR, SA-LTG and CBS methods. For SA-LR, results for both solutions with one or two dominant eigen-beamformers are provided.

In order to distinguish between LOS and NLOS scenarios, a first and straightforward intuition is to observe the evolution of the cluster mean angles: the permanent presence of a cluster (i.e., the LOS one) with time continuous evolution of the mean angle is prevailing. Such a dominant effect is also confirmed by the power ratio: in the left column (LOS) the secondary clusters have a normalized powers which are order of magnitude lower, while in the right column (NLOS) all the cluster mean powers are comparable. Similar considerations can be made for the cluster mean delay.

Analyzing the BA performance in LOS and NLOS cases, it is of interest to examine the behavior in the most critical condition, where the LOS angle most rapidly evolves. This is verified in the middle of the road (at location 0 m), where the vehicle is in front of the RSU. The SA-G technique is suited only for LOS environments, where it provides meaningful gain with respect to CBS. The SA-LR solution emerges as the most reliable BA technique in LOS/NLOS scenarios, as it is able to capture the dominant rank-1 channel component (which typically does not reduce to a single AOA/AOD) and it is more robust to space-varying multipath channel conditions (e.g., the disappearance of the LOS cluster). Furthermore, SA-LR does not require AOD/AOA computation. This confirms that the adoption of eigen-beamformers instead of classical angle-based steering vectors could strongly improve the BA performance. Moreover, we would also like to remark that a SA-LR BA technique does not require a beam sweeping procedure as CBS, thus reducing the signaling overhead and the latency due to BA, improving the communication efficiency.

## Appendix A. Modeling a mmWave channel and developing subspace-based beam alignment techniques



**Figure A.4:** *mmWave V2I communication in LOS (left) and NLOS (right) conditions: scenario, BA performance, evolution of cluster angle, power and delay.*

### A.5 Concluding remarks

In this research, we extended the NYUSIM channel model to characterize a mmWave V2I communication. The extension accounts for spatial consistency and different space/time scales of the channel parameters' dynamics. The extended channel model has been used as a tool for designing and testing a number of BA techniques, comparing sensor-assisted solutions with conventional sweeping. Results demonstrate the enhancements due to the use of the sparse LR structure of the channel, jointly with the repetitiveness of channel statistics over multiple vehicle passages, showing the profitability of sensor-assisted solutions that avoid time-consuming exhaustive sweeping procedures. The proposed SA-LR BA, relying on eigen-beamformers obtained by averaging over multiple available datasets and using precise location tracking, is shown to provide meaningful performance gains compared to conventional geometrical techniques, both in LOS and NLOS cases. Besides gains in terms of higher received power, the access to geo-referenced eigen-beamformers allows to avoid onerous sweeping which are extremely time-consuming and severely impacting on the efficiency by increasing signaling overhead over data.



---

---

## Bibliography

- [1] M. Brambilla, G. Soatti, and M. Nicoli, “Precise vehicle positioning by cooperative feature association and tracking in vehicular networks,” in *2018 IEEE Statistical Signal Process. Workshop (SSP)*, pp. 648–652, Jun. 2018.
- [2] M. Brambilla, M. Nicoli, G. Soatti, and F. Deflorio, “Augmenting vehicle localization by cooperative sensing of the driving environment: insight on data association in urban traffic scenarios,” *IEEE Trans. Intell. Transp. Syst.*, vol. 21, pp. 1646–1663, Apr. 2020.
- [3] M. Brambilla, M. Nicoli, S. Savaresi, and U. Spagnolini, “Inertial sensor aided mmwave beam tracking to support cooperative autonomous driving,” in *2019 IEEE Int. Conf. Commun. Workshops (ICC Workshops)*, pp. 1–6, May 2019.
- [4] M. Brambilla, A. Matera, D. Tagliaferri, M. Nicoli, and U. Spagnolini, “RF-assisted free-space optics for 5G vehicle-to-vehicle communications,” in *2019 IEEE Int. Conf. Commun. Workshops (ICC Workshops)*, pp. 1–6, May 2019.
- [5] M. Brambilla, D. Tagliaferri, M. Nicoli, and U. Spagnolini, “Sensor and map-aided cooperative beam tracking for optical V2V communications,” in *2020 IEEE Veh. Technol. Conf. Workshops (VTC-Spring)*, pp. 1–6, May 2020.
- [6] M. Brambilla, D. Pardo, and M. Nicoli, “Location-assisted subspace-based beam alignment in LOS/NLOS mm-wave V2X communications,” in *2020 IEEE Int. Conf. Commun. (ICC)*, pp. 1–6, Jun. 2020.
- [7] M. Brambilla, L. Combi, A. Matera, D. Tagliaferri, M. Nicoli, and U. Spagnolini, “Sensor-Aided V2X Beam Tracking for Connected Automated Driving: Distributed Architecture and Processing Algorithms,” *Sensors*, vol. 20, no. 3573, 2020.
- [8] R. Mendrzik, M. Brambilla, C. Allmann, M. Nicoli, W. Koch, G. Bauch, K. LePage, and P. Braca, “Joint multitarget tracking and dynamic network localization in the underwater domain,” in *2020 IEEE Int. Conf. Acoustics, Speech and Signal Process. (ICASSP)*, pp. 4890–4894, May 2020.
- [9] L. Barbieri, M. Brambilla, R. Pitic, A. Trabatttoni, S. Mervic, and M. Nicoli, “UWB real-time location systems for smart factory: Augmentation methods and experiments,” in *2020 IEEE Annual Int. Symposium on Personal, Indoor and Mobile Radio Commun. (PIMRC)*, pp. 1–7, Aug. 2020.

## Bibliography

---

- [10] OpenStreetMap contributors, “Planet dump retrieved from <https://planet.osm.org>.” <https://www.openstreetmap.org>, 2017.
- [11] E. D. Kaplan and C. Hegarty, *Understanding GPS: principles and applications*. Norwood: Artech House, 2006.
- [12] A. Küpper, *Location-based services: fundamentals and operation*. Wiley, 2005.
- [13] I. F. Akyildiz, D. Pompili, and T. Melodia, “Underwater acoustic sensor networks: research challenges,” *Ad Hoc Networks*, vol. 3, no. 3, pp. 257 – 279, 2005.
- [14] A. R. Barron, “Entropy and the central limit theorem,” *The Annals of probability*, pp. 336–342, 1986.
- [15] C. W. Gardiner, *Handbook of stochastic methods for physics, chemistry and the natural sciences*, vol. 13. 3rd ed., 2004.
- [16] U. Spagnolini, *Statistical signal processing in engineering*. John Wiley & Sons, 2018.
- [17] F. R. Kschischang, B. J. Frey, and H. . Loeliger, “Factor graphs and the sum-product algorithm,” *IEEE Trans. Inf. Theory*, vol. 47, pp. 498–519, Feb. 2001.
- [18] D. Gaglione, G. Soldi, F. Meyer, F. Hlawatsch, P. Braca, A. Farina, and M. Z. Win, “Bayesian information fusion and multitarget tracking for maritime situational awareness,” *IET Radar, Sonar Navigation*, vol. 14, pp. 1845–1857, Nov. 2020.
- [19] G. Ferri, A. Munafó, A. Tesei, P. Braca, F. Meyer, K. Pelekanakis, R. Petrocchia, J. Alves, C. Strode, and K. LePage, “Cooperative robotic networks for underwater surveillance: an overview,” *IET Radar, Sonar Navigation*, vol. 11, pp. 1740–1761, Dec. 2017.
- [20] P. Braca, R. Goldhahn, G. Ferri, and K. D. LePage, “Distributed information fusion in multistatic sensor networks for underwater surveillance,” *IEEE Sensors J.*, vol. 16, pp. 4003–4014, Jun. 2016.
- [21] P. Braca, P. Willett, K. LePage, S. Marano, and V. Matta, “Bayesian Tracking in Underwater Wireless Sensor Networks With Port-Starboard Ambiguity,” *IEEE Trans. Signal Process.*, vol. 62, pp. 1864–1878, Apr. 2014.
- [22] L. Elkins, D. Sellers, and W. R. Monach, “The autonomous maritime navigation (AMN) project: field tests, autonomous and cooperative behaviors, data fusion, sensors, and vehicles,” *J. Field Robot.*, vol. 27, pp. 790–818, Sep. 2010.
- [23] I. F. Akyildiz and D. abd T. Melodia, “Underwater acoustic sensor networks: research challenges,” *Ad Hoc Netw.*, vol. 3, pp. 257–279, Mar. 2005.

## Bibliography

---

- [24] F. Zafari, A. Gkelias, and K. K. Leung, "A survey of indoor localization systems and technologies," *IEEE Commun. Surveys Tuts.*, vol. 21, pp. 2568–2599, Apr. 2019.
- [25] H. Wymeersch, J. Lien, and M. Z. Win, "Cooperative localization in wireless networks," *Proc. IEEE*, vol. 97, pp. 427–450, Feb. 2009.
- [26] Y. Shen, H. Wymeersch, and M. Z. Win, "Fundamental limits of wideband localization – Part II: Cooperative networks," *IEEE Trans. Inf. Theory*, vol. 56, pp. 4981–5000, Oct. 2010.
- [27] A. Conti, M. Guerra, D. Dardari, N. Decarli, and M. Z. Win, "Network experimentation for cooperative localization," *IEEE J. Sel. Areas Commun.*, vol. 30, pp. 467–475, Jan. 2012.
- [28] H. Liu, H. Darabi, P. Banerjee, and J. Liu, "Survey of wireless indoor positioning techniques and systems," *IEEE Trans. Syst., Man, Cybern.*, vol. 37, pp. 1067–1080, Oct. 2007.
- [29] N. Patwari, J. N. Ash, S. Kyperountas, A. O. Hero, R. L. Moses, and N. S. Correal, "Locating the nodes: Cooperative localization in wireless sensor networks," *IEEE Signal Process. Mag.*, vol. 22, pp. 54–69, Jul. 2005.
- [30] Y. Li, Y. Wang, W. Yu, and X. Guan, "Multiple autonomous underwater vehicle cooperative localization in anchor-free environments," *IEEE J. Ocean. Eng.*, vol. 44, no. 4, pp. 895–911, 2019.
- [31] G. Qiao, C. Zhao, F. Zhou, and N. Ahmed, "Distributed localization based on signal propagation loss for underwater sensor networks," *IEEE Access*, vol. 7, pp. 112985–112995, Aug. 2019.
- [32] S. Zhang, E. Staudinger, T. Jost, W. Wang, C. Gentner, A. Dammann, H. Wymeersch, and P. A. Hoeher, "Distributed direct localization suitable for dense networks," *IEEE Trans. Aerosp. Electron. Syst.*, vol. 56, pp. 1209–1227, Apr. 2020.
- [33] A. Liu, L. Lian, V. Lau, G. Liu, and M. Zhao, "Cloud-assisted cooperative localization for vehicle platoons: A turbo approach," *IEEE Trans. Signal Process.*, vol. 68, pp. 605–620, Jan. 2020.
- [34] S. Sridhar and A. Eskandarian, "Cooperative perception in autonomous ground vehicles using a mobile-robot testbed," *IET Intell. Transp. Syst.*, vol. 13, pp. 1545–1556, Sep. 2019.
- [35] Y. Ma, C. Tian, and Y. Jiang, "A multitag cooperative localization algorithm based on weighted multidimensional scaling for passive UHF RFID," *IEEE Internet Things J.*, vol. 6, pp. 6548–6555, Mar. 2019.
- [36] S. Safavi, U. A. Khan, S. Kar, and J. M. F. Moura, "Distributed localization: A linear theory," *Proc. IEEE*, vol. 106, pp. 1204–1223, Jul. 2018.

## Bibliography

---

- [37] R. M. Buehrer, H. Wymeersch, and R. M. Vaghefi, “Collaborative sensor network localization: Algorithms and practical issues,” *Proc. IEEE*, vol. 106, pp. 1089–1114, May 2018.
- [38] F. Meyer, B. Etxzlinger, Z. Liu, F. Hlawatsch, and M. Z. Win, “A scalable algorithm for network localization and synchronization,” *IEEE Internet Things J.*, vol. 5, pp. 4714–4727, Mar. 2018.
- [39] G. Ferri, A. Munafó, and K. D. LePage, “An autonomous underwater vehicle data-driven control strategy for target tracking,” *IEEE J. Ocean. Eng.*, vol. 43, pp. 323–343, Feb. 2018.
- [40] M. Z. Win, A. Conti, S. Mazuelas, Y. Shen, W. M. Gifford, D. Dardari, and M. Chiani, “Network localization and navigation via cooperation,” *IEEE Commun. Mag.*, vol. 49, pp. 56–62, May 2011.
- [41] F. R. Kschischang, B. J. Frey, and H.-A. Loeliger, “Factor graphs and the sum-product algorithm,” *IEEE Trans. Inf. Theory*, vol. 47, pp. 498–519, Feb. 2001.
- [42] M. Z. Win, F. Meyer, Z. Liu, W. Dai, S. Bartoletti, and A. Conti, “Efficient multisensor localization for the internet of things: Exploring a new class of scalable localization algorithms,” *IEEE Signal Process. Mag.*, vol. 35, pp. 153–167, Sep. 2018.
- [43] F. Meyer, H. Wymeersch, M. Fröhle, and F. Hlawatsch, “Distributed estimation with information-seeking control in agent networks,” *IEEE J. Sel. Areas Commun.*, vol. 33, Nov. 2015.
- [44] S. Li, M. Hedley, and I. B. Collings, “New efficient indoor cooperative localization algorithm with empirical ranging error model,” *IEEE J. Sel. Areas Commun.*, vol. 33, pp. 1407–1417, Jul. 2015.
- [45] A. T. Ihler, J. W. Fisher, R. L. Moses, and A. S. Willsky, “Nonparametric belief propagation for self-localization of sensor networks,” *IEEE J. Sel. Areas Commun.*, vol. 23, pp. 809–819, Apr. 2005.
- [46] T. V. Nguyen, Y. Jeong, H. Shin, and M. Z. Win, “Least square cooperative localization,” *IEEE Trans. Veh. Technol.*, vol. 64, pp. 1318–1330, Apr. 2015.
- [47] F. Yin, C. Fritsche, D. Jin, F. Gustafsson, and A. M. Zoubir, “Cooperative localization in wsns using gaussian mixture modeling: Distributed ecm algorithms,” *IEEE Trans. Signal Process.*, vol. 63, pp. 1448–1463, Mar. 2015.
- [48] V. Indelman, E. Nelson, J. Dong, N. Michael, and F. Dellaert, “Incremental distributed inference from arbitrary poses and unknown data association: Using collaborating robots to establish a common reference,” *Control Syst. Mag.*, vol. 36, pp. 41–74, Apr. 2016.
- [49] Y. Shang, W. Rumi, Y. Zhang, and M. Fromherz, “Localization from connectivity in sensor networks,” *IEEE Trans. Parallel Distrib. Syst.*, vol. 15, pp. 961–974, Nov. 2004.

## Bibliography

---

- [50] S. Zhu and Z. Ding, “Distributed cooperative localization of wireless sensor networks with convex hull constraint,” *IEEE Trans. Wireless Commun.*, vol. 10, pp. 2150–2161, Jul. 2011.
- [51] S. Srirangarajan, A. H. Tewfik, and Z. Luo, “Distributed sensor network localization using SOCP relaxation,” *IEEE Trans. Wireless Commun.*, vol. 7, pp. 4886–4895, Dec. 2008.
- [52] P. Biswas, T. . Liang, K. . Toh, Y. Ye, and T. . Wang, “Semidefinite programming approaches for sensor network localization with noisy distance measurements,” *IEEE Trans. Autom. Netw. Sci. Eng.*, vol. 3, pp. 360–371, Oct. 2006.
- [53] T. Jia and R. M. Buehrer, “A set-theoretic approach to collaborative position location for wireless networks,” *IEEE Trans. Mobile Comput.*, vol. 10, pp. 1264–1275, Sep. 2011.
- [54] R. W. Sittler, “An optimal data association problem in surveillance theory,” *IEEE Trans. Mil. Electron.*, vol. 8, pp. 125–139, Apr. 1964.
- [55] R. Singer, R. Sea, and K. Housewright, “Derivation and evaluation of improved tracking filter for use in dense multitarget environments,” *IEEE Trans. Inf. Theory*, vol. 20, pp. 423–432, Jul. 1974.
- [56] Y. Bar-Shalom, “Tracking methods in a multitarget environment,” *IEEE Trans. Autom. Control*, vol. 23, pp. 618–626, Aug. 1978.
- [57] Q. Zhu, T. Li, J. Pan, and Q. Bao, “The modified probability hypothesis density filter with adaptive birth intensity estimation for multi-target tracking in low detection probability,” *IEEE Access*, vol. 8, pp. 43690–43710, Mar. 2020.
- [58] M. Baradaran Khalkhali, A. Vahedian, and H. Sadoghi Yazdi, “Multi-target state estimation using interactive kalman filter for multi-vehicle tracking,” *IEEE Trans. Intell. Transp. Syst.*, vol. 21, pp. 1131–1144, Mar. 2020.
- [59] L. Gao, G. Battistelli, and L. Chisci, “Event-triggered distributed multitarget tracking,” *IEEE Trans. Signal Inf. Process. Netw.*, vol. 5, pp. 570–584, Sep. 2019.
- [60] Y. Yu and Y. Liang, “Distributed multitarget tracking based on diffusion strategies over sensor networks,” *IEEE Access*, vol. 7, pp. 129802–129814, Sep. 2019.
- [61] X. Li, C. Zhao, X. Lu, and W. Wei, “Underwater bearings-only multitarget tracking based on modified PMHT in dense-cluttered environment,” *IEEE Access*, vol. 7, pp. 93678–93689, Jul. 2019.
- [62] F. Meyer, T. Kropfreiter, J. L. Williams, R. Lau, F. Hlawatsch, P. Braca, and M. Z. Win, “Message passing algorithms for scalable multitarget tracking,” *Proc. IEEE*, vol. 106, pp. 221–259, Feb. 2018.

## Bibliography

---

- [63] S. He, H. Shin, and A. Tsourdos, “Distributed joint probabilistic data association filter with hybrid fusion strategy,” *IEEE Trans. Instrum. Meas.*, vol. 69, pp. 286–300, Jan. 2020.
- [64] Kuo-Chu Chang, Chee-Yee Chong, and Y. Bar-Shalom, “Joint probabilistic data association in distributed sensor networks,” *IEEE Trans. Autom. Control*, vol. 31, pp. 889–897, Oct. 1986.
- [65] T. Fortmann, Y. Bar-Shalom, and M. Scheffe, “Sonar tracking of multiple targets using joint probabilistic data association,” *IEEE J. Ocean. Eng.*, vol. 8, pp. 173–184, Jul. 1983.
- [66] T. E. Fortmann, Y. Bar-Shalom, and M. Scheffe, “Multi-target tracking using joint probabilistic data association,” in *1980 IEEE Conf. Decision and Control*, pp. 807–812, Dec. 1980.
- [67] T. L. Song, H. W. Kim, and D. Musicki, “Iterative joint integrated probabilistic data association for multitarget tracking,” *IEEE Trans. Aerosp. Electron. Syst.*, vol. 51, pp. 642–653, Apr. 2015.
- [68] D. Musicki and R. Evans, “Joint integrated probabilistic data association: JIPDA,” *IEEE Trans. Aerosp. Electron. Syst.*, vol. 40, pp. 1093–1099, Sep. 2004.
- [69] D. Reid, “An algorithm for tracking multiple targets,” *IEEE Trans. Autom. Control*, vol. 24, pp. 843–854, Dec. 1979.
- [70] S. Coraluppi and C. A. Carthel, “If a tree falls in the woods, it does make a sound: multiple-hypothesis tracking with undetected target births,” *IEEE Trans. Aerosp. Electron. Syst.*, vol. 50, pp. 2379–2388, Dec. 2014.
- [71] D. E. Clark and J. Bell, “Multi-target state estimation and track continuity for the particle PHD filter,” *IEEE Trans. Aerosp. Electron. Syst.*, vol. 43, pp. 1441–1453, Oct. 2007.
- [72] R. Mahler, “PHD filters of higher order in target number,” *IEEE Trans. Aerosp. Electron. Syst.*, vol. 43, pp. 1523–1543, Oct. 2007.
- [73] B. Ristic, B. Vo, B. Vo, and A. Farina, “A tutorial on Bernoulli filters: Theory, implementation and applications,” *IEEE Trans. Signal Process.*, vol. 61, pp. 3406–3430, Apr. 2013.
- [74] B. Vo, B. Vo, and A. Cantoni, “The cardinality balanced multi-target multi-Bernoulli filter and its implementations,” *IEEE Trans. Signal Process.*, vol. 57, pp. 409–423, Oct. 2009.
- [75] J. L. Williams, “An efficient, variational approximation of the best fitting multi-Bernoulli filter,” *IEEE Trans. Signal Process.*, vol. 63, pp. 258–273, Nov. 2015.
- [76] S. Nannuru, S. Blouin, M. Coates, and M. Rabbat, “Multisensor CPHD filter,” *IEEE Trans. Aerosp. Electron. Syst.*, vol. 52, pp. 1834–1854, Nov. 2016.

- [77] S. Nagappa and D. E. Clark, "On the ordering of the sensors in the iterated-corrector probability hypothesis density (PHD) filter," in *Signal Processing, Sensor Fusion, and Target Recognition XX*, vol. 8050, p. 80500M, International Society for Optics and Photonics, 2011.
- [78] G. Battistelli, L. Chisci, C. Fantacci, A. Farina, and A. Graziano, "Consensus CPHD filter for distributed multitarget tracking," *IEEE J. Sel. Topics Signal Process.*, vol. 7, pp. 508–520, Mar. 2013.
- [79] A. Saucan, M. J. Coates, and M. Rabbat, "A multisensor multi-Bernoulli filter," *IEEE Trans. Signal Process.*, vol. 65, pp. 5495–5509, Jul. 2017.
- [80] R. Mahler, "The multisensor PHD filter: II. Erroneous solution via "Poisson magic"," in *Signal Processing, Sensor Fusion, and Target Recognition XVIII*, vol. 7336, pp. 182 – 193, International Society for Optics and Photonics, SPIE, May. 2009.
- [81] F. Meyer, P. Braca, P. Willett, and F. Hlawatsch, "Scalable multitarget tracking using multiple sensors: a belief propagation approach," in *2015 18th Int. Conf. Inf. Fusion (Fusion)*, pp. 1778–1785, Jul. 2015.
- [82] G. Soldi, F. Meyer, P. Braca, and F. Hlawatsch, "Self-tuning algorithms for multisensor-multitarget tracking using belief propagation," *IEEE Trans. Signal Process.*, vol. 67, pp. 3922–3937, Aug. 2019.
- [83] F. Meyer, P. Braca, P. Willett, and F. Hlawatsch, "A scalable algorithm for tracking an unknown number of targets using multiple sensors," *IEEE Trans. Signal Process.*, vol. 65, pp. 3478–3493, Jul. 2017.
- [84] V. Savic, H. Wymeersch, and E. G. Larsson, "Target tracking in confined environments with uncertain sensor positions," *IEEE Trans. Veh. Technol.*, vol. 65, pp. 870–882, Feb. 2016.
- [85] P. Sharma, A. Saucan, D. J. Bucci, and P. K. Varshney, "Decentralized gaussian filters for cooperative self-localization and multi-target tracking," *IEEE Trans. Signal Process.*, vol. 67, pp. 5896–5911, Nov. 2019.
- [86] P. Sharma, A. Saucan, D. J. Bucci, and P. K. Varshney, "On self-localization and tracking with an unknown number of targets," in *2018 Asilomar Conference on Signals, Systems, and Computers*, pp. 1735–1739, Oct. 2018.
- [87] F. Meyer and M. Z. Win, "Joint navigation and multitarget tracking in networks," in *2018 IEEE Int. Conf. Commun. Workshops (ICC Workshops)*, pp. 1–6, May 2018.
- [88] F. Meyer, O. Hlinka, H. Wymeersch, E. Riegler, and F. Hlawatsch, "Distributed localization and tracking of mobile networks including noncooperative objects," *IEEE Trans. Signal Inf. Process. Netw.*, vol. 2, pp. 57–71, Mar. 2016.
- [89] Y. Bar-Shalom, P. K. Willett, and X. Tian, *Tracking and Data Fusion: A Handbook of Algorithms*. Storrs, CT, USA: YBS Publishing, 2011.

## Bibliography

---

- [90] F. Meyer and M. Z. Win, “Scalable data association for extended object tracking,” *IEEE Trans. Signal Inf. Process. Netw.*, vol. 6, pp. 491–507, May 2020.
- [91] H. Zhang, S. Y. Tan, and C. K. Seow, “TOA-based indoor localization and tracking with inaccurate floor plan map via MRMSC-PHD filter,” *IEEE Sensors J.*, vol. 19, pp. 9869–9882, Jul. 2019.
- [92] H. Loeliger, J. Dauwels, J. Hu, S. Korl, L. Ping, and F. R. Kschischang, “The factor graph approach to model-based signal processing,” *Proc. IEEE*, vol. 95, pp. 1295–1322, Jun. 2007.
- [93] J. Williams and R. Lau, “Approximate evaluation of marginal association probabilities with belief propagation,” *IEEE Trans. Aerosp. Electron. Syst.*, vol. 50, pp. 2942–2959, Oct. 2014.
- [94] D. Schuhmacher, B. Vo, and B. Vo, “A consistent metric for performance evaluation of multi-object filters,” *IEEE Trans. Signal Process.*, vol. 56, pp. 3447–3457, Aug. 2008.
- [95] “IEEE Standard for Information technology– Local and metropolitan area networks– Specific requirements– Part 11: Wireless LAN Medium Access Control (MAC) and Physical Layer (PHY) Specifications Amendment 6: Wireless Access in Vehicular Environments,” *IEEE Std 802.11p-2010 (Amendment to IEEE Std 802.11-2007 as amended by IEEE Std 802.11k-2008, IEEE Std 802.11r-2008, IEEE Std 802.11y-2008, IEEE Std 802.11n-2009, and IEEE Std 802.11w-2009)*, pp. 1–51, Jul. 2010.
- [96] ETSI EN 302 637-2, “Intelligent Transport Systems (ITS); Vehicular Communications; Basic Set of Applications; Part 2: Specification of Cooperative Awareness Basic Service,” Nov. 2014.
- [97] 3GPP TR 22.885 v14.0.0, “3rd Generation Partnership Project; Technical Specification Group Services and System Aspects; Study on LTE support for Vehicle to Everything (V2X) services (Release 14),” Dec. 2015.
- [98] H. Wymeersch, G. Seco-Granados, G. Destino, D. Dardari, and F. Tufvesson, “5G mmWave positioning for vehicular networks,” *IEEE Wireless Commun.*, vol. 24, pp. 80–86, Dec. 2017.
- [99] L. Kong, M. K. Khan, F. Wu, G. Chen, and P. Zeng, “Millimeter-wave wireless communications for IoT-cloud supported autonomous vehicles: overview, design, and challenges,” *IEEE Comm. Mag.*, vol. 55, pp. 62–68, Jan. 2017.
- [100] L. Chen and C. Englund, “Cooperative ITS - EU standards to accelerate cooperative mobility,” in *2014 Int. Conf. Connected Vehicles and Expo (ICCVE)*, pp. 681–686, Nov. 2014.
- [101] H. Wymeersch, G. R. de Campos, P. Falcone, L. Svensson, and E. G. Ström, “Challenges for cooperative ITS: improving road safety through the integration of wireless communications, control, and positioning,” in *2015 Int. Conf. Comput., Netw. and Commun. (ICNC)*, pp. 573–578, Feb. 2015.

## Bibliography

---

- [102] A. Festag, “Standards for Vehicular Communication – from IEEE 802.11p to 5G,” *Elektrotechnik und Informationstechnik*, vol. 132, pp. 409–416, Nov. 2015.
- [103] M. Gerla, E. K. Lee, G. Pau, and U. Lee, “Internet of vehicles: from intelligent grid to autonomous cars and vehicular clouds,” in *2014 IEEE World Forum Internet Things*, pp. 241–246, Mar. 2014.
- [104] S. Kato, S. Tsugawa, K. Tokuda, T. Matsui, and H. Fujii, “Vehicle control algorithms for cooperative driving with automated vehicles and intervehicle communications,” *IEEE Trans. Intell. Transp. Syst.*, vol. 3, pp. 155–161, Sep. 2002.
- [105] S. Kim and W. Liu, “Cooperative autonomous driving: a mirror neuron inspired intention awareness and cooperative perception approach,” *IEEE Intell. Transp. Syst. Mag.*, vol. 8, pp. 23–32, Jul. 2016.
- [106] M. Doring and K. Lemmer, “Cooperative maneuver planning for cooperative driving,” *IEEE Intell. Transp. Syst. Mag.*, vol. 8, pp. 8–22, Fall 2016.
- [107] G. Pocovi, M. Lauridsen, B. Soret, K. I. Pedersen, and P. Mogensen, “Automation for on-road vehicles: use cases and requirements for radio design,” in *2015 IEEE Veh. Technol. Conf. (VTC-Fall)*, pp. 1–5, Sep. 2015.
- [108] 5GPPP, “5G automotive vision,” Oct. 2015.
- [109] D. Caveney, “Cooperative vehicular safety applications,” *IEEE Control Syst.*, vol. 30, pp. 38–53, Aug. 2010.
- [110] S. E. Shladover and S.-K. Tan, “Analysis of vehicle positioning accuracy requirements for communication-based cooperative collision warning,” *J. Intell. Transp. Syst.*, vol. 10, no. 3, pp. 131–140, 2006.
- [111] M. W. M. G. Dissanayake, P. Newman, S. Clark, H. F. Durrant-Whyte, and M. Csorba, “A solution to the simultaneous localization and map muilding (SLAM) problem,” *IEEE Trans. Robot. Autom.*, vol. 17, pp. 229–241, Jun. 2001.
- [112] G. Bresson, Z. Alsayed, L. Yu, and S. Glaser, “Simultaneous localization and mapping: a survey of current trends in autonomous driving,” *IEEE Trans. Intell. Veh.*, vol. 2, pp. 194–220, Sep. 2017.
- [113] C. S. Lee, D. E. Clark, and J. Salvi, “SLAM with dynamic targets via single-cluster PHD filtering,” *IEEE J. Sel. Topics Signal Process.*, vol. 7, pp. 543–552, Jun. 2013.
- [114] J. Levinson and S. Thrun, “Robust vehicle localization in urban environments using probabilistic maps,” in *2010 IEEE Int. Conf. Robot. Autom. (ICRA)*, pp. 4372–4378, May 2010.
- [115] K. lassoued, P. Bonnifait, and I. Fantoni, “Cooperative localization with reliable confidence domains between vehicles sharing GNSS pseudoranges

## Bibliography

---

- errors with no base station,” *IEEE Intell. Transp. Syst. Mag.*, vol. 9, pp. 22–34, Jan 2017.
- [116] J. Liu, B. G. Cai, and J. Wang, “Cooperative localization of connected vehicles: integrating GNSS with DSRC using a robust cubature kalman filter,” *IEEE Trans. Intell. Transp. Syst.*, vol. 18, pp. 2111–2125, Aug. 2017.
- [117] G. M. Hoang, B. Denis, J. Härrri, and D. T. M. Slock, “Cooperative localization in GNSS-aided VANETs with accurate IR-UWB range measurements,” in *2016 Workshop Positioning Navig. and Comm.*, pp. 1–6, Oct. 2016.
- [118] N. Alam, A. T. Balaei, and A. G. Dempster, “Relative positioning enhancement in VANETs: a tight integration approach,” *IEEE Trans. Intell. Transp. Syst.*, vol. 14, pp. 47–55, Mar. 2013.
- [119] M. Rohani, D. Gingras, and D. Gruyer, “A novel approach for improved vehicular positioning using cooperative map matching and dynamic base station DGPS concept,” *IEEE Trans. Intell. Transp. Syst.*, vol. 17, pp. 230–239, Jan. 2016.
- [120] H. Li and F. Nashashibi, “Cooperative multi-vehicle localization using split covariance intersection filter,” *IEEE Intell. Transp. Syst. Mag.*, vol. 5, pp. 33–44, Apr. 2013.
- [121] S. Fujii, A. Fujita, T. Umedu, S. Kaneda, H. Yamaguchi, T. Higashino, and M. Takai, “Cooperative vehicle positioning via V2V communications and onboard sensors,” in *2011 IEEE Veh. Technol. Conf. (VTC-Fall)*, pp. 1–5, Sep. 2011.
- [122] N. Alam, A. T. Balaei, and A. G. Dempster, “A DSRC doppler-based cooperative positioning enhancement for vehicular networks with GPS availability,” *IEEE Trans. Veh. Technol.*, vol. 60, pp. 4462–4470, Nov. 2011.
- [123] N. M. Drawil and O. Basir, “Intervehicle-communication-assisted localization,” *IEEE Trans. Intell. Transp. Syst.*, vol. 11, pp. 678–691, Sep. 2010.
- [124] S. Severi, h. Wymeersch, J. Härrri, M. Ulmschneider, B. Denis, and M. Bartels, “Beyond GNSS: highly accurate localization for cooperative-intelligent transport systems,” in *2018 IEEE Wireless Comm. Netw. Conf. (WCNC)*, Apr. 2018.
- [125] S. Kuutti, S. Fallah, K. Katsaros, M. Dianati, F. Mccullough, and A. Mouzakis, “A survey of the state-of-the-art localization techniques and their potentials for autonomous vehicle applications,” *IEEE Internet Things J.*, vol. 5, pp. 829–846, Apr. 2018.
- [126] N. Alam and A. G. Dempster, “Cooperative positioning for vehicular networks: facts and future,” *IEEE Trans. Intell. Transp. Syst.*, vol. 14, pp. 1708–1717, Dec. 2013.
- [127] M. Rohani, D. Gingras, V. Vigneron, and D. Gruyer, “A new decentralized bayesian approach for cooperative vehicle localization based on fusion of GPS

## Bibliography

---

- and vanet based inter-vehicle distance measurement,” *IEEE Intel. Transp. Syst. Mag.*, vol. 7, pp. 85–95, Summer 2015.
- [128] R. Parker and S. Valaee, “Vehicular node localization using received-signal-strength indicator,” *IEEE Trans. Veh. Technol.*, vol. 56, pp. 3371–3380, Nov. 2007.
- [129] A. Fascista, G. Ciccarese, A. Coluccia, and G. Ricci, “Angle of arrival-based cooperative positioning for smart vehicles,” *IEEE Trans. Intell. Transp. Syst.*, pp. 1–13, Nov. 2017.
- [130] G. Soatti, M. Nicoli, N. Garcia, B. Denis, R. Raulefs, and H. Wymeersch, “Enhanced vehicle positioning in cooperative ITS by joint sensing of passive features,” in *2017 IEEE Int. Conf. Intell. Transp. Syst. (ITSC)*, pp. 1–6, Oct. 2017.
- [131] G. Soatti, M. Nicoli, N. Garcia, B. Denis, R. Raulefs, and H. Wymeersch, “Implicit cooperative positioning in vehicular networks,” *IEEE Trans. Intell. Transp. Syst.*, vol. 19, pp. 3964–3980, Dec. 2018.
- [132] M. Frohle, C. Lindberg, and H. Wymeersch, “Cooperative localization of vehicles without inter-vehicle measurements,” in *2018 IEEE Wireless Comm. Netw. Conf. (WCNC)*, Apr. 2018.
- [133] F. R. Kschischang, B. J. Frey, and H. A. Loeliger, “Factor graphs and the sum-product algorithm,” *IEEE Trans. Inf. Theory*, vol. 47, pp. 498–519, Feb. 2001.
- [134] R. Olfati-Saber, J. A. Fax, and R. M. Murray, “Consensus and cooperation in networked multi-agent systems,” *Proc. IEEE*, vol. 95, pp. 215–233, Jan. 2007.
- [135] V. Astarita, V. Giofré, G. Guido, and A. Vitale, “The use of adaptive traffic signal systems based on floating car data,” *Wireless Comm. and Mobile Comput.*, vol. 2017, Dec. 2017.
- [136] “Exploring GLOSA Systems in the Field: technical Evaluation and Results,” *Computer Communications*, vol. 120, pp. 112 – 124, May 2018.
- [137] F. Gustafsson and F. Gunnarsson, “Mobile Positioning Using Wireless Networks: possibilities and Fundamental Limitations based on Available Wireless Network Measurements,” *IEEE Signal Process. Mag.*, vol. 22, pp. 41–53, Jul. 2005.
- [138] H. A. Loeliger, “An introduction to factor graphs,” *IEEE Signal Process. Mag.*, vol. 21, pp. 28–41, Jan. 2004.
- [139] M. S. Arulampalam, S. Maskell, N. Gordon, and T. Clapp, “A tutorial on particle filters for online nonlinear/non-Gaussian Bayesian tracking,” *IEEE Trans. Signal Process.*, vol. 50, pp. 174–188, Feb. 2002.
- [140] F. de Ponte Müller, “Survey on ranging sensors and cooperative techniques for relative positioning of vehicles,” *Sensors*, vol. 17, Feb. 2017.

## Bibliography

---

- [141] J. Barceló and J. Casas, *Dynamic Network Simulation with AIMSUN*, pp. 57–98. Boston, MA: Springer US, 2005.
- [142] F. Defflorio and L. Castello, “Assessing the performance of a charge-while-driving system in urban arterial roads: insight from a microsimulation model,” *IET Intell. Transp. Syst.*, vol. 9, pp. 505–514, Jun. 2015.
- [143] P. Hidas, “Modelling vehicle interactions in microscopic simulation of merging and weaving,” *Transp. Research Part C: emerging Technologies*, vol. 13, pp. 37–62, Jan. 2005.
- [144] SAE International, *Taxonomy and definitions for terms related to on-road motor vehicle automated driving systems*, Jan. 2014.
- [145] R. Tachet, P. Santi, S. Sobolevsky, L. I. Reyes-Castro, E. Frazzoli, D. Helbing, and C. Ratti, “Revisiting street intersections using slot-based systems,” *PLOS ONE*, vol. 11, pp. 1–9, Mar. 2016.
- [146] L. Li, D. Wen, and D. Yao, “A survey of traffic control with vehicular communications,” *IEEE Trans. Intell. Transp. Syst.*, vol. 15, pp. 425–432, Aug. 2014.
- [147] F. Duarte and C. Ratti, “The impact of autonomous vehicles on cities: a review,” *J. Urban Technol.*, vol. 25, pp. 3–18, Jul. 2018.
- [148] C.-Y. Chan, “Advancements, prospects, and impacts of automated driving systems,” *Int. J. Transp. Sci. Technol.*, vol. 6, pp. 208–216, Sep. 2017.
- [149] J. G. Andrews, S. Buzzi, W. Choi, S. V. Hanly, A. Lozano, A. C. Soong, and J. C. Zhang, “What will 5G be?,” *IEEE J. Sel. Areas Commun.*, vol. 32, pp. 1065–1082, Jun. 2014.
- [150] P. Popovski, K. F. Trillingsgaard, O. Simeone, and G. Durisi, “5G wireless network slicing for eMBB, URLLC, and mMTC: a communication-theoretic view,” *IEEE Access*, vol. 6, pp. 55765–55779, Sep. 2018.
- [151] 3GPP, “Study on enhancement of 3GPP support for 5G V2X services (Release 16),” 3rd Generation Partnership Project, TR 22.886 V16.2.0, Dec. 2018.
- [152] J. Choi, V. Va, N. González-Prelcic, R. Daniels, C. R. Bhat, and R. W. Heath, “Millimeter-wave vehicular communication to support massive automotive sensing,” *IEEE Commun. Mag.*, vol. 54, pp. 160–167, Dec. 2016.
- [153] IEEE, “IEEE Standard for Information Technology – Telecommunications and Information Exchange Between Systems – Local and Metropolitan Area Networks – Specific Requirements Part 11: Wireless LAN Medium Access Control (MAC) and Physical Layer (PHY) Specifications Amendment 10: Mesh Networking,” *IEEE Std 802.11s-2011 (Amendment to IEEE Std 802.11-2007 as amended by IEEE 802.11k-2008, IEEE 802.11r-2008, IEEE 802.11y-2008, IEEE 802.11w-2009, IEEE 802.11n-2009, IEEE 802.11p-2010, IEEE 802.11z-2010, IEEE 802.11v-2011, and IEEE 802.11u-2011)*, pp. 1–372, Sep. 2011.

## Bibliography

---

- [154] European Commission, “2008/671/EC: Commission decision of 5 August 2008 on the harmonised use of radio spectrum in the 5875 - 5905 MHz frequency band for safety-related applications of Intelligent Transport Systems (ITS),” *Official Journal of the European Union*, Aug. 2008.
- [155] C-Roads, “Radio frequencies designated for enhanced road safety in Europe - C-Roads position on the usage of the 5.9 GHz band.” [https://www.c-roads.eu/fileadmin/user\\_upload/media/Dokumente/C-Roads\\_Position\\_paper\\_on\\_59GHz\\_final.pdf](https://www.c-roads.eu/fileadmin/user_upload/media/Dokumente/C-Roads_Position_paper_on_59GHz_final.pdf), Sep. 2017. (Accessed on 01.07.2020).
- [156] C2C-CC, “CAR 2 CAR communication consortium manifesto: overview of the C2C-CC system.” [https://www.car-2-car.org/fileadmin/documents/General\\_Documents/C2C-CC\\_Manifesto\\_Aug\\_2007.pdf](https://www.car-2-car.org/fileadmin/documents/General_Documents/C2C-CC_Manifesto_Aug_2007.pdf), Aug. 2007. (Accessed on 01.07.2020).
- [157] 5GAA, “The case for cellular V2X for safety and cooperative driving.” <https://5gaa.org/wp-content/uploads/2017/10/5GAA-whitepaper-23-Nov-2016.pdf>, Nov. 2016. (Accessed on 01.07.2020).
- [158] S. Zeadally, M. A. Javed, and E. B. Hamida, “Vehicular communications for ITS: standardization and challenges,” *IEEE Commun. Standards Mag.*, vol. 4, pp. 11–17, Mar. 2020.
- [159] G. Naik, B. Choudhury, and J. Park, “IEEE 802.11bd & 5G NR V2X: evolution of radio access technologies for V2X communications,” *IEEE Access*, vol. 7, pp. 70169–70184, May 2019.
- [160] S. Han, C. I, Z. Xu, and C. Rowell, “Large-scale antenna systems with hybrid analog and digital beamforming for millimeter wave 5G,” *IEEE Commun. Mag.*, vol. 53, pp. 186–194, Jan. 2015.
- [161] S. Kuttty and D. Sen, “Beamforming for millimeter wave communications: an inclusive survey,” *IEEE Commun. Surveys Tuts.*, vol. 18, pp. 949–973, Secondquarter 2016.
- [162] A. F. Molisch, V. V. Ratnam, S. Han, Z. Li, S. L. H. Nguyen, L. Li, and K. Haneda, “Hybrid beamforming for massive MIMO: a survey,” *IEEE Commun. Mag.*, vol. 55, pp. 134–141, Sep. 2017.
- [163] L. Combi and U. Spagnolini, “Adaptive optical processing for wideband hybrid beamforming,” *IEEE Trans. Commun.*, vol. 67, pp. 4967–4979, Jul. 2019.
- [164] O. E. Ayach, S. Rajagopal, S. Abu-Surra, Z. Pi, and R. W. Heath, “Spatially sparse precoding in millimeter wave MIMO systems,” *IEEE Trans. Wireless Commun.*, vol. 13, pp. 1499–1513, Mar. 2014.
- [165] J. Wang, “Beam codebook based beamforming protocol for multi-Gbps millimeter-wave WPAN systems,” *IEEE J. Sel. Areas Commun.*, vol. 27, pp. 1390–1399, Oct. 2009.

## Bibliography

---

- [166] S. Hur, T. Kim, D. J. Love, J. V. Krogmeier, T. A. Thomas, and A. Ghosh, “Millimeter wave beamforming for wireless backhaul and access in small cell networks,” *IEEE Trans. Commun.*, vol. 61, pp. 4391–4403, Oct. 2013.
- [167] B. Li, Z. Zhou, W. Zou, X. Sun, and G. Du, “On the efficient beam-forming training for 60GHz wireless personal area networks,” *IEEE Trans. Wireless Commun.*, vol. 12, pp. 504–515, Feb. 2013.
- [168] A. Alkhateeb, O. E. Ayach, G. Leus, and R. W. Heath, “Channel estimation and hybrid precoding for millimeter wave cellular systems,” *IEEE J. Sel. Topics Signal Process.*, vol. 8, pp. 831–846, Oct. 2014.
- [169] T. Nitsche, A. B. Flores, E. W. Knightly, and J. Widmer, “Steering with eyes closed: mm-wave beam steering without in-band measurement,” in *2015 IEEE Conf. Comput. Commun. (INFOCOM)*, pp. 2416–2424, Apr. 2015.
- [170] F. Devoti, I. Filippini, and A. Capone, “Facing the millimeter-wave cell discovery challenge in 5G networks with context-awareness,” *IEEE Access*, vol. 4, pp. 8019–8034, Nov. 2016.
- [171] C. Perfecto, J. D. Ser, and M. Bennis, “Millimeter-wave V2V communications: distributed association and beam alignment,” *IEEE J. Sel. Areas Commun.*, vol. 35, pp. 2148–2162, Sep. 2017.
- [172] N. González-Prelcic, R. Mèndez-Rial, and R. W. Heath, “Radar aided beam alignment in mmwave V2I communications supporting antenna diversity,” in *2016 Inf. Theory and Appl. Workshop (ITA)*, pp. 1–7, Jan. 2016.
- [173] V. Va, T. Shimizu, G. Bansal, and R. W. Heath, “Beam design for beam switching based millimeter wave vehicle-to-infrastructure communications,” in *2016 IEEE Int. Conf. Commun. (ICC)*, pp. 1–6, May 2016.
- [174] N. Garcia, H. Wymeersch, E. G. Ström, and D. Slock, “Location-aided mm-wave channel estimation for vehicular communication,” in *IEEE Int. Workshop Signal Process. Advances in Wireless Commun. (SPAWC)*, pp. 1–5, Jul. 2016.
- [175] I. Mavromatis, A. Tassi, R. J. Piechocki, and A. Nix, “mmWave system for future ITS: a MAC-layer approach for V2X beam steering,” in *IEEE Veh. Technol. Conf. (VTC-Fall)*, pp. 1–6, Sep. 2017.
- [176] D. Killinger, “Free space optics for laser communication through the air,” *Opt. Photon. News*, vol. 13, pp. 36–42, Oct. 2002.
- [177] S. Bloom, E. Korevaar, J. Schuster, and H. Willebrand, “Understanding the performance of free-space optics (invited),” *J. Opt. Netw.*, vol. 2, pp. 178–200, Jun. 2003.
- [178] Z. Ghassemlooy and W. O. Popoola, *Terrestrial free-space optical communications*. InTech, 2010.

## Bibliography

---

- [179] A. Kaadan, H. H. Refai, and P. G. LoPresti, “Multielement FSO transceivers alignment for inter-UAV communications,” *J. Lightw. Technol.*, vol. 32, pp. 4785–4795, Dec. 2014.
- [180] F. Moll, J. Horwath, A. Shrestha, M. Brechtelsbauer, C. Fuchs, L. A. M. Navajas, A. M. L. Souto, and D. D. González, “Demonstration of high-rate laser communications from a fast airborne platform,” *IEEE J. Sel. Areas Commun.*, vol. 33, pp. 1985–1995, Sep. 2015.
- [181] H. Kaushal and G. Kaddoum, “Optical communication in space: challenges and mitigation techniques,” *IEEE Commun. Surveys Tuts.*, vol. 19, pp. 57–96, Aug. 2017.
- [182] Y. Kaymak, R. Rojas-Cessa, J. Feng, N. Ansari, and M. Zhou, “On divergence-angle efficiency of a laser beam in free-space optical communications for high-speed trains,” *IEEE Trans. Veh. Technol.*, vol. 66, pp. 7677–7687, Sep. 2017.
- [183] B. Epple and H. Henniger, “Free-space optical transmission improves land-mobile communications,” *SPIE Newsroom*, Jan. 2007.
- [184] R. Nebuloni and C. Capsoni, *Effects of Adverse Weather on Free Space Optics*, pp. 47–68. Springer, Aug. 2016.
- [185] L. C. Andrews, R. L. Phillips, C. Y. Hopen, and M. A. Al-Habash, “Theory of optical scintillation,” *J. Opt. Soc. Am. A*, vol. 16, pp. 1417–1429, Jun. 1999.
- [186] D. Tagliaferri, A. Matera, C. Capsoni, and U. Spagnolini, “Nonlinear visible light communications broadcast channel precoding: a new solution for in-flight systems,” *IEEE Photon. J.*, vol. 10, pp. 1–14, Aug. 2018.
- [187] Y. Kaymak, R. Rojas-Cessa, J. Feng, N. Ansari, M. Zhou, and T. Zhang, “A survey on acquisition, tracking, and pointing mechanisms for mobile free-space optical communications,” *IEEE Commun. Surveys Tuts.*, vol. 20, pp. 1104–1123, Feb. 2018.
- [188] B. Epple, “Using a GPS-aided inertial system for coarse-pointing of free-space optical communication terminals,” in *Free-Space Laser Communications VI*, vol. 6304, International Society for Optics and Photonics, 2006.
- [189] 3GPP TS 22.186 v16.2.0, “3rd Generation Partnership Project; technical specification group services and system aspects; study on enhancement of 3GPP support for 5G V2X services (Release 16),” Nov. 2020.
- [190] M. Giordani, M. Polese, A. Roy, D. Castor, and M. Zorzi, “A tutorial on beam management for 3GPP NR at mmwave frequencies,” *IEEE Commun. Surveys Tuts.*, vol. 21, pp. 173–196, Sep. 2019.
- [191] M. Kok, J. D. Hol, and T. B. Schön, “Using inertial sensors for position and orientation estimation,” *Foundations and Trends on Signal Processing*, vol. 11, pp. 1–153, Nov. 2017.

## Bibliography

---

- [192] F. Zhang, H. Stähle, G. Chen, C. C. C. Simon, C. Buckl, and A. Knoll, “A sensor fusion approach for localization with cumulative error elimination,” in *2012 IEEE Int. Conf. Multisensor Fusion and Integration for Intell. Syst. (MFI)*, pp. 1–6, Nov. 2012.
- [193] IEEE, “IEEE Standard for Information technology–Telecommunications and information exchange between systems–Local and metropolitan area networks–Specific requirements–Part 11: Wireless LAN Medium Access Control (MAC) and Physical Layer (PHY) Specifications Amendment 3: Enhancements for Very High Throughput in the 60 GHz Band,” *IEEE Std 802.11ad-2012 (Amendment to IEEE Std 802.11-2012, as amended by IEEE Std 802.11ae-2012 and IEEE Std 802.11aa-2012)*, pp. 1–628, Dec. 2012.
- [194] IEEE, “IEEE Draft Standard for Information Technology–Telecommunications and Information Exchange Between Systems Local and Metropolitan Area Networks–Specific Requirements Part 11: Wireless LAN Medium Access Control (MAC) and Physical Layer (PHY) Specifications–Amendment: Enhanced Throughput for Operation in License-Exempt Bands Above 45 GHz,” *IEEE P802.11ay/D3.0*, pp. 1–763, Mar. 2019.
- [195] M. Marciniak, “International standards for optical wireless communications: state-of-the-art and future directions,” in *Advanced Free-Space Optical Communication Techniques and Applications III*, vol. 10437, p. 1043706, International Society for Optics and Photonics, 2017.
- [196] G. Noh, J. Kim, H. Chung, and I. Kim, “Realizing multi-Gbps vehicular communication: Design, implementation, and validation,” *IEEE Access*, vol. 7, pp. 19435–19446, Jan. 2019.
- [197] O. Jo, J. Kim, J. Yoon, D. Choi, and W. Hong, “Exploitation of dual-polarization diversity for 5G millimeter-wave MIMO beamforming systems,” *IEEE Trans. Antennas Propag.*, vol. 65, pp. 6646–6655, Oct. 2017.
- [198] G. Soatti, A. Murtada, M. Nicoli, J. Gambini, and U. Spagnolini, “Low-rank channel and interference estimation in mm-wave massive antenna arrays,” in *2018 European Signal Process. Conf. (EUSIPCO)*, pp. 922–926, Sep. 2018.
- [199] M. R. Akdeniz, Y. Liu, M. K. Samimi, S. Sun, S. Rangan, T. S. Rappaport, and E. Erkip, “Millimeter wave channel modeling and cellular capacity evaluation,” *IEEE J. Sel. Areas Commun.*, vol. 32, pp. 1164–1179, Jun. 2014.
- [200] I. Mirrorcle Technologies, *Mirrorcle technologies MEMS mirrors - technical overview*, 2018.
- [201] R. M. Gagliardi and S. Karp, *Optical communications*. Wiley, 1995.
- [202] Huawei, “Hardware calibration requirement for dual layer beamforming,” 3GPP TSG RAN WG1 Meeting, R1-092359, San Francisco, 2009.

## Bibliography

---

- [203] E. Björnson, J. Hoydis, M. Kountouris, and M. Debbah, “Massive MIMO systems with non-ideal hardware: energy efficiency, estimation, and capacity limits,” *IEEE Trans. Inf. Theory*, vol. 60, pp. 7112–7139, Nov. 2014.
- [204] J. Hecht, “Photonic frontiers: eye-safe lasers - retina-safe wavelengths benefit open-air applications,” *Laser Focus World*, Mar. 2008.
- [205] N. Corporation, *High-speed receivers - high-speed detectors: user’s guide*, 2013.
- [206] H. Macleod, *Thin film-optical filters*. Series in Optics and Optoelectronics, Bristol, UK: CRC Press, 3 ed., 2001.
- [207] I. T. U. Telecommunication, “ITU-T G.975.1 Recommendation: Forward error correction for high bit-rate DWDM submarine systems,” series g recommendation: transmission systems and media, digital systems and networks: digital sections and digital line systems - optical fibre submarine cable systems, ITU, Feb. 2004.
- [208] G. Tzimpragos, C. Kachris, I. B. Djordjevic, M. Cvijetic, D. Soudris, and I. Tomkos, “A survey on FEC codes for 100 G and beyond optical networks,” *IEEE Commun. Surveys Tuts.*, vol. 18, pp. 209–221, Firstquarter 2016.
- [209] Bosch, *BMI055 - Small, versatile 6DoF sensor module*, 2014.
- [210] C. A. Gueymard, “Parameterized transmittance model for direct beam and circumsolar spectral irradiance,” *Solar Energy*, vol. 71, pp. 325–346, Nov. 2001.
- [211] 3GPP TR 38.901 V16.1.0, “Study on channel model for frequencies from 0.5 to 100 GHz (Release 14),” tech. rep., Dec. 2019.
- [212] METIS, “METIS channel model,” METIS2020, D1.4 v3, Jul. 2015.
- [213] MiWeb, “WP5: propagation, antennas and multi-antenna technique; D5.1: channel modeling and characterization,” Tech. Rep. D5.1, Jun. 2014.
- [214] 5GCM White Paper, “5G channel model for bands up to 100 GHz,” v2.0, <http://www.5gworkshops.com/>, Oct. 2016.
- [215] M. K. Samimi and T. S. Rappaport, “3-D millimeter-wave statistical channel model for 5G wireless system design,” *IEEE Trans. Microw. Theory Techn.*, vol. 64, pp. 2207–2225, Jul. 2016.
- [216] M. Nicoli, O. Simeone, and U. Spagnolini, “Multislot estimation of fast-varying space-time communication channels,” *IEEE Trans. Signal Process.*, vol. 51, pp. 1184–1195, May 2003.
- [217] M. Cerutti, M. Nicoli, and U. Spagnolini, “Low-latency low-complexity subspace methods for mmwave MIMO-OFDM channel estimation,” in *2020 IEEE Int. Conf. Commun. (ICC)*, Jun. 2020.

## Bibliography

---

- [218] S. Ju and T. S. Rappaport, “Simulating motion - incorporating spatial consistency into NYUSIM channel model,” in *2018 IEEE Veh. Technol. Conf. (VTC-Fall)*, pp. 1–6, Aug. 2018.
- [219] Y. Wang, Z. Shi, L. Huang, Z. Yu, and C. Cao, “An extension of spatial channel model with spatial consistency,” in *2016 IEEE Veh. Technol. Conf. (VTC-Fall)*, pp. 1–5, Sep. 2016.
- [220] S. Rangan, T. S. Rappaport, and E. Erkip, “Millimeter-wave cellular wireless networks: potentials and challenges,” *Proc. IEEE*, vol. 102, pp. 366–385, Mar. 2014.
- [221] S. Ju and T. S. Rappaport, “Millimeter-wave extended NYUSIM channel model for spatial consistency,” in *2018 IEEE Global Commun. Conf. (GLOBECOM)*, pp. 1–6, Dec. 2018.

